DISS. ETH No. 22307

Development and spectroscopic applications of a coherent, narrowband radiation source tunable from 0.1 to 14 THz

A thesis submitted to attain the degree of
DOCTOR OF SCIENCES of ETH ZURICH

presented by
CHRISTA HAASE
MSc ETH Chemistry

born on 18th of March 1987
citizen of Germany

accepted on the recommendation of
Prof. Dr. F. Merkt, examiner
Prof. Dr. J. Faist, co-examiner

2015

Für meine Eltern und meinen Bruder

Success is not final, failure is not fatal:
it is the courage to continue that counts.

Winston Churchill

Acknowledgements

I would like to thank all the people who have helped me in various ways and from whom I have learned during the delightful years I have spent as a PhD student at ETH. In particular I would like to thank:

My advisor Prof. Frédéric Merkt for all his support and guidance. I would like to thank you for your enthusiasm, your encouragement, your patience, your dedication and for the many things I have had the opportunity to learn from you throughout the years.

Prof. Jérôme Faist for being my co-referee.

Jinjun Liu for working with me during my first year as a PhD student and for sharing his experimental and theoretical knowledge with me. I would like to thank him for his enthusiastic view on THz radiation and spectroscopy and the advice he has given me.

Martin Schäfer for his (almost) unlimited knowledge of the Xe atom and for sharing his MQDT calculations with me.

Maximilian Beyer for his contributions to the para H_2 project and the fun nights in the lab.

Urs Hollenstein for always being there, inside the lab and out, when help was needed.

The entire staff of the electronics and mechanics workshops. One of the most enjoyable and productive aspects of working in the Laboratory of Physical Chemistry is having the opportunity to work with you. The experimental developments of my work would have been much more daunting without your help. In particular, I would like to thank Seppi Agner, Hansjürg Schmutz, and David Stapfer.

Irène Müller for her administrative support, insight, and her humor. Christa Leumann for her administrative support since last year and for her thoughtfulness.

All of the current and former members of the Merkt group (Alex, Bérenger, Christian, Clément, Daniel, Heiner, Jinjun, Johannes, Julie, Lorena, Paul, Pitt, Konstantina, Martin, Matija, Matthias, Maximilian, Michael, Monika, Sandro, Seppi, Stephen, Ugo) for the time we have spent together and all that I have learned from you.

My office mates Michael and Heiner for the hours we spent together, for your help, the laughter and the scientific discussions we have shared.

My parents and my brother for always being there and believing in me. I do not take this for granted and consider myself very lucky to have you in my life.

My friends for their help, their kindness, their compassion, their laughter, and their support. I cannot imagine the past few years without you. Specifically I would like to thank Anne, Lea, Ingrid, Lorena, Charlotte, and Irina.

Abstract

This thesis is concerned with the development and spectroscopic applications of a broadly tunable (tunable range $0.1 - 14\,\mathrm{THz}$), narrow-bandwidth ($2.8\,\mathrm{MHz}$), laser-based, table-top source of far-infrared radiation. It also describes a vacuum-ultraviolet-far-infrared double-resonance spectrometer in which this new source of radiation was integrated. This spectrometer was used to measure high-resolution spectra of high Rydberg states of Xe and para-H_2. The use of vacuum-ultraviolet (VUV) radiation in the double-resonance process enables the detection of low-frequency transitions by monitoring the photoionization yield of electrons and ions produced by pulsed electric fields in experiments involving Rydberg states. The detection of ions further permits mass selective detection of the carriers of the spectra.

After an introduction to radiation sources in the far-infrared and to Rydberg states of atoms and molecules in Chapter 1, Chapter 2 describes the principle of operation of the spectrometer, the principles of the far-infrared generation process and all relevant aspects of the measurement procedures and apparatuses, including the nonlinear optical methods employed to generate far-infrared and VUV laser radiation.

Chapter 3 is devoted to a study of the lowest frequency fundamental bands (asymmetric deformation modes) of selected isotopomers of chloroform and freon-11 ($CFCl_3$) in the frequency range $7.5 - 8\,\mathrm{THz}$. This far-infrared radiation was generated by difference-frequency mixing in a *trans*-4′-(dimethylamino)-*N*-methyl stilbazolium tosylate crystal. The spectra were measured in a static cell at ambient temperature using a laser-based source of tunable radiation in the terahertz region of the electromagnetic spectrum. The analysis of the rotational contours of the bands enabled the derivation of the fundamental frequencies with an accuracy of better than 3 GHz.

The principles of VUV-far-infrared double-resonance spectroscopy are illustrated in Chapter 4 by a study of high Rydberg states of Xe with principal quantum number n between 80 and 100 using a backward-wave oscillator tunable between 240 and 380 GHz as far-infrared radiation source. This chapter is also devoted to the analysis of systematic errors in spectroscopic investigations of high Rydberg states. Methods are presented with which stray electric fields were compensated to levels below 1 mV/cm and stray magnetic fields to levels below 10 mG. The mass selectivity of the detection permitted the simultaneous acquisition of spectra of the main isotopes of Xe in different mass channels. The study focused on the properties of s and d Rydberg states of ^{129}Xe (nuclear spin $I = 1/2$) and ^{132}Xe ($I = 0$)

and, in particular, on the differences in the spectra of these two isotopes resulting from the nuclear spin of ^{129}Xe. The associated hyperfine structures provided access to dynamical parameters such as the strength of the interaction between s and d Rydberg states that are not accessible from the spectrum of ^{132}Xe. The spectroscopic results were used to validate the parameters of a multichannel-quantum-defect-theory model of the ionization channels of atomic Xe.

Chapter 5 is also devoted to a study of the Rydberg states of Xe, but in a region of principal quantum number ($n = 15 - 35$) for which a far-infrared source tunable up to 14 THz is required. The source used in this study was the same source as that used in the study presented in Chapter 3 but with difference-frequency generation integrated in the vacuum chamber to avoid absorption of the far-infrared radiation by water vapor. By varying the pulse length of the near-infrared laser used to generate the far-infrared radiation, the bandwidth of the radiation could be adjusted between 85 MHz and 2.8 MHz. Spectra of transitions between nd and n'f Rydberg states were recorded for the main natural isotopes of Xe. A total of 72 transitions were measured in the range between 0.937 THz and 14.245 THz and their frequencies are compared with frequencies calculated by multichannel-quantum-defect theory. The frequency calibration of the far-infrared radiation was performed with an accuracy of up to 2.8 MHz. The narrowest lines observed experimentally had a full-width at half-maximum of ~ 3 MHz, which was sufficient to fully resolve the hyperfine structure of the Rydberg-Rydberg transitions of ^{129}Xe and ^{131}Xe.

Chapter 6 presents a measurement of the Rydberg-Rydberg transitions in para-H_2, which were used to determine, for the first time, the energy interval between the two lowest rotational levels ($N^+ = 0$ and $N^+ = 2$) of para-H_2^+ at high resolution. The procedure relied on the determination of a network of transitions connecting d, p and f Rydberg states belonging to series converging on the $X^+\,^2\Sigma_g^+$ ($v^+ = 0$, $N^+ = 0$ and 2) ionization thresholds. This network enabled the extrapolation of the positions of these ionization thresholds, and thus the determination of their energy difference, with an accuracy corresponding to 2.9 MHz. The thesis ends with short conclusions.

Zusammenfassung

Thema dieser Dissertation sind die Entwicklung und die spektroskopischen Anwendungen einer kompakten, laser-basierten, breit abstimmbaren (im Bereich zwischen 0.1 und 14 THz) Quelle schmalbandiger (2.8 MHz), ferninfraroter Strahlung. Ferner wird ein vakuumultraviolett-ferninfrarot Doppelresonanzspektrometer beschrieben, in welches die neue Strahlungsquelle integriert wurde. Dieses Spektrometer wurde verwendet um hochaufgelöste Spektren hoher Rydberg-Zustände von Xe und para-H_2 aufzunehmen. Die Verwendung von vakuumultravioletter (VUV) Strahlung im Doppelresonanz-Prozess erlaubt die Detektion tieffrequenter Übergänge, indem die Photoionisationsausbeute von Elektronen und Ionen gemessen wird, die durch gepulste elektrische Felder nach der Anregung von Rydberg-Zuständen erzeugt werden. Des Weiteren erlaubt die Detektion von Ionen die massenselektive Detektion der Träger der Spektren.

Nach einer Einführung in die Strahlungsquellen im Infrarot-Bereich und in die Rydberg-Zustände von Atomen und Molekülen in Kapitel 1 beschreibt Kapitel 2 die Funktionsweise des Spektrometers, das Erzeugungsprinzip der ferninfraroten Strahlung und alle relevanten Aspekte der Messvorgänge und -apparaturen, einschliesslich der nichtlinearen optischen Methoden, die verwendet wurden um die ferninfrarote und VUV Strahlung zu erzeugen.

Kapitel 3 widmet sich einer Untersuchung der tieffrequentesten fundamentalen Banden (asymmetrische Deformationsmoden) ausgewählter Isotopomere von Chloroform und Freon-11 ($CFCl_3$) im Frequenzbereich zwischen $7.5 - 8$ THz. Diese Ferninfrarotstrahlung wurde durch Differenzfrequenzmischung in einem *trans*-4′-(dimethylamino)-*N*-methyl-stilbazoltosylat Kristall erzeugt. Die Spektren wurden in einer statischen Zelle bei Raumtemperatur gemessen, unter Verwendung einer laserbasierten Quelle abstimmbarer Strahlung im Terahertz-Bereich des elektromagnetischen Spektrums. Die Untersuchung der Rotationskontouren der Banden erlaubte die Ableitung der fundamentalen Übergangsfrequenzen mit einer Genauigkeit unter 3 GHz.

Die Grundlagen der VUV-ferninfraroten Doppleresonanz-Spektroskopie werden anhand der Untersuchung hoher Rydbergzustände von Xe mit einer Hauptquantenzahl n zwischen 80 und 100 verdeutlicht, für die eine Backward-Wave Oscillator-Quelle ferninfraroter Strahlung verwendet wurde, die im Bereich zwischen 240 und 380 GHz abstimmbar ist. Dieses Kapitel widmet sich ferner der Analyse systematischer Fehler in spektroskopischen Untersuchungen hoher Rydberg-Zustände. Es werden Methoden dargestellt, welche elektrische Streufelder auf weniger als 1 mV/cm kompensieren, sowie magnetische Streufelder auf we-

niger als 10 mG reduzieren. Die massenselektive Detektion ermöglichte die gleichzeitige Aufnahme der Spektren der Hauptisotope von Xe auf unterschiedlichen Massenkanälen. Die Studie konzentrierte sich auf die Eigenschaften von s und d Rydberg-Zuständen von ^{129}Xe (Kernspin $I = 1/2$) und ^{132}Xe ($I = 0$) und, im besonderen, auf die Unterschiede zwischen den Spektren dieser beiden Isotope, welche auf den Kernspin von ^{129}Xe zurückzuführen sind. Die damit verbundene Hyperfeinstruktur erlaubte Zugang zu den dynamischen Parametern wie die Stärke der Wechselwirkung zwischen s und d Rydbergzuständen, die aus den Spektren von ^{132}Xe nicht zugänglich sind. Die spektroskopischen Ergebnisse wurden verwendet um die Parameter eines Multikanal Quantendefekttheorie-Modells für die Ionisationskanäle von atomarem Xe zu bestätigen.

Kapitel 5 behandelt ebenfalls die Untersuchung von Rydberg-Zuständen in Xe, aber in einem Bereich der Hauptquantenzahl ($n = 15 - 35$) für welchen eine ferninfrarote Strahlungsquelle erforderlich ist, die auf bis zu 14 THz abgestimmt werden kann. Die in dieser Arbeit verwendete Quelle war dieselbe wie in der Studie aus Kapitel 3, allerdings erfolgte die Differenzfrequenz-Erzeugung innerhalb der Vakuumkammer, um die Absorption der Strahlung durch Wasserdampf zu vermeiden. Durch Variation der Pulslänge des Nahinfrarot-Lasers, der zur Erzeugung der Ferninfrarotstrahlung verwendet wurde, konnte die Bandbreite zwischen 85 und 2.8 MHz angepasst werden. Spektren der Übergänge zwischen nd und n'f Rydbergzuständen natürlich vorkommender Isotope von Xe wurden aufgenommen. Insgesamt wurden 72 Übergänge im Bereich zwischen 0.937 THz und 14.425 THz aufgenommen und ihre Frequenzen mit den durch Multikanal Quantendefekttheorie berechneten Frequenzen verglichen. Die Kalibration der ferninfraroten Frequenzen erfolgte mit einer Genauigkeit von bis zu 2.8 MHz. Die schmalsten erfassten Linien zeigten eine Halbwertsbreite von 3 MHz, was eine vollständige Auflösung der Hyperfeinstruktur der Rydberg-Rydberg Übergänge von ^{129}Xe und ^{131}Xe ermöglichte.

Kapitel 6 behandelt die Messungen der Rydberg-Rydberg Übergänge von para-H_2, die verwendet wurden um erstmals unter hoher Auflösung das Energieintervall zwischen den zwei tiefsten Rotationsniveaus ($N^+ = 0$ und $N^+ = 2$) von para-H_2^+ zu bestimmen. Das Vorgehen beruhte auf der Bestimmung eines Netzwerks von Übergängen, welche p, d und f Rydbergzustände verbinden und die zu den $X^+\,^2\Sigma_g^+$ ($v^+ = 0, N^+ = 0$ und 2) Ionisationsschwellen konvergieren. Dieses Netzwerk erlaubte die Extrapolation der Positionen dieser Ionisationsschwellen, und damit die Bestimmung ihres Energieunterschieds, mit einer Genauigkeit von 2.9 MHz. Die Dissertation endet mit einem kurzen Fazit.

Contents

Acknowledgements **vii**

Abstract **ix**

Zusammenfassung **xi**

1 Introduction **1**

1.1 High-resolution spectroscopy with terahertz radiation 2

1.2 Properties of Rydberg states 4

1.3 Double-resonance experiments with VUV and THz radiation 6

2 Experimental **9**

2.1 Principles of THz generation 9

2.2 DAST crystal and design 13

2.3 Generation of pulsed, narrow-band NIR laser radiation 16

2.4 Detection of THz radiation 18

2.5 Frequency calibration and stabilization 19

2.5.1 Actively stabilized high-finesse etalon 20

2.5.2 Locking of the fixed-frequency Ti:Sa ring laser 21

2.5.3 Doppler-free saturated absorption spectra of iodine 22

2.6 THz spectroscopy in an ambient cell 24

2.7 VUV laser, VUV-THz double-resonance spectrometer and experimental design 25

2.7.1 Generation of VUV laser radiation 25
2.7.2 Sub-millimeter-wave radiation source 27
2.7.3 Experimental chamber 28
2.7.4 Minimization of field effects 29
2.8 VUV-THz double-resonance spectrometer 30
2.8.1 The vacuum chamber for THz-VUV double-resonance experiments . 31
2.8.2 Alignment of the THz radiation beam 33
2.8.3 Optimal measurement conditions 35

3 Vibrational Spectroscopy in an Ambient Cell 37

3.1 Introduction 37
3.2 Experimental 38
3.3 Results 38
3.4 Conclusions and Outlook 41

4 High Rydberg states in Xe as studied by sub-millimeter-wave radiation 43

4.1 Introduction 45
4.2 Experimental 49
4.3 Investigation of high Rydberg states of Xe in the range of principal quantum number $n = 65 - 100$ 53
4.3.1 High Rydberg states of ^{132}Xe 54
4.3.2 High Rydberg states of ^{129}Xe 59
4.4 Power broadening and Rabi frequencies 62
4.4.1 Power Broadening 62
4.4.2 Rabi Oscillations 65
4.5 Error Budget 68
4.6 Conclusions 69

5 Rydberg states of Xe as studied by THz radiation 71

5.1 Introduction . . . 71

5.2 Experimental . . . 72

5.2.1 Excitation Sequence and Generation of THz Radiation . . . 72

5.2.2 VUV-THz Double-Resonance Spectrometer . . . 73

5.2.3 Frequency Calibration . . . 74

5.3 Results . . . 75

5.3.1 Pulse Length and Resolution . . . 75

5.3.2 Tunability . . . 80

5.3.3 Mass-Selectivity . . . 81

5.3.4 Comparison to Calculated Transition Frequencies . . . 81

5.4 Conclusions . . . 83

6 The first rotational interval of para-H_2^+ by Rydberg spectroscopy of H_2 85

6.1 Introduction . . . 85

6.2 Experimental . . . 88

6.3 Rotational spacing and binding energies of the $20d2_1$ and $40d0_2$ Rydberg states of H_2 . . . 90

6.4 The $np0_1$ and $nf0_3$ Rydberg series . . . 95

6.5 The $nf2_2$ Rydberg series . . . 98

6.6 Frequency calibration and accuracy . . . 99

6.7 Error Budget . . . 101

6.8 Conclusions . . . 102

7 Conclusions and outlook 103

A List of transition frequencies between high-n Rydberg states of Xe and H_2 105

A.1 Observed transitions in high Rydberg states of ^{132}Xe by sub-millimeter-wave excitation 105

A.2 Observed transitions in high Rydberg states of Xe by THz excitation 108

A.3 Observed transitions in high Rydberg states of H_2 by THz excitation 110

List of Figures **112**

List of Tables **119**

Bibliography **122**

Chapter 1

Introduction

Electromagnetic radiation with frequencies in the range between 0.1 THz ($3.3\,\mathrm{cm}^{-1}$) and 10 THz ($334\,\mathrm{cm}^{-1}$) can be regarded as being part of the far-infrared and of the sub-millimeter-wave ranges of the electromagnetic spectrum (see Figure 1.1). This region is now often referred to as the "THz frequency range" and has even been referred to as the "THz frequency gap" because of the challenges associated with the generation and sensitive detection of radiation in this frequency range. Its applications range from biomedical optics, where one of the notable applications appears to be in the detection of skin cancer by imaging of epithelial tissue [1], to its use in security applications for the imaging of concealed weapons [2]. In the realm of condensed matter physics, it provides important information on the band structure of semiconductors and semiconductor nanostructures [3], as well as on the properties and dynamics of strongly correlated electron systems [4].

In the context of spectroscopy, in particular of high-resolution spectroscopy, which is the concern of the present thesis, THz radiation can be used for investigating a range of different atomic and molecular properties:

(i) The rotational energy-level structure of light molecules of relevance to astrophysics. For example, the energy interval between the two lowest rotational states of para-H_2^+, the simplest existing stable molecule, corresponds to a frequency of 5.2234851(29) THz, as determined in the realm of this thesis.

(ii) The low-frequency vibrations of molecular clusters and of polyatomic molecules, in particular those subject to large-amplitude motion. For example, the lowest frequency vibrational mode ν_6 of the atmospherically relevant freon-11 was determined to have a pure vibrational transition frequency of 7.3140(30) THz (for the $^{12}CF^{35}Cl_3$ isotopomer) in the work presented here.

(iii) The structure and dynamics of high Rydberg states, which are highly excited states of atoms and molecules (with large values for the principal quantum number n),

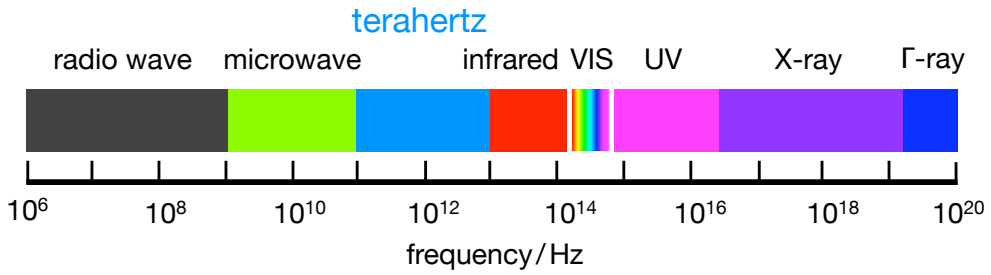

Figure 1.1: The electromagnetic spectrum.

and exhibit very different properties from those characterizing their ground state counterparts. In the work presented in this thesis, Rydberg states of the Xe atom with a principal quantum number between $n = 16$ and 97 were studied at a resolution of down to 150 kHz.

1.1 High-resolution spectroscopy with terahertz radiation

High-resolution spectroscopic data in the THz frequency range are much more limited than below 0.1 THz (microwave region of the electromagnetic spectrum), where powerful, broadly tunable and narrow-bandwidth sources have been commercially available for a long time, and above 30 THz, where coherent, narrow-bandwidth, broadly tunable, laser-based radiation sources are routinely used in laboratory investigations. A combination of several factors renders high-resolution spectroscopy in the THz range challenging: i) Available narrow-bandwidth sources in this range are usually of limited tunability; ii) the sensitive detection of the THz radiation necessitates more efforts than in neighboring frequency ranges; iii) the abundance of H_2O lines throughout the THz range makes it necessary to carry out spectroscopic experiments under conditions where the partial pressure of water is strongly reduced.

In the realm of high-resolution spectroscopy, experiments on samples in cold, pulsed, supersonic beams, which permit the study of clusters and a wide range of reactive species under conditions where Doppler and pressure broadenings are negligible, are complicated by the fact that most narrow-bandwidth THz radiation sources operate in a continuous-wave mode. The sensitivity of the measurements is therefore reduced by the unfavorable duty cycle: a typical pulsed nozzle delivers 200 μs-long gas pulses at repetition rates below 100 Hz, which reduces the available radiation power by a factor of more than 50. Despite these difficulties, considerable progress has been made in recent years in the development and use of narrow-bandwidth THz radiation in high-resolution molecular spectroscopy. Nonlinear frequency upconversion [5] of backward-wave oscillators [6–9] and Gunn oscil-

lators [10] can be used to access the range up to about 3 THz at a resolution better than 1 kHz. Broad tunability and narrow bandwidth (below 1 MHz) can be reached in the range below 4 THz by difference-frequency generation using photoconductive antennas [11, 12] and by difference-frequency mixing in nonlinear crystals (i.e., GaSe, quartz, $LiNbO_3$, GaP, ZnTe, DAST...) [13].

Quantum-cascade lasers [14–16] appear very promising for use in high-resolution THz spectroscopy (Ref. [17] and references therein) because they have intrinsic linewidths down to ~ 90 Hz [18]. In combination with THz laser frequency combs [19, 20] one could imagine direct frequency-comb spectroscopy in the THz range. Recently, frequency-comb-assisted spectroscopy of a rotational transition in methanol with a THz quantum cascade laser has been reported that allowed for the determination of the transition frequency with an accuracy of 10 kHz, a value that is currently limited by Doppler broadening [21]. Such lasers are not yet commercially available.

High resolution over the entire THz range can be achieved using synchrotron radiation in combination with Fourier-Transform spectrometers (Ref. [22] and references therein), the resolution being currently limited to $\sim 0.0007\,\mathrm{cm}^{-1}$ (21 MHz) by the path length of the moving mirror in the Michelson interferometer [23, 24]. Fourier-transform spectroscopy in the THz range further offers the multiplex advantage [25] and represents one of the most attractive ways of performing high-resolution molecular spectroscopy in the THz range, the only drawback being that the experiments require large synchrotron facilities with limited access.

This thesis presents an extension of a pulsed, laser-based THz radiation source described in Ref. [26] and its integration into a vacuum-ultraviolet-THz (VUV-THz) double-resonance spectrometer that can be used to study transitions between 0.1 to 14.5 THz with a resolution adjustable between 2.8 and 85 MHz. The source is based on difference-frequency mixing in the nonlinear crystal DAST [27, 28]. THz generation takes place in a DAST crystal placed in vacuum, which eliminates the problem of power reduction by water vapor absorption. The combination of this THz source with VUV radiation enables THz studies of high Rydberg states, and opens up the possibility of photoionization-detected rotational and vibrational spectroscopy. A special feature of the THz-radiation source is the ability to adjust the pulse length, and thus the spectral resolution: Short pulses ($\sim$ 10 ns) with a larger bandwidth ($\sim$ 85 MHz) can be used to record spectra over broad regions, whereas long pulses ($\sim$ 400 ns) with a narrow bandwidth ($\sim$ 3 MHz) are suited to study selected regions at high resolution. The bandwidth of the radiation can be matched to the width of a transition. In addition to the broad tunability and narrow bandwidth of the THz radiation, the spectrometer also offers the advantage of high sensitivity (background-free detection with single-ion sensitivity) and mass selectivity because the transitions are detected by photoionization or pulsed-field ionization. Furthermore, it is possible to work with rotationally and vibrationally cold samples in supersonic beams, which minimizes

Doppler and collisional broadenings.

The spectrometer was developed in the realm of studies of atomic and molecular Rydberg states. Broadly tunable radiation in the range of 0.1-14.5 THz indeed enables the investigation of transitions between Rydberg states in the range of principal quantum number n between 10 and 80. High-resolution spectroscopic data on Rydberg states in this range of principal quantum number are scarce but are ideally suited to derive information on the energy-dependence of the quantum defects and are needed as input to global analyses of the Rydberg spectra of rare-gas atoms [29, 30] and molecular hydrogen [31] using multichannel-quantum-defect-theory (MQDT). At a resolution of ~ 3 MHz, the hyperfine structure of atomic and molecular Rydberg states can be resolved and the analysis of the spectra using MQDT provides information on the role of nuclear spins in atomic and molecular photoionization [32, 31, 33]. Additionally, high-resolution spectroscopic information on atomic and molecular cations can be derived by Rydberg series extrapolation [34, 35, 31].

1.2 Properties of Rydberg states

Rydberg states are electronically excited states of atoms or molecules in which one of the electrons is in a highly excited state, exhibiting a large mean distance from the remaining ionic core. In Rydberg states of sufficiently large principal quantum number n, the motion of the electron is completely decoupled from that of the ion core. The values of their energies can be described by the Rydberg formula [36]:

$$E = E_i - \frac{hcR}{(n-\mu)^2} = E_i - \frac{hcR}{(n^*)^2}\,, \tag{1.1}$$

where E_i is the ionization energy of the atom or molecule in question, h represents Planck's constant, R the Rydberg constant and c the speed of light. The quantum number n represents the principal quantum number of the excited electron, μ the quantum defect, and n^* the effective principal quantum number. For the case of the hydrogen atom, the Schrödinger equation can be solved analytically and the energies of its excited electronic states depend only on the principal quantum number, the quantum defect being equal to zero. Rydberg states of atoms and molecules, particularly for high values of n, can be thought of as being hydrogenic in the sense that at large distances, the effective potential they are subject to by the ion core is approximately a Coulomb potential. The origin of the quantum defect μ lies in the deviation from a perfect Coulomb potential at short ion-core–Rydberg-electron distances: The energies of the Rydberg states (and thus the quantum defects) depend on the orbital angular momentum l. Low-l states, such as s ($l = 0$) or p ($l = 1$) states, display higher Rydberg-electron densities close to the ionic core, and their energies are therefore more strongly affected by the deviation from a Coulombic potential. These states have larger quantum defects. For instance, in the case of the Xe atom discussed in Chapters 4 and 5, s Rydberg states have a value for μ of about 4, p

Table 1.1: Several properties of Rydberg states and their scaling with the principal quantum number n [38]. All values given for the hydrogen atom except for [a].

property	n scaling	$n = 10$	$n = 50$	$n = 100$
mean radius	n^2	5.3 nm	132 nm	530 nm
electron binding energy	n^{-2}	$1097\,\mathrm{cm}^{-1}$	$44\,\mathrm{cm}^{-1}$	$11\,\mathrm{cm}^{-1}$
threshold field for ionization	n^{-4}	32 kV/cm	50 V/cm	3.2 V/cm
level spacing	n^{-3}	$190\,\mathrm{cm}^{-1}$	$1.7\,\mathrm{cm}^{-1}$	$0.19\,\mathrm{cm}^{-1}$
radiative lifetime	$n^3 - n^{5\,a}$	1.0 μs	125 μs	1.0 ms
polarizability[b] / ($\mathrm{MHz\,cm^2V^{-2}}$)	n^7	0.21	$1.6 \cdot 10^4$	$2.1 \cdot 10^6$

[a] The radiative lifetimes in H are very strongly dependent on electric fields (l and m_l mixing) [39].

[b] Extrapolated from the value of the Na(10d) Rydberg state.

states a value for μ of about 3.5, d states a value for μ of about 2.5 and f states a value for μ of about 0 [30].

In atoms with a non-zero nuclear spin and an open-shell ion core, there are Rydberg series converging on the different hyperfine levels of the ion core, as shown, for example, in Figure 4.2 for $^{129}Xe^+$. This figure illustrates an additional property: Channel interactions that perturb Rydberg series converging on different ionic thresholds can be observed. These interactions occur when Rydberg states belonging to series converging on one threshold are energetically degenerate, or nearly degenerate, with states of the same symmetry but belonging to series converging on another ionization threshold. Channel interactions are not limited to bound states: The bound states of one Rydberg series can interact with the continua above the convergence limits of other Rydberg series, leading to autoionization. A similar behavior can be observed in molecules, where Rydberg series converge on different rotational and vibrational levels of the ion. An example of such channel interactions studied in the present thesis concerns np ($J = 1$) series converging on the $v^+ = 0$, $N^+ = 0$ and 2 ionization thresholds of H_2 (see Figures 6.3, 6.7 and 6.8). Such channel interactions can be exploited, for example, to determine rotational and vibrational spacings of an ionic species by Rydberg spectroscopy of its neutral counterpart and subsequent extrapolation of the Rydberg series. Rydberg series extrapolation has been applied to determine the energy spacing between different hyperfine levels of $^{83}Kr^+$ [29, 35, 37]. In the case of molecules, this method can be applied to determine the rovibrational level spacings of molecular cations including fine and hyperfine structures [34, 35, 31]. In Chapter 6, the use of Rydberg series extrapolation in combination with the spectroscopy of high Rydberg states of para-H_2 to determine the first rotational interval in para-H_2^+ is presented.

A further feature of Rydberg states is that most of their physical properties scale as integer

powers of the principal quantum number n. Table 1.1 lists several such properties for the hydrogen atom and illustrates their dependence on n. The mean radius scales as n^2 and evolves from a value of 5.3 nm at $n = 10$ to 132 nm at $n = 50$. The highest Rydberg states observed in the realm of this thesis have $n \approx 100$ and display a size of nearly 1μm. A further important property is the binding energy, which scales as n^{-2}, and makes it possible to extract ionization thresholds with the Rydberg formula (Eq. 6.1). The electric field strength required for the ionization of a Rydberg state scales as n^{-4} and is equal to only 3.2 V/cm at $n = 100$. This property can be exploited to selectively ionize Rydberg states of different quantum numbers. An additional, essential characteristic in the context of high-resolution spectroscopy is the radiative lifetime, which scales as n^3 and equals 1.0 ms at $n = 100$. The natural width of Rydberg states is thus extremely narrow so that spectroscopic measurements are usually not limited in resolution by the lifetime of the Rydberg states, but by other effects, such as transit-time broadening or Doppler broadening. The level spacing between Rydberg states scales as n^{-3}, which makes it difficult to resolve individual Rydberg levels with conventional vacuum-ultraviolet (VUV) radiation sources at high values for the principal quantum number. Narrow-bandwidth THz or sub-millimeter-wave radiation is ideally suited to resolve and study the energy level structure of high Rydberg states. The final property listed in Table 1.1 that is important for performing high-precision measurements is the polarizability, which scales as n^7 in penetrating Rydberg states with a nonzero quantum defect. This makes Rydberg states highly susceptible to stray electric fields. For instance, at $n = 100$, the polarizability of Na d-Rydberg states is $2.1 \cdot 10^6\,\mathrm{MHz\,cm^2\,V^{-1}}$ and great care needs to be taken in the minimization of stray electric fields for the derivation of reliable spectral positions.

One of the key properties of Rydberg states exploited in this dissertation is the n^{-2} dependence of the Rydberg-electron binding energies, which was used to determine ionization thresholds by extrapolation. Whereas the Rydberg formula (Eq. (6.1)) can be used to reliably extrapolate Rydberg series measured at high-n values ($n \gg 100$), the extrapolation of series from lower n-values can be affected by perturbations caused by rovibrational channel interactions. In such cases, one uses multichannel quantum-defect theory (MQDT) [40–42], which is a collisional theory ideally suited to treat interacting ionization channels. In this thesis, the MQDT calculations on H_2 [43] were performed using the parameters derived for molecular hydrogen in the dissertation of D. Sprecher [44]. The MQDT calculations on Xe were performed using the parameter set derived for Xe and reported in Ref. [30].

1.3 Double-resonance experiments with VUV and THz radiation

This thesis describes the development of a VUV-THz double-resonance spectrometer designed for the study of high Rydberg states. Single-photon excitation by VUV radia-

tion allows for the study of Rydberg states by exciting Rydberg-Rydberg transitions with narrow-bandwidth THz radiation. The broad tunability of the THz source allows for the study of intermediate Rydberg states from $n \sim 15$ up to high Rydberg states with principal quantum numbers of $n \sim 80$ within one measurement sequence at a resolution of up to 3 MHz. By inversion of the excitation scheme, i.e., THz absorption followed by VUV absorption, this spectrometer could also be used for the measurement of pure rotational and vibrational transitions. For a vibrational spectroscopy experiment, the excitation sequence would involve a THz transition to a rovibrationally excited state, followed by selective photoionization of the upper vibrational level using VUV laser radiation. This would allow for the background-free measurement of THz absorption, and, by use of the time-of-flight spectrometer that is part of the experimental setup, for recording isotope- or isotopomer-selective spectra and to selectively record spectra of different components present within a gas mixture.

Chapter 3 describes vibrational spectroscopic experiments performed on $CHCl_3$, $CDCl_3$ and $CFCl_3$, resolving the structure of their different chlorine isotopomers and allowing for the determination of their pure vibrational transition frequencies with an accuracy of ~ 3 GHz. These measurements were performed in an ambient cell, where the detection of THz absorption took place by recording the transmitted THz radiation through a cell filled with sample. The spectra thus recorded showed signs of pressure broadening and were complicated by undesired features caused by water absorption lines. The idea for the construction of a VUV-THz double-resonance spectrometer originated from these measurements.

As a first step towards this goal, a VUV-sub-millimeter-wave spectrometer was built, and used for the study of Xe Rydberg states in the range between $n = 80 - 100$, as presented in Chapter 4. In this range, s/d channel interactions between series converging on the $F^+ = 2$ and $F^+ = 1$ hyperfine levels of the $^2P_{3/2}$ lower spin-orbit component of $^{129}Xe^+$ had been predicted by calculations [30] and could be confirmed by the new measurements. In the realm of these measurements, systematic errors, such as line shifts induced by electric and magnetic stray fields, were quantified and minimized. In an effort to determine the resolution limit of the experimental procedure, the power broadening of the $70p[5/2]_2 \leftarrow 58d[3/2]_1$ transition in ^{132}Xe was studied at different sub-millimeter-wave intensities and these experiments led to the observation of Rabi oscillations between the two Rydberg states.

Overall, these measurements served the purpose of characterizing the experimental setup and set the ground for the development of the VUV-THz double-resonance spectrometer introduced in Chapter 5. In this chapter, the properties of the spectrometer are illustrated by measurements of Rydberg states in Xe in the range of principal quantum number between 15 and 35. The mass-selectivity, broad tunability and adjustable resolution make this spectrometer ideal for high-resolution spectroscopic studies of Rydberg states of atoms

having several naturally occurring isotopes, and of the Rydberg states of molecules.

In the last part of this thesis, the spectrometer was used for the measurement of Rydberg-Rydberg transitions in H_2, leading to the most precise experimental determination to date of the first rotational interval in para-H_2^+. The measurement of this interval represented one of the major goals of the dissertation and justified the efforts invested in the experimental and methodological developments.

Chapter 2

Experimental

This chapter describes the evolution and development of an experimental apparatus for high-resolution (down to $\sim 3\,\mathrm{MHz}$) spectroscopy between $0.1 - 14\,\mathrm{THz}$ and describes the instruments and methods employed to obtain the data presented in the following chapters. First, the basic principles of the THz generation process, which relies on difference-frequency generation of near-infrared (NIR) radiation are described. Then, the experimental setup for performing vibrational spectroscopy in an ambient cell is presented. The evolution of the THz source for use in a VUV-THz double-resonance spectrometer is outlined by first introducing an experimental setup that was constructed in the realm of this thesis for VUV-submillimeter-wave double-resonance experiments. In the final VUV-THz spectrometer, radiation is generated in vacuum and absorption takes place in the environment of a translationally, vibrationally and rotationally cold supersonic beam. The background-free detection of absorption takes place within the same vacuum chamber. This new experimental setup allows for i) completely avoiding interfering water absorption by carrying out the THz radiation generation, absorption and detection processes inside a vacuum chamber, ii) minimizing Doppler broadenings by exciting perpendicularly to the main velocity component of the molecular beam, iii) working in the collision-free and low temperature environment of a molecular beam which minimizes pressure broadening, iv) performing mass-selective spectroscopy, and thus avoiding the overlap of spectral features from different isotopes of atomic samples and isotopomers of molecular samples. In favorable cases, the mass selectivity also enables the identification of the carrier of the spectrum by its mass.

2.1 Principles of THz generation

The THz source used in the realm of this thesis is a further development of the source described in Ref. [26] and relies on difference-frequency generation. In this process, two

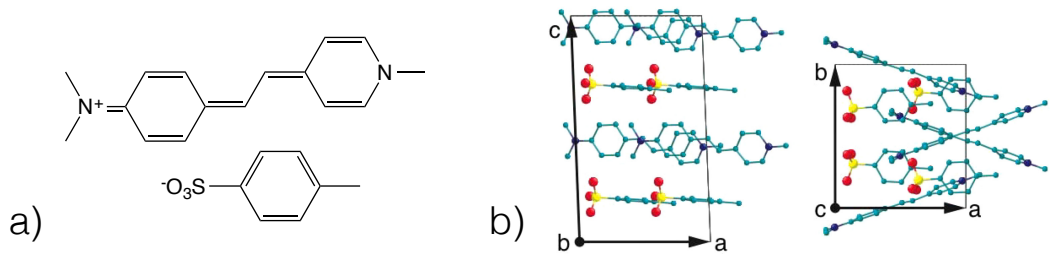

Figure 2.1: Panel a): Chemical structure of *trans*-4′-(dimethylamino)-*N*-methyl-4-stilbazolium tosylate (DAST). Panel b): X-ray structure of DAST showing molecules from one unit cell projected along the crystallographic axes a and b. The SO_3^--group of the tosylate anion is shown in yellow and red. The ac crystallographic plane is the mirror plane. The lattice parameters are $a = 10.365\,\text{Å}$, $b = 11.322\,\text{Å}$ and $c = 17.893\,\text{Å}$ [45, 46]. Figure taken from Ref. [45].

lasers are incident on a nonlinear optical medium and radiation is generated at their difference frequency. In the realm of this thesis, two narrow-band near-infrared (NIR) lasers were used as input frequencies and the nonlinear optical medium of choice was a *trans*-4′-(dimethylamino)-*N*-methyl-4-stilbazolium tosylate crystal (DAST), which offers a large nonlinear optical susceptibility and was first reported in Ref. [47]. Panel a) of Figure 2.1 shows the chemical structure of the components of DAST: It consists of a stilbazolium cation and a tosylate anion. Panel b) of Figure 2.1 displays its X-Ray structure [45], showing molecules from one unit cell. The components of DAST can, in principle, crystallize in either of two forms: the centrosymmetric form belonging to the point group $\bar{1}$, and the monoclinic form of point group m, which is the form shown in Figure 2.1b) and used for THz frequency generation [45].

Important contributions to the development of DAST were made by the group of Prof. Günter in the Physics Department of ETH, particularly by the production of DAST crystals that exhibit a high optical quality and large sizes, which is achieved by crystallization from methanol solutions by the slow cooling method [46, 45]. The DAST crystals used in the experiments presented here were produced by the company Rainbow Photonics, which originated from the group of Prof. Günter. THz generation using DAST has been reported by optical rectification of fs laser pulses [48, 27] or by difference-frequency generation from infrared radiation using ns pulses [49–52, 28, 26].

When the two NIR beams impinge on the DAST crystal, a polarization $\boldsymbol{P}$ is induced by the interaction of the incident light with the crystal that can be described as a power series in the overall electric field strength $\boldsymbol{E}$ of both lasers [53]: [a]

[a] It is also common to write $\boldsymbol{P}$ as a Taylor series in the overall electric field strength $\boldsymbol{E}$ of both lasers. The i-th component of the dielectric polarization is then given by [54] $P_i = \epsilon_0 \left(\chi_e^{(1)} E_i + (1/2)\chi_e^{(2)} E_i^2 + (1/6)\chi_e^{(3)} E_i^3 + \ldots \right)$, where $\chi_e^{(n)}$ are the electric susceptibility tensors of rank $n+1$ and E_i the component i of the electric field strength.

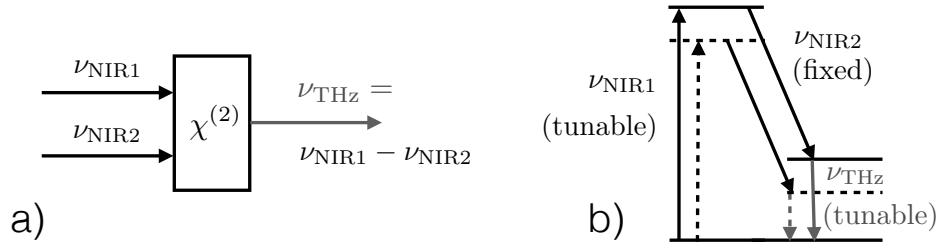

Figure 2.2: Panel a): Schematic representation of the THz generation process, where $\chi^{(2)}$ represents the nonlinear optical susceptibility tensor of DAST for THz generation. Panel b) Generation of tunable THz radiation by keeping one NIR laser at a fixed frequency (ν_{NIR2}), and tuning the frequency of the second NIR laser (ν_{NIR1}).

$$\boldsymbol{P} = \epsilon_0 \left(\chi^{(1)} \boldsymbol{E} + \chi^{(2)} \boldsymbol{EE} + \chi^{(3)} \boldsymbol{EEE} + \ldots \right) . \tag{2.1}$$

In Equation (2.1), $\chi^{(n)}$ represent tensors of rank $n+1$ and are the electric susceptibilities of order n. For any nonlinear optical process such as sum- or difference-frequency mixing or third-harmonic generation, it is necessary that the relevant elements of the electric susceptibility tensors are non-zero. For the process of difference frequency generation, it is therefore required that at least one element of $\chi^{(2)}$ is nonzero, which is the case in crystals that do not have a center of inversion symmetry, such as the monoclinic form of DAST. In Cartesian coordinates, the i-th component of the second-order nonlinear polarizability responsible for THz generation by difference-frequency mixing is given by [53]:

$$P_i^{(2)} \left(\omega_{\mathrm{THz}} \right) = \sum_{j,k} \epsilon_0 \chi_{ijk}^{(2)} \left(\omega_{\mathrm{THz}}, \omega_{\mathrm{NIR1}}, -\omega_{\mathrm{NIR2}} \right) E_j(\omega_{\mathrm{NIR1}}) E_k^*(\omega_{\mathrm{NIR2}}) , \tag{2.2}$$

where ω_{NIR1} and ω_{NIR2} correspond to the frequency output of the two NIR lasers, and ω_{THz} to the frequency of the generated THz radiation (in angular frequency units, for a schematic representation of the process, see Fig. 2.2b)), $\chi_{ijk}^{(2)}$ are the components of the relevant second-order nonlinear optical susceptibility tensor, and $E_{j,k}$ are the Cartesian components of the electric field vector of the NIR radiation beams. For the work presented in this thesis, tunable THz radiation between 0.1 and 14 THz was generated by tuning the frequency of one NIR laser (ω_{NIR1}) while keeping the frequency of the second NIR laser fixed (ω_{NIR2}). The relevant nonlinear optical process is shown schematically in Figure 2.2 .

An important aspect for an efficient difference-frequency generation process is the necessity to fulfill the phase-matching condition (see below) which is required by conservation of momentum and can typically only be fulfilled in crystals that display sufficient birefringence (i.e., the refractive index n depends on the polarization direction of the incident radiation) [53]. For example, GaAs possesses a very high nonlinear optical susceptibility (see Table 1.5.3 of Ref. [53]) but generally cannot be used in phase-matched second-order

optical conversion processes because, on account of its crystal symmetry, it exhibits no birefringence.

In the experiments described in this thesis, the two NIR beams were polarized along the same direction and co-propagating (this was ensured by coupling both beams into a polarization-maintaining optical fiber, see Section 2.6 for details). In this configuration, the two beams interfere with one another and a beat is generated that oscillates at the difference frequency $\omega_{\mathrm{diff}} = \omega_{\mathrm{THz}} = \omega_{\mathrm{NIR1}} - \omega_{\mathrm{NIR2}}$. When the phase-matching condition is fulfilled, the generated THz radiation and the induced polarization remain in phase along the propagation axis so that the THz field is coherently amplified [13].

For fixed propagation (z) and polarization directions of the NIR beams with respect to the geometry of the crystal, the nonlinear polarization for THz generation of Equation (2.2) can be written in scalar form [53, 13] as

$$P^{(2)}_{\mathrm{THz}}(z) = 4\epsilon_0 d_{\mathrm{eff}} E_{\mathrm{NIR1}}(z) E^*_{\mathrm{NIR2}}(z) = 4\epsilon_0 d_{\mathrm{eff}} A_{\mathrm{NIR1}} A^*_{\mathrm{NIR2}} e^{i(k_{\mathrm{NIR1}} - k_{\mathrm{NIR2}})z}\,, \tag{2.3}$$

where $P^{(2)}_{\mathrm{THz}}(z)$, the polarization of the THz radiation, is perpendicular to the polarizations of the two NIR beams in the DAST crystal for frequencies above 3.2 THz [28]. The wave vectors of the two NIR beams in Equation (2.3) are represented by k_{NIR1} and k_{NIR2}, and the amplitudes of their optical fields by A_{NIR1} and A^*_{NIR2}. The effective nonlinear optical coefficient of the crystal, $d_{\mathrm{eff}} = \frac{1}{2}\chi_{\mathrm{eff}}$, can be determined explicitly by evaluating the expression $\boldsymbol{P}_{\mathrm{THz}} = \epsilon_0 \chi^{(2)} \boldsymbol{EE}$, or it can be calculated from the general instructions for each of the crystal classes given in Ref. [55] (DAST belongs to the monoclinic space group with crystal class m, see Section 2.2). By making use of the relations [13] for the THz field and polarization

$$E_{\mathrm{THz}}(z,t) = A_{\mathrm{THz}}(z) e^{i(k_{\mathrm{THz}} z - \omega_{\mathrm{THz}} t)} + c.c.\,, \quad \text{and} \tag{2.4}$$

$$P^{(2)}_{\mathrm{THz}}(z,t) = P_{\mathrm{THz}}(z) e^{-i\omega_{\mathrm{THz}}} + c.c.\,, \tag{2.5}$$

Equation (2.3) can be substituted into the wave equation [13]

$$\frac{\partial^2 E_{\mathrm{THz}}(z,t)}{\partial z^2} - \frac{n^2_{\mathrm{THz}}}{c^2} \frac{\partial^2 E_{\mathrm{THz}}(z,t)}{\partial t^2} = \frac{1}{\epsilon_0 c^2} \frac{\partial^2 P^{(2)}_{\mathrm{THz}}(z,t)}{\partial t^2}\,, \tag{2.6}$$

where n_{THz} is the refractive index for the THz beam in the DAST crystal. After making the slowly varying envelope approximation one obtains

$$\frac{dA_{\mathrm{THz}}}{dz} = \frac{2id_{\mathrm{eff}}\omega^2_{\mathrm{THz}}}{\epsilon_0 n_{\mathrm{THz}} c} A_1 A^*_2 e^{i\Delta k z}\,, \tag{2.7}$$

where $\Delta k = k_{\mathrm{NIR1}} - k_{\mathrm{NIR2}} - k_{\mathrm{THz}}$ is the wave vector or momentum mismatch. Because the two NIR beams are polarized along the same direction, and because they have similar frequencies, the dispersion with respect to one another is small and one can make the approximation that $n_{\mathrm{NIR1}} \approx n_{\mathrm{NIR2}} = n_{\mathrm{NIR}}$. The momentum mismatch and refractive index mismatch $\Delta n = n_{\mathrm{NIR}} - n_{\mathrm{THz}}$ are thus proportional to each other

$$\Delta k = n_{\mathrm{NIR}} \frac{\omega_{\mathrm{NIR1}}}{c} - n_{\mathrm{NIR}} \frac{\omega_{\mathrm{NIR2}}}{c} - n_{\mathrm{THz}} \frac{\omega_{\mathrm{THz}}}{c} = \Delta n \frac{\omega_{\mathrm{THz}}}{c}\,. \tag{2.8}$$

Equation (2.7) can be integrated across the propagation distance L through the DAST crystal and an expression for the THz intensity is obtained [13]

$$I_{\mathrm{THz}}(L) = \frac{1}{2}\epsilon_0 c n_{\mathrm{THz}} |A_{\mathrm{THz}}(L)|^2 = \frac{8 d_{\mathrm{eff}}^2 \omega_{\mathrm{THz}}^2 I_{\mathrm{NIR1}} I_{\mathrm{NIR2}}}{\epsilon_0^3 c^3 n_{\mathrm{NIR1}} n_{\mathrm{NIR2}} n_{\mathrm{THz}}} L^2 \mathrm{sinc}^2\left(\frac{\Delta k L}{2}\right). \tag{2.9}$$

Equation (2.9) shows that the intensity is maximal for $\Delta k = 0$. This is called the phase-matching condition and requires that $\Delta n = 0$ for plane waves (see Equation (2.8)). This can only be achieved if the birefringent properties of DAST are made use of because its refractive indices along the principal axes all exhibit normal dispersion [56] (i.e. $(dn_i/d\omega) > 0$, $i = a, b, c$) which would make it impossible to find conditions for which $\Delta n = 0$ if all radiation beams were polarized along the same optical axis and made use of the same refractive index n_i. A further important property is the coherence length l_c that dictates the thickness of the crystal needed for optimal THz generation. From Equation (2.2), it follows for a given Δk that $I_{\mathrm{THz}} \propto \sin^2\left(\frac{\Delta k L}{2}\right)$ and the THz intensity is maximal when the crystal thickness is equal to $l_c = \frac{\pi}{\Delta k}$ [13]. Section 2.2 below describes how phase-matching in DAST was achieved in the realm of the experiments presented in this thesis to maintain efficient THz generation over the entire range of $0.1 - 14\,\mathrm{THz}$. This required the crystal to be cut in a specific manner with respect to its crystallographic axes, as calculated by J. Liu [28] for two collinear, normal-incident NIR beams with $\lambda \sim 800\,\mathrm{nm}$.

2.2 DAST crystal and design

THz generation in DAST crystals was first reported using as-grown, c-cut DAST. However, if collinear NIR radiation of 800 nm wavelength at normal incidence is used as input, no THz radiation is generated beyond a frequency of $\sim$ 3 THz [28, 57]. Panel a) of Figure 2.3 shows the optical axes of the DAST crystal (x_1, x_2 and x_3) with respect to the crystallographic axes a, b, and c. The x_2 and b axes coincide perfectly, whereas the x_3 axis makes an angle of 3.2° with the c axis, and the x_1 axis an angle of 5.4°. Because these angles are very small and they show only a minor variation with wavelength [45], the assumption is typically made that they coincide. Panel b) of Figure 2.3 shows an as-grown DAST crystal (dashed, red rectangle) and a crystal cut specifically to enable phase-matching above 3 THz. A simple rotation of the polarization vector of the incident NIR beams allowed for THz radiation to be generated across the entire range of 0.1−14 THz with the cut DAST crystal [28].

At frequencies below 3 THz, the most efficient way of generating THz radiation is by using an as-grown DAST crystal, with the two collinear NIR beams being polarized along the a-axis of the crystal. The propagation direction $\vec{k}$ of the two NIR beams for this case is shown in red in Figure 2.3b), and their corresponding polarization as a red, dashed arrow. This configuration makes use of the χ_{111} and χ_{311} components of the nonlinear optical susceptibility tensor, which have values of $1230 \pm 130\,\mathrm{pm/V}$ and $239 \pm 32\,\mathrm{pm/V}$,

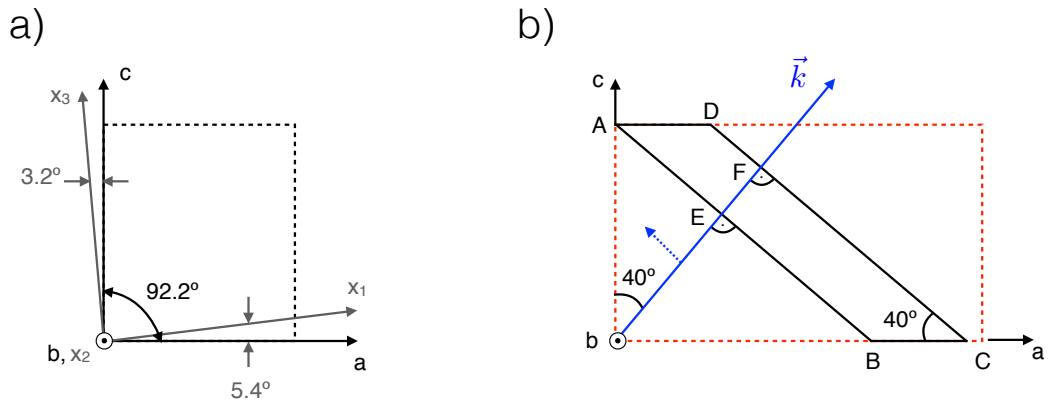

Figure 2.3: Panel a): Schematic representation of the optical axes of the DAST crystal (x_1, x_2, x_3) and the angles they make with respect to the crystallographic axes a, b, c. Angles shown are not drawn to scale. Panel b): Schematic representation of the cut of the DAST crystal. The dashed rectangle represents the as-grown crystal. The black, full parallelogram is a crystal cut so as to facilitate phase-matching in the difference-frequency generation process across the range $0.1 - 14\,\mathrm{THz}$. $\vec{k}$ corresponds to the propagation direction of the NIR and THz beams. The blue colors show the polarization (dashed arrow) and propagation (full arrow) direction of the NIR beams for use with the cut crystal, red colors those for use with the as-grown crystal.

respectively [27]. These conditions, however, prevent phase matching to be achieved at frequencies above $\sim 3\,\mathrm{THz}$ [28, 57].

The spectroscopic experiments performed in the realm of this thesis for which THz generation took place inside vacuum (see Section 2.8) required the use of a single crystal with which the entire range between $0.1 - 14\,\mathrm{THz}$ could be accessed and the tedious task of opening the vacuum chamber and exchanging crystals avoided. A crystal was therefore employed that was cut as delineated by the black parallelogram in panel b) of Figure 2.8 with respect to the crystallographic a, b and c axes, and as reported in Refs. [28, 26]. At frequencies below 3.2 THz, the THz generation process is most efficient for a polarization of the two collinear NIR beams perpendicular to the b-axis and within the ac-plane of the crystal (shown as a blue, dashed arrow in Figure 2.3b)), as well as a propagation direction of the two beams within the same plane and at an angle $\theta = 40°$ to the c-axis. This configuration was ensured by the cut of the crystal and the normal-incident configuration of the NIR beams in the experimental design. Pumping the crystal in such a configuration makes use of the χ_{111} and χ_{311}[b] components of the nonlinear susceptibility tensor of DAST, and is therefore less efficient than if the polarization were parallel to the a axis. To generate radiation at a frequency above 3.2 THz, the same propagation direction can be used, but the polarization of the NIR beams is rotated so as to be parallel to the b-axis of the DAST

[b]In this notation, the components χ_{nml} of the second-order nonlinear optical susceptibility tensor are given in the coordinate system of the optical axes x_1, x_2 and x_3. The identification $x_1 \to 1$, $x_2 \to 2$ and $x_3 \to 3$ is made.

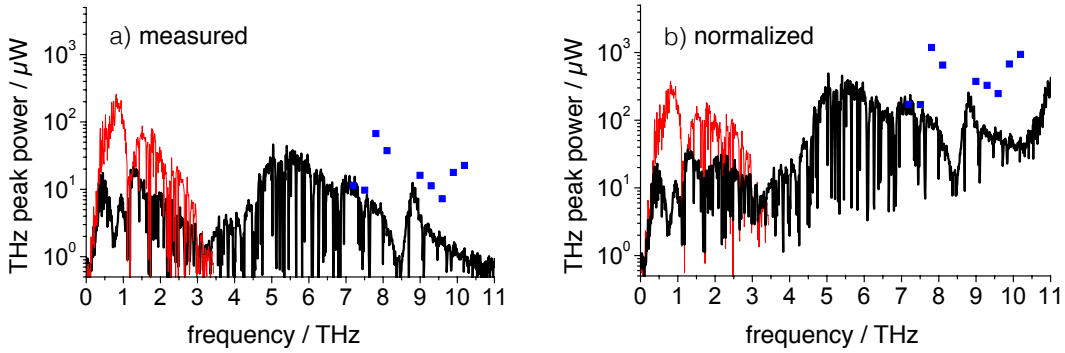

Figure 2.4: Panel a): THz peak power as measured by a bolometer. Sharp dips correspond to water absorption lines, broader features at 1.1 and 3.2 THz correspond to crystal absorptions. Panel b): THz peak power after normalization by window and filter absorptions (see text for details). Figures taken from [26]. For both panels, the red, solid line represents a normal-incident pump beam with polarization perpendicular to the b axis, the black, solid line represents a normal-incident NIR pump beam with a polarization parallel to the b axis and the blue squares a polarization parallel to the b axis and with an optimal angle of incidence.

crystal, making use of the χ_{122} component of the nonlinear susceptibility tensor, which exhibits a value of $166 \pm 16\,\mathrm{pV/cm}$ [27].

Two DAST crystals were used in the experiments described in this thesis. The crystal used for the ambient cell measurements and the experiments on Xe Rydberg states had an active area of $\sim 2\,\mathrm{mm}^2$, and a geometry as reported in [28] (the area of the crystal was given by AB = CD = 5 mm and a thickness of EF = 1.087 mm, see Figure 2.3b). For the experiments presented on H_2, the crystal had dimensions of AB = CD = 5 mm and a thickness of EF = 0.99 mm, although the active area was specified to be only $1\,\mathrm{mm}^2$.

Panel a) in Figure 2.4 shows the THz peak power in the range between 0.1-11 THz (as published in [26]) recorded in the presence of a black polyethylene filter that was used to block the NIR beams while transmitting the THz beam. This filter, however, also partially absorbed the THz beam, particularly at the high-frequency end of the spectrum ($\sim 90\%$). In addition, there was an absorption by the THz cut-on filter of the bolometer detector (see Section 2.4 for details) and of the vacuum window of its dewar. In panel b), the THz peak power is shown after normalization by the transmission of the filters. The sharp dips in the THz peak power correspond to water absorption lines, whereas the broader absorption features at 1.1 and 3.2 THz correspond to absorptions of the DAST crystal itself [27, 58]. In the design of the VUV-THz double-resonance spectrometer, the filters could be avoided.

The THz radiation intensity is limited by the intensity of the incident NIR radiation, which should not exceed the damage threshold of the DAST crystal. For the ambient cell and Xe measurements, care was taken not to exceed the threshold of $\sim 3\,\mathrm{MW/cm}^2$ reported in Refs. [26] and [28]. It could be extended by a factor of ~ 6 by glueing the crystal on an

aluminum mount which served the purpose of reducing heating. Therefore, typical NIR peak powers used for the experiments on H_2 were $\sim 100\,\mathrm{kW}$ as opposed to $\sim 16\,\mathrm{kW}$ used in previous experiments. Because of the quadratic dependence of the THz power on the power of the incident NIR beam (see Equation (2.9)), an increase of the damage threshold by a factor of ~ 6 enabled an increase in THz power by a factor of ~ 40 . In these experiments, the overall THz peak power was therefore a factor of ~ 40 higher than indicated in panel b) of Figure 2.4 and approached 10 mW in the region beyond 5 THz. It should be noted that Ref. [26] reports the THz peak power in Figure 2.4 to be underestimated by a factor of ~ 10 and attributes this factor to the acceptance angle of the detector and to the absorption efficiency of the diamond substrate which is coupled to the semiconductor structure inside of the bolometer (see Section 2.4 for a description of the detector). For the experiments on Xe and H_2, the THz generation and detection took place entirely inside of a vacuum chamber so that the sharp dips in THz peak power resulting from water absorption could be avoided (see Section 2.8 for details). THz generation is most efficient for a given damage threshold if the two NIR beams are equally intense, which were the conditions used in all of the experiments presented here.

2.3 Generation of pulsed, narrow-band NIR laser radiation

The pulsed, high-power NIR radiation used to produce THz radiation by difference-frequency mixing was generated with a Ti:Sa laser system, a schematic representation of which is depicted in Figure 2.5. The Ti:Sa ring laser and amplification system used in this thesis were constructed by R. Seiler and Th. Paul in the realm of their dissertations and a detailed description can be found in Refs. [59] and [60], respectively. This source is particularly suitable in combination with difference-frequency generation in a DAST crystal because it produces pulsed, narrow-bandwidth and easily tunable NIR radiation, which allows for a straightforward adjustment of the THz frequency. Such an all-solid-state source with Ti:Sa as the amplification medium brings the following advantages: Whereas conventional dye amplifiers are limited in their frequency bandwidth by the length of the pump pulse (typically 5 ns for a Nd:YAG pump laser) because of their short spontaneous emission lifetime, Ti:Sa allows for the generation of programmable pulse shapes between $10 - 500\,\mathrm{ns}$, which translates to a similar length of the THz radiation pulses (and corresponding bandwidths). The same laser system can be used to record overview scans at low resolution by selecting a short pulse length, and to carry out precision measurements (with narrow bandwidth) of specific spectral features by choosing long pulse lengths. Additionally, the frequency is easily tunable between $\sim 760\,\mathrm{nm}$ and $\sim 790\,\mathrm{nm}$, which is necessary to cover the entire frequency range between 0.1 and 14 THz and permits one to adjust the frequency over this range within seconds. Using a pulsed source of NIR radiation has an additional advantage: the DAST crystal has a damage threshold of $\sim 18\,\mathrm{MW\,/\,cm^2}$ and if the power goes beyond this threshold, burning of the crystal is observed (see Section 2.1 for details). Pulsed op-

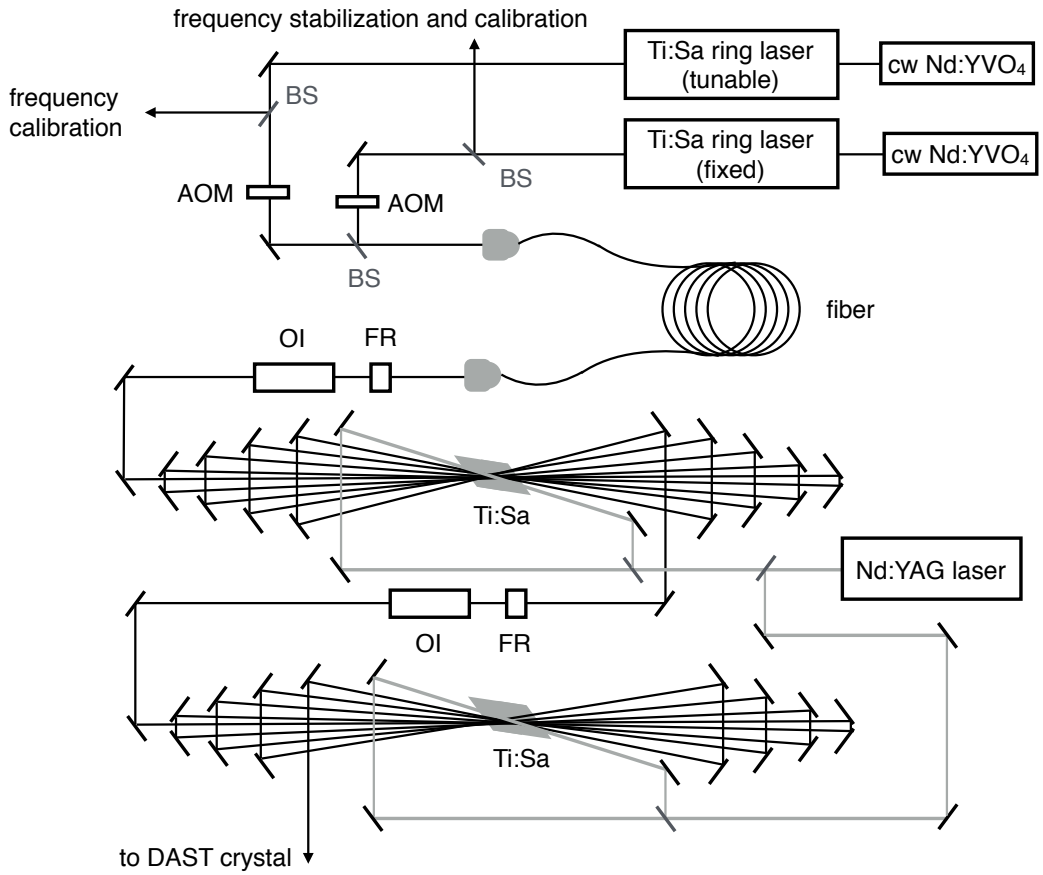

Figure 2.5: Schematic representation of the Ti:Sa laser system used for generating short (10-500 ns), high-power NIR pulses of Fourier-transform-limited bandwidth, including bowtie-amplification system. BS: beamsplitter, FR: Fresnel rhomb, OI: optical isolator.

eration allows for higher peak powers while remaining below the damage threshold of the crystal. Consequently, higher THz peak powers can be reached than by operation in cw mode because the generation efficiency scales quadratically with the incoming NIR power (see Section 5.3.1 for details).

A cw Ti:Sa ring laser (Coherent 899-21) was pumped by the frequency-doubled output of a diode-pumped, cw Nd:YVO_4 laser (Coherent Verdi, $\lambda = 532\,\text{nm}$) and its wavelength stabilized to $\sim 792.37\,\text{nm}$. A second cw Ti:Sa ring laser (Coherent 899-29 autoscan), tunable between $\sim 760\,\text{nm}$ and $\sim 790\,\text{nm}$ was pumped by the frequency-doubled output of a second, diode-pumped, cw Nd:YVO_4 laser (Coherent Verdi, $\lambda = 532\,\text{nm}$), as shown in Figure 2.5. Part of the output of each ring laser was directed to a frequency calibration and stabilization setup (see Section 2.5 for details), the remaining output was focused onto the active areas of an acousto-optic modulator (AOM, Brimrose GPF-100-500-800) operated at a driving frequency of 1 GHz. Modulation of the envelope of the AOM driving wave by two arbitrary waveform generators (AWGs, Agilent AWG-33250A) with waveforms having lengths between $\sim 10\,\text{ns}$ and 500 ns at a repetition rate of 25 Hz produced NIR pulses of the

desired length and shape in the first diffraction order of the AOM. The pulsed NIR output of the two AOMs with energies between $0.7 - 35\,\mathrm{nJ}$ were coupled into the same optical fiber by way of a PBS and transferred to the optical table where amplification took place. The optical fiber facilitated scanning of the ring laser without necessitating an adjustment of the amplifier alignment. Additionally, coupling both beams into the same optical fiber ensured that the two beams were perfectly overlapped, which is critical for THz generation. The Ti:Sa crystals (0.15% doping) used as gain medium within the amplifier were cut at Brewster's angle for the incident pump laser wavelength $\lambda = 532\,\mathrm{nm}$ that is generated by the frequency-doubled output of a pulsed Nd:YAG laser (Spectra Physics Quanta Ray). The NIR output from the optical fiber was directed towards the first Ti:Sa crystal after passing through a Fresnel rhomb (FR) and an optical isolator (OI) to avoid amplified spontaneous emission that would damage the crystal, as shown in Figure 2.5. Upon each pass through the crystal, the NIR beam power is amplified by a factor of $2 - 3$, as long as the entire population inversion generated by the YAG pulse is not depleted. The NIR radiation is directed through the crystal a total of 9 times with a set of mirrors that are arranged in a bow-tie configuration, giving an amplification of the original beam power by a factor of up to $2 \cdot 10^4$. The amplified beam then passes through another FR and OI before entering a second bow-tie amplifier, the output of which is directed towards the DAST crystal where THz generation takes place. Typical NIR pulse energies in the range $1 - 10\,\mathrm{mJ}$ were used as input for difference-frequency generation. A frequency shift in the range $1 - 10\,\mathrm{MHz}$ depending on the Nd:YAG pump power arises during the amplification process, which can be measured by monitoring the frequency beat between the amplified radiation and the cw output of the NIR laser [61]. Because both NIR beams are amplified in the same amplifier, they are subject to the same frequency shift, which cancels out when generating the difference frequency.

2.4 Detection of THz radiation

Detectors of THz radiation are classified either as coherent detectors that measure the amplitude and phase of the incident THz beam, or as incoherent detectors that only measure the power of the THz radiation (see Chapters 1 and 4 of Ref. [13] for details). Examples of coherent detectors are those operating by electro-optic sampling, photoconductive switching, photomixing (the sub-millimeter-wave radiation experiments presented in Chapter 4 made use of such a detector for frequency stabilization of the BWO source described in Section 2.7.2) and heterodyne detection techniques. These types of detectors operate over a more limited frequency range than incoherent detectors. Examples of incoherent detectors are bolometers, Golay cells and pyroelectric devices which share the common feature that a thermal sensor is used for the detection of THz radiation. An absorber with a low heat-capacity (leading to considerable changes in temperature even for small changes in THz intensity), small reflectivity and flat absorption profile over the THz frequency range

is chosen, such as the diamond absorber used in the IR Labs HDL-5 series (see below). A thermal sensor is then used that produces a voltage or current that is correlated to the temperature change.

The bolometer is the most sensitive of these detectors and has the shortest time constant (typically $\sim 0.1\,\mathrm{ms}$), which is why it was chosen for the measurements presented in Chapter 3. In these measurements, molecular absorption was detected by a variation in the transmitted THz radiation intensity through an ambient cell, as described in greater detail in Section 2.6. The IR Labs bolometer (HDL-5) employed in this thesis uses a diamond absorber mounted on a heavily doped Si substrate, the resistivity of which changes with temperature. The Si substrate is part of a balanced Wheatstone bridge that becomes unbalanced because of the resistivity change caused by THz absorption, resulting in a current flow through the galvanometer connecting its two midpoints. The entire unit is cooled to liquid-helium temperatures (4 K), which leads to a lower background and therefore a higher sensitivity.

The vacuum insulation of the dewar surrounding the absorber was kept at a pressure on the order of $\sim 10^{-7}$mbar by continuous pumping with a turbo-molecular pump. The bolometer therefore required a vacuum window (made of high-density, white polyethylene) that allows the THz radiation to be transmitted into the bolometer. After passing through a cut-on filter (low-pass filter, diamond on polyethylene) which served the purpose of filtering as much background radiation as possible, a Winston cone was used to guide the radiation onto the diamond absorber. Its entrance aperture, distance from the vacuum window, and the width of this window defined the angular acceptance of the bolometer. As mentioned in Section 2.2, Ref. [26] suggests that the THz peak power shown in Figure 2.4 is underestimated by a factor of ~ 10 because of the angular acceptance of the bolometer and the absorption efficiency of the diamond absorber. Additionally, the vacuum window and cut-on filter of the detector lead to a reduction in THz intensity because of partial absorption.

Recently, superconducting bolometers have become commercially available (for example by SCONTEL) that have response times of $< 0.1\,\mathrm{ns}$ while still maintaining a high sensitivity over a very large frequency range. In such detectors, the semi-conductor is replaced by a superconductor, the resistivity of which depends very strongly on temperature in the vicinity of its critical temperature. Because of their short response times, such detectors could be used in lock-in detection schemes, and would further increase the detection sensitivity.

2.5 Frequency calibration and stabilization

The frequency of the THz radiation was calibrated by determining the frequencies of the two NIR lasers used for THz generation. To this end, a small portion of the laser light

was separated from the output of the two Ti:Sa ring lasers used for generation of the NIR radiation and directed to a calibration setup. For the ambient-cell measurements (see Chapter 3), it sufficed to calibrate these frequencies with a commercial wavemeter that specified an accuracy of $\sim 1\,\mathrm{GHz}$. The frequency ω_{NIR2} (see Figure 2.2) was kept fixed by locking to a transmission maximum of a length-stabilized, confocal Fabry-Pérot etalon. In this context, the etalon served as a transfer cavity and transferred the frequency stability of the He-Ne laser used for length-stabilization to the NIR ring laser.

For the experiments on Rydberg states of Xe and H_2, the absolute frequency of the etalon peak used for locking was determined by scanning to the closest-lying iodine (I_2) transition and recording a Doppler-free saturation spectrum of I_2. The frequency ω_{NIR1} of the tunable ring laser was calibrated while recording spectra of Xe or H_2 by simultaneously recording both Doppler-free saturated absorption spectra of I_2 for absolute frequency calibration and the transmission spectrum through the Fabry-Pérot etalon for relative frequency calibration. In this context, the etalon primarily served as a regularly-spaced frequency marker used for linearization of the frequency scale of the spectra. Examples of calibration of THz frequencies are presented along with the actual data in Chapters 5 and 6 (see, e.g., Figure 5.2 and Figure 6.10). In the following subsections, the main calibration principles and devices used in the work presented in this thesis are described.

2.5.1 Actively stabilized high-finesse etalon

The actively length-stabilized, confocal Fabry-Pérot etalon used for frequency calibration and locking of the NIR ring lasers was constructed by Th. Paul and is described in detail in Section 2.9.2 of his thesis [60]. One of the cavity mirrors was mounted on a piezoelectric transducer (PZT) as shown in Figure 2.6. The beam of a linearly polarized, polarization-stabilized He-Ne laser (Thorlabs HRS015-ASSY3, $\lambda = 633\,\mathrm{nm}$) passed through an AOM that shifted the frequency of the He-Ne laser by 80 MHz and modulated the shifted frequency by $\sim 100\,\mathrm{kHz}$. The beam was then directed to a dichroic mirror (where it could be combined with the two NIR laser beams) and aligned through the cavity. The electric potential of the PZT was adjusted to ensure maximal transmission of the HeNe laser beam through the cavity, and its length was stabilized to this transmission maximum. The frequency modulation produced by the AOM resulted in an intensity modulation around the transmission maximum that was lock-in amplified and used to generate an error signal that was sent to the PZT to counteract fluctuations in the cavity length. In this way, the length, and therefore the free spectral range (FSR) of the etalon, could be kept fixed. The long-term stability of the absolute position of the etalon markers over a period of 10 h was measured by D. Sprecher (see Section 3.2.2 of his thesis [44]) and no measurable drift of the position was detected (the measured positions were randomly distributed and showed a standard deviation of 0.5 MHz).

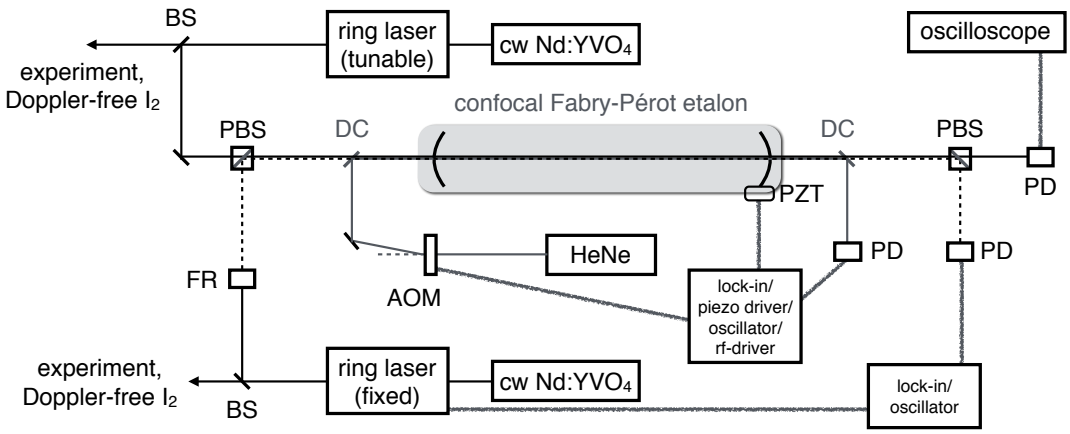

Figure 2.6: Schematic representation of the length-stabilized, confocal etalon used for frequency calibration of both NIR lasers and stabilization of the fixed-frequency NIR laser. PD: photo-diode, PBS: polarization beamsplitter, PZT: piezo-electric transducer, DC: dichroic mirror, FR: Fresnel rhomb, BS: beamsplitter, AOM: acousto-optic modulator.

For the experiments presented in Chapters 5 and 6 of the current thesis, the optical layout of [60] was modified to be able to use the same etalon for calibration and locking of the two NIR lasers. The polarization of the NIR beam from the tunable ring laser was rotated so as to be perpendicular to that of the fixed NIR ring laser. Therefore the two beams could be combined by a polarization beamsplitter (PBS) and overlapped with the He-Ne-laser beam using a dichroic mirror, as shown in Figure 2.6. After passing through the cavity, the three beams were separated and detected individually.

2.5.2 Locking of the fixed-frequency Ti:Sa ring laser

The frequency of the fixed Ti:Sa ring laser used for THz generation was stabilized to a transmission maximum of the high-finesse etalon described above. The system for stabilizing the frequency was developed by Th. Paul and is described in detail in Section 2.9.3 of his thesis [60]. Only a short outline is given here. Rotation of the Brewster plate inside of the Ti:Sa ring laser allows for modification of its frequency. Changing the voltage applied to the PZT on which the Brewster plate is mounted allows for scanning the frequency of the ring laser. For stabilization of its frequency, part of the output beam of the ring laser was aligned through the confocal cavity presented above. The transmission signal was maximized by adjusting the electric potential applied to the PZT of the Brewster plate. At the same time, a frequency dither of 222 Hz was applied to the PZT to modulate the transmission intensity through the etalon in a periodic manner so that a correction signal could be generated in a lock-in amplifier if the frequency drifted. The correction signal could then be fed to the PZT to counteract any drifts, similarly to the way in which variations in cavity length were counteracted (see Section 2.5.1).

The absolute frequency of the ring laser could be determined by first recording a Doppler-free saturated absorption spectrum of molecular iodine while recording a transmission spectrum through the Fabry-Pérot etalon and then choosing a transmission maximum for locking. Because the FSR was fixed, comparing the recorded values for I_2 transition frequencies to reference values [62] allowed for determining the absolute frequency of the transmission maximum used for locking. Details of this process are described below.

The long-term stability of the ring-laser lock was tested by recording a transition in H_2 ($54f0_3 \leftarrow 40d0_2$) successively over a period of 24 hours while the etalon and ring laser remained locked. There was no detectable drift over this time range and the transition frequencies were randomly distributed around the value of 0.9296102(26) THz for the transition specified above. This transition frequency was determined from measurements on separate days and after separate locking of the fixed-frequency laser (see Chapter 6 for details). The statistical error of 2.6 MHz for the transition frequency gives an upper limit for a possible drift of the laser frequency.

2.5.3 Doppler-free saturated absorption spectra of iodine

To obtain highly accurate values for the measured THz frequencies of transitions between high Rydberg states of Xe and H_2 in the entire range of 0.1-15 THz, the precise frequency of the tunable NIR laser needed to be determined over large frequency ranges. For this purpose, saturated absorption spectra of molecular iodine are particularly well suited as absolute frequency standards. Saturated absorption spectroscopy allows for the elimination of Doppler broadenings and therefore the determination of line centers with an accuracy of better than 1 MHz [63]. Molecular iodine offers a dense network of transitions in the visible and NIR regions that have been published in various atlases (see, for example, Refs. [64] and [65]) and are widely used for frequency calibration in atomic and molecular spectroscopy. Refs. [66–71] provide sets of reference lines that were determined at high accuracy as well as potential functions of I_2 and effective Hamiltonians that can be used to predict the frequencies of a broad range of transitions of I_2.

For the experiments presented here, the iodine calibration setup constructed by D. Sprecher and described in greater detail in Section 3.2.1 of his thesis [44] was used. A cell filled with iodine vapor was heated to temperatures of ~ 900 K. A cold finger kept at ~ 300 K served the purpose of reducing the pressure inside the heated part of the iodine cell. The polarizations of the two NIR beams were adjusted so as to be perpendicular to one another and were combined by a polarization beamsplitter (PBS) before being aligned through the iodine calibration setup (see Figure 2.7). Depending on which frequency was to be calibrated, one of the two laser beams was blocked and the other was transmitted to the PBS. The selected NIR beam was directed onto a thick quartz plate and a small portion of the beam was reflected by the front and back surfaces of this plate, producing two

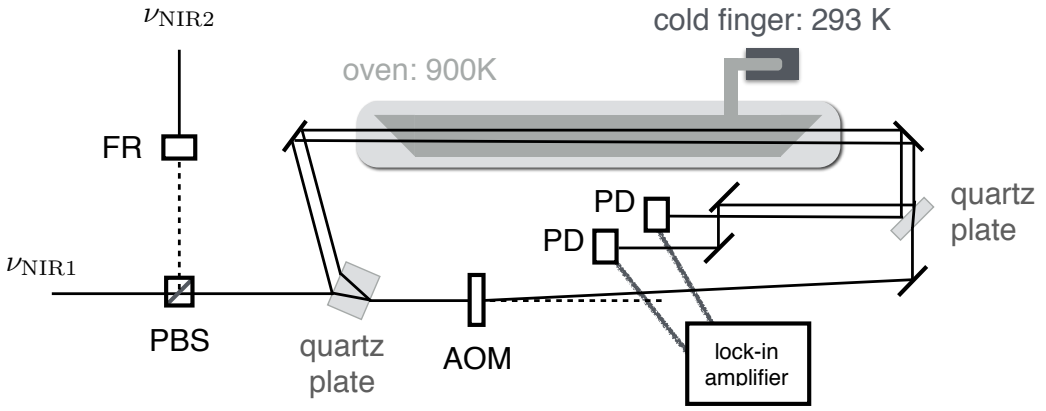

Figure 2.7: Schematic representation of the setup used for Doppler-free spectroscopy of I_2 to perform calibration of absolute frequencies. PD: photo-diode, FR: Fresnel rhomb, AOM: acousto-optic modulator, PBS: polarization beamsplitter.

beams that were aligned through the iodine cell, as shown schematically in Figure 2.7. One of the reflections from the quartz plate was used as probe beam, the other as reference beam. The remainder of the beam passed through an AOM where its frequency was offset by $\Delta\nu_{\mathrm{AOM}} = 80\,\mathrm{MHz}$ and its intensity modulated at a frequency of 20 kHz. This pump beam was then aligned through the iodine cell counter-propagating to the other beams and overlapped with the probe beam.

Transitions of molecular iodine in the heated cell are Doppler broadened by the thermal motion of the iodine molecules. Because the NIR radiation has a narrow bandwidth ($\sim 1\,\mathrm{MHz}$), the pump beam selectively excites iodine molecules having a certain velocity component along the direction of the laser beam when its frequency lies within the Gaussian profile of the Doppler-broadened molecular transition. The reference beam is absorbed by the same velocity component if its frequency is detuned by $+\Delta\nu_{\mathrm{AOM}}/2$ from the absorption maximum (and that of the pump beam therefore by $-\Delta\nu_{\mathrm{AOM}}/2$). Because the pump beam saturates the absorption, a much smaller portion of the probe beam is absorbed than is the case for the reference beam. Both the pump and reference beams are directed onto separate photodiodes and the difference between the photodiode signals is lock-in amplified. The Doppler-free iodine spectrum is obtained by monitoring the difference as a function of the laser frequency.

The absolute frequencies of the NIR lasers could then be determined by comparing to reference data calculated by the simulation software 'IodineSpec 5' [62]. Knöckel and coworkers developed this program by making use of a highly precise model they developed for the description of the rovibronic structure of the initial $X(v'', J'')$ and final $B(v', J')$ state of I_2 [69–71] that was based on high precision measurements available in the literature. Table 3.1 of Ref. [44] lists the frequencies of several transitions to B $v' = 0$ levels of I_2

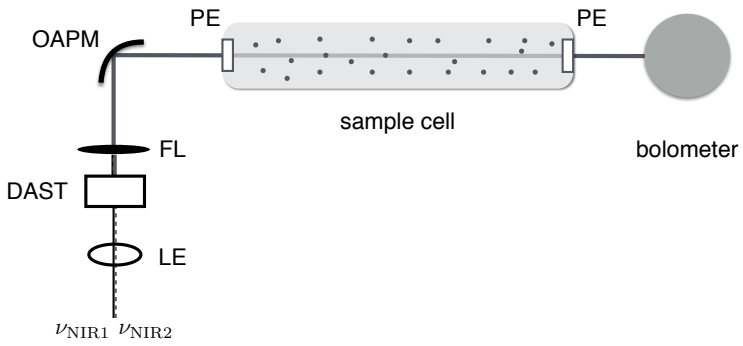

Figure 2.8: Schematic representation of the experimental setup used for performing vibrational spectroscopy in an ambient cell in the THz frequency range. PE: white polyethylene window; LE: lens; DAST: *trans*-4′-(dimethylamino)-*N*-methyl-4-stilbazolium tosylate crystal; FL: black polyethylene filter; OAPM: off-axis parabolic mirror.

calculated with this software and compares them to frequencies measured with a frequency comb in the group of W. Ubachs in Amsterdam. This table also shows that, for transitions to $v' = 1$ states, the shift can be as high as $\sim 39\,\mathrm{MHz}$, depending on the value of J'. A systematic shift of $\nu_{\mathrm{obs}} - \nu_{\mathrm{calc}} = -0.4\,\mathrm{MHz}$ between experimental (ν_{obs}) and calculated (ν_{calc}) frequencies was found for $v' = 0$ levels that is attributed to a pressure shift resulting from the gas in the iodine cell. In the present work, a cell identical to the one used in Amsterdam was used. The pressure shift, however, cancels out in the THz frequency because it is the same for both NIR lasers.

2.6 THz spectroscopy in an ambient cell

The vibrational-spectroscopy experiments presented in Chapter 3 of this thesis were performed under ambient conditions and the sample filled into a glass cell of length $\sim 50\,\mathrm{cm}$ at pressures between $100 - 200\,\mathrm{mbar}$. The transmission of THz radiation through this cell via two white ultra-high-molecular-weight (UHMW) polyethylene (PE) windows was recorded by a bolometer, as shown schematically in Figure 2.8. The THz radiation was generated by difference-frequency mixing of NIR radiation in a DAST crystal as described in Section 2.2. This experimental setup suffered from several deficiencies such as pressure broadening, absorption of THz radiation by water, which led to overlap of the water absorption lines with spectral features of the sample, as well as overlap of spectral features from different isotopomers (see Section 3.4). All of these deficiencies could be eliminated in the design of the VUV-THz double-resonance spectrometer presented in the following subsection.

2.7 VUV laser, VUV-THz double-resonance spectrometer and experimental design

For the development of the VUV-THz double-resonance spectrometer described in the final section of this chapter, a VUV source and an experimental chamber were constructed, as shown schematically in Figure 2.9. Two Nd:YAG-pumped (Continuum PL9030, pulse length 8 ns, repetition rate 25 Hz), pulsed dye lasers (a Lambda-Physik Scanmate and a RadiantDyes NarrowScan 1800 dye laser) were used to generate VUV radiation. VUV radiation was produced by interaction of the dye laser output beams with xenon gas as nonlinear medium in a resonant four-wave-mixing process (see Section 2.7.1). To avoid the use of windows, which would absorb the VUV radiation, a pulsed, supersonic jet was used to introduce the nonlinear gas into the windowless evacuated set of experimental chambers where VUV generation took place. A monochromator was installed, consisting of a toroidal grating that separated the input frequencies used for four-wave mixing and the frequencies generated in the nonlinear optical conversion process, and focused only the desired frequency component, i.e. the sum-frequency $(2\nu_1 + \nu_2)$, into the excitation region (marked by a grey dot in Figure 2.9).

All pulsed components of the experiment were synchronized using a digital delay generator and operated at a repetition rate of 25 Hz. For the experiments presented in this thesis, an experimental chamber originally designed in the realm of the dissertation of M. Raunhardt [72] was used because of the large openings designed specifically for use with millimeter-wave radiation. A detailed description of the different components can be found in the following sections. The experimental apparatus was characterized and its stability tested by very high resolution spectroscopy (down to ~ 140 kHz) of high Rydberg states of Xe. For this purpose, a backward wave oscillator (BWO)-based source of sub-millimeter-wave (sub-millimeter-wave) radiation was used. Because high Rydberg states are very susceptible to stray fields (their polarizability scales as n^7), they are ideally suited for determining and minimizing residual stray electric and magnetic fields present in the excitation region [73]. The following subsections describe in more detail the VUV radiation source (Subsection 2.7.1), the sub-millimeter-wave source (Subsection 2.7.2), the photoexcitation and detection region (Subsection 2.7.3), and the procedure used to measure and compensate stray electric and magnetic fields (Subsection 2.7.4).

2.7.1 Generation of VUV laser radiation

VUV radiation cannot propagate freely in a typical laboratory environment because it is immediately absorbed by air. To perform spectroscopic experiments with VUV radiation, one therefore needs to work inside vacuum. Coherent VUV radiation was generated by four-wave mixing, making use of the third-order nonlinear optical susceptibility $\chi^{(3)}$ (see

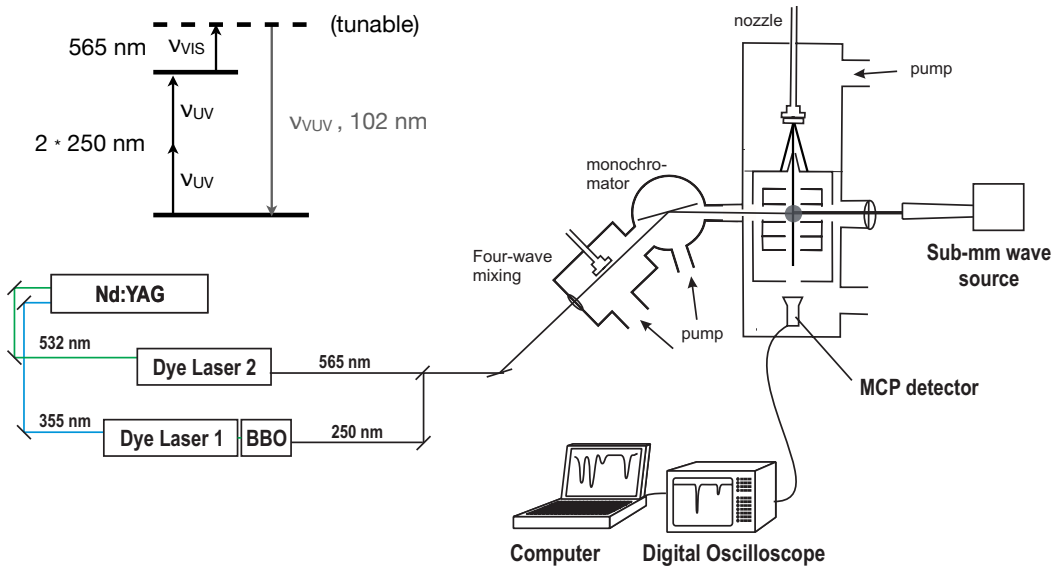

Figure 2.9: Schematic representation of experimental setup constructed for recording sub-millimeter-wave spectra of high Rydberg states in Xe following VUV excitation.

Equation (2.1)) because it is the first nonlinear optical term that is non-zero for isotropic media such as the rare-gas mixtures typically used for VUV generation [74]. In four-wave-mixing, VUV radiation can be generated at either the sum frequency ($\omega_{4(\mathrm{s})} = \omega_1 + \omega_2 + \omega_3$) of three incident photons or the difference frequency ($\omega_{4(\mathrm{d})} = \omega_1 + \omega_2 - \omega_3$). The process of third-harmonic generation ($\omega_{\mathrm{VUV}} = 3\omega_1$) is a special case of sum-frequency mixing. To increase the efficiency of VUV generation, the radiation beams used for sum and difference-frequency generation are focused in the nonlinear medium. As for THz generation (see Section 2.1), the wave vector mismatch of the different beams involved in the four-wave mixing process is very important for efficient VUV generation. For an optimal value of the wave vector mismatch, the incident beams are first overlapped with one another by way of a dichroic mirror, their angles with respect to one another adjusted, and they are focussed at the same spot using a telescope to adjust the divergence of the second dye laser beam. The elements of $\chi^{(3)}$ are greatly enhanced if either of the incoming beams, or higher harmonics thereof, are in resonance with an atomic transition of Xe [75, 76]. In general, the fundamental frequency is absorbed strongly if it is in resonance with an atomic transition. Consequently, the only case of practical relevance for the generation of tunable VUV radiation is fixing the second harmonic of one of the input beams to a two-photon resonance of the nonlinear medium and using a third, tunable laser beam (ω_3) to generate tunable VUV radiation.

In the experiments described in this thesis, the monochromator chamber shown in Figure 2.9 was used, where the first-order diffractions from a toroidal, gold-coated grating were separated according to their frequency. The frequency component entering the ex-

perimental chamber was chosen by rotating the angle of the grating. Because of the toroidal geometry of the grating used here, the radiation was focused near the excitation region (marked by a grey dot in Figure 2.9). Two input lasers were used and the frequency $\omega_1 = \omega_2 = \omega_{\mathrm{Xe}}/2$ of the first laser was set so as to be resonant with the $(5\mathrm{p})^6\,{}^1S_0 \rightarrow (5\mathrm{p})^5\,6\mathrm{p}[1/2]_0$ two-photon resonance at $\tilde{\nu}_{\mathrm{Xe}} = 80\,118.9839\,\mathrm{cm}^{-1}$ in Xe for resonance-enhanced sum-frequency mixing. The frequency ω_3 of the second laser was scanned to obtain tunable VUV radiation of frequency $2\omega_1 + \omega_3$. This method for generating tunable VUV radiation was established by Wallenstein and coworkers [76, 75] who used a cell to contain the nonlinear gas. In general, VUV generation with rare gases below 105 nm is best achieved using a gas jet, as first demonstrated by Kung [77]. A jet was chosen here because it offers greater versatility; for the case of a cell, a window needs to be used for separating the nonlinear gas from the vacuum chamber in which the spectroscopic experiments are carried out. Below a frequency of $\sim 105\,\mathrm{nm}$, all known materials that could be used as a window absorb VUV radiation and it becomes necessary to use a jet to generate the radiation. Using pulse energies of about $200\,\mu\mathrm{J}$ at the wavenumber $\tilde{\nu} = \tilde{\nu}_{\mathrm{Xe}}/2$ and of about 0.5 mJ at the wavenumber $\tilde{\nu}_2$, about 10^{10} photons per pulse at 25 Hz could be generated at the sum-frequency $2\tilde{\nu}_1 + \tilde{\nu}_2$ after the monochromator. When carrying out high-resolution measurements, the VUV radiation intensity was attenuated to avoid the generation of ions or of too high densities of excited atoms or molecules.

2.7.2 Sub-millimeter-wave radiation source

A phase-stabilized, backward-wave oscillator (BWO) source was used for the generation of the sub-millimeter-wave radiation in the range below 400 GHz. This source was developed as a high-frequency extension of the sub-millimeter-wave source described in Ref. [78] and its components, designed in the realm of a collaboration with the group of G. Winnewisser, are described in detail in Ref. [79]. The source consisted of a BWO tube mounted on a 0.7 T permanent magnet and operated with a potential difference of 1.5 to 3.8 kV being applied between cathode and anode. An electron beam was generated at the heated cathode, and its energy modulated by the spatially periodic structure of the electric field resulting from a comb slow-wave structure placed between cathode and anode. This resulted in an electromagnetic wave propagating in the opposite direction to the electron beam and which was coupled out of the BWO by a rectangular waveguide and transmitted by a horn antenna. The frequency could be adjusted by changing the bias voltage. Part of the output power was directed to a harmonic mixer where its frequency was down-converted and compared to a synthesized local oscillator. The BWO produced an output power of up to 40 mW at a bandwidth of $< 1\,\mathrm{kHz}$ in the frequency range between $240 - 380\,\mathrm{GHz}$.

2.7.3 Experimental chamber

A schematic view of the experimental chamber is presented in the top right corner of Figure 2.9. The excitation region, marked by a grey dot at the center of the main chamber, is the point where the supersonic, VUV-radiation, and sub-millimeter-wave-radiation beams intersect. It is surrounded by a stack of resistively coupled, cylindrical electrodes (length: 7.6 cm) that is used for the application of strong electric-field pulses and designed to produce a homogeneous field distribution. The cylindrical symmetry ensures that stray fields along the radial direction are less than 1 mV/cm. Electric potentials of several kV can be applied across the stack for selective field-ionization of the high Rydberg states produced by VUV and sub-millimeter-wave excitation.

By applying two successive pulsed electric potentials across the electrode stack, the initial Rydberg states produced by VUV excitation can be ionized at a different time than the final Rydberg states produced by sub-millimeter-wave excitation. Consequently, the ion signal from these two pulses can be monitored separately (see Figure 4.6). These potentials also served to accelerate the electrons or ions produced by field ionization or direct ionization onto a micro-channel-plate (MCP) detector along the axis of the atomic beam. Ions of different mass were distinguished on the basis of the times of flight. The polarity of the voltage determined whether ions or electrons are detected and spectra were recorded by monitoring their signal while scanning the VUV or sub-millimeter-wave frequencies. The electric potentials were pulsed at a repetition rate of 25 Hz, which translates to one pulse every 40 ms. Although the pulse length was on the order of only $\sim 10\,\mu$s, small residual stray fields could be present in the photoexcitation volume. Because these small residual fields remained more or less constant during the length of the excitation process (between $1 - 10\,\mu$s), they could be eliminated by applying small dc compensation fields pointing in the opposite direction (see Section 2.7.4 for details).

The electrode stack was surrounded by a set of two concentric magnetic shields made of mumetal for the passive minimization of stray magnetic fields such as the Earth's magnetic field or magnetic fields generated by laboratory devices. Both the electrode stack and mumetal shields had large openings (~ 5 cm) for the introduction of the sub-millimeter-wave radiation, which was produced outside the vacuum chamber by the BWO source described in Section 2.7.2 and entered the measurement chamber via a Teflon window.

The atomic or molecular beam was generated by expanding a sample kept in a reservoir at high pressure using a pulsed valve (General valve, Series 9, pulse length $\sim 200\,\mu$s, orifice diameter 0.5 mm) at a repetition rate of 25 Hz (see gas source chamber in Figure 2.9). By adiabatic expansion into a vacuum chamber maintained at a pressure of $\sim 10^{-4}$ mbar, the sample was translationally, rotationally and vibrationally cooled. After propagating freely for a distance of ~ 15 cm, the pulsed gas beam passed through a skimmer with an aperture of 1 mm diameter. This skimmer selected the central, coldest part of the

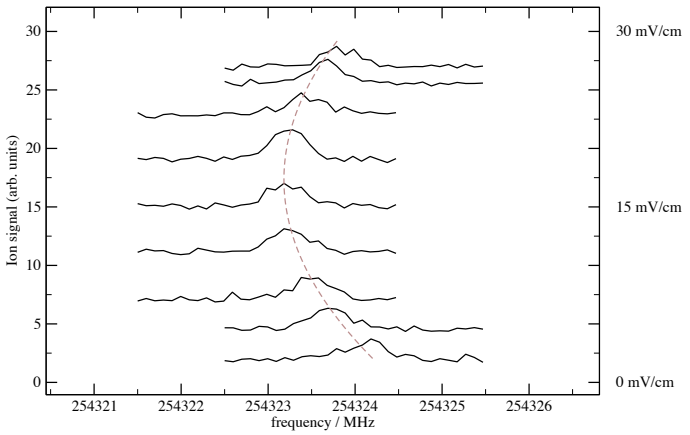

Figure 2.10: Shift of the frequency of the $69p[3/2]_2(5/2) \leftarrow 84s[3/2]_1(3/2)$ transition (note that the assignment of the K quantum number for the 69p state is ambiguous) in ^{129}Xe in dependence on applied compensation fields. Spectra are shifted vertically by an offset corresponding to the value of the applied compensation field in mV / cm (between 0 mV / cm and 30 mV / cm).

molecular beam so that only molecules with a very small velocity component perpendicular to the propagation direction traveled to the excitation region. This served to minimize Doppler broadenings. The pressure in the experimental chamber was on the order of $\sim 10^{-6}$ mbar while the sample nozzle was under operation. Specific settings depended on the experimental conditions and are mentioned in the relevant chapters of this thesis.

2.7.4 Minimization of field effects

Stray electric fields remain constant during the timescale of the excitation process ($\sim 10\,\mu s$) and do not fluctuate from one experimental cycle to the next. They are parallel to the main symmetry axis of the electrode stack described in Section 2.7.3 and can therefore be compensated by applying small dc offset potential differences along the length of the stack. High Rydberg states, in combination with recorded sub-millimeter-wave spectra, could be used as sensors for such stray fields [73]. Figure 2.10 illustrates the quadratic shift of the frequency of the $69p[3/2]_2(5/2) \leftarrow 84s[3/2]_1(3/2)$ transition in ^{129}Xe resulting from the Stark effect as the applied electric field was varied between 0 mV/cm and 30 mV/cm. Spectra were shifted vertically by an offset corresponding to the value of the applied field in mV/cm. In this case, the stray electric field could be compensated to ~ 0 mV/cm by applying a compensation field of 13.3 mV/cm. Exact values for compensation fields varied slightly depending on experimental conditions and had to be determined in regular intervals. Broadenings of transitions resulting from the interaction between Rydberg atoms and ions were also observed and minimized by reducing the VUV laser intensity. Power broadening by the sub-millimeter-wave radiation intensity was observed and Rabi oscillations could be measured for these transitions. A description and analysis of these effects

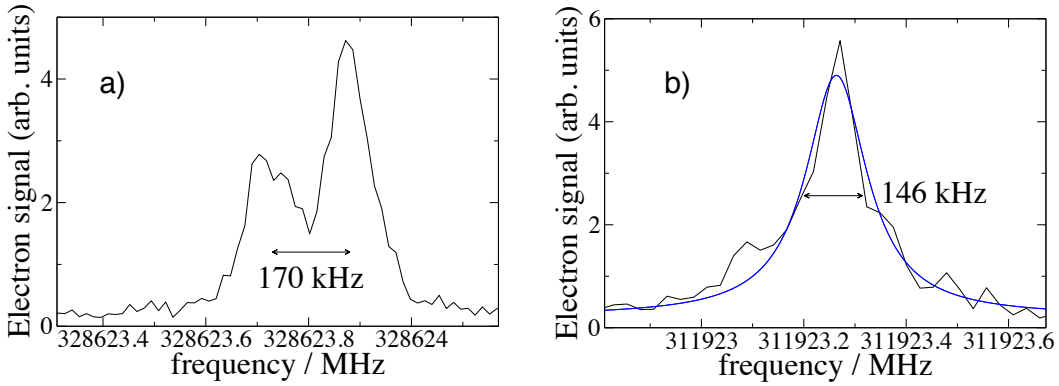

Figure 2.11: Panel a): $59f[3/2]_1 \leftarrow 53d[3/2]_1$ transition of Xe that is split into a doublet because of a stray magnetic field present in the excitation region. Panel b): $70p[5/2]_2 \leftarrow 58d[3/2]_1$ transition of Xe with its transit-time limited linewidth of 150 kHz.

is presented in Section 4.4. By reducing sub-millimeter-wave and VUV radiation intensities, it was possible to observe transitions with linewidths of ~ 140 kHz (see panel b) of Figure 2.11). This lower limit to the linewidth is attributed to transit-time broadening: it takes the beam of excited Xe atoms about 7 μs moving at a velocity of ~ 350 m/s to traverse the sub-millimeter-wave radiation beam.

Initially, after installation of the experimental chamber, unexpected splittings were observed for most transitions, as illustrated with the example of the $59f[3/2]_1 \leftarrow 53d[3/2]_1$ transition in ^{132}Xe in panel a) of Figure 2.11, where the splitting is 170 kHz. This splitting was later attributed to the presence of a small magnetic field (on the order of $\sim 10\,\mu$T) present in the excitation region and resulting from a slightly magnetized screw that was inadvertently used when assembling the electrode stack. After a detailed analysis of the above effects and a minimization of stray fields, shifts and splittings, the newly constructed experimental setup was well-characterized and could be used for the development of the VUV-THz double-resonance spectrometer described below.

2.8 VUV-THz double-resonance spectrometer

In this subsection, the extension of a pulsed, laser-based THz radiation source described in Ref. [26] is presented, and its integration into a VUV-THz double-resonance spectrometer is described. The source is based on difference-frequency mixing of NIR radiation in the nonlinear crystal DAST (see Section 2.2 for details). THz generation takes place in a DAST crystal placed in vacuum, which eliminates the problem of power reduction by water vapor absorption. The combination of this THz source with VUV radiation enables studies of Rydberg-Rydberg transitions in the THz frequency range, and opens up the possibility of photoionization-detected rotational and vibrational spectroscopy. A special feature of the

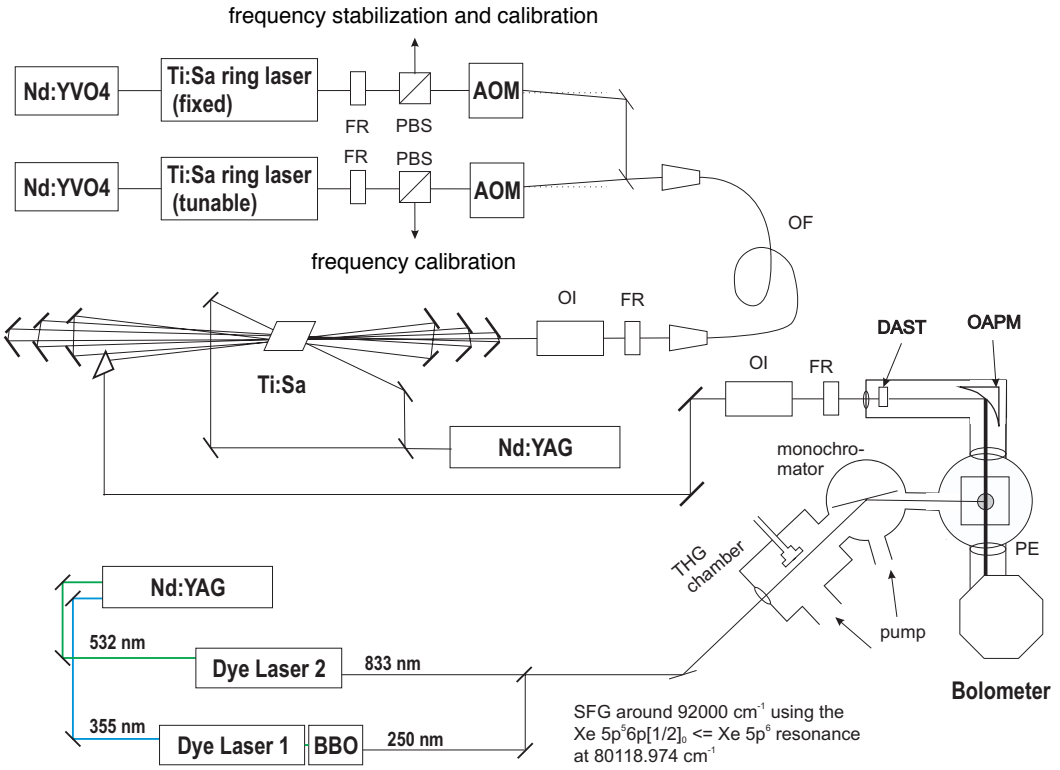

Figure 2.12: Schematic representation of experimental setup used for VUV-THz experiments. FR: Fresnel rhomb, PBS: polarization beamsplitter, AOM: acousto-optic modulator, OF: optical fiber, OI: optical isolator, OAPM: off-axis parabolic mirror, PE: white polyethylene window.

THz-radiation source presented here is the possibility of adjusting the pulse length, and thus the spectral resolution: Short pulses ($\sim$ 10 ns) with a larger bandwidth ($\sim$ 85 MHz) can be used to record spectra over broad regions, whereas long pulses ($\sim$ 400 ns) with a narrow bandwidth ($\sim$ 3 MHz) are suited to study selected regions at high resolution (see Section 2.6 and Chapter 5).

In addition to the broad tunability and narrow bandwidth of the THz radiation, the spectrometer also offers the advantage of high sensitivity, resulting from the background-free detection of transitions with single-ion sensitivity. This also allows for mass-selective measurements because the transitions are detected by photoionization or pulsed-field ionization.

2.8.1 The vacuum chamber for THz-VUV double-resonance experiments

In the experimental chamber developed in the realm of this thesis, THz generation and the detection of THz absorption took place inside a vacuum chamber. A schematic overview of the entire experimental setup is presented in Figure 2.12. For clarity, only one of the

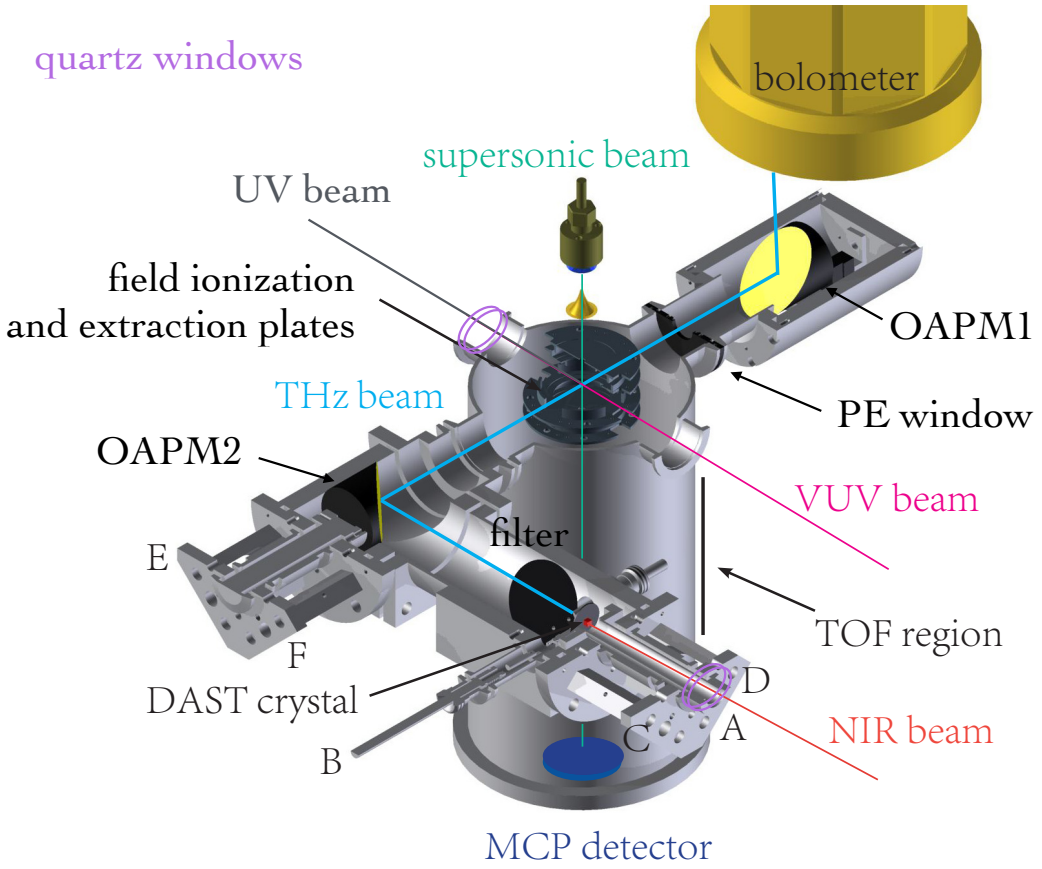

Figure 2.13: Schematic representation of experimental chamber of VUV-THz double resonance spectrometer. C, D, A: tilt angles of DAST crystal mount, B: horizontal displacement of crystal, E, F: tilt angles of off-axis parabolic mirror. TOF: time-of-flight, MCP: micro-channel plate, OAPM: off-axis parabolic mirror, PE: polyethylene.

two bow-tie amplifiers that were used to generate intense pulses of NIR laser radiation is shown (see Section 2.6 for a description of the generation of the pulsed, high-power NIR radiation). The vacuum chamber used for THz generation, as well as the experimental chamber, are depicted in Figure 2.13. The DAST crystal was placed on a translational stage and could be displaced horizontally by turning the screw at position B from outside of the vacuum chamber. The tilt angle of the crystal could be adjusted by the screws at positions C, D and A. The displacement was transferred to the crystal from outside the vacuum chamber by placing the crystal mount on a firm, solid tube that was surrounded by a flexible tube. The tubes were joined at one end, where a quartz window was placed for introduction of the NIR radiation, as shown schematically in Figure 2.14. The other end of the firm tube, where the DAST crystal was placed, extended into the vacuum chamber by about 2 cm. The NIR radiation could therefore pass through the flexible part of the tube and reach the crystal on the other end. The flexible outer tube was necessary for maintaining vacuum conditions. By adjusting the screws at C, D, and A, the flexible tube

was contracted on one side. Because the firm and flexible tubes were joined at one end, the firm tube had to change its tilt angle to compensate this movement, which directly led to a change in the tilt angle of the DAST crystal. Pressures of $\sim 10^{-6}$ mbar were maintained by a turbo-molecular pump that was placed at the back side of the TOF region shown in Figure 2.13.

After THz generation in the DAST crystal, the beam was directed to a gold-coated, off-axis parabolic mirror (OAPM1) with effective focal length (EFL) of 190.5 mm that focused the beam in the excitation region, near the intersection of VUV and atomic/molecular beams. For the experiments on H_2 (see Chapter 6), a third, UV beam was introduced into the chamber, as shown by the grey line labeled B Figure 2.13. The tilt angles of OAPM1 could be adjusted by the screws designated E and F by transferring the displacement to the evacuated region with a combination of a solid rod on which the mount for the OAPM was placed, and a flexible tube that surrounded it, similarly as for the DAST crystal. For initial alignment of the THz beam, a second OAPM (OAPM2) was used that was separated from the vacuum chamber by a white UHMW PE window. This OAPM had an EFL of 101.6 mm and was placed at a distance of twice its EFL from the focus of the THz beam so that it refocused the THz beam near the entrance aperture of the Winston cone of the bolometer (see Section 2.4), which was also at a distance of ~ 200 mm from the OAPM.

The atomic or molecular beam was generated by expansion of the sample into vacuum, and its innermost part separated by a skimmer for minimization of Doppler broadenings (see Section 2.7.3). Once the atomic or molecular species was excited by a combination of VUV, THz and UV radiation beams, a high electric potential was applied to the electrode stack used for field ionization and ion/electron extraction (see Section 2.7.3). Depending on the polarity of the potential difference, the electrons or the ions were accelerated to the micro-channel plate (MCP) detector. Ions could be separated by their different times of flight. UV and VUV radiation beams produced initial Rydberg states that were further excited to higher-lying Rydberg states by THz absorption. By selectively ionizing only these higher-lying Rydberg states (see Chapters 5 and 6 for details), the background-free detection of THz absorption was achieved.

2.8.2 Alignment of the THz radiation beam

Alignment of the THz radiation beam through the experimental chamber presented some challenges because THz radiation is not visible by eye. To obtain an initial, rough alignment of the THz beam, the NIR beam was first aligned through the experimental chamber. The focus of the NIR beam close to the excitation region was tested by viewing with an IR camera that could be inserted into the vacuum chamber perpendicularly to the NIR beam by removing the quartz window through which the UV beam was directed into the chamber (see Figure 2.13). A card was inserted into the chamber after removal of OAPM2 as well

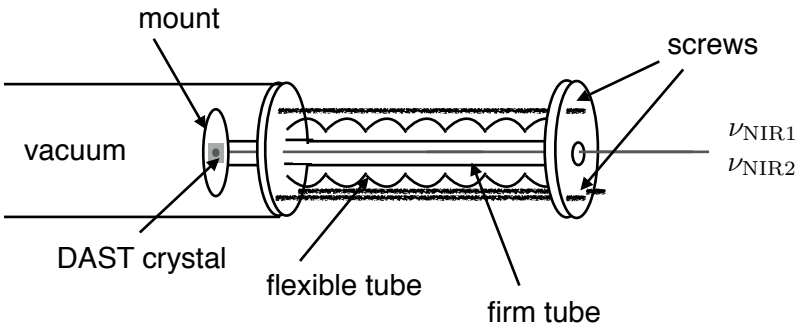

Figure 2.14: Schematic representation of the mechanical system used to adjust the tilt angle of the DAST-crystal mount from outside the vacuum chamber (see text for details).

as the PE window. This allowed the determination of the focal point of the NIR beam by measuring the lateral displacement of the card once it reached the focus of the beam, as observed by the IR camera. For the initial alignment of the NIR beam, it was first made sure that the NIR beam entered the chamber through the center of the quartz window and was incident on the center of OAPM1. The beam was then aligned through the chamber by changing the tilt angles of OAPM1.

The mount of OAPM1 was placed, by experimental design, at such a position as to ensure that the center of OAPM2 was in line with the center of the main experimental chamber. The NIR beam was aligned so that it exited the chamber through the center of the PE window, which was in line with the center of OAPM2. With the help of an IR viewer, the NIR beam was directed into the bolometer near the center of its wedged PE window. The NIR power was then strongly reduced and the alignment optimized by maximizing the bolometer signal upon adjusting the tilt angles of OAPM2 and then those of OAPM1. The DAST crystal was then placed in the beam path and the above alignment procedure repeated. Afterwards, a black PE filter was placed in the beam path that absorbed the NIR radiation while transmitting the THz radiation. The NIR power was increased to the level of normal usage ($\sim 100\,\mathrm{mW}$) and the generated THz signal detected at the bolometer. The THz signal could be differentiated from the background NIR signal by blocking the output of either of the two NIR ring lasers. A decrease by a factor of more than 2 indicated that THz radiation was generated. The alignment of the THz beam was then optimized by first adjusting the tilt angles of OAPM2 and then those of OAPM1. The position and tilt angles of the DAST crystal were adjusted and the NIR beam shifted laterally by two mirrors that were located in front of the quartz window and outside of the vacuum chamber. Finally, the polarization of the incident NIR beam was optimized because it had different values in the regions below and above 3.3 THz (see Section 2.2), although the optimal polarization angle was constant within these two regions.

After the initial alignment procedure had been performed, it was possible to detect and

optimize the THz radiation by recording transitions between Rydberg states of H_2 or Xe and detecting them by selective field ionization (see Section 2.7.3). A Rydberg-Rydberg transition in Xe or H_2 was recorded and the scan stopped at the transition maximum. The alignment of the UV, VUV and THz beams was then further optimized in an iterative procedure by maximizing the ion or electron signal generated by selective field ionization. For these measurements, the black polyethylene filter could be removed because the NIR radiation created no detectable background signal. Indeed, the only way by which a NIR-ionization background could have been created would have been by direct ionization of the Rydberg states with NIR radiation. This process is unfavorable because the frequency of the NIR radiation is shorter than the orbiting frequency of the Rydberg electron. Ionization by NIR radiation could only be observed when the focus of the NIR beam coincided perfectly with the intersection of VUV, UV and molecular beams, which was not the case after optimization of the THz beam. Once initial alignment of THz radiation had been performed and a signal in H_2 or Xe found, it was not necessary to use the bolometer for alignment purposes on a daily basis. The direction of the NIR beam was marked by two pinholes, and by a mark on the white PE window at the exit of the vacuum chamber, so that a signal strong enough for optimization could easily be detected.

2.8.3 Optimal measurement conditions

An optimal signal-to-noise ratio (SNR) was obtained when applying the THz radiation pulses $\sim$ 50 ns after VUV and UV excitation. Particularly in the case of H_2, it was important to perform the laser excitation in the front part of the gas pulse, where the signal strength from the initial Rydberg state was considerably reduced. In this part of the gas pulse, densities and temperature of the supersonic beam are low, which proved to be optimal conditions for recording THz spectra. Another critical parameter was the pulse sequence used for ionization: The low-voltage (150 V) and 1.4 μs-long pre-pulse used and applied 200 ns after THz excitation and followed by a second, high-voltage pulse ($\sim$ 600 V in the case of H_2) proved to be optimal. The pre-pulse served to eliminate background ion signal and further improve the observed SNR. Specific conditions and settings that were used varied depending on the measured species and are mentioned in the corresponding chapters of this thesis.

Chapter 3

Vibrational Spectroscopy in an Ambient Cell

3.1 Introduction

This chapter presents vibrational spectra of the atmospherically relevant freon-11 ($CFCl_3$), chloroform and selected isotopomers recorded in the region between 7 and 8 THz using the broadly tunable THz source described in Chapter 2 of this thesis. $CHCl_3$ and $CFCl_3$ are prototypical oblate-top molecules with C_{3v} symmetry and have been investigated comprehensively in both experimental and theoretical works. The pure rotational spectra of the vibronic ground state and of the first excited vibrational levels of the degenerate (e) modes: the stretching mode ν_5 [80] and deformation mode ν_6 [81] of chloroform have been measured previously, and so have rotationally resolved infrared spectra of the fundamental bands of the degenerate bending mode ν_4 [82] and ν_5 [80]. For the lowest vibrational level ν_6, the fundamental transition wavenumber was determined from low-resolution infrared [83] and Raman [84, 85] spectra to be $\sim$260 cm^{-1} (7.80 THz), but none of the infrared and Raman spectroscopic studies [83–85] reported at the time this research was carried out had provided information on the fundamental bands of the different chlorine isotopomers. The situation is very similar for the asymmetric deformation modes of $CFCl_3$ and its isotopomers, for which only Raman spectra recorded at moderate resolution had been reported (see, for instance, Ref. [86]). This chapter is based on the article "Vibrational spectra of chloroform, freon-11 and selected isotopomers in the terahertz region" by myself, J. Liu and F. Merkt [87]. Note that meanwhile a very high resolution study of the ν_6 fundamental in chloroform has become available [88] .

3.2 Experimental

A measurement of the absorption spectra of $^{12}CHCl_3$, $^{13}CHCl_3$, $CDCl_3$ and $CFCl_3$ with natural isotopic abundance of chlorine in the region of the ν_6 fundamental band is presented in the following. This mode is of e symmetry for the C_{3v} isotopomers but splits into two modes, $\nu_6(a')$ and $\nu_9(a'')$, in isotopomers of C_s symmetry. In the following, the convention for numbering the normal modes as described on p. 25 of Ref. [54] is used: vibrational modes ν_r are grouped according to their symmetry, the totally symmetric species having the lowest index r and subsequent indices being given by the order of the irreducible representations in the character table. Within one symmetry species, the index increases with decreasing vibrational frequency.

The experimental setup was identical to the one described in Ref. [26] and is described in Chapter 2. It was placed under an N_2-purged plexiglas cage to reduce water absorption. $^{12}CHCl_3$, $^{13}CHCl_3$, $^{12}CDCl_3$ and $^{12}CFCl_3$ were supplied by Sigma-Aldrich ($\geq$ 99.5% purity) and used without further purification. A one-meter-long absorption cell with white, ultra-high molecular weight (UHMW) polyethylene windows was filled with 120 mbar ($^{13}CHCl_3$) or 200 mbar (all other compounds) of the sample gas. A 4-Å-mesh molecular sieve was placed in both the liquid sample and the absorption cell to adsorb water and so reduce the interference of water absorption lines. The THz transmission signal was measured using a 4.2 K germanium bolometer and divided by the square of the NIR power for normalization purposes. Because of the width of several GHz of the observed bands (see below), calibrating the NIR radiation frequency with an accuracy of $\sim$1 GHz using a commercial wavemeter proved to be sufficient.

3.3 Results

Rotational contours were generated by convolution with a Lorentzian line profile with a full width at half-maximum of 1 GHz. Decreasing the vapor pressure reduced the pressure broadening without inducing a measurable shift of the band origins. The precision of the measurement was limited by pressure broadening in combination with spectral congestion, which prevented us from resolving individual rotational lines. Under these conditions, the central Q branch represents the spectral feature most suitable to derive the vibrational transition frequencies. The minimum pressure compatible with a satisfactory signal-to-noise ratio is limited to $\approx$ 50 mbar by the sensitivity of the measurement, which itself is limited by the pulse-to-pulse fluctuations of the laser power (see Ref. [26] for further details). Using a longer (or a multipass) absorption cell would enable a further reduction of the pressure.

A computer program was written to simulate the frequencies and intensities of the rovi-

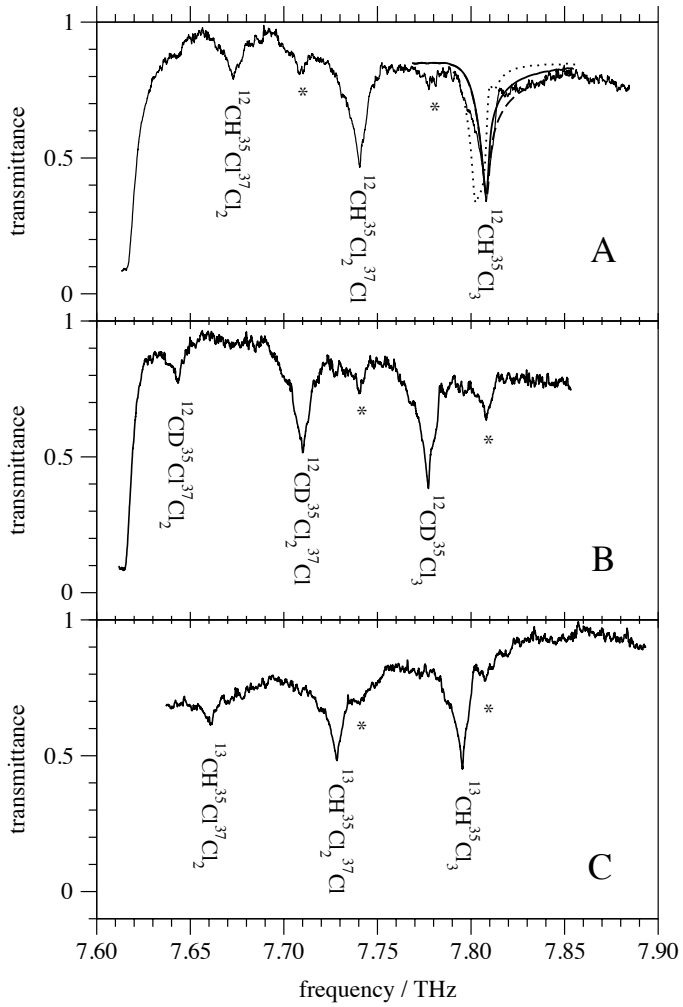

Figure 3.1: Spectra of the fundamental band of the CCl_3 asymmetric deformation mode of chloroform and selected isotopomers. The strong line on the far left-hand side of the spectra in a) and b) corresponds to a water line. The lines marked by asterisks correspond to impurities of $^{12}CDCl_3$ in panel a) and $^{12}CHCl_3$ in panels b) and c). In panel a), simulated profiles of the $^{12}CH^{35}Cl_3$ isotopomer, assuming values of -0.84 (dashed line), -0.86 (full line) and -0.88 (dotted line) for ζ_6 are displayed (see text for details).

brational transitions of the ν_6 fundamental band of the isotopomers of C_{3v} symmetry. The Hamiltonian used for this simulation is the same as the one given in Eqs. (1-2) of Ref. [82], which includes the Coriolis interaction and the $l(2,2)$ interaction. Rotational contours were generated by convolution with a Lorentzian line profile with a full width at half-maximum of 1 GHz. The program was tested with the available pure rotational and rovibrational spectra reported in Refs. [80] and [81].

	Sym.	Expt.	Calc.
$^{12}CHCl_3$			
$^{12}CH^{35}Cl^{37}Cl_2$	a'	7.6725(20)	7.798
	a''		7.822
$^{12}CH^{35}Cl_2{}^{37}Cl$	a''	7.7400(20)	7.869
	a'		7.889
$^{12}CH^{35}Cl_3$	e	7.8076(20)	8.008
$^{12}CDCl_3$			
$^{12}CD^{35}Cl^{37}Cl_2$	a'	7.6428(20)	7.766
	a''		7.791
$^{12}CD^{35}Cl_2{}^{37}Cl$	a''	7.7096(20)	7.835
	a'		7.857
$^{12}CD^{35}Cl_3$	e	7.7768(20)	7.915
$^{13}CHCl_3$			
$^{13}CH^{35}Cl^{37}Cl_2$	a'	7.6604(20)	7.783
	a''		7.809
$^{13}CH^{35}Cl_2{}^{37}Cl$	a''	7.7279(20)	7.854
	a'		7.875
$^{13}CH^{35}Cl_3$	e	7.7949(20)	7.933
$^{12}CFCl_3$			
$^{12}CF^{35}Cl^{37}Cl_2$	a'	7.2058(20)	7.307
	a''		7.345
$^{12}CF^{35}Cl_2{}^{37}Cl$	a''	7.2593(20)	7.364
	a'		7.400
$^{12}CF^{35}Cl_3$	e	7.3140(30)	7.438

Table 3.1: Experimental and calculated fundamental frequencies of the CCl_3 asymmetric deformation modes of chloroform, freon-11 and selected isotopomers in units of THz. This mode corresponds to ν_6 for molecules of C_{3v} symmetry and ν_6 and ν_9 with A' and A'' symmetry, respectively, for molecules of C_s symmetry. The numbers in parentheses represent the experimental uncertainties. a): Calculated values at MP2/cc-pVTZ level of approximation with frozen-core approximation, unscaled (see text for details). b): The experimental uncertainty is larger for $^{12}CF^{35}Cl_3$ than for the other molecules because of the partial overlap of the central Q-branch with a water line (see text for details).

The main intensity contribution to the sharpest features observed in the spectra displayed in Fig. 1 arises from the central Q-branch of the vibrational band because other branches are spread out over a very broad range. In isotopomers of C_s symmetry, the ν_6 mode

splits into two modes, ν_6 and ν_9 of A' and A'' symmetry, respectively. The spectra do not reveal any evidence for this splitting. The band maxima of the different chlorine isotopomers shift linearly with increasing number of ^{37}Cl atoms (by $-67.5(3)$ MHz per additional ^{37}Cl atom in $^{12}CHCl_3$, $-67.0(3)$ MHz in $^{12}CDCl_3$, $-67.3(3)$ MHz in $^{13}CHCl_3$ and $-54.1(6)$ MHz in $^{12}CFCl_3$). The shapes of the unresolved Q-branches of all isotopomers appear identical within the resolution and sensitivity limits of the measurement presented here. The harmonic vibrational frequencies of the $\nu_6(a')$ and $\nu_9(a'')$ modes calculated *ab initio* also appear degenerate within the expected precision limit of the method used (see Table 1).

In simulating the ν_6 fundamental band of $^{12}CH^{35}Cl_3$, the ground state molecular constants were fixed to the values given in Table 1 of Ref. [82] and those of the vibrationally excited state to those listed in Table VIII of Ref. [81]. In particular, the value of $(C_6 - B_6 - C_6\zeta_6)$ was fixed at -87.23874 MHz, as reported in Ref. [81]. Simulations with the same value for $(C_6 - B_6 - C_6\zeta_6)$, but values for ζ_6 of -0.84 (dashed line), -0.86 (full line) and -0.88 (dotted line) are also shown in Fig. 1. Comparison with the experimental data suggests that the value of -0.86 for ζ_6 proposed in Ref. [81] yields the best agreement.

From the simulations, we conclude that the band maximum is shifted by $\sim$0.5 GHz with respect to the vibrational band origin for all compounds investigated. When also considering the uncertainty of the NIR laser frequency (see above) and the uncertainty in the location of the intensity maximum, an overall uncertainty in the band origins of 2 GHz results for all compounds except $CF^{35}Cl_3$, for which an uncertainty in the fundamental frequency of 3 GHz results from the partial overlap of the central Q-branch with a water line. The fundamental transition frequencies are listed in Table 1, where they are compared with values calculated *ab initio* by J. Liu at the MP2/cc-pVTZ level of approximation with frozen-core approximation for the CCl_3 asymmetric deformation mode with Gaussian03 [89]. The calculated harmonic frequencies systematically overestimate the experimental fundamental frequencies by a factor of $\sim$1.02. The small discrepancy of 2.4σ between the result of $260.594\,114\,6\,(67)\,cm^{-1}$ for the band origin of the ν_6 vibration of $CH^{35}Cl_3$ reported in the high resolution study [88] and the result of $260.43(7)\,cm^{-1}$ given in Table 3.1 could be caused by modification of the vibrational contour by the $2\nu_6 - \nu_6$ hot band, as suggested in Ref. [88]. It may also be a result of our assumption that $\zeta = -0.86$ while ref. [88] finds a value of $\zeta = -0.88$.

3.4 Conclusions and Outlook

The laser-based source of tunable THz radiation developed in the realm of this thesis was used to obtain information on low-frequency vibrations of chloroform, freon-11 and several of their isotopomers. The fundamental frequencies of the CCl_3 asymmetric deformation modes of these species were determined. The results presented above also open up several

issues that leave room for improvement. As can be seen from the spectra displayed in Figure 3.1, when recording THz spectra in transmission mode under ambient conditions, the spectra feature interfering water absorption lines. Additionally, even if spectra are recorded in pure absorption mode, if THz generation takes place in air, the intensity of the THz radiation will vary greatly because of water absorption (see Figure 2.4 in Chapter 2). Working in a sample cell under ambient conditions lead to pressure broadenings on the order of GHz. Additionally, spectral features from different isotopomers overlap, increasing the difficulty of spectral assignment. These issues can be overcome by placing the entire THz generation and detection in vacuum, recording spectra in the collision-free environment of a supersonic beam and by performing mass-selective spectroscopy. To achieve this goal, the spectrometer described in Chapter 2 was constructed that combines an improved version of the THz radiation source with a source of vacuum ultra-violet (VUV) radiation that can be used for the photoionisation of the upper vibrational level. This spectrometer has been been applied to study high Rydberg states in Xe atom and H_2 molecule and to determine rotational and vibrational spacings in H_2^+ molecule, the details of which will be described in Chaper 5 and 6. In future, it should be possible to use the same experimental apparatus to measure THz spectra of molecules in supersonic jet expansions to partially resolve their rotational structure. In such an experiment, the vibrational excitation would be followed by photoionization of the upper vibrational level using another laser source. By tuning the frequency of the THz source and detecting the photoions, this double-resonance scheme should enable sensitive, background-free and isotopomer-selective absorption measurements.

Chapter 4

High Rydberg states in Xe as studied by sub-millimeter-wave radiation

Rydberg states are excited states of atoms or molecules that are characterized by a high value for the principal quantum number n [38, 90] (see also Section 1.2). They can be considered as consisting of an ion core (in the present case Xe^+) that is singly positively charged, and an electron at a rather large average distance from the ion core. Their lifetimes scale with n^3 and Rydberg states with $n \sim 20$ exhibit radiative lifetimes of several microseconds. States with $n \sim 50$ even have lifetimes exceeding $10\,\mu$s. They are thus ideally suited for high-resolution spectroscopy measurements. Their polarizability scales as n^7, which makes them very sensitive to even small electric fields. This property makes a careful minimization of stray electric fields necessary (see Figure 2.10 and Ref. [73]). Pulsed electric fields can be used to selectively ionize Rydberg states with specific principal quantum number in a process referred to as selective-field ionization (SFI), which enables a very efficient detection [38].

A further characteristic of (high) Rydberg states is that the motion of the electron is almost completely decoupled from that of the ion core, the limiting case of an excited Rydberg state at $n = \infty$ being the ionic species itself and a free electron. Spectroscopic measurement of the (high) Rydberg states of neutral species and extrapolation of the Rydberg series to their ionic limit with multi-channel quantum-defect theory (MQDT) enables one to determine the energy level structure of cations [91–93, 31] and obtain ionization energies of atoms and molecules, which represent important thermochemical quantities [94–96]. Compared to other methods of measuring ionization energies such as He I photoelectron spectroscopy, spectroscopy of high Rydberg states combined with Rydberg series extrapolation offers the advantage of being solely limited in resolution by the bandwidth of the radiation source used in the photoexcitation process [97]. In recent years, this advantage has been exploited to measure the ionization and dissociation energies of molecular hydrogen H_2 [98], D_2 [99]

and HD [100] with precision and accuracy sufficiently high to rigorously test the most advanced calculations of these quantities, which include the evaluation of relativistic and quantum electrodynamics corrections to terms proportional to the fourth power of the fine-structure constant α [101]. It has also enabled the first experimental determination of the hyperfine structure of ortho H_2^+ [31], para D_2^+ [102], $^{83}Kr^+$ ($^2P_{3/2}$ and $^2P_{1/2}$ states [29, 35]), as well as $^{129}Xe^+$ and $^{131}Xe^+$ [32, 30]. In the case of the Rydberg states of Xe, despite the high precision and accuracy of ~ 1 MHz of the extrapolation results, several parameters of the extrapolation model by MQDT remain poorly defined, such as the energy-dependence of the quantum defects and the strength of the interaction coupling s and d Rydberg series [30].

High resolution spectroscopic measurements at n values between $70-100$ would be needed to test the accuracy the of s/d interaction parameters determined in Ref. [30], and measurements at n values between 10 and 30 would provide information on the energy dependence of the quantum defect parameters that could not be determined so far. Such measurements are the subject of the present chapter. The former necessitate the use of a sub-millimeter-wave radiation source with a bandwidth of less than 100 kHz tunable in the range from about $200-400$ GHz. For the latter, a narrow-band radiation source that is tunable over the entire THz range is required (see Chapter 5). This chapter describes such measurements carried out with the radiation source described in Section 2.7.2. The sub-millimeter-wave radiation source is tunable between 240-380 GHz and allows for measurements of transition frequencies that are limited in precision to ~ 10 kHz by transit-time broadening. Although the energy range accessible by this radiation source is limited, the high resolution with which Rydberg spectra can be measured with this source allows for a highly accurate determination of MQDT parameters that can be used to predict the energy level structure of Rydberg states of Xe over a much larger energy range. The broadly tunable (0.1-14 THz) source of THz radiation presented in Chapter 5 complements the sub-millimeter-wave radiation source. Although it exhibits a lower precision (~ 3 MHz) it allows for accessing a much wider energy range, and to obtain information on Rydberg states of intermediate values of n between 16 and 33, where experimental data available in the literature [103, 104] are not of sufficient accuracy (see Section 5.3.4).

The study of Xe Rydberg states presented in Chapter 5 represents the first application of the VUV-THz spectrometer developed in the realm of this dissertation and described in Chapter 2. Xe represents an ideal system for this application because the theoretical tools required for the analysis of the data are available [30]. Moreover, the atomic (as opposed to the more complicated molecular) nature of the systems was better suited to implement and rigorously test our experimental procedure. Finally, a very large body of data is available on the rare gas atoms (see the recent review in [105]) with which the current results could be compared.

4.1 Introduction

Studies of the VUV absorption spectrum [106–108] and the photoionization spectrum [94, 109] of Xe have played a very important role in the characterization of the process of photoionization. By exciting an electron out of the outer valence shell (5p), one accesses the s ($l = 0$) and d ($l = 2$) ionization channels associated with the $^2P_{3/2}$ ground and $^2P_{1/2}$ excited spin-orbit states of Xe^+ (for a schematic representation of the energy level ordering including values for the relative energies of the different hyperfine levels see Figure 4.1). Below the $^2P_{3/2}$ ionization threshold, five Rydberg series with $J = 1$ are accessible from the $^1S_0$ ground state by single-photon excitation. These series are commonly labeled in Racah notation $nl[K]_J(F)$ corresponding to the angular momentum coupling hierarchy [110]:

$$\vec{L}^+ + \vec{S}^+ = \vec{J}^+ , \quad \vec{J}^+ + \vec{l} = \vec{K} , \quad \vec{K} + \vec{s} = \vec{J} , \quad \vec{J} + \vec{I} = \vec{F} , \tag{4.1}$$

where $\vec{L}^+$ and $\vec{S}^+$ are the orbital and spin angular momenta of the ion core, $\vec{l}$ and $\vec{s}$ the orbital and spin angular momenta of the Rydberg electron, and $\vec{I}$ the nuclear spin. The isotopes of even mass number have zero nuclear spin ($I = 0$) and only ^{129}Xe ($I = 1/2$) and ^{131}Xe ($I = 3/2$) display a hyperfine structure and require labeling by F. This coupling scheme is commonly used to label atomic Rydberg states having an open-shell ion core [104].

Three of these series, the $ns[3/2]_1$, $nd[1/2]_1$, and $nd[3/2]_1$ series, converge to the $^2P_{3/2}$ ionization threshold. The remaining two $ns'[1/2]_1$ and $nd'[1/2]_1$ series converge to the $^2P_{1/2}$ threshold. Above the $^2P_{3/2}$ threshold, the members of these series autoionize and form resonances imbedded in the continua associated with the $^2P_{3/2}$ state of Xe^+. Their shapes, broad and asymmetric for the $nd'[1/2]_1$ resonances and sharp for the $ns'[1/2]_1$ resonances, were first analyzed in detail by Beutler and interpreted by Fano as arising from the interference between several ionization channels [111–113]. Their profiles are known today as Fano profiles, or Beutler-Fano profiles, and have been investigated in great detail by a multitude of experimental methods [114–127]. The np and nf Rydberg series of Xe, which are not accessible from the $^1S_0$ ground state by single-photon excitation, were observed when powerful lasers became available in the relevant ranges, by resonant and nonresonant two-photon excitation from the ground state [128–130]. To quantitatively describe the experimental observations, Lu and Fano developed a collisional treatment known today as multi-channel quantum-defect theory (MQDT), and which is widely used to interpret the Rydberg and photoionization spectra of atoms and molecules [42, 41]. It is only in the past 15 years that the resolution of spectra of the Rydberg states and autoionizing resonances of Xe have become sufficiently high to resolve the hyperfine structure in the spectra of ^{129}Xe and ^{131}Xe [131, 132, 32, 30], which are the only natural isotopes of Xe with a nonzero nuclear spin. To understand the pronounced differences observed in the photoionization spectra of ^{129}Xe, ^{131}Xe and the $I = 0$ isotopes, the MQDT formalism of Lu and Fano was extended to include the effects of the nuclear spins [32].

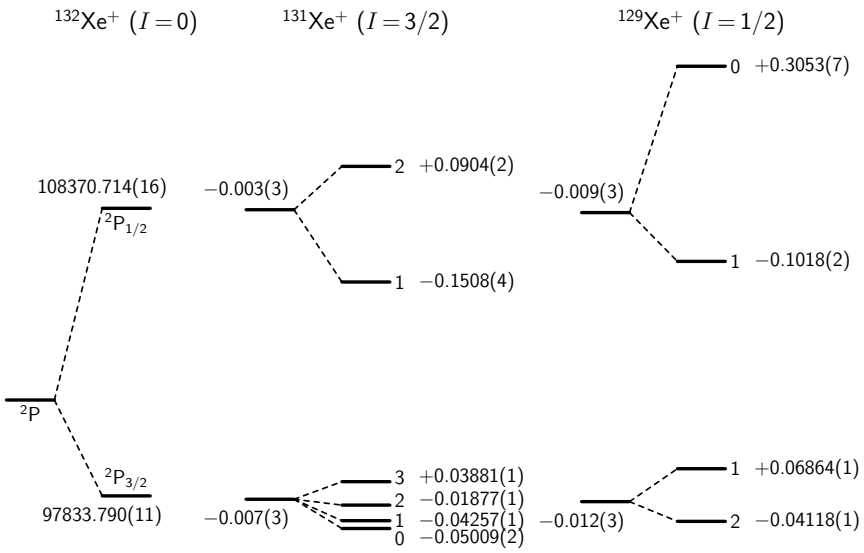

Figure 4.1: Schematic representation of the energy level diagram of ^{132}Xe$^+$, ^{131}Xe$^+$ and ^{129}Xe$^+$. The two spin orbit components of ^{132}Xe$^+$ are shown and their ionization energies with respect to the ^{1}S$_0$ ground state given in units of cm^{-1}. For ^{131}Xe$^+$ and ^{129}Xe$^+$, the isotope shifts of the spin-orbit components are given. The positions of the hyperfine levels are given relative to the center of gravity of the hyperfine structure and labeled by the F$^+$ quantum number (between 0 and 3 of ^{131}Xe$^+$ $I = 3/2$ and between 0 and 2 for ^{129}Xe$^+$ ($I = 1/2$)). Figure taken from Ref. [30].

Sub-millimeter-wave (sub-millimeter-wave) radiation is well-suited for the study of high Rydberg states [78, 133] because of its narrow bandwidth and high frequency accuracy. Its bandwidth can easily be matched to the linewidth of transitions between high Rydberg states and therefore allows for very efficient population transfer. It has been chosen here for the study of high Rydberg states in Xe near $n = 100$, where hyperfine interactions of $I \neq 0$ isotopes (^{129}Xe and ^{131}Xe) are observed. These lead to channel interactions between s and d eigenchannels that are predicted to lie in the region around and above $n = 90$. In the $I = 0$ isotopes (Xe isotopes with even mass number), s/d interactions are also important and lead to the observation of transitions between ns and nf Rydberg states that would otherwise be forbidden by the $\Delta l = \pm 1$ selection rule. However, in the case of $I = 0$ isotopes, the interacting levels never become degenerate, and the effects of the s/d interaction remain difficult to quantify. The situation is different in ^{129}Xe and ^{131}Xe because accidental degeneracies between ns and nd series converging on different hyperfine levels of the ion become possible and are frequent, particularly at high n values. Another property that makes sub-millimeter-wave radiation ideally suited for the study of high Rydberg states is the accessible energy range and range of principal quantum number. For example, radiation with a frequency of $\sim 320\,\mathrm{GHz}$ can be used to record $\Delta n = 1$ transitions at n values as low as $n = 27$ and would be sufficiently energetic to directly ionize states with $n = 102$. Therefore, Rydberg states with n between 27 and ∞ can be studied with a sub-millimeter-wave source tunable around 340 GHz. Additionally, Doppler

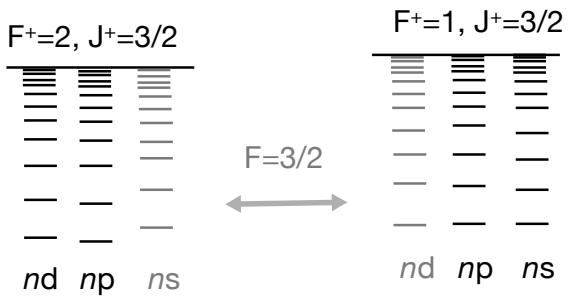

Figure 4.2: Schematic representation of ns, nd and np Rydberg series converging on different hyperfine levels of $^{129}Xe^{+}$. An interaction between an $ns, F = 3/2$ Rydberg series converging on the $F^{+} = 2$, $J^{+} = 3/2$ level and an $nd, F = 3/2$ series converging on the $F^{+} = 1$, $J^{+} = 3/2$ level is indicated by a grey arrow.

broadenings scale linearly with frequency and are negligible below 1 THz in experiments on atoms and molecules in skimmed supersonic beams: In fact, the linewidths of the narrowest transitions observed in the realm of this dissertation (146 kHz, see Section 4.4) are close to the limit imposed by the finite transit time of the atoms through the radiation field. A final advantage is that the transition moments for transitions between Rydberg states of similar principal quantum numbers scale as n^2 and are therefore extremely large at high n values. The phase-stabilized, backward-wave oscillator-based source used here (see Section 2.7.2 for details) provides a stable frequency output in the range between $240 - 380$ GHz with a bandwidth of less than 1 kHz.

Naturally occurring isotopes of Xe are ^{124}Xe (0.095%), ^{126}Xe (0.089%), ^{128}Xe (1.91%), ^{129}Xe (26.40%), ^{130}Xe (4.07%), ^{131}Xe (21.23%), ^{132}Xe (26.91%), ^{134}Xe (10.44%) and ^{136}Xe (8.86%), of which only isotopes $128 - 136$ could be detected within the sensitivity limits of our experiments. All isotopes of Xe with an even mass number have a nuclear spin $I = 0$, whereas ^{129}Xe and ^{131}Xe exhibit nuclear spins of $I = 1/2$ and $I = 3/2$, respectively, and therefore possess a hyperfine structure. In these isotopes, there are Rydberg series converging to the different hyperfine levels of the ion, as shown in Figure 4.2, where the interaction between $ns, F = 3/2$ Rydberg series converging on the $F^{+} = 2$ level of the $^2P_{3/2}$ state of $^{129}Xe^{+}$ and an $nd, F = 3/2$ Rydberg series converging on the $F^{+} = 1$ level of the same state are depicted schematically. Such s/d interactions, which are important for the dynamics of Rydberg states of Xe, can then be quantified directly from Rydberg spectra of ^{129}Xe (see Figure 4.3).

Schäfer *et al* [30] have used a multichannel quantum defect theory (MQDT) model to estimate the strength of the s/d interaction for ^{129}Xe and ^{131}Xe in a fit of all spectroscopic data known on the Rydberg states of Xe. However, the data set did not allow for an accurate determination of this interaction because of correlations between MQDT fit parameters. The MQDT analysis presented in Ref. [30] nevertheless led to a precise

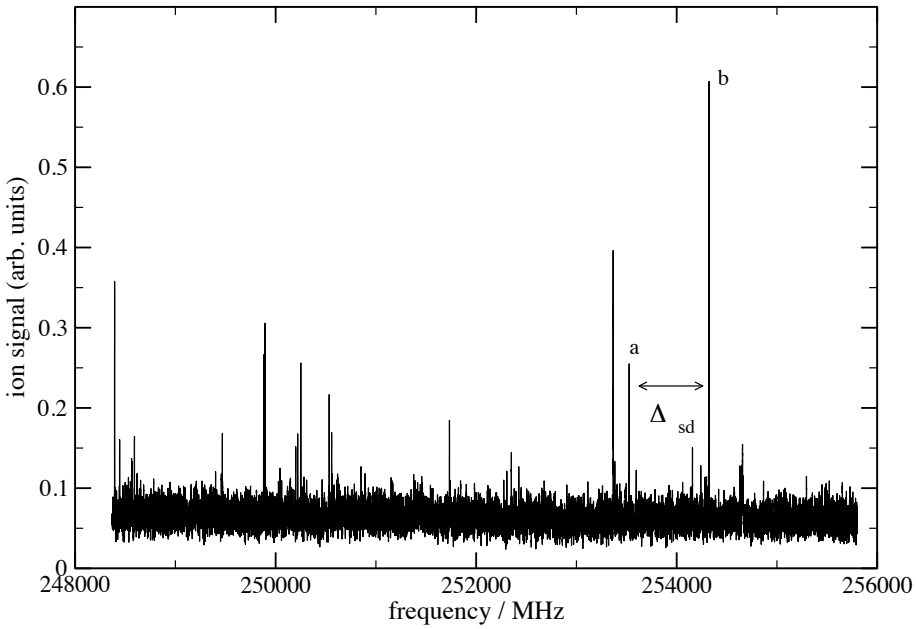

Figure 4.3: Spectrum of ^{129}Xe between $248 - 256\,\mathrm{GHz}$ after excitation to initial states around $n = 82$ and final states around $n = 69$. Transition a: $69\mathrm{p}[5/2]_2(5/2) \leftarrow 82\mathrm{d}[3/2]_1(3/2)$, transition b: $69\mathrm{p}[5/2]_2(5/2) \leftarrow 84\mathrm{s}[3/2]_1(3/2)$. Transitions with the same final state can be used to quantify s,d splittings by calculating combination differences.

determination of the hyperfine structure of $^{129}Xe^+$ and $^{131}Xe^+$ [32, 30], which had not been determined before (see Figure 4.1). One of the main goals of the sub-millimeter-wave experiments presented in this chapter was to determine the s/d interaction in Rydberg states of Xe from perturbations in the hyperfine structure of high Rydberg states of ^{129}Xe and ^{131}Xe. According to the analysis presented in Ref. [30], the perturbations should be particularly pronounced in ns and nd Rydberg states in the range $n = 80 - 100$. Rydberg series extrapolation actually turns out to be the only reliable method for determination of the hyperfine structure of rare-gas atomic ions Rg^+ with a nonzero nuclear spin. Indeed the direct spectroscopy of the ionic species presents considerable experimental challenges considering that no allowed transitions lie in easily accessible frequency regions (IR, VIS and UV) for these ions.

Mass-selective measurements carried out in the realm of this thesis greatly simplified spectral assignments of Xe Rydberg states at high n values by avoiding spectral congestion resulting from the overlap of spectral features from different isotopes. The observed transition frequencies were compared to frequencies calculated by multi-channel quantum de-

fect theory (MQDT) based on the parameter set reported in Ref. [30], which facilitated the assignment. Initially, an analysis of the transitions in ^{132}Xe was performed in order to simplify the assignment procedure for ^{129}Xe and ^{131}Xe. This allowed for the determination of the range of initial Rydberg states for sub-millimeter-wave spectroscopy that were accessed by excitation with VUV radiation. This was very important because the bandwidth of the VUV radiation exceeded the level spacing in the range of n where excitation took place (see Section 4.3). The resulting increase of line density complicates the assignment procedure, especially for ^{129}Xe and ^{131}Xe, which display transitions that are more densely spaced than in $I = 0$ isotopes because of the hyperfine interaction (see Figure 4.4). Additionally, MQDT parameters could be refined by incorporating the newly determined level energies of s and d Rydberg states in ^{132}Xe into a global fit including all Rydberg states of Xe [134] which should further simplify the assignments for ^{129}Xe and ^{131}Xe.

Transition moments vary considerably depending on the Rydberg states involved in a measurement and this presents several challenges. In the realm of the measurements presented here, several hundreds of transitions were recorded, making it impossible to record each transition under conditions where saturation by the sub-millimeter-wave radiation and other sources of systematic errors were eliminated. Because the intensities observed in the spectra do not only reflect the transition strengths but also the populations in the initial Rydberg states (see Section 4.3.1), the best manner in which information can be gained on transition strengths is from the observed linewidths in the spectra. A study of the effects of sub-millimeter-wave intensities on the linewidth observed in spectroscopic measurements was therefore performed. This study was complemented by measurements of Rabi oscillations. An analysis of the general error budget was performed to estimate the overall contribution of systematic errors to the accuracy with which level energies could be determined. This included studying the effects of VUV radiation intensities on the linewidths, and the shift and broadening of spectral lines induced by the presence of stray electric and magnetic fields. By helping to reduce all forms of systematic errors and to understand the underlying processes, the sub-millimeter-wave spectroscopic investigations presented in this chapter served as premise for the construction of the VUV-THz spectrometer described in Chapter 2 and the THz spectroscopic measurements of Xe and H_2 presented in Chapters 5 and 6, respectively.

4.2 Experimental

High ns and nd Rydberg states of Xe with $n = 81 - 98$ were prepared by irradiation of a skimmed, supersonic atomic beam of Xe with VUV radiation in a perpendicular configuration. Tunable VUV radiation near 97 800 cm^{-1} was generated by resonant $(2 + 1')$ sum-frequency mixing, making use of the $(5p)^5\left(^2P_{3/2}\right)6p[1/2]_0 \leftarrow (5p)^6\ ^1S_0$ two-photon resonance of Xe at 80 118.9839 cm^{-1}, which was accessed by the frequency-doubled UV out-

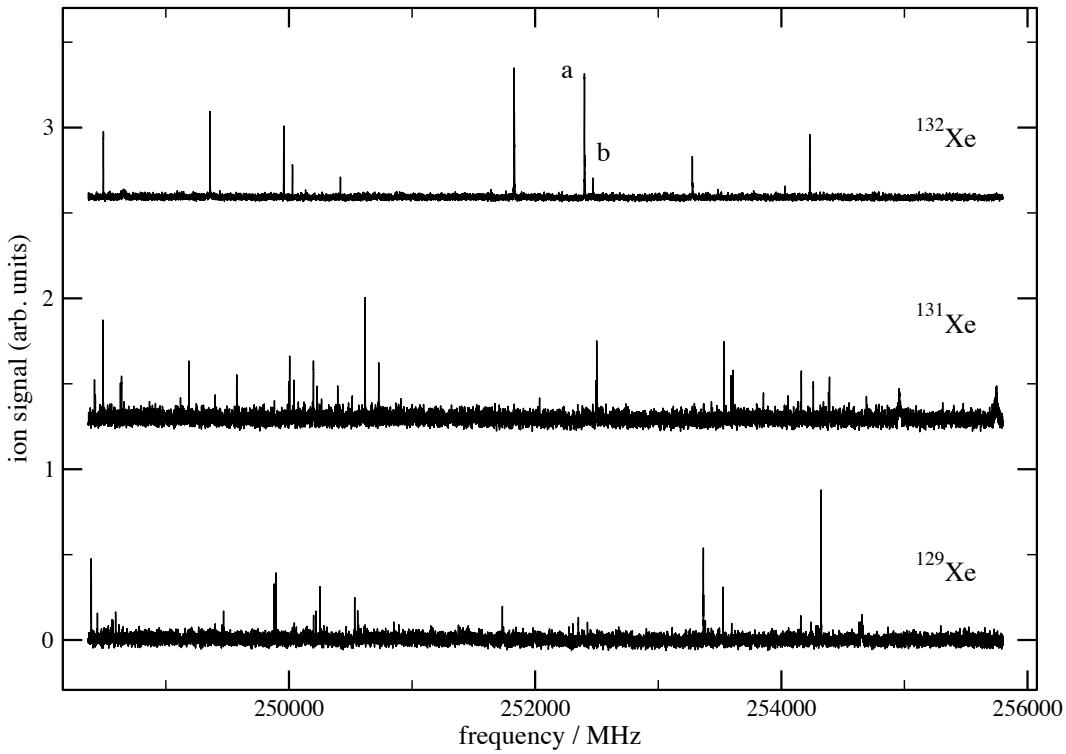

Figure 4.4: Sub-millimeter-wave spectra of Rydberg-Rydberg transitions of ^{132}Xe ($I = 0$), ^{131}Xe ($I = 3/2$) and ^{129}Xe ($I = 1/2$) that were recorded simultaneously in the range between 248 and 256 GHz. Spectra of ^{128}Xe, ^{130}Xe, ^{134}Xe and ^{136}Xe (all $I = 0$ isotopes) were also recorded but are not shown here because the transition frequencies were the same as for ^{132}Xe within our experimental resolution. The transitions labeled a and b in the top trace correspond to the $66f[3/2]_2 \leftarrow 83d[3/2]_1$ and $66f[3/2]_1 \leftarrow 83d[3/2]_1$ transitions of ^{132}Xe. The vertical scale of the spectra of ^{129}Xe and ^{131}Xe has been multiplied by a factor of 2.

put of a dye laser. Sum-frequency mixing was then performed with the output of a second, tunable dye laser, as explained in Section 2.7.1. The frequency-tunable and frequency-fixed dye lasers were pumped by the frequency-doubled (532 nm) and frequency-tripled (355 nm) outputs of a Nd:YAG laser, respectively. Sub-millimeter-wave radiation produced by the BWO source presented in Section 2.7.2 was introduced into the vacuum chamber in a direction counter-propagating to the VUV radiation beam and was used to excite transitions to either higher- or lower-lying p or f Rydberg states, as shown schematically in Figure 4.5. The region where the atomic, VUV and sub-millimeter-wave radiation beams crossed each other was surrounded by a stack of resistively coupled, cylindrical extraction plates and a double-layer magnetic shield made of mumetal to eliminate stray magnetic fields such as those emanating from pressure gauges and the Earth's magnetic field.

Mass-selective measurements that helped to elucidate the hyperfine structure were performed by applying selective field-ionization pulses and detecting the ions using a time-of-

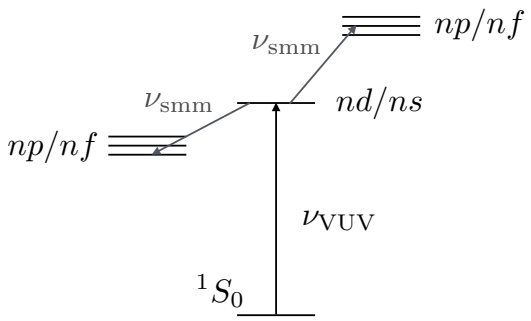

Figure 4.5: Schematic representation of the excitation sequence (not to scale) used to study high Rydberg states of Xe below the $^2P_{3/2}$ ionization threshold. smm stands for "sub-millimeter-wave".

flight mass spectrometer. For measurements where the initial Rydberg state accessed by the VUV radiation was located higher in energy than the final Rydberg state, an electric field of $\sim 20\,\mathrm{V/cm}$ was first applied for a duration of $2\,\mu$s and was then gradually turned off during the next $2\,\mu$s (see Figure 4.6). At this point, a second pulse of $\sim$132 V/cm was applied for a duration of $1.8\,\mu$s. The first pulse led to the ionization of the upper Rydberg state, the second pulse ionized the lower Rydberg state (see panels b) and c) of Figure 4.6). The ions were then accelerated towards a micro-channel-plate detector, the delay between the pulses allowing for a clear separation of all isotopes by their time-of-flight (TOF) differences and simultaneously avoiding overlap of the time-of-flight distributions originating from the field ionization of the upper and lower levels. As an illustration, Figure 4.6 a) shows the time-of-flight spectrum obtained following excitation to the $83\mathrm{d}[3/2]_1$ Rydberg state of Xe with VUV radiation followed by the stimulated emission to the $66\mathrm{f}[3/2]_2$ level with sub-millimeter-wave radiation. In the isotopic distribution of the upper state, the intensity of the $I = 0$ isotopes of Xe (their transition frequencies are the same within our experimental resolution) are reduced compared to the intensities one would expect from their natural abundance. This reduction is caused by the emission stimulated by the sub-millimeter-wave radiation, which was chosen to be in resonance with Rydberg-Rydberg transitions of $I = 0$ isotopes. Correspondingly, the time-of-flight spectrum observed following field ionization with the second, stronger electric field pulse only contains contributions from the $I = 0$ isotopes. This example also illustrates that it is possible to achieve substantial population transfer in this double-resonance experiment and demonstrates the sensitivity of the measurement method.

Mass-selective spectra were recorded by placing temporal gates on the corresponding positions in the TOF spectrum. In cases where the initial Rydberg state lies lower in energy than the final Rydberg state, it is sufficient to use a single field-ionization pulse and select a field strength low enough to only ionize the higher-lying Rydberg state. In this case, only one isotopic distribution is observed in the TOF spectrum. Figure 4.4 displays, as an example, the spectra of the main naturally occurring isotopes of Xe (^{132}Xe, ^{131}Xe

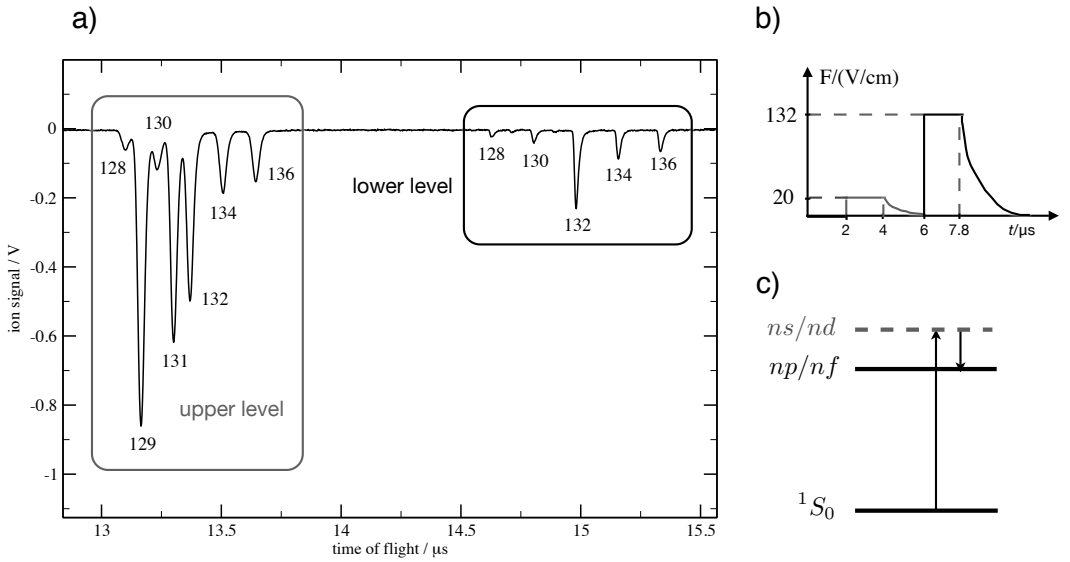

Figure 4.6: a) Time-of-flight mass spectrum of Xe^+ ions produced following field ionization of Xe Rydberg states using the sequence of pulsed electric fields depicted in panel b). c) Excitation scheme. The applied pulse sequence allowed for separating the isotopic distribution of the higher-lying, initial Rydberg state from that of the lower-lying, final state, as can be seen in the time-of-flight spectrum (see text for details).

and ^{129}Xe) recorded simultaneously in the range between $248 - 256\,\mathrm{GHz}$ following initial laser excitation to the $83\mathrm{d}[3/2]_1$ state and stimulated emission pumping to Rydberg states around $n = 66$. The spectra observed for ^{128}Xe, ^{130}Xe, ^{134}Xe and ^{136}Xe were identical to those of ^{132}Xe within the sensitivity and resolution limits of our measurement. The very different structure of the spectra of ^{129}Xe and ^{131}Xe is a consequence of the hyperfine structure.

Stray electric fields present in the excitation region could be minimized to values below $\sim 1\,\mathrm{mV/cm}$ following the procedure reported in Ref. [73] and described in detail in Section 2.7.4. The shift of a transition frequency by the quadratic Stark effect was measured in dependence on small dc compensation fields that were applied along the axis of the electrode stack. The value for which the shift is minimal and therefore the field compensated was determined as shown in Figure 2.10. In some cases, an effect of VUV radiation intensity on the linewidths in the observed spectra could be detected, the highest VUV intensities leading to broadenings that are attributed to ions generated by multi-photon ionization processes or interactions between Rydberg atoms in the gas sample.

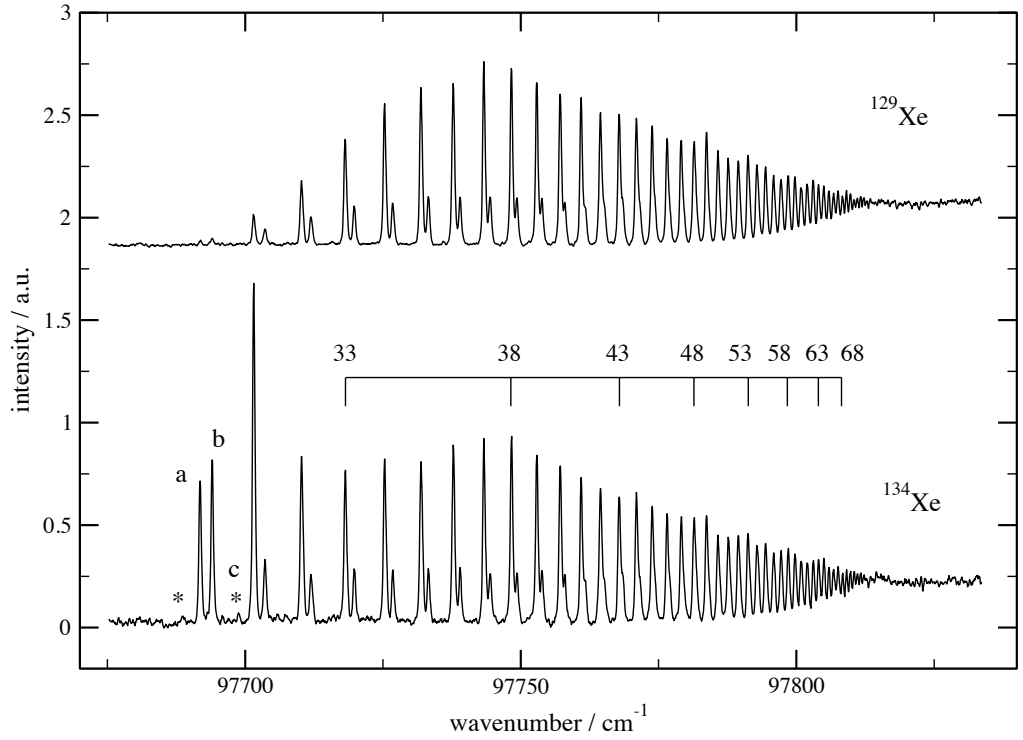

Figure 4.7: Rydberg spectra of ^{129}Xe and ^{134}Xe recorded as a function of VUV wavenumber. a) Transition to 30d$[3/2]_1$, b) transition to 32s$[3/2]_1$ and c) transition to 31d$[1/2]_1$ Rydberg states accessed from the $^1S_0$ ground state. Transitions marked by asterisks correspond to nd$[1/2]_1$ Rydberg series. Assignment bar gives principal quantum number n for the nd$[3/2]_1$ Rydberg series. The irregularly high intensities of the lowest-n transitions in ^{134}Xe as compared to ^{129}Xe are attributed to a leakage from the ^{132}Xe mass channel because a clear separation of these isotopes is difficult to achieve at low values of the principal quantum number and correspondingly high extraction voltages.

4.3 Investigation of high Rydberg states of Xe in the range of principal quantum number $n = 65 - 100$

To test the validity of the MQDT parameters determined in Ref. [30] in a region where the effects of s/d interactions might be observable as perturbations of the hyperfine structure, systematic measurements were carried out. To facilitate data acquisition, the bandwidth of the VUV laser radiation used for the preparation of the initial ns and nd Rydberg states of sub-millimeter-wave transitions was chosen to be broad enough ($\sim 0.8\,\mathrm{cm}^{-1}$) to simultaneously excite several levels. At $n \simeq 90$, the spacing between adjacent members of a Rydberg series $\left(2R/n^3\right)$ is $\sim 0.3\,\mathrm{cm}^{-1}$. Because three Rydberg series (the ns$[3/2]_1$, nd$[3/2]_1$ and nd$[1/2]_1$ series) converge to the $^2P_{3/2}$ ground state of ^{132}Xe$^+$, up to nine initial Rydberg levels could be expected to be accessible within the VUV laser bandwidth

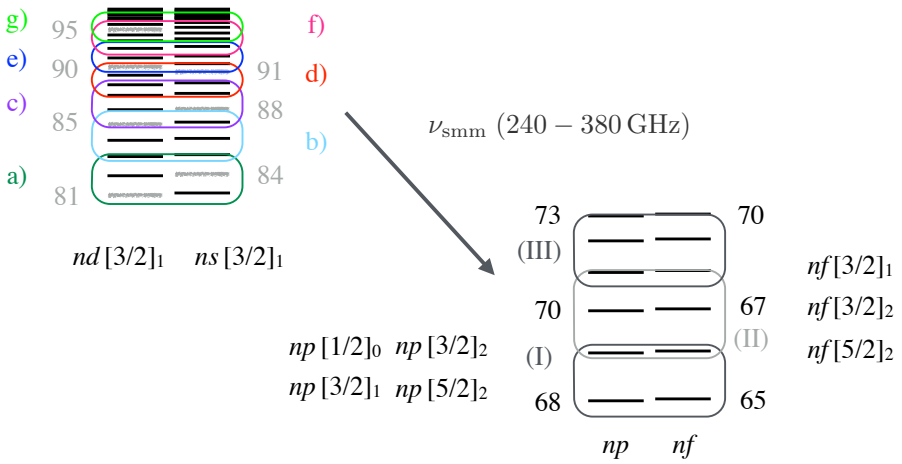

Figure 4.8: Rydberg levels observed in the sub-millimeter-wave spectra (see text for details). Note: drawing not to scale, p,f Rydberg states would be considerably lower in energy than s,d Rydberg states in the range of principal quantum number that is indicated.

from the $^1S_0$ ground state. The nd$[1/2]_1$ series, which has a dominant $S = 1$ character near the ionization threshold, and is not easily accessed from the ^{1}S$_0$ ground state, turned out to be too weak to be observed in the sub-millimeter-wave measurements.

The single-photon excitation spectra of the ns and nd Rydberg states of ^{129}Xe and ^{134}Xe with $n \geq 30$ recorded as a function of the VUV wavenumber are depicted in Figure 4.7. A field-ionization pulse with a strength of 600 V/cm was applied to record the spectra. At low n values, the ns$[3/2]_1$ and nd$[3/2]_1$ series appear as closely spaced pairs of strong transitions, the nd$[3/2]_1$ series being the most intense. The much weaker nd$[1/2]_1$ series (marked by asterisks in Figure 4.7) is only observable up to $n = 31$. From $n = 41$ onwards, the ns$[3/2]_1$ and nd$[3/2]_1$ series are no longer resolved and no distinct structure is observed beyond $n \sim 70$. Within the resolution limit of the experiment and in the range of principal quantum number under investigation, no effect of the hyperfine interaction in ^{129}Xe is observed from the Rydberg spectra.

4.3.1 High Rydberg states of ^{132}Xe

The sub-millimeter-wave spectra of Rydberg-Rydberg transitions were recorded after setting the VUV laser to the range marked by colored rectangles in Figure 4.8 and centered at the positions of a) the 84s / 82d levels, b) the 87s / 85d levels, c) the 89s / 87d levels, d) the 91s / 89d levels, e) the 93s / 91d levels, f) the 95s / 93d, and g) the 98s / 96d levels. Starting from the Rydberg states marked f), for example, it was only possible to excite transitions to the p, f states marked by the grey rectangle (III) in Figure 4.8 because this already required frequencies above 300 GHz and the maximum tunable range of the sub-

Table 4.1: Principal quantum numbers of the s and d Rydberg states of ^{132}Xe populated at the VUV wavenumbers marked by colored rectangles in Figure 4.8 and observed in the sub-millimeter-wave spectra. The underlined levels are those that were observed in several sub-millimeter-wave spectra and were used to build combination differences.

	nd$[3/2]_1$	ns$[3/2]_1$
a)	$81, 82, \underline{83}$	84
b)	$\underline{83}, 84, 85, \underline{86}$	$85, 86$
c)	$\underline{86}, \underline{87}, \underline{88}, \underline{89}$	$88, 89, \underline{90}$
d)	$\underline{87}, \underline{88}, \underline{89}, \underline{90}$	$\underline{90}, 91$
e)	$\underline{89}, 90, 91, \underline{92}$	93
f)	$\underline{92}, 93, 94$	
g)	$95, 96, 97$	

millimeter-wave source is $240 - 380$ GHz. Starting from the s, d Rydberg states marked a), on the other hand, allowed only for excitation to p, f states marked by the grey rectangle (I) because this required frequencies of ~ 250 GHz that were at the lower end of the tunable range.

For the determination of the energies of all recorded Rydberg states relative to a selected Rydberg level (the 66f$[5/2]_2$ level, see Table 4.2 and description below), it was necessary to make sure that each starting level is connected to at least two distinct other levels by sub-millimeter-wave transitions. This condition could be fulfilled by recording transitions to the set of np, nf Rydberg levels marked (I) and (II) starting from the ns, nd states marked c) in Figure 4.8, and, starting from the ns, nd states marked e), transitions to the set of levels marked (II) and (III). For all other ranges of ns, nd states, transitions to only one set of np, nf levels could be recorded: (I) $\leftarrow$ a), (I) $\leftarrow$ b), (II) $\leftarrow$ d), (III) $\leftarrow$ f), (III) $\leftarrow$ g).

Table 4.1 lists the ns and nd levels that were identified in the recorded sub-millimeter-wave spectra. The states for which transitions to two ranges of np, nf levels (either (I) and (II) or (II) and (III)) were recorded are underlined. These levels were used for building the combination differences that interconnected all recorded energy levels. Figure 4.9 illustrates this principle by showing a selected set of transitions labeled (I) $-$ (IX) between nd$[3/2]_1$ Rydberg states ($n = 82, 85, 87, 89, 91, 96$), as well as the 91s$[3/2]_1$ state, and np$[1/2]_0$ Rydberg states ($n = 69, 71, 73$) in ^{132}Xe. By building combination differences between transition frequencies connecting these different states an energy level network can be obtained, for example by referencing the energies of all other states to the 69p$[1/2]_0$ state, the energy of which would be arbitrarily set to $E\,(69\text{p}[1/2]_0) = 0$. For the energy level network presented in Table 4.2, the origin of the energy scale was set to the position

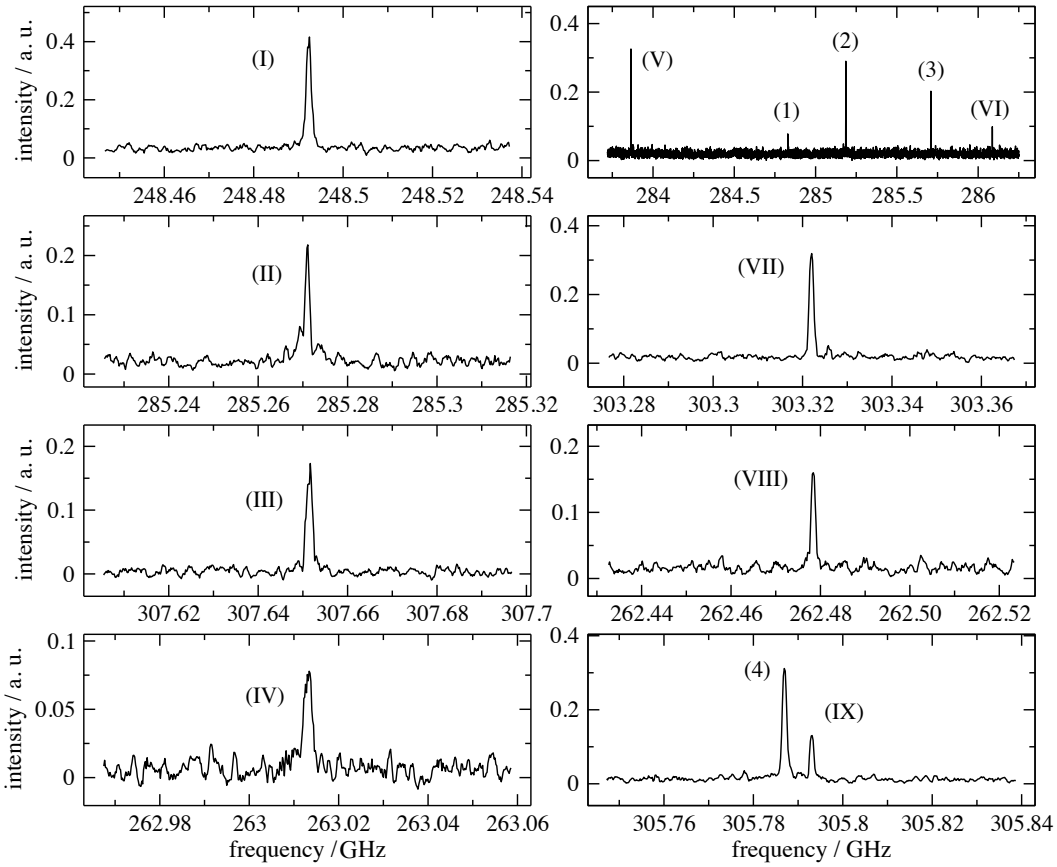

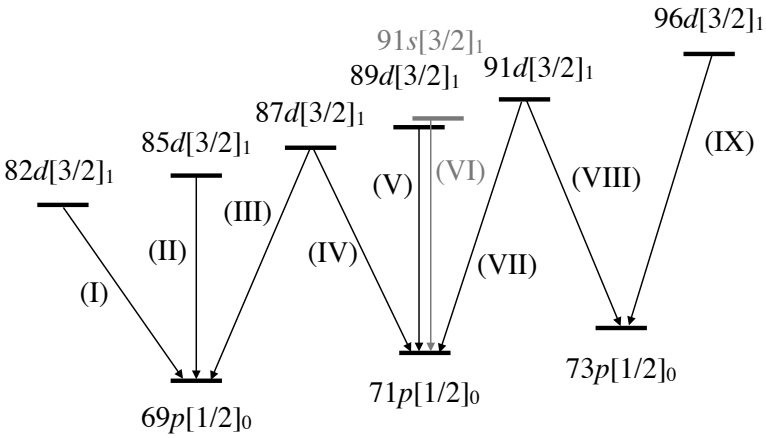

Figure 4.9: Sub-millimeter-wave spectra recorded between $ns[3/2]_1$, $nd[3/2]_1$ Rydberg states and $np[1/2]_0$ states. Assignments for transitions (I)-(IX) are given by the energy level diagram. Transition labeled (1) is $70p[1/2]_0 \leftarrow 87d[3/2]_1$, transition (2) $68f[5/2_2] \leftarrow 90d[3/2]_1$, transition (3) $68f[3/2_2] \leftarrow 90d[3/2]_1$, and transition (4) $70f[5/2]_2 \leftarrow 97d[3/2]_1$.

of the $66f[5/2]_2$ state, i.e. $E(66f[5/2]_2) = 0$ (see below).

A total of 86 transitions in ^{132}Xe were observed and assigned, and a full list including the linewidth and signal-to-noise ratio (SNR) of each transition can be found in Appendix A.1. Because the number of transitions observed in the sub-millimeter-wave spectra exceeded the number of energy levels connected by them (altogether 53 levels), the relative positions of all levels were fitted to the observed transition frequencies in a least-squares-fitting procedure. To this end, the origin of the energy scale ($E = 0$) was placed at the position of the 66f$[5/2]_2$ level because it was one of the levels observed in the largest number of transitions and therefore statistically well-defined. The results of this procedure are summarized in Table 4.2, where all levels are given with their statistical uncertainty. Most of the recorded transitions had linewidths in the range between 200 kHz − 2 MHz. Several transitions, primarily those associated with large transition moments such as transitions having $\Delta l = +1, \Delta K = +1$, were power-broadened as discussed in Section 4.4. The power broadening did not affect the central positions significantly but led to larger uncertainties in the determination of the line centers. A more detailed description of the uncertainties associated with these measurements and an error budget including systematic effects such as Doppler shifts, pressure shifts and AC-Stark shifts can be found in Section 4.5.

The observed SNRs do not necessarily reflect the relative transition strengths in a given spectrum because the population of initial ns and nd Rydberg states varied with the different transition strengths from the ground state and the central frequency of the VUV laser. Transitions from ns$[3/2]_1$ Rydberg states were generally less intense than transitions from nd$[3/2]_1$ Rydberg states (see Figure 4.7). The main effect on the initial state population comes from the VUV laser: because several ns, nd levels lie within its bandwidth, populations can vary depending on how far from the central excitation frequency an energy level is. Consequently, sub-millimeter-wave transitions with poor SNRs can still be power broadened. Additionally, one would have to integrate over the entire peak and not only compare peak maxima (which is effectively what one does when comparing SNRs in a given spectrum) to accurately determine a transition strength, and it is therefore more meaningful to study its linewidth than its observed intensity. A more detailed discussion of linewidths and transition moments is presented in Section 4.4, where Rabi frequencies determined from the power-broadened linewidth are compared to those determined from Rabi-oscillation measurements.

In all of the spectra recorded for ^{132}Xe, the $\Delta J = 0, \pm 1$ selection rule was obeyed. In general, the $\Delta l = \pm 1$ rule was also adhered to, although transitions from ns$[3/2]_1$ Rydberg states to nf Rydberg states (seemingly $\Delta l = 3$) were also observed as a result of s/d interactions (see Figure 4.10). Whereas transitions (1) and (3) in Figure 4.10, which were assigned to the 69p$[3/2]_2 \leftarrow$ 88s$[3/2]_1$ and 69p$[3/2]_1 \leftarrow$ 88s$[3/2]_1$ transitions, respectively, appear less intense than transition (4), for which the assignment is 66f$[3/2]_2 \leftarrow$ 89s$[3/2]_1$, they do, in fact, exhibit a larger transition strength. This can be seen in Table A.1 from the observed linewidths and is consistent with the expectation that nominally forbidden transitions have a smaller transition strength and should be narrow. The $\Delta l = 3$ transitions

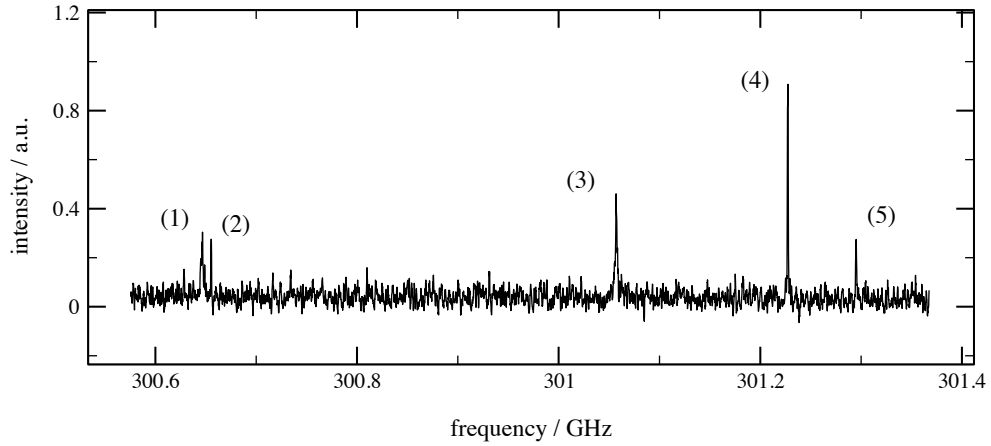

Figure 4.10: Sub-millimeter-wave spectra showing transitions from ns$[3/2]_1$ Rydberg states to nf Rydberg states which are forbidden by the $\Delta l = \pm 1$ selection rule. (1) 69p$[3/2]_2 \leftarrow$ 88s$[3/2]_1$, (2) 66f$[5/2]_2 \leftarrow$ 89s$[3/2]_1$, (3) 69p$[3/2]_1 \leftarrow$ 88s$[3/2]_1$, (4) 66f$[3/2]_2 \leftarrow$ 89s$[3/2]_1$ and (5) 66f$[3/2]_1 \leftarrow$ 89s$[3/2]_1$.

originating from ns$[3/2]_1$ Rydberg states are weakly allowed because of the interaction between s and d eigenchannels (see also Ref. [30]). Such s/d interactions can also be observed in ^{129}Xe and ^{131}Xe, where they are mediated by the hyperfine interaction (see Section 4.3.2) which leads to accidental degeneracies between s and d states.

Table 4.2 lists the positions $E_{\rm exp}/h$ of ^{132}Xe Rydberg states relative to the 66f$[5/2]_2$ state, as determined from the experimental data, and compares them to calculated values $E_{\rm calc}/h$ obtained from MQDT calculations carried out with the model and parameters reported in Ref. [30]. The deviation is typically smaller than 1.5 MHz. Uncertainties of the experimental level positions are given in parentheses and are commonly on the order of $\sim 10-50$ kHz. These uncertainties are statistical and were derived solely from the uncertainty in locating the positions of the transition maxima in the recorded spectra. They do not take into account systematic uncertainties. The calculated positions obtained by MQDT calculations with the parameter set reported in Ref. [30] exceed experimental ones by ~ 1 MHz for all nd$[3/2]_1$ Rydberg states. For ns Rydberg series, the calculated values are typically ~ 0.7 MHz higher than experimental ones. For np$[5/2]_2$ states the deviations are ~ 1.4 MHz, for np$[3/2]_2$ states ~ -1 MHz, for np$[1/2]_0$ states ~ 0 MHz, and for np$[3/2]_1$ states ~ -0.5 MHz. For most nf states, the deviation is ~ 400 kHz. For the 68p$[1/2]_0$ state, the deviation is surprisingly large (-4.7 MHz) and this suggests that the assignment may be erroneous, especially because this level was only observed in a single transition. It is possible that the VUV laser frequency drifted during the measurement in this case. The comparison of experimental level energies with calculated ones suggests that the MQDT parameter set of Ref. [30] could be improved, especially for ns and nd Rydberg series.

Table 4.2: Experimentally determined values for level energies in ^{132}Xe given relative to the $66f[5/2]_2$ state and compared to calculated values. Statistical uncertainties are given in parentheses. In addition, the level positions are subject to a systematic uncertainty of 200 kHz.

level	E_{exp}/h MHz	$(E_{exp} - E_{calc})/h$ MHz	level	E_{exp}/h MHz	$(E_{exp} - E_{calc})/h$ MHz
$65f[5/2]_2$	−23449.323 (0.012)	0.15	$68p[1/2]_0$	−33269.994 (0.017)	−0.01
$65f[3/2]_2$	−24048.145 (0.012)	−0.3	$68p[3/2]_1$	−35291.347 (0.073)	−4.70 [a]
$65f[3/2]_1$	−24118.980 (0.008)	−0.29	$69p[5/2]_2$	−12259.406 (0.023)	1.41
$66f[3/2]_2$	−572.047 (0.013)	−0.47	$69p[3/2]_2$	−10894.421 (0.049)	−0.74
$66f[3/2]_1$	−639.634 (0.007)	−0.26	$69p[3/2]_1$	−11305.459 (0.009)	−0.38
$66f[5/2]_2$	0.000 (0.012)	0.000	$69p[1/2]_0$	−9379.700 (0.014)	0.36
$67f[5/2]_2$	22406.806 (0.005)	−0.04	$70p[3/2]_1$	11601.985 (0.050)	−0.61
$67f[3/2]_2$	21860.006 (0.006)	−0.47	$70p[3/2]_2$	11994.637 (0.500)	−1.08
$67f[3/2]_1$	21795.376 (0.004)	−0.22	$70p[1/2]_0$	13442.517 (0.015)	−0.17
$68f[5/2]_2$	43831.854 (0.007)	−0.18	$71p[5/2]_2$	32627.125 (0.043)	1.35
$68f[3/2]_2$	43308.877 (0.012)	−0.46	$71p[3/2]_2$	33874.065 (0.029)	−1.28
$69f[5/2]_2$	64331.681 (0.010)	−0.24	$71p[1/2]_0$	35258.654 (0.006)	−0.12
$69f[3/2]_2$	63831.150 (0.006)	−0.60	$73p[1/2]_0$	76102.197 (0.007)	−0.21
$69f[3/2]_1$	63772.151 (0.017)	−0.18			
$70f[5/2]_2$	83959.074 (0.011)	−0.21			
$70f[3/2]_2$	83479.612 (0.010)	−0.63			
$81d[3/2]_1$	225909.765 (0.013)	−0.73	$84s[3/2]_1$	241971.627 (0.023)	−0.82
$82d[3/2]_1$	239112.599 (0.016)	−0.94	$85s[3/2]_1$	254583.932 (0.038)	0.29
$83d[3/2]_1$	251828.534 (0.016)	−0.73	$87s[3/2]_1$	278451.624 (0.054)	−0.74
$84d[3/2]_1$	264080.612 (0.020)	−0.87	$88s[3/2]_1$	289752.649 (0.291)	0.09
$85d[3/2]_1$	275891.307 (0.038)	−1.00	$89s[3/2]_1$	300655.290 (0.015)	−0.99
$86d[3/2]_1$	287282.007 (0.021)	−0.83	$90s[3/2]_1$	311181.092 (0.040)	−0.84
$87d[3/2]_1$	298271.793 (0.015)	−0.93	$91s[3/2]_1$	321345.905 (0.018)	−0.79
$88d[3/2]_1$	308879.579 (0.009)	−0.91			
$89d[3/2]_1$	319122.820 (0.011)	−0.89			
$90d[3/2]_1$	329017.934 (0.009)	−0.93			
$91d[3/2]_1$	338580.600 (0.014)	−0.92			
$92d[3/2]_1$	347825.498 (0.014)	−0.99			
$93d[3/2]_1$	356766.622 (0.016)	−1.00			
$94d[3/2]_1$	365417.206 (0.021)	−0.93			
$95d[3/2]_1$	373789.509 (0.027)	−0.93			
$96d[3/2]_1$	381895.227 (0.036)	−1.15			
$97d[3/2]_1$	389746.033 (0.056)	−1.10			

[a] Assignment ambiguous because of large deviation from calculated value (see text for details).

4.3.2 High Rydberg states of ^{129}Xe

The objective of the spectroscopic measurements performed on high Rydberg states of ^{129}Xe was to quantify from experimental data the interaction of s and d eigenchannels in the

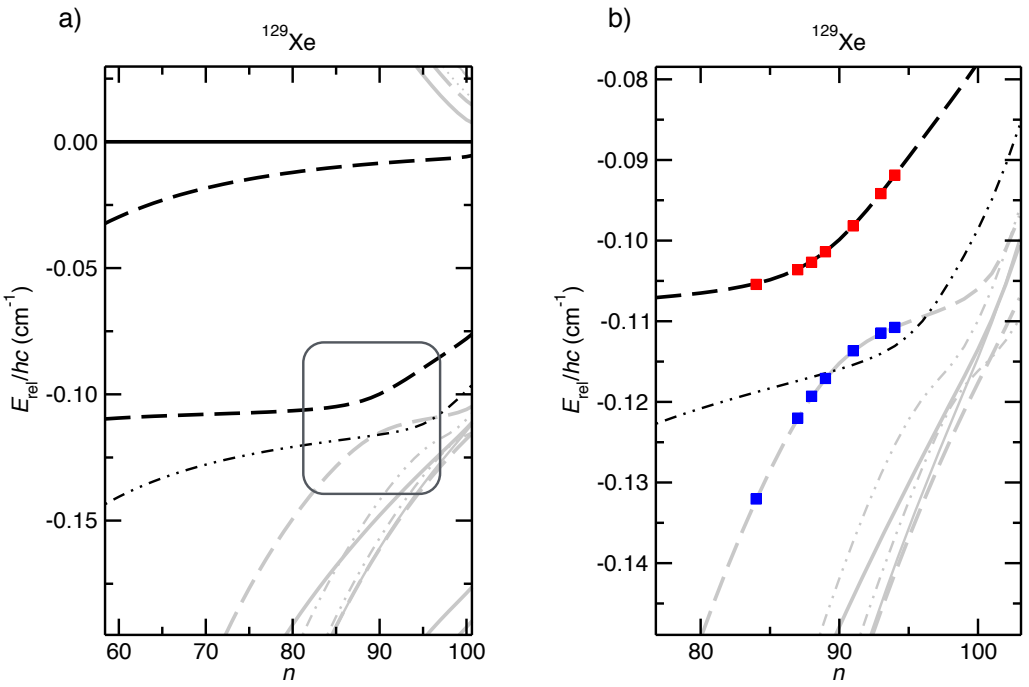

Figure 4.11: Panel a): Calculated correlation diagram between $n = 60$ and $n = 100$ for ^{129}Xe taken from [30]. The grey rectangle marks a region where an interaction between $ns[3/2]_1(3/2)$ (black, thick, dashed line) and $(n-2)\mathrm{d}[3/2]_1(3/2)$ (grey, thick, dashed line) series is predicted. Panel b): Comparison of experimentally determined (red and blue squares) and calculated values determined from a first analysis of transitions in ^{129}Xe, see text for details.

region around $n = 90$. Ref. [30] predicts values for s/d interactions that are manifested as avoided crossings in correlation diagrams such as that shown in panel a) of Figure 4.11. One such interaction, between $ns[3/2]_1(3/2)$ (black, thick, dashed line) and $(n-2)\mathrm{d}[3/2]_1(3/2)$ (grey, thick, dashed line) series is marked by a grey rectangle. Another s/d interaction, between $ns(F = 5/2)$ (black, thin, dash-dotted line) and $(n-2)\mathrm{d}(F = 5/2)$ (grey, thin, dash-dotted line) is also clearly visible in this region. The main goal of the measurements presented here was the verification of the s/d interaction predicted between $ns[3/2]_1(3/2)$ and $(n-2)\mathrm{d}[3/2]_1(3/2)$ (see Fig. 11 of Ref. [30] and also Figure 4.11 below). Only $F = 1/2$ and $F = 3/2$ states can be excited from the $^1S_0$, $F = 1/2$ ground state in ^{129}Xe, because of the $\Delta F = 0, \pm 1$ selection rule. In general, the $\Delta F = 0, \pm 1$ and $\Delta l = \pm 1$ selection rules were observed starting from $ns[3/2]_1(3/2)$ and $(n-2)\mathrm{d}[3/2]_1(3/2)$ Rydberg states. Because of the s/d channel interaction, transitions to $nf[K]_J(F)$ states were also observed from $ns[3/2]_1(3/2)$ Rydberg states, as discussed above.

Because a very large number of transitions were observed for ^{129}Xe, only those originating from $ns[3/2]_1(3/2)$ and $(n-2)\mathrm{d}[3/2]_1(3/2)$ states were analyzed in a first step. Using transitions from these states, it was not possible to build a global energy-level network that allowed for referencing the energies of all levels to one state. To nevertheless determine

Table 4.3: Experimentally determined energy splittings $\Delta E_{\mathrm{exp}}\,(n\mathrm{s}/(n-2)\mathrm{d})$ between $n\mathrm{s}[3/2]_1(3/2)$ and $(n-2)\mathrm{d}[3/2]_1(3/2)$ states as compared to calculated ones $\Delta E_{\mathrm{calc}}\,(n\mathrm{s}/(n-2)\mathrm{d})$ as a function of principal quantum number n.

n	$\Delta E_{\mathrm{exp}}/h$ MHz	$(\Delta E_{\mathrm{exp}} - \Delta E_{\mathrm{calc}})/h$ MHz
84	797.6	−6.8
87	552	−5.2
88	498.1	−7.1
89	471	−1.2
91	464.3	−1.3
93	518.3	−4.3
94	566.2	+1.1

the energy differences between ns and $(n-2)$d states near $n = 90$, a different approach was employed. Locating transitions from ns and $(n-2)$d states recorded to the same final n'f Rydberg state within one spectrum allowed for extraction of the energy splitting $\Delta E\,(n\mathrm{s}/(n-2)\mathrm{d}) = E\,(n\mathrm{s}[3/2]_1(3/2)) - E\,((n-2)\mathrm{d}[3/2]_1(3/2))$ between the two states as a function of the principal quantum number n. Whenever several values for the same splittings could be determined in this manner for a given n, these values were averaged. The results thus obtained are summarized in Table 4.3, where they are compared to calculated energy differences based on the MQDT parameter set reported in [30]. For a more visual representation, the experimentally determined splittings are shown as red and blue squares in panel b) of Figure 4.11. To this end, the average energy $E_{\mathrm{avg}}(n)$ of the calculated energies of $n\mathrm{s}[3/2]_1(3/2)$ ($E_{\mathrm{calc}}(ns)$) and $(n-2)\mathrm{d}[3/2]_1(3/2)$ ($E_{\mathrm{calc}}((n-2)\mathrm{d})$) Rydberg states was determined as $E_{\mathrm{avg}} = \left(E_{n\mathrm{s}} + E_{(n-2)\mathrm{d}}\right)/2$. Then, the experimental energies ($E_{\mathrm{exp}}(n\mathrm{s})$) of the ns states (shown as red squares in Figure 4.11) and the experimental energies ($E_{\mathrm{exp}}((n-2)\mathrm{d})$) of the $(n-2)$d states (shown as blue squares in Figure 4.11) were determined as follows:

$$E_{\mathrm{exp}}(n\mathrm{s}) = E_{\mathrm{avg}}(n) + \Delta E_{\mathrm{exp}}\,(n\mathrm{s}/(n-2)\mathrm{d})\,/2 \tag{4.2}$$

$$E_{\mathrm{exp}}((n-2)\mathrm{d}) = E_{\mathrm{avg}}(n) - \Delta E_{\mathrm{exp}}\,(n\mathrm{s}/(n-2)\mathrm{d})\,/2\,. \tag{4.3}$$

In the range of effective principal quantum number $n = 84 - 94$ (of ns states), it was found that transitions originating from ns Rydberg states were generally more intense than their counterparts originating from nd Rydberg states. Overall, calculations overestimate the splitting $\Delta E\,(n\mathrm{s}/(n-2)\mathrm{d})$ by $\sim 5\,\mathrm{MHz}$ as compared to experiment. The agreement is nevertheless excellent and is consistent with the general observation that calculated frequencies for transitions originating from $n\mathrm{s}[3/2]_1(3/2)$ states exceed experimental frequencies by $\sim 5\,\mathrm{MHz}$. This circumstance, however, provides several challenges for the assignment of

many other recorded transitions in ^{129}Xe. Because the spectra are much more dense than is the case for ^{132}Xe, it is not uncommon that several calculated transition frequencies lie within ~ 5 MHz of an experimentally observed one, making definite assignments impossible at this stage.

4.4 Power broadening and Rabi frequencies

Although transition moments between Rydberg states are typically large (they scale as n^2), transition strengths can vary greatly depending on the types of levels involved in a transition. In the case of excitation by sub-millimeter-wave radiation, it is additionally favorable that the change in principal quantum number is small [38]. As discussed in Section 4.3.1, intensities of the sub-millimeter-wave transitions recorded between high Rydberg states of ^{129}Xe and ^{132}Xe described in the preceding sections of this chapter were not representative of actual transition strengths. It is nevertheless important to have a measure for relative transition strengths to better understand the lineshapes and possible line shifts and broadenings. For each observed transition, the experimentally observed linewidth was tabulated along with its assignment (see Table A.1 in Appendix A.1). Several transitions are power broadened to ~ 3 MHz (although power broadenings were typically 2 MHz or less) because of their strong transition dipole moments, whereas others exhibited linewidths of only ~ 200 kHz, which were the minimal linewidths compatible with the experimental conditions, in particular with the 10 μs time interval used between the VUV laser pulse used for preparation of the initial Rydberg states and the field ionization pulse used to detect the transition.

4.4.1 Power Broadening

This section is concerned with the examination of the broadening of a single Rydberg-Rydberg transition ($70p[5/2]_2 \leftarrow 58d[3/2]_1$) by the sub-millimeter-wave radiation field. This examination also enabled the determination of possible errors associated with the shift of experimentally observed transition frequencies by the ac Stark effect. The Rabi frequencies determined from the observed full widths at half maximum (FWHM) were compared to values obtained from direct measurements of Rabi oscillations between the two Rydberg states connected by the transition. Initial and final Rydberg states can be approximated well by a two-level system because of the narrow bandwidth of the sub-millimeter-wave radiation source and the long lifetimes of the high Rydberg states. For the experiments described in this subsection, the $58d[3/2]_1$ Rydberg state of ^{132}Xe was chosen as initial state ($|1\rangle$) and the $70p[5/2]_2$ Rydberg state as final state ($|2\rangle$). The effect of the sub-millimeter-wave intensity on the full width at half maximum of an observed

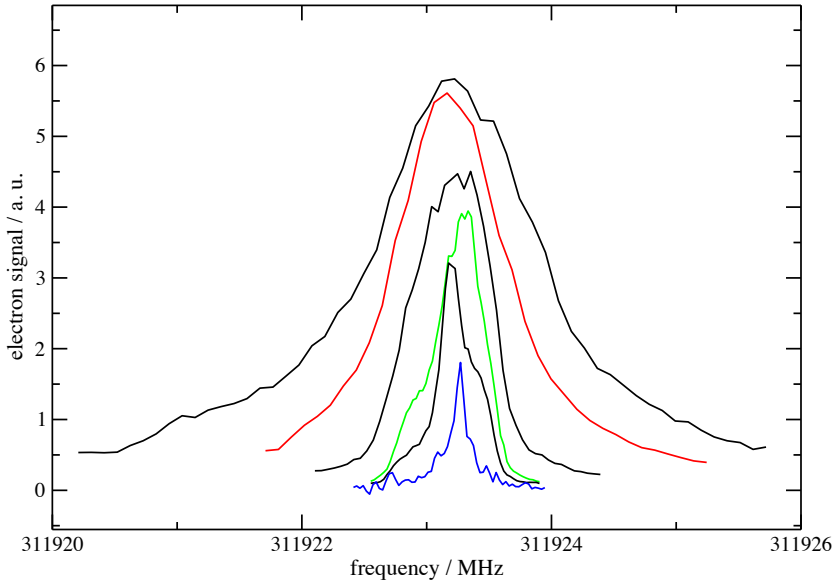

Figure 4.12: Panel a): $70p[5/2]_2 \leftarrow 58d[3/2]_1$ transition in ^{132}Xe for different sub-millimeter-wave attenuations of 0 dB (top black trace), −5 dB (red trace), −10 dB (middle black trace), −15 dB (green trace) −20 dB (lower black trace) and −35 dB (blue trace). The scale of the blue trace was increased for clarity.

transition can be described by the following equation [135]:

$$\Gamma_{\mathrm{FWHM}} = 2\left(\gamma^2 + \frac{1}{2}\Omega^2\right)^{1/2}, \tag{4.4}$$

where, in the present case, γ is a phenomenological angular frequency incorporating all mechanisms for decay, decoherence or dephasing. Taking only radiative coupling terms into account and neglecting all other forms of decoherence or dephasing, γ is related to the Einstein A_{21} coefficient as $\gamma = \frac{1}{2}A_{21}$. The Rabi frequency Ω is dependent on the electric field amplitude E_0 and the transition dipole moment $\mu_{12} = \langle 1|er|2\rangle$

$$\Omega = \frac{E_0\mu_{12}}{\hbar}. \tag{4.5}$$

Figure 4.12 illustrates qualitatively the reduction of the observed FWHM for the $70p[5/2]_2 \leftarrow 58d[3/2]_1$ transition in ^{132}Xe observed upon attenuation by factors of up to ~ 3000 of the sub-millimeter-wave radiation intensity, which leads to a reduction of Ω because the intensity is proportional to the square of the electric field amplitude E_0. The narrowest line was observed for an attenuation of 35 dB (green trace). This transition exhibits a linewidth of $\Gamma_{\mathrm{FWHM}}(-35\,\mathrm{dB})/(2\pi) = 146(10)\,\mathrm{kHz}$ that is only slightly broader than the limit imposed by the finite observation time (10 μs) and the transit-time resulting from the propagation of the atomic beam of Xe atoms through the sub-millimeter-wave radiation. Effects of dephasing occurring as the atomic beam propagates through the radiation beam and experiences varying radiation intensities seem to be weak (see Section 4.4.2 below) because the value of γ determined from the Rabi oscillation measurements does not change

upon increasing the velocity of the atomic beam from 350 to 1000 m/s, nor is the line significantly broadened. Table 4.4 lists the observed FWHM (Γ_{FWHM}) and transition frequency ω_{12} (in units of angular frequency) for the different sub-millimeter-wave radiation intensities used in the experiments presented in Figure 4.12. These values were obtained by fitting a Lorentzian lineshape to the observed peaks. For the calculation of the Rabi frequency, the approximation was made that at -35 dB attenuation, $\Omega^2/2 \ll \gamma^2$ and therefore $\gamma = \Gamma_{\mathrm{FWHM}}(-35\,\mathrm{dB})/2 = 0.459 \cdot 10^6\,\mathrm{s}^{-1}$. This value of γ was used for the calculation of the Rabi frequencies at all other sub-millimeter-wave attenuations. Predicted values for the Rabi frequency Ω_{p} were also calculated by making use of the fact that $\Omega \propto \sqrt{I}$ (see Eq. 4.5). The values of I relative to I_0 (corresponding to 0 dB) could be calculated from the attenuation factors. Ω_{p} was then calculated from the value of $\Omega_0 = 6.39 \cdot 10^6\,\mathrm{s}^{-1}$ found at 0 dB and could be used to estimate the value of Ω at -35 dB. This allowed for verification of the approximation made that $\gamma = \Gamma_{\mathrm{FWHM}}/2 = 0.459 \cdot 10^6\,\mathrm{s}^{-1}$ because at this attenuation, $\gamma^2 \gg \frac{1}{2}\Omega^2$. In general, Ω_{p} differs from the value of Ω by up to $\sim 40\%$, the largest deviations being for the case of very strong attenuation, which is attributed to the experimental error associated with the measurement of the attenuation factors under conditions of strong attenuation. Overall, the uncertainties of the line position of

Table 4.4: Observed transition frequencies ω_{12}, FWHM and calculated Rabi frequencies Ω, as well as values Ω_{p} predicted from the attenuation factors for the $70\mathrm{p}[5/2]_2 \leftarrow 58\mathrm{d}[3/2]_1$ transition of ^{132}Xe (see text for details). Frequencies are given in units of angular frequency ($10^6\,\mathrm{s}^{-1}$). To convert to the observed transition frequencies and FWHM in units of MHz, division by the factor 2π is necessary.

	0 dB	-5 dB	-10 dB
FWHM	9.09(50)	5.73(40)	3.94(27)
ω_{12}	1 959 871.40(11)	1 959 871.150(93)	1 959 871.363(93)
I	I_0	$0.36 I_0$	$0.1 I_0$
Ω_{p}	$\Omega_0 \propto \sqrt{I_0}$	$0.6\,\Omega_0$	$0.32\,\Omega_0$
Ω	6.39	4.00	2.71
$\Omega_{\mathrm{p}}/\Omega$	–	0.96	0.75
	-15 dB	-20 dB	-35 dB
FWHM	2.89(27)	1.89(19)	0.918(61)
ω_{12}	1 959 871.71(18)	1 959 871.39(20)	1 959 871.67(19)
I	$0.032 I_0$	$0.01 I_0$	$3.2 \cdot 10^{-4} I_0$
Ω_{p}	$0.18\,\Omega_0$	$0.1\,\Omega_0$	$0.018\,\Omega_0$
Ω	1.94	1.17	0
$\Omega_{\mathrm{p}}/\Omega$	0.59	0.55	–

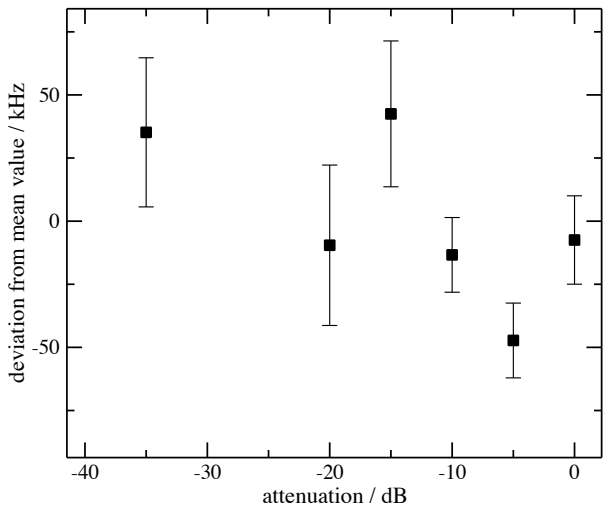

Figure 4.13: Deviations of observed frequencies of the $70p[5/2]_2 \leftarrow 58d[3/2]_1$ transition of ^{132}Xe from the mean value of 311 923.229 (34) MHz as a function of sub-millimeter-wave attenuation. Error bars take into account solely the error in the determination of the transition frequency given in Table 4.4 that results from fitting a Lorentzian function to the observed transition.

the $70p[5/2]_2 \leftarrow 58d[3/2]_1$ transition of ^{132}Xe determined from the Lorentzian fit were less than 50 kHz. The average of all transition frequencies in Table 4.4 led to a value of 311 923.229 (34) MHz. There appeared to be no systematic shift of transition frequencies with increasing power of the sub-millimeter-wave radiation, as can be seen from the random distribution of the deviations from the mean value for the transition frequency shown as a function of sub-millimeter-wave attenuation in Figure 4.13.

4.4.2 Rabi Oscillations

The analysis of power broadening and the determination of Rabi frequencies Ω and phenomenological decay rates γ led the conclusion that Rabi oscillations occur on a microsecond timescale and should be observable between Xe Rydberg states. This subsection is devoted to their direct measurement. Because the BWO source used for the sub-millimeter-wave experiments provided a continuous-wave output, the time-evolution of the population ρ_{22} during sub-millimeter-wave excitation was determined by varying the delay between the production of $|1\rangle$ by VUV excitation and the selective field ionization of $|2\rangle$. Figure 4.14 shows a set of measurements of the field ionization signal as a function of this time delay which clearly reveal the expected oscillatory behavior of the population transfer. Panels (a)-(d) present measurements recorded at 0 dB for a detuning of the driving frequency from the resonance frequency varying between 0 and 3.14 MHz, which was the highest detuning for which the field ionization signal could be recorded with sufficient signal-to-noise ratio. These detunings are indicated by dashed lines in panel (h), which displays the lineshape

of the $70p[5/2]_2 \leftarrow 58d[3/2]_1$ transition measured at the maximal power (0 dB) of the sub-millimeter-wave source. For a detuning $\delta = \omega - \omega_{12}$ from the resonance frequency ω_{12}, the optical Bloch equations can be written as [135]:

$$\frac{\mathrm{d}\rho_{11}}{\mathrm{d}t} = +2\gamma\rho_{22} + \frac{i}{2}\left(\Omega\tilde{\rho}_{12} - \Omega\tilde{\rho}_{21}\right) \tag{4.6}$$

$$\frac{\mathrm{d}\rho_{22}}{\mathrm{d}t} = -2\gamma\rho_{22} + \frac{i}{2}\left(\Omega\tilde{\rho}_{21} - \Omega\tilde{\rho}_{12}\right) \tag{4.7}$$

$$\frac{\mathrm{d}\tilde{\rho}_{12}}{\mathrm{d}t} = -\left(\gamma + i\delta\right)\tilde{\rho}_{12} + \frac{i}{2}\Omega\left(\rho_{11} - \rho_{22}\right) \tag{4.8}$$

$$\frac{\mathrm{d}\tilde{\rho}_{21}}{\mathrm{d}t} = -\left(\gamma - i\delta\right)\tilde{\rho}_{21} + \frac{i}{2}\Omega\left(\rho_{22} - \rho_{11}\right) \tag{4.9}$$

where $\rho_{11} = \tilde{\rho}_{11}$ is the population of $|1\rangle$, $\rho_{22} = \tilde{\rho}_{22}$ the population of the excited state and $\tilde{\rho}_{12} = \rho_{12}e^{(-i\delta t)} = \tilde{\rho}^*_{21}$. For $\delta = 0$, the analytical expression

$$\rho_{22}(t) = \frac{\Omega^2/2}{2\gamma^2 + \Omega^2}\left\{1 - \left[\cos\left(\lambda t\right) + \frac{3\gamma}{2\lambda}\sin\left(\lambda t\right)\right]\exp\left(-\frac{3\gamma t}{2}\right)\right\} \tag{4.10}$$

can be derived starting from the initial conditions $\rho_{22}(0) = 0$ and $\tilde{\rho}_{12}(0) = 0$ [135]. In Eq. 4.10, $\lambda = \left(\Omega^2 - \frac{1}{4}\gamma^2\right)^{1/2}$. This equation was used to extract the values of Ω and γ from the Rabi oscillations recorded at zero detuning. The results for this case are listed in Table 4.5. Figure 4.14 shows measurements for $\delta = 0$ and different VUV intensities (traces (e) and (f)), as well as for a supersonic beam of a mixture of 10% Xe in Ne (trace (g)), which is considerably faster (~ 1000 m/s) than a supersonic beam of pure Xe (~ 350 m/s). Only insignificant changes to the value of γ were observed, pointing to the conclusion that the main contribution to the damping of the oscillation was neither from inhomogeneities in the dc electric-field distribution (this would have resulted in larger values of γ for a faster beam) nor from background ions that could have caused inhomogeneous broadening and dephasing (one would have expected decreasing values of γ for decreasing VUV intensities in this case). These findings are consistent with the observations made from spectroscopic measurements, where the observed FWHM depended neither on the VUV

Table 4.5: Values of Ω and γ obtained from the analysis of Rabi oscillations for different detunings $\delta/(2\pi)$. The values of Ω and γ are given in units of angular frequency.

$\delta/(2\pi)$ MHz	Ω $10^6\,\mathrm{s}^{-1}$	γ $10^6\,\mathrm{s}^{-1}$
0	6.0(1.3)	1.34(0.28)
0.54	5.2*	1.1*
1.84	6.3(2.3)	1.20(0.38)
3.14	6.9*	1.1*

* only one measurement was performed, therefore no statistical uncertainty can be given.

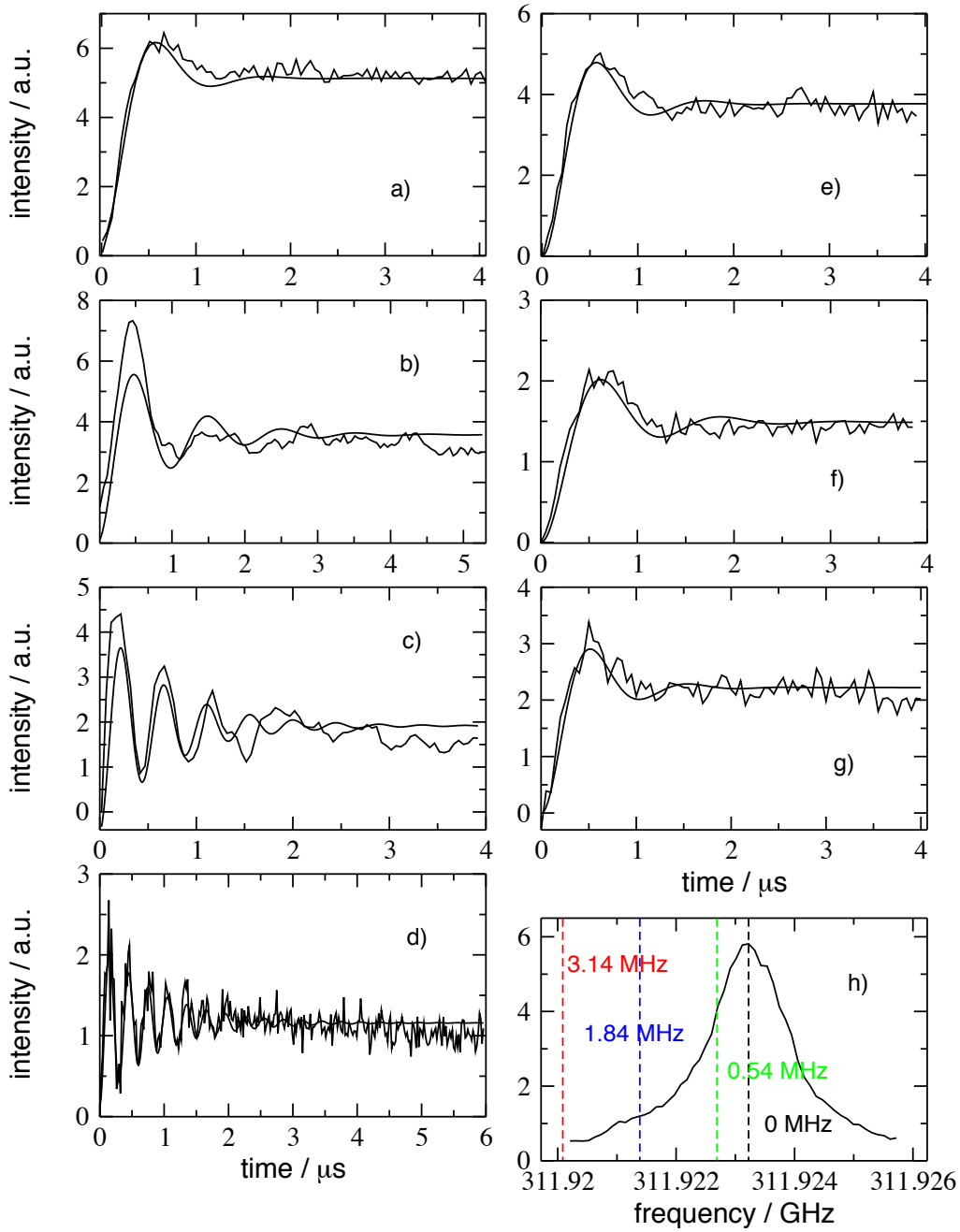

Figure 4.14: Panels a)-d): Measurements of Rabi oscillations associated with the $70p[5/2]_2 \leftarrow 58d[3/2]_1$ transition of Xe for detunings $\Delta\nu = \delta/(2\pi)$ of 0 MHz, 0.54 MHz, 1.84 MHz and 3.14 MHz, respectively. Panels e) and f): Rabi oscillations recorded on resonance at VUV intensities reduced by a factor of 3 and 7, yielding values of $\gamma = 1.5$ and $\gamma = 1.1$, respectively. Panel g): Rabi oscillations for a mixture of 10% Xe in Ne, yielding a value of $\gamma = 1.5$.

laser power nor on the beam velocity. Rabi oscillation measurements were also performed for different values of δ between $0.54 \cdot 2\pi\,\mathrm{MHz}$ and $3.14 \cdot 2\pi\,\mathrm{MHz}$ (see Figure 4.14), and also for varying VUV intensities (at a detuning $\delta = 0\,\mathrm{MHz}$). For the case of $\delta \neq 0$, an analytical expression for $\rho_{22}(t)$ cannot be obtained from the optical Bloch equations. The following phenomenological expression was used for deriving the values of Ω' and γ' from the experimental data in a least-squares-fit procedure:

$$\rho_{22}(t) = \frac{\Omega'^2}{\delta^2 + \Omega'^2} \sin\left(\frac{t}{2}\sqrt{\delta^2 + \Omega'^2}\right)^2 \exp\left(-\gamma' t\right) . \tag{4.11}$$

The population modeled by Eq. (4.11) was then compared to the population obtained by an exact numerical integration of Equations (4.6)-(4.9), substituting Ω' for Ω and γ' for γ, so that the relationships between these parameters could be determined. The values determined for Ω are in good agreement with those obtained from the lineshape analysis and listed in Table 4.4. However, the values of γ obtained from the Rabi oscillations are larger by a factor of ~ 2.5 than the one determined from the spectroscopic measurement at $-35\,\mathrm{dB}$ (see Table 4.4). A possible explanation for this difference is that the dephasing observed in Figure 4.14 has a contribution from the spatially inhomogeneous intensity distribution of the sub-millimeter-wave radiation across the sample that led to a broader distribution of Rabi frequencies.

4.5 Error Budget

In addition to the statistical uncertainties in the level positions that resulted from the determination of line centers and the least-squares-fit procedure discussed above, systematic errors may also affect these level positions. The following sources of such errors were considered:

(i) DC Stark shifts by residual electric fields
Because our measurement procedure involved compensating stray dc electric fields (see Section 2.7.4), we estimate the maximal value of the residual field to be $1\,\mathrm{mV/cm}$. From previous measurements of the Stark effect in s $\rightarrow$ p and d $\rightarrow$ f transitions of Xe [30], and by exploiting the n^7 scaling of the polarizability, we can estimate the maximal shift for the transitions caused by the residual stray electric field to be $100\,\mathrm{kHz}$ in the range of n values investigated.

(ii) Pressure shift
The pressure shift in high Rydberg states arises primarily from the scattering of the Rydberg electron with neutral atoms and molecules located within the Rydberg orbit [136]. Because this shift is approximately the same for the initial and final states of the sub-millimeter-wave transitions, its effect on the transition frequencies is negligible (see discussion in [31]).

(iii) AC Stark shift
An AC Stark shift would lead to a shift of the transition frequencies that is dependent on the intensity of the sub-millimeter-wave radiation. Because no such shift could be observed within the sensitivity limits of our measurements upon changing the intensity by a factor of more than 1000 (see Section 4.4), we conclude that AC Stark shifts contribute to a systematic uncertainty of less than 50 kHz.

(iv) Doppler shifts
Such shifts can be estimated from the velocity component v_t of the supersonic beam along the sub-millimeter-wave propagation axis according to $\nu = \nu_0 (1 + v_t/c)$. Because the supersonic beam propagates perpendicularly to the sub-millimeter waves, and the geometric constraints of the experiment limit a possible deviation for a perpendicular arrangement to less than 1°, we estimate from the Xe beam velocity of 350 m/s that the maximal shift at the highest transition frequencies (350 GHz) is less than 150 kHz. This represents the largest source of systematic uncertainty in the present measurements.

Because these sources of systematic uncertainties appear independent, we estimate the overall systematic uncertainty to be 200 kHz.

4.6 Conclusions

The experimental apparatus that was set up for the measurement of sub-millimeter-wave transitions between high Rydberg states was characterized by measurement of transitions between Rydberg states of Xe. Coherent excitation was observed for the $70\mathrm{p}[5/2]_2 \leftarrow 58\mathrm{d}[3/2]_1$ transition in ^{132}Xe. Additionally, the effect of power broadening by sub-millimeter-wave radiation was studied to better understand transition strengths observed in the spectra. After studying and minimizing effects of stray electric and magnetic fields (see also Section 2.7.4), it was possible to determine level energies for 53 states of ^{132}Xe at a precision of typically less than 100 kHz and an overall systematic uncertainty of less than 200 kHz. These results agreed to within ~ 1 MHz with values predicted by calculation. It was further possible to determine values for s/d splittings in ^{129}Xe in the range between $n = 84 - 94$ that agreed with values predicted by MQDT calculations to within ~ 5 MHz. This proved that the experimental setup was well-suited for the development of the THz-VUV spectrometer used for the experiments on H_2 and Xe Rydberg states presented in the following chapters.

Chapter 5

Rydberg states of Xe as studied by THz radiation

5.1 Introduction

In this chapter, the first application of the THz-VUV double-resonance spectrometer developed in the realm of this thesis and described in detail in Chapter 2 is presented. Its power to study Rydberg-Rydberg transitions in an arbitrary atomic or molecular system is illustrated by an investigation of high Rydberg states of Xe and the high sensitivity and resolution as well as the mass-selectivity of this experimental approach are demonstrated. The generation, manipulation and detection of radiation tunable in the range of 0.1-14 THz provides several challenges (for a description see Chapters 1 and 2) and therefore radiation sources affording a high resolution over this entire frequency range are still rare. Yet radiation that is tunable in this range is particularly well-suited for gaining spectral information on atomic and molecular Rydberg states at intermediate n values. For example in ^{132}Xe, exciting a transition between states with a principal quantum number of $n = 18$ and 19 requires a frequency of ~ 1 THz, whereas exciting a transition between $n = 7$ and 8 requires a frequency of ~ 15 THz. Analogously, radiation with a frequency of ~ 15 THz has sufficient energy to ionize states at $n = 15$, whereas at a frequency of ~ 1 THz this would correspond to a state with $n = 57$. The THz-VUV spectrometer developed in the realm of this thesis is therefore a powerful tool for obtaining high-resolution spectral information over a very large range of principal quantum number n and extracting highly accurate values for level spacings. In this context, it can be used to characterize channel interactions mediated by electronic, rotational, vibrational and hyperfine interactions and also to study the energy-dependence of eigen-quantum defects. The spectrometer has been used to study Rydberg transitions in atoms and molecules (demonstrated in Chapter 6) and, without further modification, can also be used to study rotational and vibrational spectra of molecules and clusters in the THz frequency range. The present chapter is based on

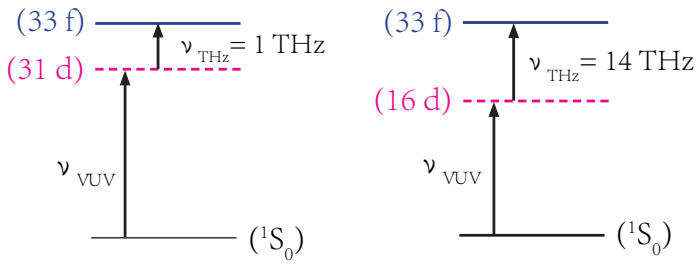

Figure 5.1: Excitation scheme used to measure spectra of 33f ← nd Rydberg-Rydberg transitions of Xe. The transitions were detected by selective field ionization of the final 33f level. The figure illustrates the range of initial states corresponding to the frequency range from 0.9 THz ($n = 31$) to 14.3 THz ($n = 16$).

the article "High-resolution laser spectroscopy between 0.9 and 14.3 THz in a supersonic beam: Rydberg-Rydberg transitions of atomic Xe at intermediate n values" by myself, J. Agner and F. Merkt [137].

5.2 Experimental

5.2.1 Excitation Sequence and Generation of THz Radiation

Rydberg states of effective principal quantum number n^* in the range of $13.8 - 28.8$ were prepared by irradiation of a supersonic beam of Xe with VUV radiation. Tuning the frequency of the VUV radiation provided access from the $^1S_0$ ground state to 16d − 31d Rydberg states belonging to series converging on the $^2P_{3/2}$ ground state of Xe^+. The THz radiation source was used to record spectra of transitions from these Rydberg states to higher-lying Rydberg states. The excitation scheme is presented in Figure 5.1 and the schematic optical layout used in the experiment is depicted in Fig. 2. In the experiments described in this article, we chose 33f as the final state of all transitions, which enabled us to study the d Rydberg states in the intermediate range of principal quantum number between 16 and 31. The transitions were detected by selective field ionization and recording either the electrons or ions, the latter offering the advantage of mass selectivity.

The pulsed VUV radiation of wave number $\tilde{\nu}_{\mathrm{VUV}} = 2\tilde{\nu}_{\mathrm{UV}} + \tilde{\nu}_{\mathrm{VIS}}$ was generated by resonance-enhanced sum-frequency mixing in Xe as described in the experimental section of this thesis (see Chapter 2). The frequency-doubled output (wave number $\tilde{\nu}_{\mathrm{UV}}$) of a dye laser was used to access the $(5p)^5(^2P_{3/2})6p[1/2](J{=}0) \leftarrow (5p)^6(^1S_0)$ two-photon resonance of atomic Xe at $2\tilde{\nu}_{\mathrm{UV}} = 80118.97\,\mathrm{cm}^{-1}$. The output ($\tilde{\nu}_{\mathrm{VIS}}$) of a second, tunable dye laser was used to generate tunable VUV radiation at wave numbers around $97700\,\mathrm{cm}^{-1}$.

The basic principle of THz generation relies on difference-frequency mixing using two near-infrared (NIR) lasers, one of which is kept fixed in frequency while the frequency of the other is tuned, resulting in tunable THz radiation (see Chapter 2). Narrow-bandwidth NIR radiation is produced by two titanium-doped sapphire (Ti:Sa) ring lasers, the cw outputs of which are converted into pulses using two acousto-optic modulators (AOMs) and subsequently pulse-amplified in a bow-tie configuration [138] as shown in Figure 2.12. The same bow-tie amplifier is used for amplification of the two NIR lasers so that the frequency shifts and chirps occurring in the amplification process are identical for both and cancel out in the difference-frequency mixing process. The amplified NIR pulses are directed into a vacuum chamber, where difference-frequency generation takes place in a *trans*-4′-(dimethylamino)-*N*-methyl-4-stilbazolium tosylate (DAST) crystal (details on the crystal and the cut used for optimal generation of THz radiation are given in Chapter 2). The THz spectrometer is depicted in Figure 2.13 and is described in detail below.

5.2.2 VUV-THz Double-Resonance Spectrometer

The VUV-THz double-resonance spectrometer has been designed in such a way as to be able to: (i) easily adjust the frequency across the range from $0.1 - 14.3\,\mathrm{THz}$, (ii) avoid reduction of THz power caused by water absorption, (iii) easily optimize the interaction volume between the molecular beam and the THz- and VUV-radiation beams, and (iv) exploit the collision-free environment of a supersonic beam and the strong reduction of the Doppler shift that results from the perpendicular propagation of THz-radiation and supersonic beams. To avoid losses of THz-radiation intensity, only two gold-coated, off-axis parabolic mirrors (OAPMs) have been used as optical elements. Such mirrors have very high reflectivities across the entire above-mentioned frequency range and are used to align and focus the THz radiation inside of the vacuum chamber.

The two collinear pulse-amplified NIR beams enter the vacuum chamber via a side window (A in Figure 2.13) and are incident on the DAST crystal, the position (B) and orientation (C,D) of which can be adjusted from outside the vacuum chamber. The generated THz radiation propagates toward the first OAPM, the tilt angle of which can also be adjusted (E,F). The OAPM focuses the THz radiation near the point of intersection with the VUV and supersonic beams. The THz radiation then propagates toward a second OAPM that focuses it behind a polyethylene window inside a bolometer, which is used solely for alignment purposes. This design allows for a straightforward adjustment of the frequency between $0.1 - 14.3\,\mathrm{THz}$. In moving from the low-frequency to the high-frequency end of this region, only a slight modification of the tilt angles (E,F) of the OAPM is necessary, as well as a rotation of the polarization of the incident NIR beams by $\sim 30°$.

The relative timings of the VUV, NIR and gas pulses can be adjusted using a digital delay generator. The Rydberg-Rydberg transitions were detected by selective field ionization of

the 33f final states of the transitions by applying a pulsed electric field about 1μs after the THz-radiation pulse. When recording the ion signal in mass-selective measurements, an electric field of 530 V/cm was applied. For transitions recorded by monitoring the electron signal, an electric-field ramp was used that enabled us to distinguish electrons produced by the field ionization of Rydberg states of different n^* values by their different detection times. The electric field also served the purpose of extracting the ions or electrons toward a micro-channel plate (MCP) detector.

The photo-excitation region and ion/electron time-of-flight (TOF) tube were surrounded by two concentric magnetic shields. The stray electric fields along the TOF axis can be minimized by applying weak compensation fields as explained in Ref. [73] and illustrated in Chapter 2. The spectra were recorded by monitoring the ion or electron signal arriving in a selected time window as a function of the frequency of the THz radiation. The length of the NIR and THz pulses were adjusted in the range of 10 ns−400 ns by modifying the length of the pulses applied to the AOM, as will be illustrated in Section 5.3.1.

5.2.3 Frequency Calibration

The frequency of the THz radiation (ν_{THz}) was determined from the frequencies of the tunable (ν_{NIR1}) and fixed-frequency (ν_{NIR2}) Ti:Sa ring lasers by calculating their difference $\nu_{\mathrm{THz}} = \nu_{\mathrm{NIR1}} - \nu_{\mathrm{NIR2}}$. The frequency ν_{NIR1} was calibrated by simultaneously recording Doppler-free saturated absorption spectra of molecular iodine for the determination of the absolute frequency, and transmission spectra through a confocal Fabry-Perot (FP) etalon (FSR = 149.963(3) MHz, finesse = 30) for the relative frequency calibration. The length of this etalon was stabilized by locking to a polarization-stabilized HeNe laser, as described in Ref. [26]. The frequency ν_{NIR2} of the fixed ring laser was stabilized to a transmission maximum of the FP etalon. The absolute frequency of this laser was determined in a similar manner to that of the tunable laser by scanning to the closest-lying I_2 transition while simultaneously recording an etalon transmission spectrum.

The frequency calibration procedure is illustrated in Figure 5.2 with the example of the $33f[5/2]_2 \leftarrow 17d[3/2]_1$ transition of Xe. Panel a) depicts the spectrum as a function of the wave number of the tunable laser (bottom trace), the transmission spectrum through the FP etalon (middle trace) and the Doppler-free I_2 absorption spectrum (top trace). The etalon spectrum was used for wave-number linearization by cubic spline interpolation and the absolute wave number was calibrated by recording the frequency of the a_{10} hyperfine component of the P70, $B - X$ (0-13) rovibrational transition of I_2 and comparing to reference data [62]. In an analogous manner, the a_4 hyperfine component of the P79, $B - X$ (0-15) transition of I_2 was used for determining the absolute frequency of the fixed-frequency laser. Panel b) of Figure 5.2 shows the same spectrum after taking the difference of the wave numbers of the two NIR lasers. Because the frequency chirps and shifts [98] of

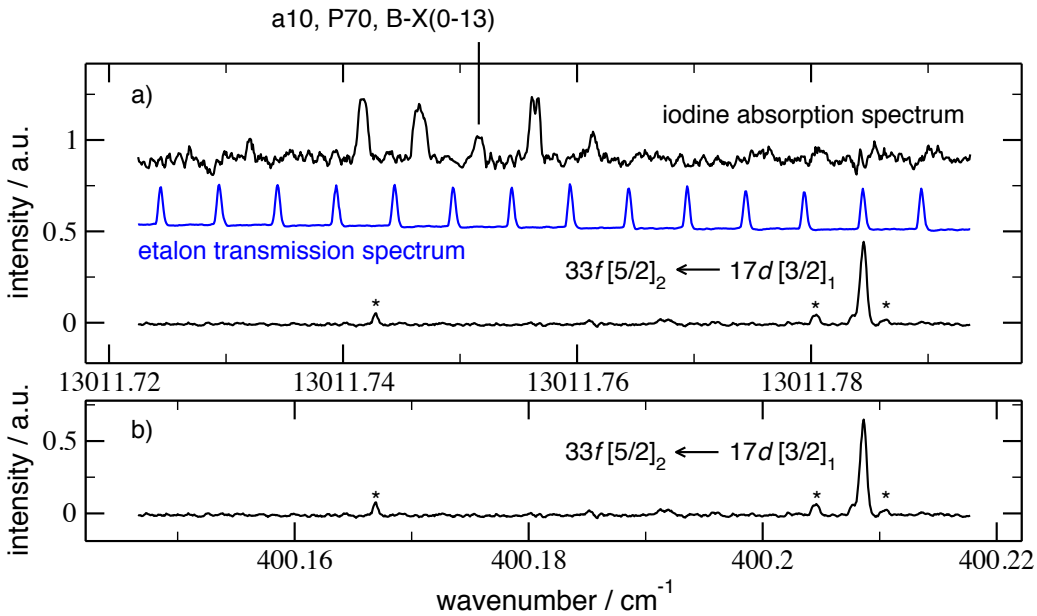

Figure 5.2: Spectrum of the $33f[5/2]_2 \leftarrow 17d[3/2]_1$ transition of Xe plotted as a function of the wave number $\tilde{\nu}_{\mathrm{NIR1}}$ of the tunable NIR laser (a) and as a function of the difference $\tilde{\nu}_{\mathrm{NIR1}} - \tilde{\nu}_{\mathrm{NIR2}}$ of the wave numbers of the tunable and fixed-frequency NIR lasers (b). The top and middle traces in panel (a) represent the Doppler-free absorption spectrum of I_2 and the transmission spectrum through an etalon, respectively. The asterisks designate transitions of ^{129}Xe and ^{131}Xe.

the two NIR beams occurring in the Ti:Sapphire bow-tie amplifiers are equal (see above), they cancel out when determining the difference $\nu_{\mathrm{NIR2}} - \nu_{\mathrm{NIR1}}$.

Systematic and statistical errors could be evaluated and minimized by making separate measurements of the frequency of the $33f[3/2]_2 \leftarrow 21d[3/2]_1$ transition on different days, after realignment of the optical setup and separate locking of the fixed-frequency ring laser. This procedure resulted in a value of 6. 284 561 9(28) THz, the standard deviation of 2.8 MHz representing the absolute frequency accuracy of the method, which is currently limited by the accuracy of the frequency calibration procedure. This uncertainty could be reduced by locking the frequency of the fixed laser using a phase-locked frequency comb or by recording spectra by scanning ν_{NIR1} on both sides of ν_{NIR2}, i.e., $\nu_{\mathrm{NIR1}} - \nu_{\mathrm{NIR2}}$ and $\nu_{\mathrm{NIR2}} - \nu_{\mathrm{NIR1}}$.

5.3 Results

5.3.1 Pulse Length and Resolution

Figure 5.3 illustrates, by example of the $33f[3/2]_{J=1,2} \leftarrow 31d[3/2]_1$ transitions of Xe, how the spectral resolution can be adjusted in the range between ∼2.8 MHz and ∼85 MHz by changing the duration of the NIR laser pulses. The spectra were recorded for NIR pulse

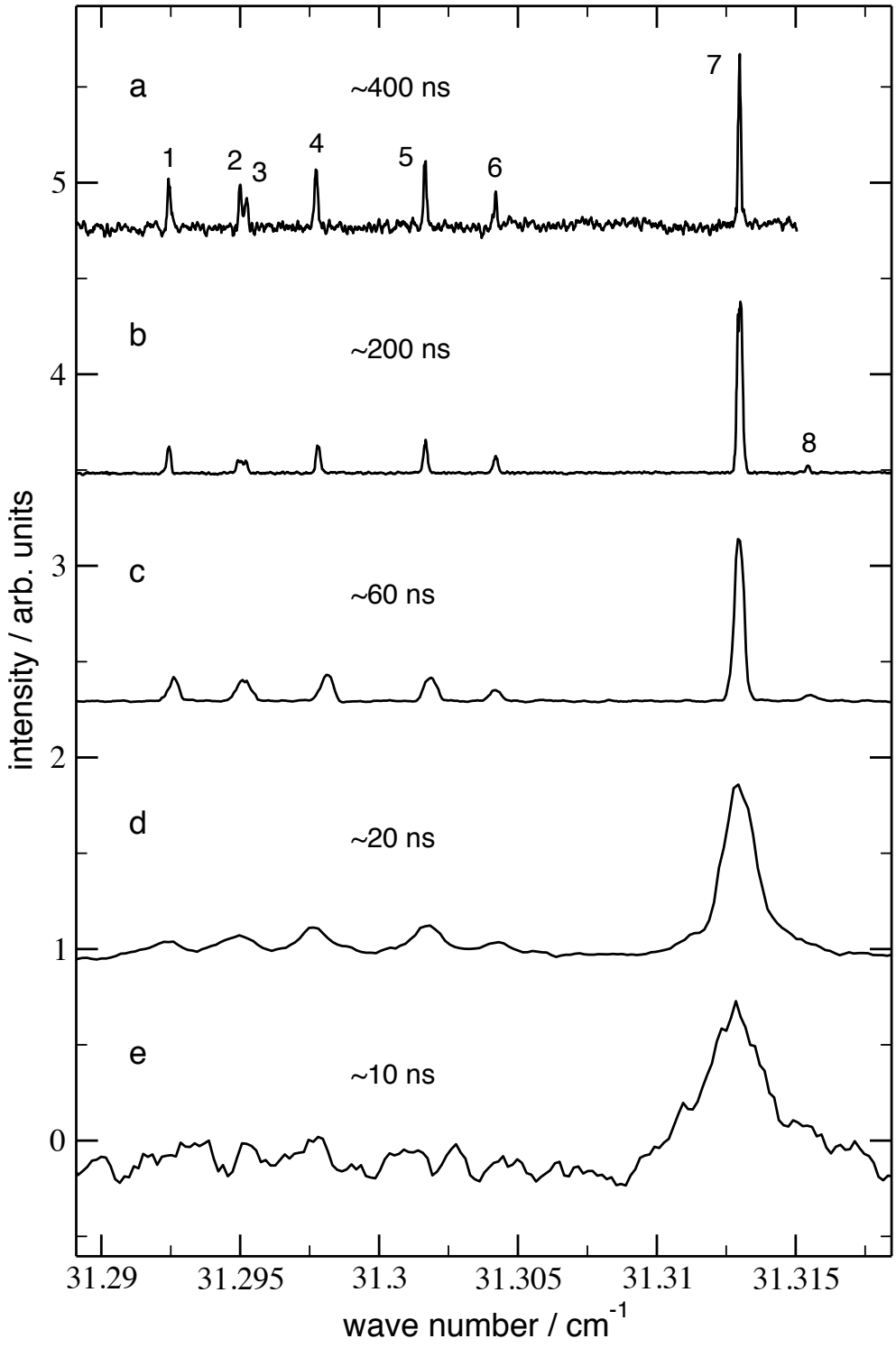

Figure 5.3: Spectra of the 33f ← 31d transition of Xe recorded using pulse lengths of a) 400 ns, b) 200 ns, c) 60 ns, d) 20 ns, e) 10 ns. The assignments of the lines labeled 1-8 are given in Table 5.1. The spectra have been shifted along the vertical axis for clarity.

Table 5.1: Assignments and relative positions (in cm^{-1}) of the fine and hyperfine-structure components of the 33f ← 31d transitions of ^{129}Xe, ^{131}Xe and ^{132}Xe observed in Figure 5.3.

peak	wave number cm^{-1}	isotope	assignment
1[a]	−0.020516(54)	^{129}Xe	$33f[3/2]_2(3/2) \leftarrow 31d[3/2]_1(1/2)$
2[a]	−0.018002(51)	^{129}Xe	$33f[3/2]_1(3/2) \leftarrow 31d[3/2]_1(3/2)$
3[a]	−0.017776(57)	^{132}Xe	$33f[3/2]_1 \leftarrow 31d[3/2]_1$
4[a]	−0.015175(51)	^{131}Xe	$33f[3/2]_2(7/2) \leftarrow 31d[3/2]_1(5/2)$
5[a]	−0.011319(51)	^{129}Xe	$33f[3/2]_2(5/2) \leftarrow 31d[3/2]_1(3/2)$
6[a]	−0.008801(51)	^{131}Xe	$33f[3/2]_2(5/2) \leftarrow 31d[3/2]_1(3/2)$
7	31.31303(22)	^{132}Xe	$33f[3/2]_2 \leftarrow 31d[3/2]_1$
8[a]	0.00258(12)	^{131}Xe	$33f[3/2]_2(3/2) \leftarrow 31d[3/2]_1(1/2)$

[a] The spectral positions are given relative to the $33f[3/2]_2 \leftarrow 31d[3/2]_1$ transition of ^{132}Xe. Note that the uncertainties of the relative positions (transitions $1-6$, 8) are smaller than the uncertainty of the absolute position (transition 7).

lengths of 400 ns, 200 ns, 60 ns, 20 ns and 10 ns, as displayed in panels a)-e), respectively. The assignments of the transitions labeled $1-8$ are presented in Table 5.1. The transitions labeled 2 and 3 in Figure 5.3 could only be resolved in the spectra recorded with the longest pulses (400 ns).

Table 5.2: Comparison of the NIR laser pulses with the measured (exp) full widths at half-maximum (FWHM) of the Rydberg-Rydberg transitions. The calculated (calc) widths were determined by convolution and Fourier-transformation assuming a Gaussian temporal profile of the NIR pulses.

pulse length ns	FWHM exp MHz	FWHM calc MHz
400	2.78(0.62)	1.56
200	5.06(0.54)	3.12
60	9.9(1.3)	10.4
20	29.7(4.2)	31.2
10	85(12)	62.4

The signal-to-noise ratio (SNR) of the spectra depicted in Figure 5.3 first increases with increasing pulse length and then decreases. This observation can be understood by considering the effect of the NIR pulse length on the power and the bandwidth of the THz

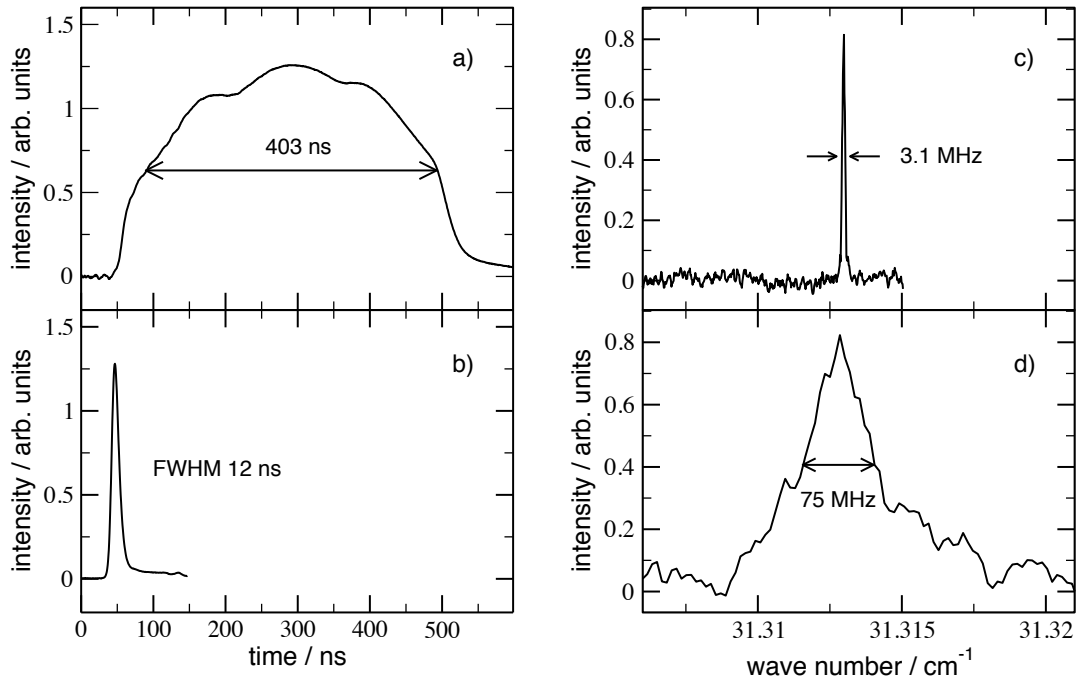

Figure 5.4: Effect of the NIR pulse length on the spectral resolution with the example of the $33f[3/2]_1 \leftarrow 31d[3/2]_1$ transition of the $I = 0$ isotopes of Xe. a) and b) display two measured NIR pulse shapes and c) and d) the corresponding spectral lineshapes.

radiation. For the process of difference-frequency generation, the i-th component of the second-order nonlinear polarizability tensor $\mathbf{P}^{(2)}$ is given by [139]:

$$P_i^{(2)}\left(\omega_{\mathrm{NIR1}} - \omega_{\mathrm{NIR2}}\right) = \sum_{j,k} 2\epsilon_0 d_{ijk}^{(2)}\left(\omega_{\mathrm{NIR1}} - \omega_{\mathrm{NIR2}}\right) E_j(\omega_{\mathrm{NIR1}}) E_k^*(\omega_{\mathrm{NIR2}})\,, \tag{5.1}$$

where ω_{NIR1} and ω_{NIR2} correspond to the frequency output of the tunable and fixed NIR ring lasers, respectively, $d_{ijk}^{(2)} = \frac{1}{2}\chi_{ijk}^{(2)}$ is the relevant second-order nonlinear optical coefficient, and $E_{j,k}$ are components of the electric field vector. Because the THz-generation process is nonlinear (see Eq. (5.1)), the power of the THz radiation P_{THz} is proportional to the product of the incident NIR powers ($P_{\mathrm{THz}} \propto P_{\mathrm{NIR1}} P_{\mathrm{NIR2}}$), and the maximal incident power is determined by the damage threshold of the DAST crystal ($\sim 6\,\mathrm{W/cm^2}$, or a peak power of $4\,\mathrm{MW/cm^2}$ for a pulse of 60 ns duration), shorter NIR pulse lengths with correspondingly higher peak powers lead to quadratically higher THz peak powers. One therefore expects the SNR to be best for the shortest pulses and to decrease with increasing pulse length. However, because the bandwidth of the THz radiation is larger than the Doppler width $\Delta\nu_{\mathrm{D}}$ of the transitions ($\Delta\nu_{\mathrm{D}} \approx 5 \cdot 10^{-8}\,\nu$ in the present case), the photon density at the transition frequency and the SNR of the spectra are reduced for the shortest pulses, even though the overall photon number is higher. Moreover, the efficiency of the pulse generation in the AOM decreases for pulses shorter than 40 ns. The best SNR

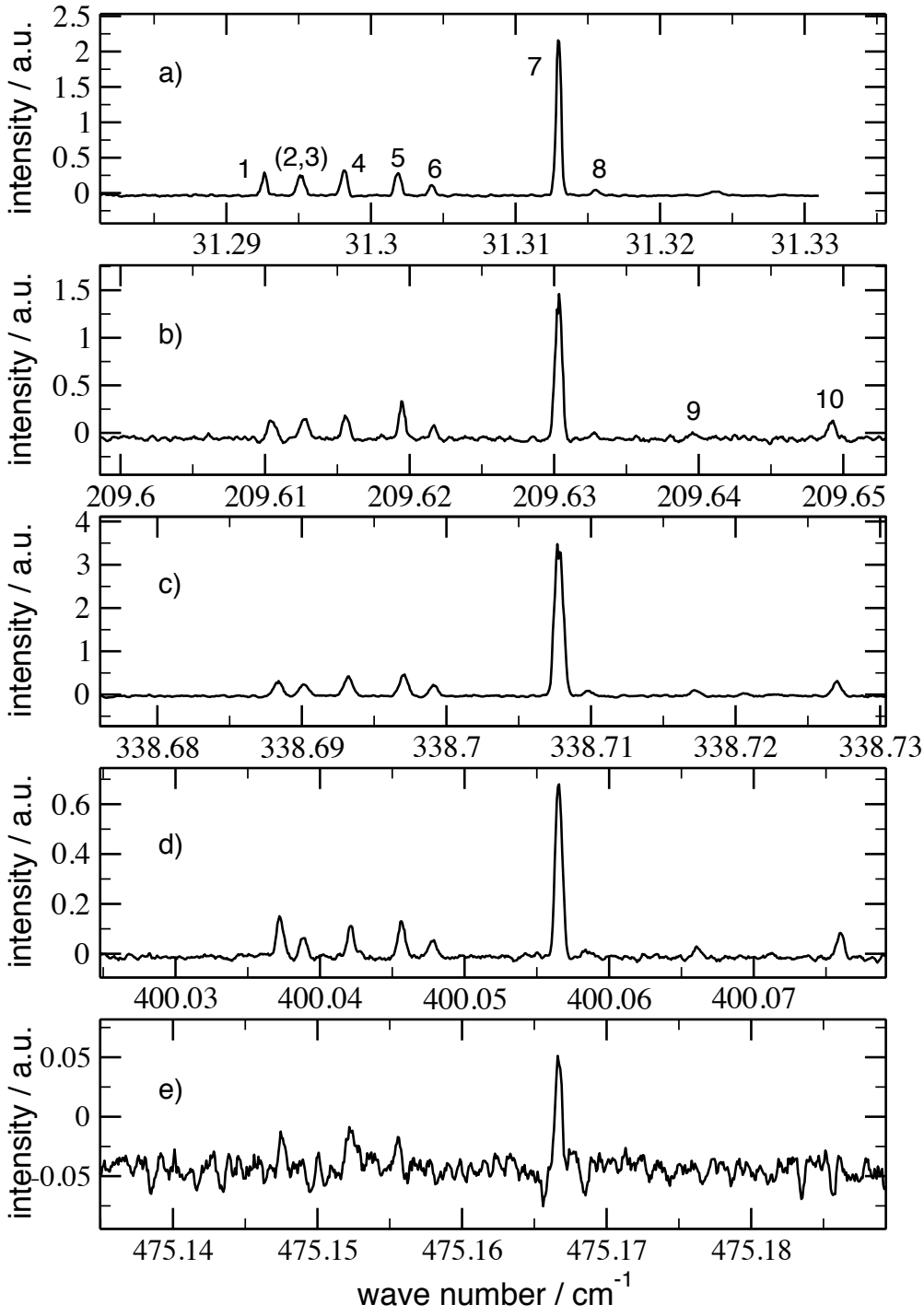

Figure 5.5: Fine and hyperfine structure of the 33f ← nd transitions of Xe for $n = 31$ (a), 21 (b), 18 (c), 17 (d) and 16 (e). The assignments of the lines labeled 1 to 8 are given in Table 5.1. Lines 9 and 10 correspond to the 33f$[3/2]_2(5/2)$ ← 21d$[3/2]_1(5/2)$ transitions of ^{131}Xe and 33f$[3/2]_1(3/2)$ ← 21d$[3/2]_1(1/2)$ of ^{129}Xe, respectively.

is obtained for pulse lengths of about 60 ns.

In Figure 5.4, the pulses with the longest ($\sim$ 400 ns, panel a)) and shortest ($\sim$ 10 ns, panel b)) lengths are shown next to the corresponding spectra of the 33f$[3/2]_2 \leftarrow$ 31d$[3/2]_1$ transition of ^{132}Xe, which exhibit full widths at half-maximum (FWHMs) of 3.1 MHz and 75 MHz, respectively. Table 5.2 summarizes an analysis of the FWHM in dependence on the pulse length. The experimental results (second column) agree closely with the FWHMs determined by convolution of two Gaussian NIR pulses that are perfectly overlapped in time and subsequently Fourier-transformed (third column). For intermediate pulse lengths, the experimental and calculated FWHMs agree to within the error margins. We attribute the larger observed widths for the measurements with the longest and shortest pulses to the deviations from a pure Gaussian pulse shape under these conditions.

5.3.2 Tunability

Figure 5.5 depicts spectra of transitions between nd$[3/2]_1$ and 33f$[K]_J$ Rydberg states in ^{132}Xe, ^{131}Xe and ^{129}Xe for selected values of the initial-state principal quantum number between $n = 16$ and 31. The figure illustrates that the frequency of our THz radiation source can be adjusted between 0.9 and 14.3 THz. Spectra were also recorded at $\sim$ 1.2 THz and $\sim$ 1.5 THz but are not shown here (see Table A.2 of Appendix A.2 for a list of all measured transition frequencies). The strongest line in these spectra corresponds to the transitions of the $I = 0$ isotopes (^{128}Xe, ^{130}Xe, ^{132}Xe, ^{134}Xe, ^{136}Xe) which are not resolved because a pulse length of $40 - 60$ ns was chosen for these measurements which offers the best SNR (see Section 5.3.1). The weaker lines correspond to transitions between the hyperfine components of the nd and 33f levels of the isotopes ^{129}Xe ($I = 1/2$) and ^{131}Xe ($I = 3/2$).

The hyperfine structure of the spectra changes only slightly with n because all transitions have the same final states and the hyperfine intervals in the initial state result primarily from the hyperfine structure of the ions [30]. Consequently, the assignment of the lines labeled 1-8 in Figure 5.5 is the same as presented for the 33f $\leftarrow$ 31d transitions in Table 5.1, and the lines 9 and 10 correspond to the 33f$[3/2]_2(5/2) \leftarrow$ 21d$[3/2]_1(5/2)$ transition of ^{131}Xe and the 33f$[3/2]_1(3/2) \leftarrow$ 21d$[3/2]_1(1/2)$ transition of ^{129}Xe, respectively. The SNR of the spectra displayed in Figure 5.5 decreases rapidly beyond 350 cm^{-1} ($\sim$ 11 THz) primarily because the intensity of the VUV radiation used to prepare initial states with n below 20 rapidly decreased. The intensities of Rydberg-Rydberg transitions decrease with increasing Δn value [38]. This decrease is almost entirely compensated by the fact that the power of the THz radiation increases with increasing frequency [26]. The spectra were recorded for several pulse lengths between 10 ns and 400 ns, the latter pulse length resulting in an optimal resolution of $\sim$3 MHz over the entire THz frequency range. Indeed, the Doppler width in our supersonic Xe beam is smaller than the laser bandwidth even at

Table 5.3: Observed and calculated frequencies of the $33f[3/2]_2 \leftarrow nd[3/2]_1$ and $33f[5/2]_2 \leftarrow nd[3/2]_1$ transitions for $n = 16, 17, 18, 21, 29, 30$ and 31. The calculated frequencies were obtained using the set of MQDT parameters reported in Ref. [30].

	$33f[3/2]_2 \leftarrow nd[3/2]_1$		$33f[5/2]_2 \leftarrow nd[3/2]_1$	
n	ν_{exp} / THz	$(\nu_{exp} - \nu_{calc})$ / MHz	ν_{exp} / THz	$(\nu_{exp} - \nu_{calc})$ / MHz
31	0.938 741 2(67)[a]	21.7	0.943 292 7(97)[a]	−3.0
30	1.229 493(26)[b]	−11.2	1.234 074(20)[a]	−6.1
29	1.553 439(11)	4.2	1.557 995(14)[a]	−15.7
21	6.284 561 9(28)	49.8	-	-
18	10.154 203 9(72)[b]	99.9	10.158 762 0(73)[b]	81.8
17	11.993 391 3(45)	133.9	11.997 950 4(49)	116.9
16	14.245 138 7(49)[b]	182.1	-	-

[a] Values obtained from several measurements of the transition frequency, however, without separate locking of the fixed-frequency laser.
[b] Only one measurement of transition frequency was performed.

the highest frequencies (14.3 THz).

5.3.3 Mass-Selectivity

Panel a) of Figure 5.6 shows that the main naturally occurring isotopes of Xe can be resolved by time-of-flight (TOF) mass spectrometry following pulsed field ionization of the Rydberg states and demonstrates the possibility of simultaneously recording mass-selective spectra of these isotopes, as presented in panels b)-d) of Figure 5.6. Spectra of ^{128}Xe, ^{130}Xe, ^{134}Xe and ^{136}Xe (all of them isotopes with $I = 0$) are not depicted here because the transition frequencies are the same as for ^{132}Xe within our experimental resolution. Spectra of ^{129}Xe ($I = 1/2$) and ^{131}Xe ($I = 3/2$) have more transitions because of the hyperfine structure. The ability to obtain separate spectra of the different isotopes facilitates the spectral assignments.

5.3.4 Comparison to Calculated Transition Frequencies

The results of the measurements of the $33f[3/2]_2 \leftarrow nd[3/2]_1$ and $33f[5/2]_2 \leftarrow nd[3/2]_1$ transitions of ^{132}Xe are presented in Table 5.3, where they are compared with the results of MQDT calculations based on the MQDT parameter set reported in Ref. [30]. A complete list of all observed transitions, including those of ^{129}Xe and ^{131}Xe, is provided in Table A.2 of the Appendix A.2. Whereas the deviations between measured and calculated frequencies

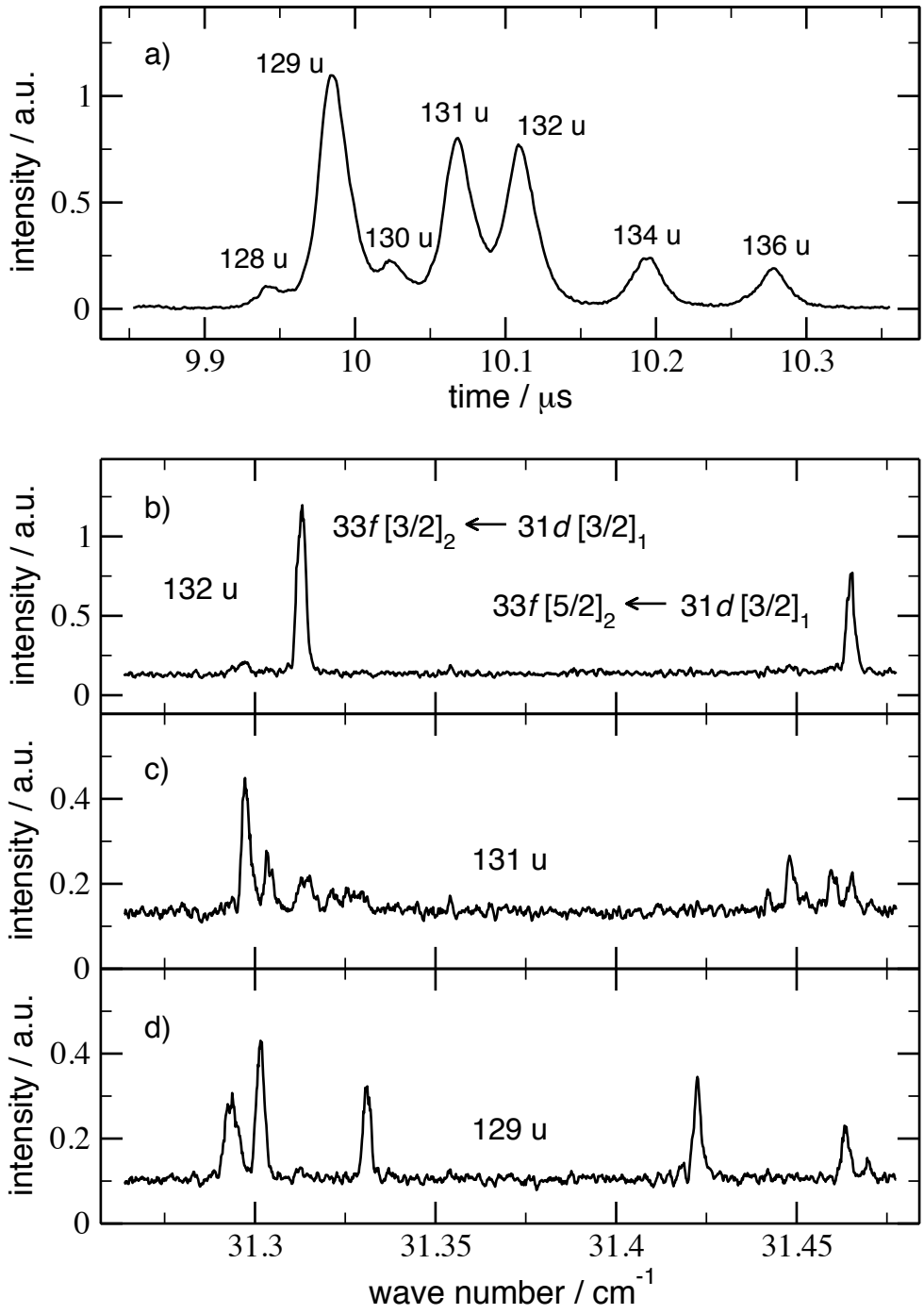

Figure 5.6: a) Time-of-flight (TOF) spectrum of Xe^+ ions formed following photoionization above the $^1S_0 \rightarrow {}^2P_{3/2}$ ionization threshold. b) Spectra of the 33f ← 31d transitions of ^{132}Xe (b), ^{131}Xe (c), and ^{129}Xe (d) recorded following selective field ionization of the 33f level and measuring the ion signal at the relevant TOF position.

are of the same order of magnitude as the experimental uncertainty of our measurement at n values between 29 and 33, they become significantly larger at lower n values. The good agreement at high n values is expected because the MQDT parameters used for the comparison were derived from very-high-resolution millimeter-wave spectroscopic measurements at n values beyond 40. The increasing disagreement at lower n values (and therefore at lower energies) suggests that the energy dependence of the MQDT eigen-quantum defects might be improved using the present data set.

5.4 Conclusions

The THz radiation source and VUV-THz double-resonance spectrometer presented above are well-suited for high-resolution atomic and molecular spectroscopy. Its narrow bandwidth ($\sim$3 MHz) and broad tunability ($0.1 - 14.3$ THz) make this radiation source ideal for investigations of rotational transitions in light molecules, low-frequency vibrational transitions in large molecules and clusters, and Rydberg-Rydberg transitions in a range of principal quantum numbers where high-resolution spectroscopic data are still rare. Moreover, the 25 Hz repetition rate of the pulsed supersonic beam in combination with detection of terahertz transitions by photoionization opens up the possibility of mass-selective spectroscopy.

Chapter 6

First rotational interval of para-H_2^+ by Rydberg spectroscopy of H_2

6.1 Introduction

H_2^+ is the simplest stable molecule, consisting of two protons and one electron. It exists as two nuclear-spin isomers, ortho-H_2^+, in which the two proton spins are aligned parallel to one another, and para-H_2^+, with an antiparallel alignment. As a three-particle system, its energy level structure can be calculated to extremely high precision by quantum chemical methods [140–142]. The most recent calculations include relativistic corrections and quantum electrodynamics corrections up to terms proportional to α^8 [143, 141], where α is the fine-structure constant. For instance, the first vibrational interval in H_2^+ and HD^+ (65 688 323.708 (2) MHz and 57 350 154.371 (2) MHz, respectively) are believed to be accurate to within 2 kHz. Other rovibrational intervals are calculated with uncertainties of at most 15 kHz for transitions involving vibrational levels below $v^+ = 8$. H_2^+, HD^+ and D_2^+ are thus the molecules with the most precisely known energy-level structure.

Paradoxically, H_2^+ is the molecular system that is most resistant to spectroscopic investigations. Not only does its positive charge prevent the generation of significant concentrations in the gas phase, but, more importantly, the absence of a permanent electric dipole moment ($\vec{\mu}(H_2^+) = 0$ and $d\mu(H_2^+)/dR = 0$) implies that H_2^+ has neither a pure rotational nor a rovibrational spectrum in the electric-dipole approximation. Moreover, H_2^+ does not have bound excited electronic states except the $(1\sigma_u)^1\ A\,^2\Sigma_u^+$ state, which has a shallow potential well at large internuclear distance. Because of the Franck-Condon principle, the transitions to bound levels of the $A\,^2\Sigma_u^+$ electronic state are only possible from the highest vibrational levels of the $X\,^2\Sigma_g^+$ ground state. Consequently, the low rotational and vibrational levels of the $X\,^2\Sigma_g^+$ ground state of H_2^+ and D_2^+ are virtually unobservable by optical spectroscopy. The spectroscopic data available to date on H_2^+ are limited to:

(i) Studies by Carrington and his coworkers of the electronic spectrum of the $X^+ - A^+$ transitions, which, as mentioned above, only provides information on the highest vibrational level of the X^+ state ($v^+ = 18$ and 19) [144]. Because of this very unusual situation, the observable electronic spectrum of H_2^+ lies in the microwave range of the electromagnetic spectrum.

(ii) Studies by Jefferts [145, 146] of the magnetic-dipole spectrum connecting the different spin-rotation components of the $N^+ = 2$ rotational levels of the $X\,^2\Sigma_g^+$ ($v^+ = 4 - 8$) states of para-H_2^+ and the different hyperfine components of the $N^+ = 1$ rotational levels of the $v^+ = 4 - 8$ state of ortho H_2^+. These studies only provided the fine and hyperfine structure intervals but not the relative positions of the rovibrational levels.

(iii) Studies by Jungen and Herzberg [91] of the Rydberg spectrum of H_2, from which the positions of the ($v^+ = 0 - 4, N^+ = 0 - 3$) rovibrational levels of H_2^+ could be determined with a precision of about $0.2\,\mathrm{cm}^{-1}$, insufficient to resolve fine or hyperfine structures.

(iv) Measurement of the hyperfine structure of the $v^+ = 0, N^+ = 1$ levels of ortho H_2^+ [31, 147] and para D_2^+ [102] and of the $N^+ = 1 - N^+ = 3$ rotational interval of ortho H_2^+ [148] by millimeter-wave spectroscopy of Rydberg-Rydberg transitions.

(v) Studies of the photoelectron spectrum of H_2, starting with the work of Åsbrink [149], who was the first to partially resolve the rotational structure by recording a Ne I photoelectron spectrum (resolution in the range $40 - 80\,\mathrm{cm}^{-1}$). Later measurements by PFI-ZEKE photoelectron spectroscopy enabled a higher resolution down to about $1\,\mathrm{cm}^{-1}$ [150], and for almost all bound vibrational levels of H_2^+ [151].

(vi) Measurements of the ($v^+ = 0, N^+ = 0$) to ($v^+ = 4, N^+ = 1$) and the ($v^+ = 0, N^+ = 0$) to ($v^+ = 0, N^+ = 1$) transitions of HD^+, which has a small permanent electric dipole moment and thus weak pure rotational and vibrational spectra, have also been reported [152, 153]. The frequency of the ($v^+ = 0, N^+ = 0$) to ($v^+ = 1, N^+ = 1$) transition was determined to be 58 605 052.000(64) MHz [153] and found to deviate by $2.6\,\sigma$ from the calculated value (58 605 052.156 (2) MHz [141]), a discrepancy attributed to unknown systematic errors. The $N^+ = 0$ to $N^+ = 1$ pure rotational transition in HD^+ was detected [152] but its frequency was not reported.

This chapter presents the first experimental determination of the $N^+ = 0 \rightarrow N^+ = 2$ rotational interval of the $X\,^2\Sigma_g^+(v^+ = 0)$ ground state by THz spectroscopy, exploiting rotational channel interactions between Rydberg states of H_2. Rydberg series in H_2 converge on different rovibrational levels of the molecular cation and the Rydberg formula for H_2 (ignoring spins) describes these series approximately as

$$\tilde{\nu} = \frac{E_i(H_2)}{hc} + \frac{E^+(v^+, N^+)}{hc} - \frac{R_{H_2}}{(n - \mu_{\mathrm{eff}})^2} \tag{6.1}$$

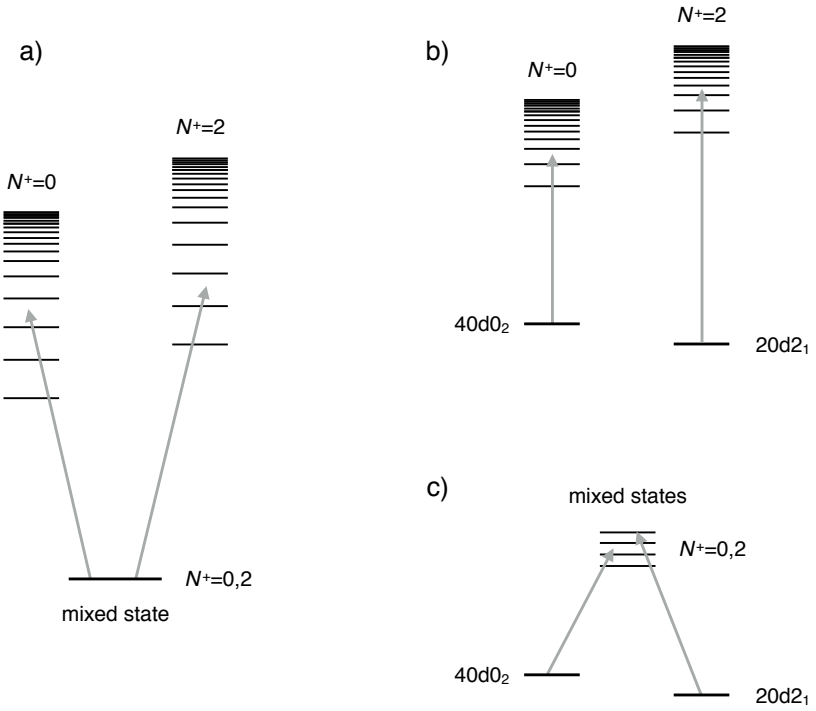

Figure 6.1: Schematic representation of Rydberg series converging on different rotational levels of H_2^+. Panel a): Excitation of both series from an initial Rydberg level with rotationally mixed character ($N^+ = 0, 2$). Panel b): Excitation of both series from the different starting levels $40d0_2$ (excitation to a series converging on $N^+ = 0$) and $20d2_1$ (excitation to a series converging on $N^+ = 2$). Panel c): Excitation to states with mixed rotational character from the two starting levels of panel b) used to determine their relative energy spacing.

where $E^+(v^+, N^+)$ are the ionic rovibrational energies relative to the $(v^+ = 0, N^+ = 0)$ level of the $X^+\,^2\Sigma_g^+$ ground state of H_2^+ and the adiabatic ionization energy of H_2 is equal to $E_i(H_2)/(hc) = 124\,417.4911\,(4)\,\mathrm{cm}^{-1}$ [98]. The notation used to label high Rydberg states of H_2 throughout this chapter is nlN_N^+, where n is the principal quantum number and l the orbital angular momentum quantum number of the Rydberg electron, $\vec{N}^+$ the overall angular momentum of the ion core and $\vec{N} = \vec{N}^+ + \vec{l}$ the total angular momentum of para-H_2. It is possible to excite H_2 to an initial Rydberg state of mixed rotational character ($N^+ = 0, 2$) resulting from a channel interaction between series converging on two different rotational states of the ion. From excitation to Rydberg series converging on the rovibrational ground state of H_2^+ and Rydberg series converging on a rovibrationally excited state of H_2^+ from the same initial Rydberg state (see panel a) of Figure 6.1 for a schematic representation of the excitation sequence), it is possible to directly determine the rovibrational level spacing by extrapolation of the two Rydberg series to their ionic limits and calculating their difference. Transitions to both series become allowed because of the mixed rotational character of the starting level, even though transitions between Rydberg states typically do not change the rotational character of the ion core.

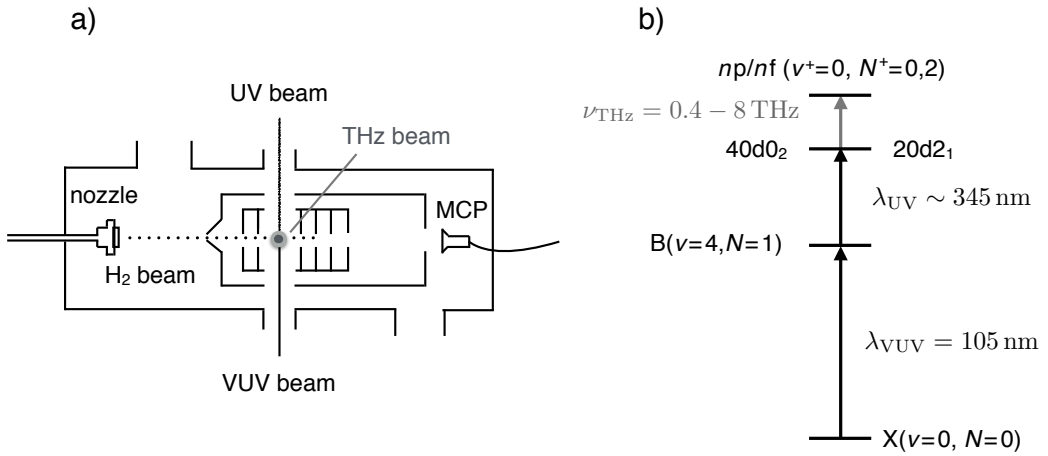

Figure 6.2: Panel a): Schematic representation of the experimental configuration used for excitation of the supersonic beam of H_2 molecules. Panel b): Excitation sequence used to access Rydberg series converging on either of the two lowest-lying rotational levels of para-H_2^+.

The method chosen here involves the extrapolation of two Rydberg series converging on different rotational states of the ion, accessed from two different initial states (see panel b) of Figure 6.1), the $40d0_2$ and $20d2_1$ Rydberg states. The spacing between the $20d2_1$ and $40d0_2$ initial states was extracted from measurements of transitions to the same set of $np N_1^+$ ($N^+ = 0, 2$) states with rotationally mixed character from both initial states (see panel c) of Figure 6.1) and determining the relative positions of all energy levels connected by the transitions in a least-squares fit procedure in a manner similar to the one described in Section 4.3.1. The THz radiation source described in detail in Chapter 2 was ideally suited for this purpose because of its narrow bandwidth and broad tunability, making it possible to access a large range of states converging on the $N^+ = 0$ and $N^+ = 2$ ionization thresholds and requiring frequencies between 0.4 and 7.5 THz.

6.2 Experimental

VUV radiation near $\lambda = 105\,\text{nm}$ was used to excite molecular hydrogen from its $X\,^1\Sigma_g^+$ ground state ($v = 0, N = 0$) to its $B\,^1\Sigma_u^+(v = 4, N = 1)$ state. Tunable VUV radiation in this region was generated by sum-frequency mixing ($\nu_{\text{sum}} = 2\nu_{\text{UV}} + \nu_{\text{VIS}}$) making use of the $(5p)^5\left(^2P_{3/2}\right)6p[1/2]_0 \leftarrow (5p)^6\,^1S_0$ two-photon resonance of Xe at $\tilde{\nu} = 80\,118.9839\,\text{cm}^{-1}$ described in greater detail in Section 2.7.1. UV and VIS radiation beams used for sum-frequency mixing were generated by two Nd:YAG-pumped, pulsed dye lasers, the frequency output of one of which was doubled to generate $\lambda_{\text{UV}} \sim 250\,\text{nm}$ for the two-photon resonance. UV radiation between $340 - 348\,\text{nm}$ created by the frequency-doubled output of a third, pulsed dye laser pumped by the same Nd:YAG laser was then used to excite

from the $B(v = 4, N = 1)$ state to an initial $40d0_2$ or $20d2_1$ Rydberg state (see panel b) of Figure 6.2). Radiation between 0.4 and 8 THz was then used to excite to $np0_1$ or $nf0_3$ Rydberg states starting from the $40d0_2$ state and converging on the rovibrational ground state $X^+\,^2\Sigma_g^+$ ($v^+ = 0, N^+ = 0$) of H_2^+, or to $np0_1$, $np2_1$ and $nf2_2$ states starting from the initial $20d2_1$ state and converging on the first rotationally excited state of H_2^+ ($v^+ = 0, N^+ = 2$), as shown schematically in panel b) of Figure 6.2. Pulsed, tunable THz radiation was generated by difference-frequency mixing in a DAST crystal of the near-infrared (NIR), pulse-amplified output of two narrow-band, Nd:YVO_4-pumped Ti:Sa ring lasers (see Section 2.1 for details). The cw outputs of these Ti:Sa ring lasers were converted into pulses by two acousto-optic modulators, and then pulse-amplified in Nd:YAG-pumped Ti:Sa crystals using a multi-pass bow-tie configuration to generate pulse energies of $\sim$ 8mJ and THz pulse energies of about $\sim$ 15 nJ. For these measurements, NIR pulse lengths were typically set to $\sim$ 40 ns, corresponding to THz bandwidths of $\sim$ 15 MHz (see Table 5.2). Tunable THz radiation was generated by fixing the frequency of one NIR ring laser while tuning the frequency of the second NIR ring laser.

Figure 6.2 shows a schematic representation of the experimental chamber used for the H_2 experiments and indicates the propagation directions of the different laser beams involved in the excitation process. A supersonic beam of H_2 molecules was generated by expansion into vacuum of pure H_2 through the orifice of a pulsed nozzle that was operated at a repetition rate of 25 Hz and a stagnation pressure of $\sim$ 3 bar. The innermost part of the beam was then selected with a skimmer, allowing for selection of molecules having only a small velocity component perpendicular to the propagation direction of the supersonic beam. THz, VUV and UV radiation beams intersected the supersonic beam in a perpendicular configuration (see Figure 6.2) which allowed for a strong reduction of Doppler broadenings. The excitation region, marked by the intersection of all afore-mentioned beams, was surrounded by a set of resistively coupled extraction plates that were used for selective field ionization of the final Rydberg states. They served the additional purpose of accelerating the generated H_2^+ ions towards a micro-channel plate (MCP) detector, after having been separated from H^+ fragment ions in the time-of-flight (TOF) region. This entire region was surrounded by two sets of concentric mumetal tubes to shield the experimental and TOF regions from magnetic fields. Stray electric fields that were present in the excitation region were minimized by applying small dc compensation fields along the symmetry axis of the electrode stack, as described in detail in Section 2.7.4. The quadratic shift of the transition frequency resulting from the Stark effect was measured as a function of the applied dc electric field. The field strength for which this shift was minimal could be determined and therefore the stray field minimized.

The electric field applied for the detection of the final Rydberg state consisted of a sequence of two pulses, separated in time by 1 μs, the first pulse having been applied about 400 ns after THz excitation. The THz excitation pulse was applied 20 ns after the VUV and UV excitation pulses, which were set to overlap in time because of the short lifetime of the

$B(v = 4, N = 1)$ state. The first pulse had an electric field strength of $\sim 13.2\,\mathrm{V/cm}$ and the second pulse a strength between $79 - 132\,\mathrm{V/cm}$, depending on the principal quantum number of the final Rydberg state. The field strengths of the pulses and their lengths were determined by optimizing the SNR of the recorded transitions. The first pulse served the purpose of extracting prompt ions and separating them in time from ions generated by the selective field-ionization pulse. Spectra were obtained by monitoring the H_2^+ signal generated at the MCP detector as a function of the frequency of the THz radiation.

A fraction of the output of both the tunable and fixed-frequency ring lasers was directed to a frequency stabilization and calibration setup. The absolute frequency of both lasers was determined by Doppler-free saturation spectroscopy of I_2 as described in Section 2.5.3. The relative frequency calibration was performed by recording the transmission spectrum through a confocal Fabry-Perot etalon (FSR = 149.963(3) MHz, finesse = 30) that was length-stabilized using a HeNe laser (see Section 2.5.1). The frequency of the frequency-fixed ring laser was actively stabilized to a transmission maximum of the same Fabry-Perot etalon, as described in Section 2.5.2.

6.3 Rotational spacing and binding energies of the $20d2_1$ and $40d0_2$ Rydberg states of H_2

Panel a) of Figure 6.3 shows the possible p and f Rydberg series converging on the two lowest rotational levels of para-H_2^+. Considering that $\vec{N} = \vec{N}^+ + \vec{l}$, only one p series, with $N = 1$, and one f series, with $N = 3$, are possible for $N^+ = 0$. For the $N^+ = 2$ threshold, p series with $N = 1, 2, 3$, and f series with $N = 1, 2, 3, 4, 5$ exist (see Figure 6.3). Because of the $\Delta N = 0, \pm 1$, $\Delta N^+ = 0$ and $\Delta l = \pm 1$ selection rules, only the $n\mathrm{p}0_1$ and $n\mathrm{f}0_3$ Rydberg series are accessible from the $40\mathrm{d}0_2$ state by THz excitation. Transitions to both series were recorded: In the case of the $n\mathrm{f}0_3$ and $n\mathrm{p}0_1$ series, Rydberg states with principal quantum number between $n = 45 - 80$ and levels with $n = 47 - 64$ could be observed, respectively. Starting from the $20\mathrm{d}2_1$ state, the $n\mathrm{p}2_1$,$n\mathrm{p}2_2$, $n\mathrm{f}2_1$ and $n\mathrm{f}2_2$ Rydberg series are accessible, as shown in full color in Figure 6.3. For the determination of the rotational interval in para-H_2^+, the energy spacing between the $20\mathrm{d}2_1$ and $40\mathrm{d}0_2$ states needed to be determined. This was achieved by measuring transitions from both states to $n\mathrm{p}0_1$ states in the range between $n = 54 - 58$, where the $n\mathrm{p}0_1$ series strongly interacts with the $23\mathrm{p}2_1$ level, as shown in Figure 6.3 and 6.4. Some transitions originating from the $20\mathrm{d}2_1$ state display a broader linewidth than their counterparts originating from the $40\mathrm{d}0_2$ state. The reason for this difference is that larger NIR pulse intensities had to be used in these cases, leading to a decrease in the NIR pulse length and thus to a broader bandwidth (see Section 5.3.1 for a discussion of this effect).

Many $n\mathrm{p}0_1$ states lie in the energetic vicinity of perturbing states belonging to the $n\mathrm{p}2_1$

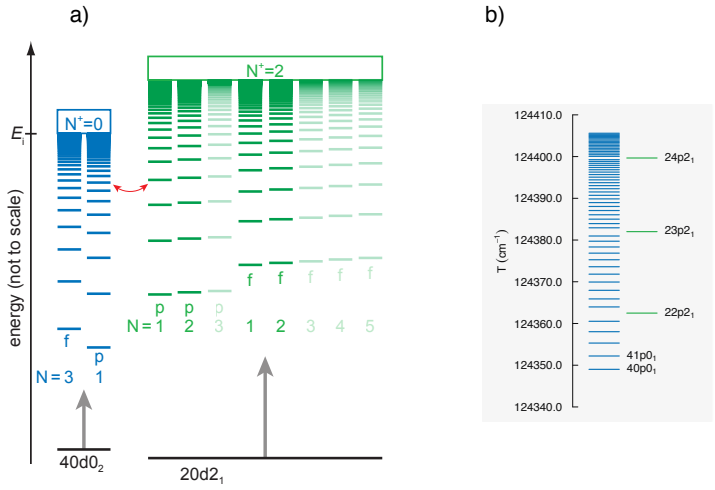

Figure 6.3: Panel a) p and f Rydberg series converging on the $N^+ = 0$ and $N^+ = 2$ ionization thresholds. Excitation to series colored opaque are forbidden by selection rules. Panel b) Relative energies $E = hc\,\mathrm{T}$ of selected states belonging to $n\mathrm{p}0_1$ and $n\mathrm{p}2_1$ Rydberg series.

Rydberg series that converges on $N^+ = 2$. For symmetry reasons, $n\mathrm{p}0_1$ and $n\mathrm{p}2_1$ Rydberg series can interact. In the proximity of the perturbers, states within the $n\mathrm{p}0_1$ series exhibit a mixed rotational character of the ion core ($N^+ = 0, 2$). Panel b) of Figure 6.3 shows the calculated energies of the $n\mathrm{p}0_1$ series (blue lines) and the $22\mathrm{p}2_1$, $23\mathrm{p}2_1$ and $24\mathrm{p}2_1$ perturbers (shown in green) relative to the ground state energy. States of mixed $N^+ = 0$ and $N^+ = 2$ character can be excited from both the $40\mathrm{d}0_2$ and $20\mathrm{d}2_1$ states. Because of this interaction, the transition from the $40\mathrm{d}0_2$ state to the $23\mathrm{p}2_1$ state should also be observable (see Figure 6.4), but this was not the case within the sensitivity limits of our experimental method.

Similarly, interactions between $n\mathrm{f}0_3$ and $n\mathrm{f}2_3$ Rydberg series take place and transitions from the $40\mathrm{d}0_2$ state to $22\mathrm{f}2_3$ and $23\mathrm{f}2_3$ Rydberg states were observed (underlined levels in Table 6.1). The fact that these transitions could be observed while a $23\mathrm{p}2_1 \leftarrow 40\mathrm{d}0_2$ transition could not be observed is attributed to the greater transition strengths associated with transitions to $n\mathrm{f}$ Rydberg states ($\Delta l = \Delta N$ transitions were observed to be particularly strong, see Section 6.4). In contrast to the interacting $n\mathrm{p}0_1$ and $n\mathrm{p}2_1$ states, $n\mathrm{f}0_3$ and $n\mathrm{f}2_3$ states cannot be excited from the $20\mathrm{d}2_1$ initial state because they are forbidden by the $\Delta N = 0, \pm 1$ selection rule. Consequently, they could not be used for a determination of the energy spacing $\Delta E_{40,20} = h\Delta\nu_{40,20}$ between $20\mathrm{d}2_1$ and $40\mathrm{d}0_2$ states, despite their mixed $N^+ = 0$ and $N^+ = 2$ ion-core character.

Table 6.1 lists all energy levels in para-H_2 observed in the realm of the measurements presented here, along with their assignments. Because the number of transitions observed in the spectra exceeded the number of energy levels connected by them (altogether 44 levels), the relative positions of all levels were fitted to the observed transition frequencies in

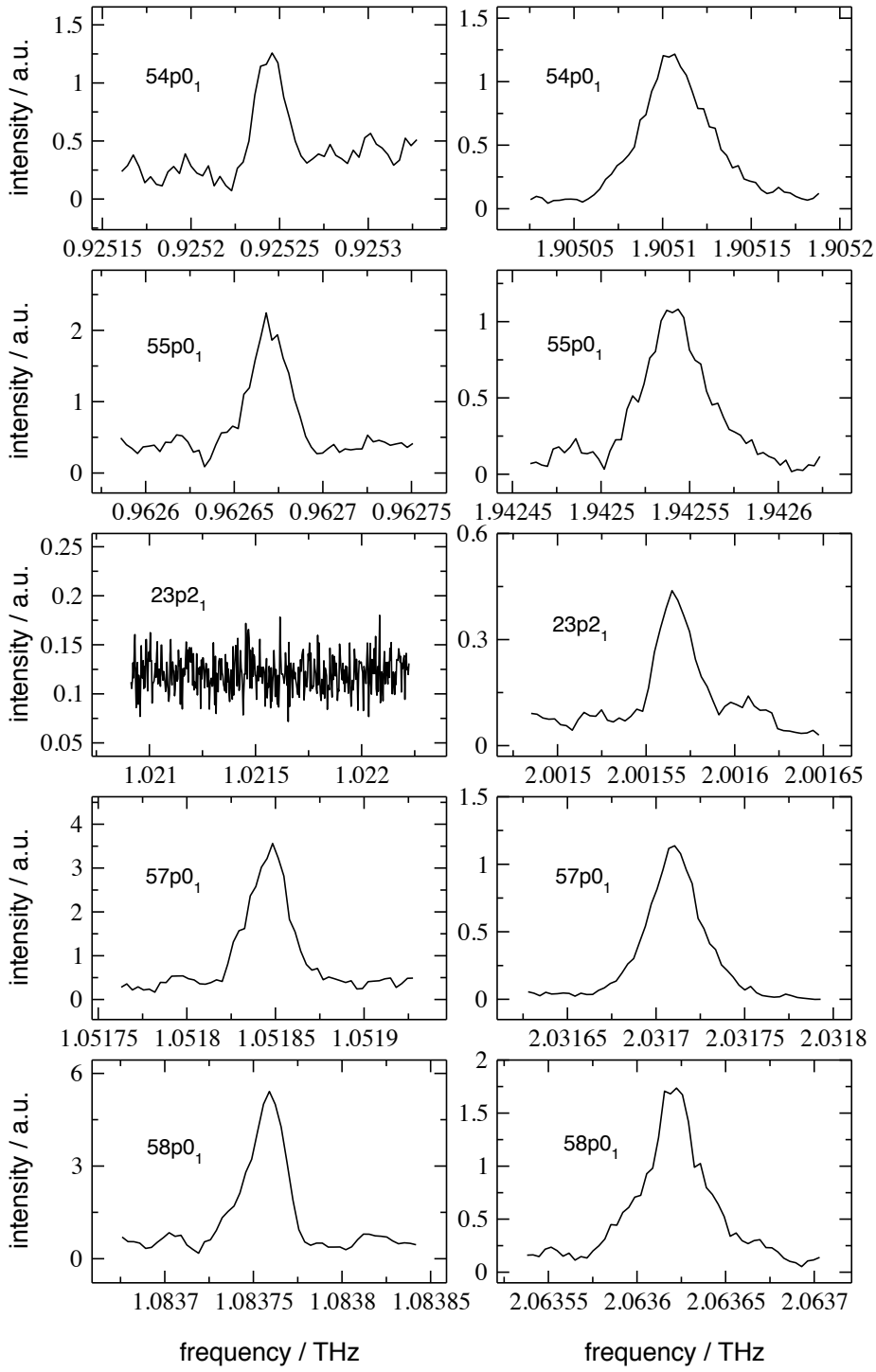

Figure 6.4: Left column: transitions from the $40d0_2$ state to $np0_1$ Rydberg states. Right column: transitions from the $20d2_1$ state to $np0_1$ Rydberg states.

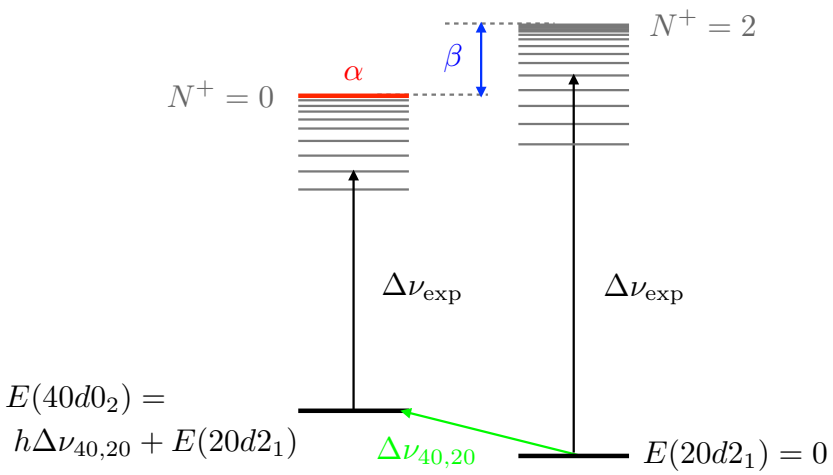

Figure 6.5: Schematic representation of the scheme used to determine the rotational spacing β.

a least-squares-fitting procedure in a manner similar to the one described in Section 4.3.1. To this end, the origin of the energy scale ($E = 0$) was placed at the position of the $20d2_1$ level because it was the observed level with the lowest energy. The experimental uncertainties of most levels are in the range between 3 and 6 MHz and correspond roughly to a fifth of the full-width at half-maximum of the observed transitions. The energy spacing between the $40d0_2$ and $20d2_1$ states determined from experiment is $\Delta E_{40,20}/hc = 32.684\,693\,(46)\,\mathrm{cm}^{-1}$ (or $\Delta E_{40,20}/h = 979\,862.45\,(57)\,\mathrm{MHz}$, see Table 6.1). Figure 6.5 illustrates how this value was used for the determination of the first rotational interval β. Table 6.1 also lists the deviation of experimental from calculated values, which were obtained from MQDT calculation [34] and make use of the newly determined binding energies of $40d0_2$ and $20d2_1$ states (see below). Generally, the deviations are on the order of a few MHz, although there are three cases where the deviation is markably larger: the $22f2_3$, $23f2_3$ and $23p2_1$ levels, which are underlined in Table 6.1.

Calculated values for the relative energies of all observed states relative to the $20d2_1$ state could be obtained from MQDT calculations with the quantum-defect parameter set listed in Appendix F of the thesis of D. Sprecher [44]. While the calculated binding energies for high members of the p and f series ($n > 50$) are expected to be accurate to better than 1 MHz, the accuracy with which the energies of the d Rydberg states, particularly the $20d2_1$ state, can be calculated is several orders of magnitude lower. To obtain β, the experimentally determined value for $\Delta E_{40,20}$ was used and the values of the energies of the first ($E_{N^+=0} = \alpha$) and second ($E_{N^+=2} = \alpha + \beta$) ionization thresholds relative to the $20d2_1$ state were determined from the experimental data by minimizing the difference between the experimental level energies and those calculated by MQDT as a function of α and β in a least-squares-fit procedure [43]. This procedure yielded a value of $\beta = 174.236707(96)\,\mathrm{cm}^{-1}$ (or $5\,223\,485.1(2.9)\,\mathrm{MHz}$), which is in perfect agreement with

Table 6.1: Measured energies in para-H_2^+ relative to the $20d2_1$ state. Uncertainties resulting from fits of the line centers of observed transitions and from the determination of the line centers of the Doppler-free I_2 transitions of both lasers are given in parentheses (see Section 6.6).

level	E_{exp}/h THz	$(E_{\mathrm{exp}}-E_{\mathrm{calc}})/h$ MHz	level	E_{exp}/h THz	$(E_{\mathrm{exp}}-E_{\mathrm{calc}})/h$ MHz
$20d2_1$	0.000 000 0(13)	0	$47p0_1$	1.552 261 0(31)	−1.0
$40d0_2$	0.979 862 45(57)	0	$48p0_1$	1.611 844 4(31)	−3.9
$45f0_3$	1.412 939 7(31)	10.0	$49p0_1$	1.668 371 4(31)	−3.2
$\underline{22f2_3}$	$\underline{1.463\,059\,8(32)}$	$\underline{237}$	$51p0_1$	1.772 028 4(38)	−7.4
$46f0_3$	1.483 155 2(31)	0.5	$52p0_1$	1.819 358 6(41)	−9.3
$47f0_3$	1.548 464 0(31)	10.6	$53p0_1$	1.863 778 4(33)	−3.1
$48f0_3$	1.609 837 6(31)	10.4	$54p0_1$	1.905 106 6(26)	−3.7
$49f0_3$	1.667 510 0(32)	9.7	$55p0_1$	1.942 543 3(31)	6.4
$51f0_3$	1.772 848 5(34)	1.7	$\underline{23p2_1}$	$\underline{2.001\,566\,0(48)}$	$\underline{19.3}$
$52f0_3$	1.821 025 0(32)	3.0	$57p0_1$	2.031 709 4(27)	1.6
$53f0_3$	1.866 497 5(31)	1.6	$58p0_1$	2.063 620 6(28)	6.0
$54f0_3$	1.909 472 3(15)	6.6	$59p0_1$	2.095 141 0(32)	4.5
$55f0_3$	1.950 114 4(31)	4.0	$64p0_1$	2.234 745 4(34)	3.0
$56f0_3$	1.988 593 3(32)	4.4	$35f2_2$	5.575 034 7(38)	−6.4
$57f0_3$	2.025 014 4(33)	−9.7	$40f2_2$	6.204 710 9(52)	−7.2
$\underline{23f2_3}$	$\underline{2.043\,722\,8(38)}$	$\underline{31.3}$	$43f2_2$	6.481 757 0(46)	1.3
$58f0_3$	2.059 830 7(36)	−5.9	$44f2_2$	6.561 700 6(57)	−0.5
$59f0_3$	2.092 635 6(33)	8.1	$46f2_2$	6.706 267 0(40)	−1.7
$64f0_3$	2.234 498 1(34)	5.8	$56f2_2$	7.212 021 7(36)	0.9
$69f0_3$	2.346 671 4(38)	5.0	$61f2_2$	7.376 947 5(36)	−4.7
$74f0_3$	2.436 879 5(36)	0.1			
$78f0_3$	2.496 902 4(47)	−3.6			
$79f0_3$	2.510 503 8(40)	−			
$80f0_3$	2.523 594 6(61)	2.5			

the most recent calculated value obtained by quantum chemical methods (174.2367424824 cm^{-1} [141]). From the values of α and β that were thus obtained, the binding energies of the $40d0_2$ and $20d2_1$ states could be determined. The resulting values are $E_{\mathrm{bind}}(20d2_1)/hc = 101.322\,556\,(39)\,\mathrm{cm}^{-1}$ and $E_{\mathrm{bind}}(40d0_2)/hc = 68.637\,863\,(39)\,\mathrm{cm}^{-1}$.

6.4 The np0$_1$ and nf0$_3$ Rydberg series

The evolution of the splitting $\Delta_{\mathrm{p,f}}$ between transitions to nf0$_3$ and np0$_1$ Rydberg states accessed from the 40d0$_2$ initial state is displayed in Figures 6.7 and 6.8. In the range $n = 48 - 64$, the nf0$_3$ Rydberg series remains unperturbed, except between $n = 57$ and 58, where a perturbation by the 23f2$_3$ state takes place. Because f levels are core-non-penetrating, channel interactions involving these levels are very weak and do not induce strong perturbations of level positions and transition intensities. Consequently, the 23f2$_3$ level only leads to a small perturbation in the quantum defects of the nf0$_3$ levels and does not affect the regularity of the observed transition frequencies. The situation is completely different for the p levels: The np0$_1$ series is strongly perturbed by the np2$_1$ series and the strong irregularities in the observed quantum defects resulting from this perturbation can be seen in Figure 6.6. Experimentally determined values (blue crosses) for the quantum defects μ_{eff} of a given state are plotted along with those obtained from MQDT calculation [154] (black circles) as a function of the energy of the state with respect to the $\mathrm{X}\,^1\Sigma_g^+(v = 0, N = 0)$ ground state of H_2. Principal quantum numbers indicated on the upper horizontal axis are given with respect to the $N^+ = 0$ threshold. Experimentally determined values for the quantum defects were calculated from the observed transition wavenumbers $\tilde{\nu}_{\mathrm{obs}}$ in the recorded spectra with the help of Equation 6.1, where the newly determined values for absolute energies of the 40d0$_2$ and 20d2$_1$ states were used (see Section 6.3). In the absence of any perturbers, one would expect a constant value for the quantum defect, as shown by the horizontal, dashed line at $\mu_{\mathrm{eff}} = 0.012$. The energies

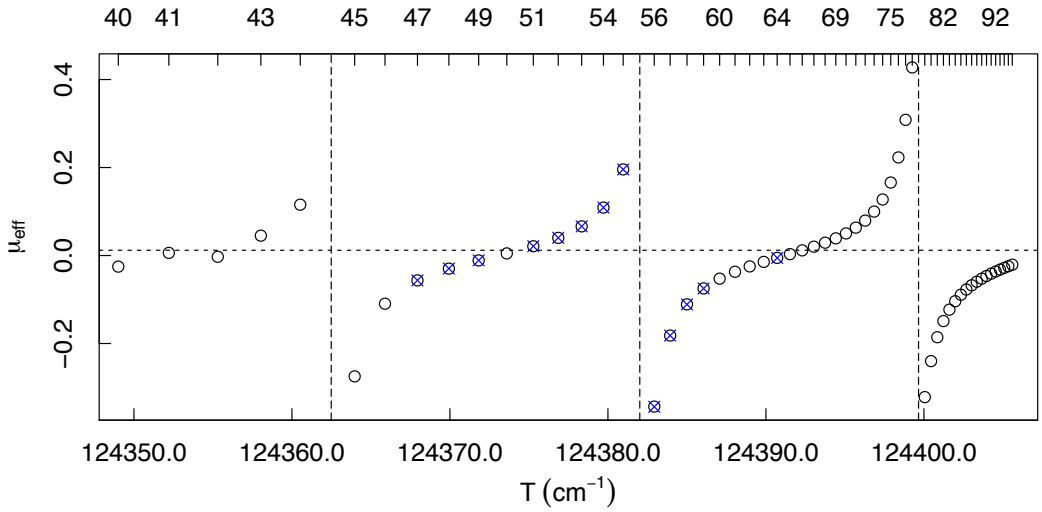

Figure 6.6: Evolution of the effective quantum defect μ_{eff} of the np0$_1$ Rydberg series as a function of principal quantum number n and overall energy $E/hc = \mathrm{T}$. The dashed, vertical lines represent the positions of the np2$_1$ perturbers. Calculated values are marked as black circles, experimental values as blue crosses.

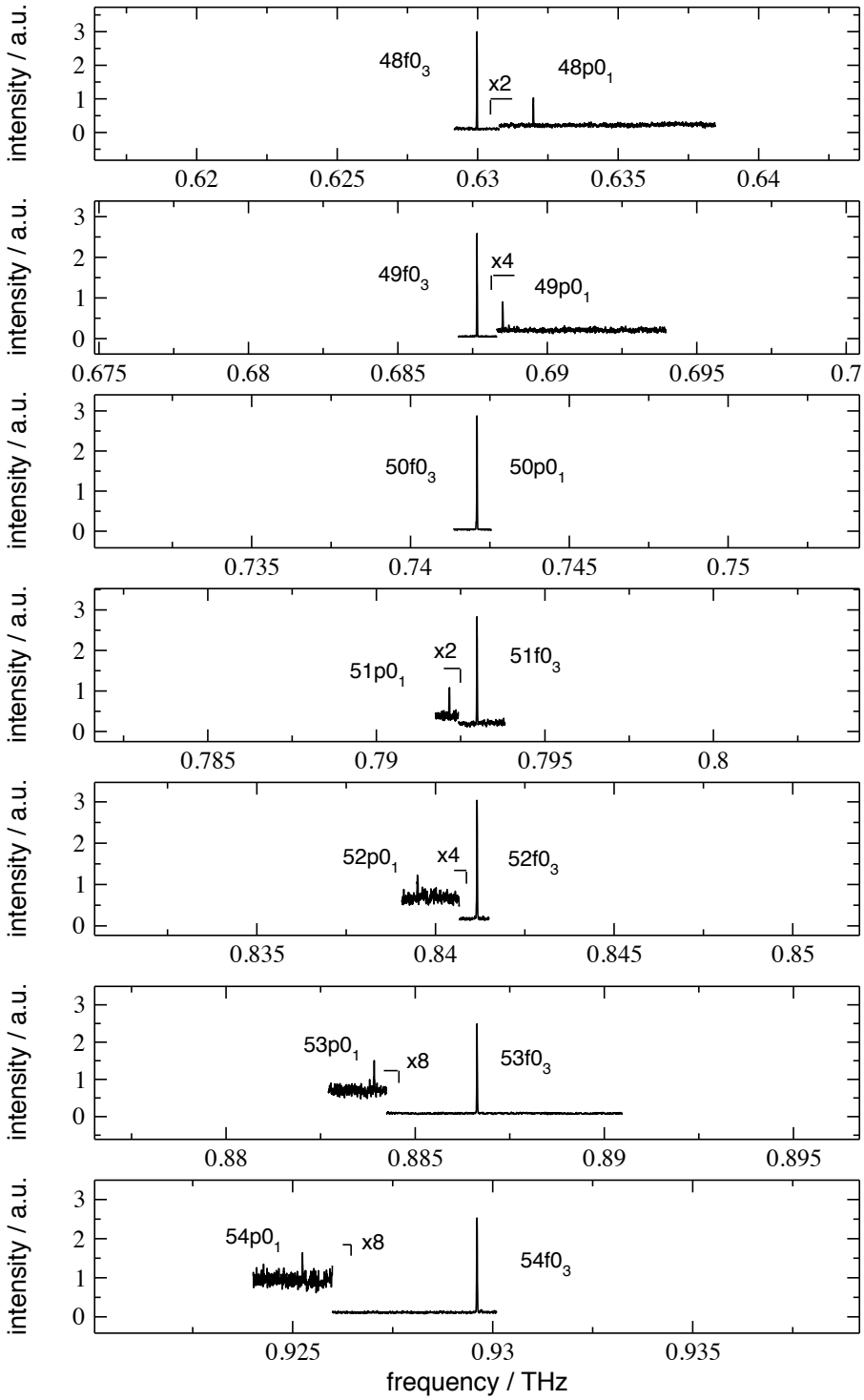

Figure 6.7: Frequency splitting between transitions from the $40d0_2$ state to $nf0_3$ and $np0_1$ Rydberg states.

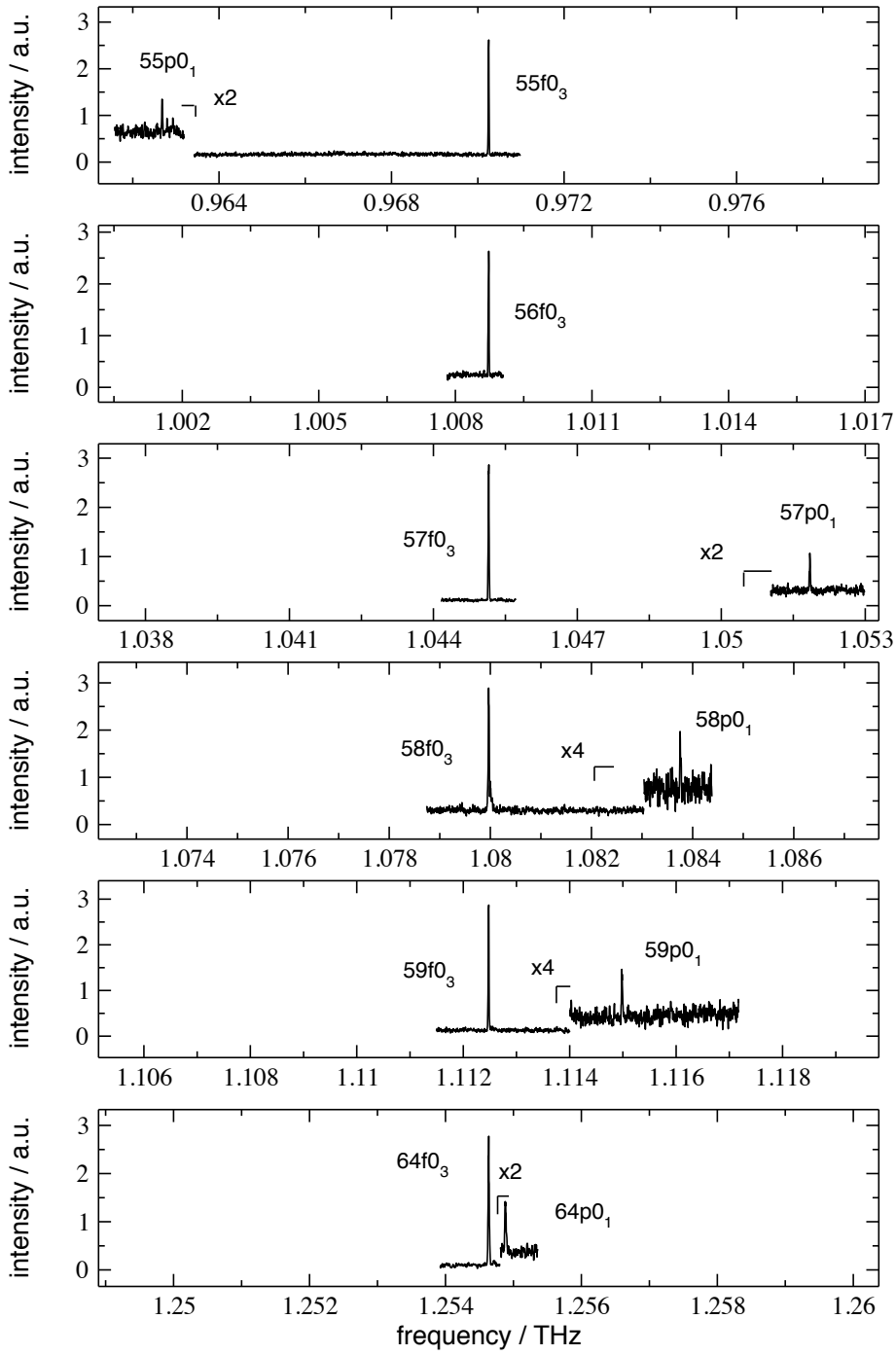

Figure 6.8: Frequency splitting between transitions from the 40d0$_2$ state to nf0$_3$ and np0$_1$ Rydberg states.

of the perturbing states converging on the $N^+ = 2$ threshold of the ion are marked by vertical, dashed lines in Figure 6.6. In their vicinity, the effective quantum defects with respect to $N^+ = 0$ show very strong irregularities. The $n\mathrm{p}0_1$ levels located immediately above (below) the $n\mathrm{p}2_1$ perturbers are shifted to higher (lower) energies and therefore the effective quantum defect $\mu_{\mathrm{eff}} = n^* - n$ is smaller (larger). The overall agreement with the calculated values is excellent.

The transitions to $n\mathrm{f}0_3$ Rydberg states shown in Figures 6.7 and 6.8 exhibit intensities that are typically a factor of $20-30$ stronger than transitions to $n\mathrm{p}0_1$ states. This made it challenging to observe transitions to the p series, particularly in the range $n = 54-58$ used for the determination of $\Delta E_{40,20}$. To record these transitions, the experimental conditions had to be carefully optimized and increased NIR pulse energies had to be used ($\sim 2\,\mathrm{x}$ higher than described in Section 6.2). This led to a broadening of lines because increased pulse energies resulted in shorter NIR (and thus THz) pulse lengths. Indeed, the population inversion of the Ti:Sa gain medium was depleted during the early part of the NIR pulse as it passed through the bow-tie amplifier on its final loop (see Section 2.6 for a description of the amplification system). A list of all observed transitions including assignments and estimated uncertainties can be found in Table A.3 of Appendix A.3. The relative energies of all observed levels, except the $50\mathrm{f}0_3$ and $50\mathrm{p}0_1$ states which could not be resolved, are listed in Table 6.1.

The irregularity in the progression of transition frequencies for the $n\mathrm{p}0_1$ Rydberg series compared to the regular $n\mathrm{f}0_3$ series can clearly be seen in Figures 6.7 and 6.8: Whereas the p level is located $0.066940\mathrm{cm}^{-1}$ above the f level at $n = 48$, the energy separation between these levels gradually becomes smaller and vanishes at $n = 50$, where peaks corresponding to transitions to both states coalesce. At $n = 52$, the separation is negative ($-0.055585\,\mathrm{cm}^{-1}$) and decrease further until $n = 55$, where it is $-0.25254\,\mathrm{cm}^{-1}$. No transition could be detected from the $40\mathrm{d}0_2$ initial state for $n = 56$ within our experimental sensitivity. This is where the perturbation from the $23\mathrm{p}2_1$ Rydberg state to which a transition was observed from the $20\mathrm{d}2_1$ starting level (see Figure 6.4) is strongest (see also panel b) of Figure 6.3). The separation then abruptly becomes positive again at $n = 57$, where it equals $0.223321\,\mathrm{cm}^{-1}$, and once again decreases towards $n = 64$, where it takes a value of $0.008249\,\mathrm{cm}^{-1}$. The energy of this state is located almost exactly in the middle between the $23\mathrm{p}2_1$ and $24\mathrm{p}2_1$ interlopers.

6.5 The $n\mathrm{f}2_2$ Rydberg series

Figure 6.9 displays exemplary spectra resulting from excitation from the $20\mathrm{d}2_1$ state to the $n\mathrm{f}2_2$ Rydberg series in the range between $n = 22 - 70$. All states with $n > 25$ lie above the ionization continuum of the $N^+ = 0$ threshold in energy. Nevertheless, strong transitions were observed in these cases and no effects of fast autoionization could

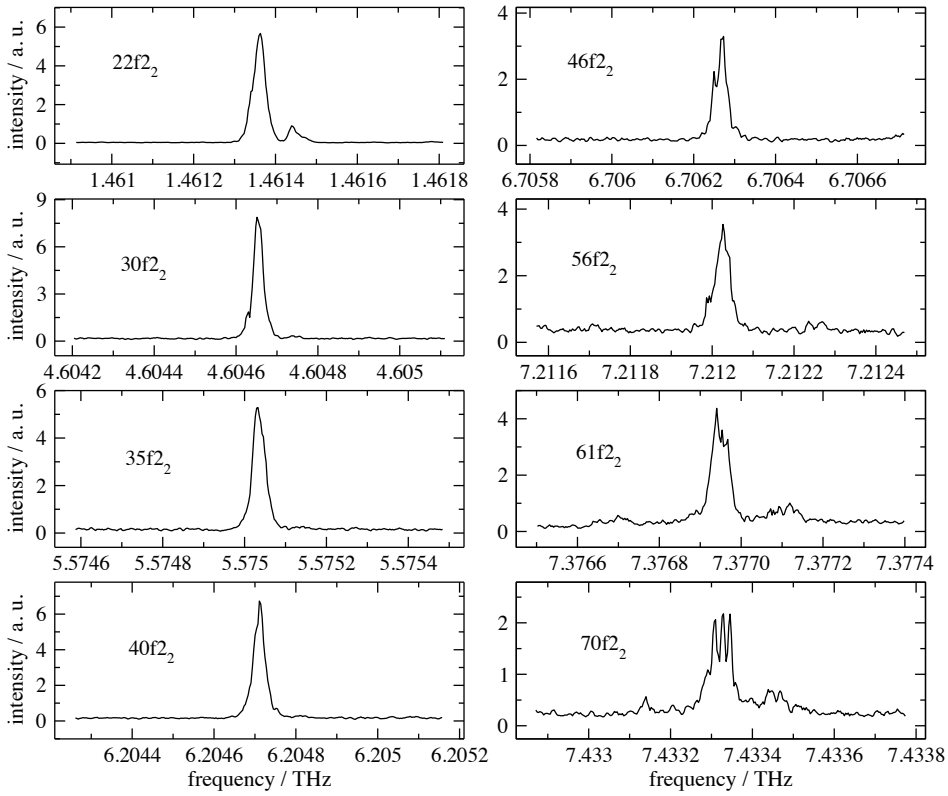

Figure 6.9: Transitions from the $20d2_1$ state to $nf2_2$ Rydberg states.

be detected, which would have been observable by a broadening of transitions to states lying above the ionization continuum. This is attributed to the fact that there are no autoionization channels because there are no p or f series with $N = 2$ series that converge on the $N^+ = 0$ threshold. Figure 6.9 shows that two transitions were observed at $n = 22$, but an unambiguous assignment has so far not been possible. At the highest values of n, a triplet structure starts to evolve that is particularly pronounced at $n = 70$. All observed energy levels except the $22f2_2$ and $70f2_2$ states are listed in Table 6.1 and the corresponding transition frequencies are given in Appendix A.3.

6.6 Frequency calibration and accuracy

Figure 6.10 illustrates the frequency calibration procedure with the example of the $54f0_3 \leftarrow 40d0_2$ transition in para-H_2. While recording the molecular transition (bottom trace of panel a)), a Doppler free iodine absorption spectrum was recorded for absolute frequency calibration (top trace of panel a)). In this case, the a(10), R(36), $B - X(0 - 15)$ transition of I_2 was used and compared to a tabulated value obtained by calculations, the absolute frequency accuracy of which is better than 100 kHz [62]. Simultaneously, a rela-

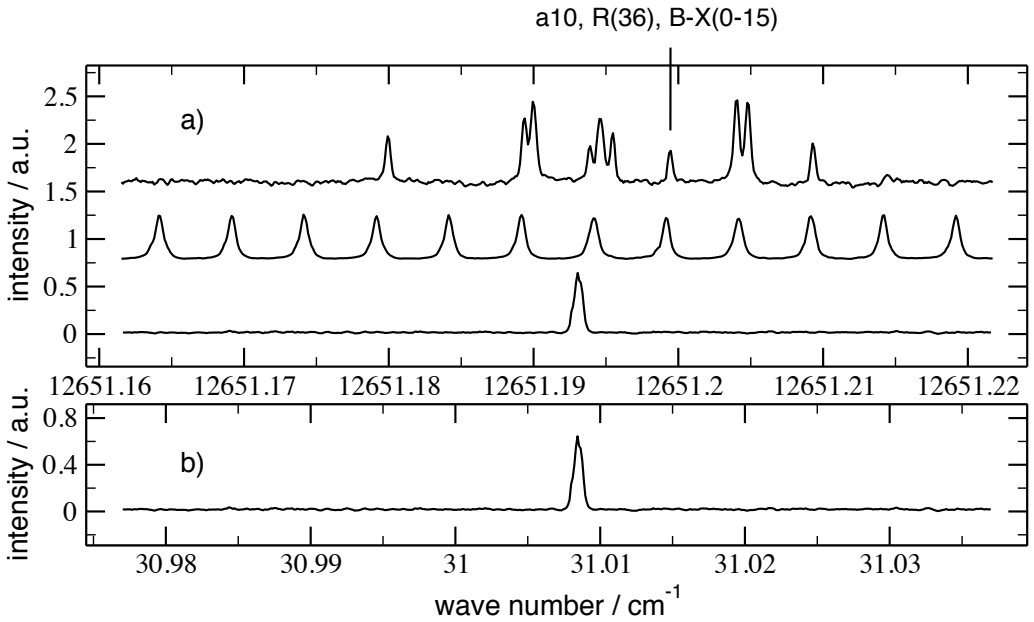

Figure 6.10: Frequency calibration for the $54f0_3 \leftarrow 40d0_2$ transition in H_2. Panel a) Doppler free I_2 absorption spectrum (top trace), etalon transmission spectrum (middle trace) and molecular transition (bottom trace) as a function of the absolute frequency of the tunable ring laser. Panel b) Absolute frequency of the transition obtained by subtraction of the absolute frequency of the fixed ring laser.

tive frequency calibration was performed by recording the transmission spectrum through a length-stabilized, confocal Fabry-Perot etalon with a FSR of 149.963(3) MHz (middle trace in panel a)), which was used for linearization by cubic-spline interpolation. The absolute frequency of the fixed laser was determined in a similar manner by recording Doppler free I_2 absorption and etalon transmission spectra and then determining the absolute frequency of the etalon transmission maximum used for active frequency stabilization (for details concerning the entire frequency calibration process, see Section 2.5). The a(2), P(181), $B - X(0 - 14)$ transition of I_2 was used for the absolute frequency calibration of the fixed-frequency ring laser. This frequency was then subtracted from the absolute frequency of the tunable ring laser to determine the frequency of the THz radiation shown along the horizontal axis in panel b) of Figure 6.10.

The accuracy of the frequency calibration method was assessed by performing measurements of the $54f0_3 \leftarrow 40d0_2$ transition on different days and after separate locking of the fixed-frequency ring laser. This method yielded a value of 0.929 609 8(15) THz for the transition frequency. Figure 6.11 shows these measurements as a deviation from the average transition frequency, the error bars representing a value of $\pm\sigma$. The values appear randomly distributed around the mean transition frequency. σ is composed of the error associated with the uncertainty in the determination of the line centers of the iodine

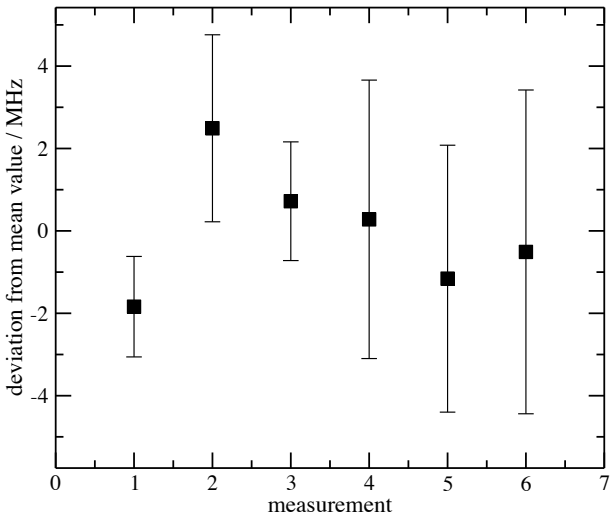

Figure 6.11: Different measurements of $54f0_3 \leftarrow 40d0_2$ transition in H_2 and their deviation from the mean value of 0.929 609 8(15) THz. Error bars represent a deviation of $\pm\sigma$, where σ was determined from the uncertainties in the determination of the line centers as obtained by fit of a Gaussian lineshape and the uncertainties associated with the determination of the line centers of the Doppler-free I_2 transitions.

absorption maxima of both lasers, the uncertainty in the determination of the transition frequency itself by fit of a gaussian lineshape, and the uncertainty in the determination of the position of the etalon transmission maximum. It does not take into account systematic statistical errors such as those described in Section 6.7.

6.7 Error Budget

Apart from the statistical uncertainties in the level positions that resulted from the determination of the line centers of the observed transitions in H_2, the determination of the line centers of the Doppler-free I_2 spectra used for absolute frequency calibration of both NIR lasers and the least-squares-fit procedure used for the determination of their positions, these positions were also subject to possible systematic errors. The following sources of such errors were considered:

(i) DC Stark shifts by residual electric fields
Our measurement procedure involved compensating stray dc electric fields (see Section 6.2), and we estimate the maximal value of the residual field to be 1 mV/cm. From measurements of the Stark effect in $d \rightarrow f$ transitions between $n = 40$ and 51, and by exploiting the n^7 scaling of the polarizability, we estimate the maximal shift for the transitions to be 100 kHz.

(ii) Pressure shift
The pressure shift in high Rydberg states arises primarily from the scattering of the Rydberg electron with neutral atoms and molecules located within the Rydberg orbit [136]. Because the shift is approximately the same for the initial and final states of the measured transitions, its effect on the transition frequencies is negligible (see also discussion in [31]).

(iii) AC Stark shift
An AC Stark shift would lead to a shift of the transition frequencies that is dependent on the intensity of the THz radiation. To determine a possible shift, measurements of the $54f0_3 \leftarrow 40d0_2$ transition were performed for differing NIR (and thus differing THz) intensities. No shift in the transition frequency was observed within the accuracy of the experimental method ($\sim 2.8\,\mathrm{MHz}$, see Section 5.2.3).

(iv) Doppler shifts
Such shifts can be estimated from the velocity component of the supersonic beam along the propagation axis of the THz radiation according to $\nu = \nu_0\,(1 + v/c)$. Because the supersonic beam propagates perpendicularly to the THz radiation beam and the geometric constraints of the experiment limit a possible deviation from a perpendicular arrangement to less than 0.5°, we estimate from the H_2 beam velocity of $2\,500\,\mathrm{m/s}$ the maximal shift to be at most $2.25\,\mathrm{MHz}$ at the highest frequencies ($8\,\mathrm{THz}$) and at most $300\,\mathrm{kHz}$ at $1\,\mathrm{THz}$. This represents the largest source of systematic uncertainty in the present measurements.

Because these sources of systematic uncertainties appear independent, we estimate the overall systematic uncertainty to be $2\,\mathrm{MHz}$.

6.8 Conclusions

From the spectroscopy of high Rydberg states of H_2 it was possible to determine the first rotational interval of para-H_2^+ with a precision of $2.9\,\mathrm{MHz}$ (i.e., $174.236707(96)\,\mathrm{cm}^{-1}$), which was in agreement with the most recent value calculated by quantum chemical methods. To extract this value, the nf Rydberg series accessed from the $20d2_1$ and $40d0_2$ states and converging on the two lowest rotational thresholds were extrapolated using MQDT. These measurements were combined with the measurement of a perturbed np Rydberg series exhibiting a mixed $N^+ = 0$ and $N^+ = 2$ rotational character and which was therefore accessible from both states and enabled us to extract the energy spacing between these two levels. From these values and with the use of calculated level energies by MQDT, the rotational interval was determined.

Chapter 7

Conclusions and outlook

This dissertation has presented a broadly tunable source of far-infrared radiation and its application to the high-resolution spectroscopy of gas-phase samples, with an emphasis on measurements of atomic and molecular Rydberg states. To study Rydberg-Rydberg transitions, the far-infrared source was combined with VUV radiation in double-resonance experiments. These experiments enabled the efficient detection of the far-infrared transitions which, in turn, permitted studies of the ionization channels of Xe and their interactions, and the first measurement of the fundamental rotational interval in para-H_2^+. The source was integrated in a spectrometer allowing for measurements in rotationally and vibrationally cold samples in supersonic beams, under conditions where Doppler and pressure broadenings were minimized. Within this spectrometer, both the THz generation and detection process took place inside vacuum, permitting the elimination of undesirable absorption by water vapor. Mass-selective measurements could be performed that enabled the recording of isotope-selective spectra.

In the realm of the development of the VUV-far-infrared spectrometer, an experimental apparatus for the measurement of sub-millimeter-wave transitions between high Rydberg states was designed, built and fully tested. The properties were characterized by measurements of transitions between Rydberg states of Xe. The experimental application of the VUV-far-infrared spectrometer was demonstrated by a study of Rydberg states of Xe at intermediate n values. The frequency of the far-infrared laser source was shown to be easily adjustable in the region between $0.1 - 15\,\mathrm{THz}$ and to have an absolute accuracy of up to $2.8\,\mathrm{MHz}$ with a bandwidth adjustable between ~ 3 and $85\,\mathrm{MHz}$. From the spectroscopy of high Rydberg states of para-H_2, it was possible to determine the first rotational interval of para-H_2^+. A value of $5\,223\,485.1\,(2.9)\,\mathrm{MHz}$ was found which agrees with the most recent value calculated by quantum chemical methods [140, 141] within the experimental uncertainty of $2.9\,\mathrm{MHz}$. The value was determined from the measurement and extrapolation of nf Rydberg series of para-H_2 converging on the two lowest rotational thresholds of para-H_2^+.

This method of measuring a rotational interval in a molecular ion having no permanent electric dipole moment by Rydberg spectroscopy of the corresponding neutral molecule and extrapolation to the rovibronic levels of the ion is general and could be used to measure rotational intervals in other cations, such as D_2^+, He_2^+, Li_2^+, Be_2^+, etc. In future studies, one may also use the spectrometer for high resolution studies of molecular rotation and vibration in polyatomic molecules and clusters. In this case, the VUV photon would simply serve the purpose of ionizing the sample following the absorption of a far-infrared photon, thus also providing the advantages of high detection efficiency and mass selectivity.

Appendix A

List of transition frequencies between high-n Rydberg states of Xe and H_2

A.1 Observed transitions in high Rydberg states of ^{132}Xe by sub-millimeter-wave excitation

Table A.1: Experimentally observed transition frequencies ν_{exp} as compared to calculated values [30] including observed full-widths at half-maximum Γ_{FWHM} obtained by fit of a Gaussian lineshape. Uncertainties for transition frequencies obtained from fit given in parentheses in units of the last two digits. Signal-to-noise ratios (SNR) and assignments also included.

ν_{exp} GHz	$\nu_{exp} - \nu_{calc}$ MHz	Γ_{FWHM} MHz	SNR	assignment
248.492299(18)	-0.57	1.05	6.6	$69p[1/2]_0 \leftarrow 82d[3/2]_1$
249.359099(19)	-0.86	1.57	7.7	$65f[5/2]_2 \leftarrow 81d[3/2]_1$
249.957945(30)	-0.41	1.98	6.2	$65f[3/2]_2 \leftarrow 81d[3/2]_1$
250.028733(13)	-0.46	0.52	5.1	$65f[3/2]_1 \leftarrow 81d[3/2]_1$
250.418057(13)	-0.56	0.28	4.8	$69p[3/2]_1 \leftarrow 82d[3/2]_1$
251.828577(39)	-0.68	1.09	7.6	$66f[5/2]_2 \leftarrow 83d[3/2]_1$
252.400420(71)	-0.43	1.92	9.9	$66f[3/2]_2 \leftarrow 83d[3/2]_1$
252.468169(19)	-0.46	0.48	3.3	$66f[3/2]_1 \leftarrow 83d[3/2]_1$
253.277087(16)	-0.44	0.61	5.7	$69p[3/2]_1 \leftarrow 84s[3/2]_1$
254.231029(27)	-2.24	1.97	5.5	$69p[5/2]_2 \leftarrow 84s[3/2]_1$
285.098528(21)	-0.71	0.45	2.9	$68p[1/2]_0 \leftarrow 83d[3/2]_1$
285.271005(28)	-0.65	0.9	4.2	$69p[1/2]_0 \leftarrow 85d[3/2]_1$

continued on next page

continued from previous page

ν_{exp} GHz	$\nu_{exp} - \nu_{calc}$ MHz	Γ_{FWHM} MHz	SNR	assignment
287.119881(73)	3.97	1.03	2	$68p[3/2]_1 \leftarrow 83d[3/2]_1$
287.282052(26)	-0.79	1.46	9.7	$66f[5/2]_2 \leftarrow 86d[3/2]_1$
287.529928(17)	-1.02	1.17	13	$65f[5/2]_2 \leftarrow 84d[3/2]_1$
287.853926(27)	0.32	1.26	5.7	$68p[1/2]_0 \leftarrow 85s[3/2]_1$
288.128762(15)	-0.57	1.35	12.4	$65f[3/2]_2 \leftarrow 84d[3/2]_1$
288.199591(11)	-0.58	0.54	4.8	$65f[3/2]_1 \leftarrow 84d[3/2]_1$
289.346052(49)	0.01	1.79	3.3	$69p[3/2]_2 \leftarrow 87s[3/2]_1$
289.75706(11)	-0.39	1.59	2	$69p[3/2]_1 \leftarrow 87s[3/2]_1$
290.711028(44)	-2.15	1.87	2.9	$69p[5/2]_2 \leftarrow 87s[3/2]_1$
307.651476(46)	-0.58	1.54	4.6	$69p[1/2]_0 \leftarrow 87d[3/2]_1$
308.879362(47)	-1.13	2.12	3.2	$66f[5/2]_2 \leftarrow 88d[3/2]_1$
309.451660(49)	-0.41	1.25	2.2	$66f[3/2]_2 \leftarrow 88d[3/2]_1$
309.519288(26)	-0.56	0.7	2.8	$66f[3/2]_1 \leftarrow 88d[3/2]_1$
309.577254(27)	-0.55	0.84	4	$69p[3/2]_1 \leftarrow 87d[3/2]_1$
310.03510(12)	-0.52	3.5	1.1	$69p[1/2]_0 \leftarrow 89s[3/2]_1$
310.731316(44)	-0.98	1.1	3.1	$65f[5/2]_2 \leftarrow 86d[3/2]_1$
311.330119(23)	-0.57	0.89	3.8	$65f[3/2]_2 \leftarrow 86d[3/2]_1$
311.401068(34)	-0.46	0.74	2.2	$65f[3/2]_1 \leftarrow 86d[3/2]_1$
296.66141(50)	-0.77	1.05	2.4	$69p[1/2]_0 \leftarrow 86d[3/2]_1$
296.71591(50)	-0.95	3.12	1.6	$67f[5/2]_2 \leftarrow 89d[3/2]_1$
297.26270(50)	-0.53	3.15	2.4	$67f[3/2]_2 \leftarrow 89d[3/2]_1$
297.277595(50)	-0.3	0.51	10.5	$70p[3/2]_1 \leftarrow 88d[3/2]_1$
297.327512(29)	-0.59	0.52	4.1	$67f[3/2]_1 \leftarrow 89d[3/2]_1$
298.271848(46)	-0.87	4.87	24	$66f[5/2]_2 \leftarrow 87d[3/2]_1$
298.843956(31)	-0.34	3.24	32.7	$66f[3/2]_2 \leftarrow 87d[3/2]_1$
298.9114163(77)	-0.67	0.64	49.2	$66f[3/2]_1 \leftarrow 87d[3/2]_1$
299.18646(50)	0.24	1.75	2	$70p[3/2]_2 \leftarrow 90s[3/2]_1$
299.93994(50)	-0.23	3.35	1.6	$65f[3/2]_2 \leftarrow 85d[3/2]_1$
300.64630(50)	0.06	3.17	1.7	$69p[3/2]_2 \leftarrow 88s[3/2]_1$
300.655280(19)	-1	0.31	5.8	$66f[5/2]_2 \leftarrow 89s[3/2]_1$
301.05717(50)	-0.47	2.28	2.9	$69p[3/2]_1 \leftarrow 88s[3/2]_1$
301.227311(17)	-0.55	0.58	11.9	$66f[3/2]_2 \leftarrow 89s[3/2]_1$
301.294980(38)	-0.67	0.54	3.6	$66f[3/2]_1 \leftarrow 89s[3/2]_1$
302.01376(50)	0.38	6.34	1.6	$69p[5/2]_2 \leftarrow 88s[3/2]_1$
263.01315(11)	-0.8	2.04	2.7	$71p[1/2]_0 \leftarrow 87d[3/2]_1$
264.875106(80)	-0.88	2.01	3.5	$67f[5/2]_2 \leftarrow 86d[3/2]_1$

continued on next page

continued from previous page

ν_{exp} GHz	$\nu_{\mathrm{exp}} - \nu_{\mathrm{calc}}$ MHz	Γ_{FWHM} MHz	SNR	assignment
265.047554(44)	-0.91	1.48	5	$68f[5/2]_2 \leftarrow 88d[3/2]_1$
265.421930(38)	-0.43	0.87	4.3	$67f[3/2]_2 \leftarrow 86d[3/2]_1$
265.570735(41)	-0.41	0.7	4.9	$68f[3/2]_2 \leftarrow 88d[3/2]_1$
266.781307(34)	0.38	0.95	2.6	$71p[3/2]_2 \leftarrow 89s[3/2]_1$
268.028166(43)	-2.33	0.23	3	$71p[5/2]_2 \leftarrow 89s[3/2]_1$
283.8641614(76)	-0.77	0.45	10.9	$71p[1/2]_0 \leftarrow 89d[3/2]_1$
284.829286(35)	-0.74	0.54	1.8	$70p[1/2]_0 \leftarrow 87d[3/2]_1$
285.1860907(95)	-0.75	0.49	9.2	$68f[5/2]_2 \leftarrow 90d[3/2]_1$
285.709053(13)	-0.48	0.54	5.7	$68f[3/2]_2 \leftarrow 90d[3/2]_1$
286.087268(15)	-0.66	0.38	2.5	$71p[1/2]_0 \leftarrow 91s[3/2]_1$
286.472843(21)	-0.8	2.14	14.1	$67f[5/2]_2 \leftarrow 88d[3/2]_1$
287.0195698(58)	-0.44	0.64	18.4	$67f[3/2]_2 \leftarrow 88d[3/2]_1$
287.084201(36)	-0.69	0.64	1.9	$67f[3/2]_1 \leftarrow 88d[3/2]_1$
287.471600(58)	0.25	0.96	1.4	$71p[3/2]_2 \leftarrow 91s[3/2]_1$
289.321087(39)	-0.37	0.65	1.6	$67f[3/2]_2 \leftarrow 90s[3/2]_1$
303.321946(13)	-0.8	0.69	8.4	$71p[1/2]_0 \leftarrow 91d[3/2]_1$
303.993641(11)	-0.83	0.38	6.9	$68f[5/2]_2 \leftarrow 92d[3/2]_1$
305.680300(16)	-0.71	0.59	4	$70p[1/2]_0 \leftarrow 89d[3/2]_1$
306.6111243(49)	-0.9	0.76	12.7	$67f[5/2]_2 \leftarrow 90d[3/2]_1$
307.157972(17)	-0.42	0.93	16.7	$67f[3/2]_2 \leftarrow 90d[3/2]_1$
307.2225600(39)	-0.7	0.4	10.2	$67f[3/2]_1 \leftarrow 90d[3/2]_1$
308.879583(31)	-0.91	1.03	2.5	$66f[5/2]_2 \leftarrow 88d[3/2]_1$
309.451615(28)	-0.45	0.88	2.3	$66f[3/2]_2 \leftarrow 88d[3/2]_1$
262.478402(15)	-0.72	0.56	4.5	$73p[1/2]_0 \leftarrow 91d[3/2]_1$
264.345886(50)	-0.37	0.91	1.4	$70f[3/2]_2 \leftarrow 92d[3/2]_1$
264.686248(20)	-0.69	0.88	4.1	$69f[5/2]_2 \leftarrow 90d[3/2]_1$
265.186780(18)	-0.33	0.67	6.5	$69f[3/2]_2 \leftarrow 90d[3/2]_1$
265.823279(40)	0.43	0.63	1.3	$73p[3/2]_2 \leftarrow 93s[3/2]_1$
280.664425(10)	-0.8	0.4	4.4	$73p[1/2]_0 \leftarrow 93d[3/2]_1$
281.458199(36)	-0.66	1.65	3	$70f[5/2]_2 \leftarrow 94d[3/2]_1$
281.937568(23)	-0.33	0.96	2.5	$70f[3/2]_2 \leftarrow 94d[3/2]_1$
283.493829(15)	-0.74	0.65	4.1	$69f[5/2]_2 \leftarrow 92d[3/2]_1$
283.9943468(52)	-0.39	0.46	8.5	$69f[3/2]_2 \leftarrow 92d[3/2]_1$
305.786954(11)	-0.91	0.73	6.6	$70f[5/2]_2 \leftarrow 97d[3/2]_1$
305.793030(13)	-0.94	0.46	3.6	$73p[1/2]_0 \leftarrow 96d[3/2]_1$
306.266428(10)	-0.47	0.64	6.6	$70f[3/2]_2 \leftarrow 97d[3/2]_1$

continued on next page

continued from previous page

ν_{exp} GHz	$\nu_{exp} - \nu_{calc}$ MHz	Γ_{FWHM} MHz	SNR	assignment
309.457811(20)	-0.71	1.09	5.4	$69f[5/2]_2 \leftarrow 95d[3/2]_1$
309.958411(35)	-0.28	1.5	5.1	$69f[3/2]_2 \leftarrow 95d[3/2]_1$
310.017359(17)	-0.75	0.45	3.2	$69f[3/2]_1 \leftarrow 95d[3/2]_1$

A.2 Observed transitions in high Rydberg states of Xe by THz excitation

Table A.2: Experimentally observed transition frequencies ν_{exp} as compared to calculated values [30] including assignments, the observed isotope, the experimental uncertainty σ and the number of times a peak was observed (obs.). Values for $I = 0$ isotopes were averaged because no isotope shift was observed.

ν_{exp} THz	$\nu_{exp} - \nu_{calc}$ MHz	assignment	isotope	σ MHz	obs.
0.9370252	0.56	$33f[3/2]_2(3/2) \leftarrow 31d[3/2]_1(3/2)$	129	25.9	1
0.9376393	-27.98	$33f[3/2]_1(1/2) \leftarrow 31d[3/2]_1(1/2)$	129	26.2	1
0.9381985	-5.29	$33f[3/2]_1 \leftarrow 31d[3/2]_1$	$I = 0$	13.4	4*
0.9382805	16.60	$33f[3/2]_2(7/2) \leftarrow 31d[3/2]_1(5/2)$	131	13.7	3*
0.9384002	12.31	$33f[3/2]_2(5/2) \leftarrow 31d[3/2]_1(3/2)$	129	9.6	7*
0.9384628	5.10	$33f[3/2]_2(5/2) \leftarrow 31d[3/2]_1(3/2)$	131	26.2	1
0.9387412	21.71	$33f[3/2]_2 \leftarrow 31d[3/2]_1$	$I = 0$	6.7	15*
0.9392783	2.48	$33f[3/2]_1(3/2) \leftarrow 31d[3/2]_1(1/2)$	129	10.7	5*
0.9420288	-10.95	$33f[5/2]_2(5/2) \leftarrow 31d[3/2]_1(3/2)$	129	10.5	5*
0.9426175	3.78	$33f[5/2]_2(3/2) \leftarrow 31d[3/2]_1(1/2)$	131	18.7	2*
0.9431471	-4.53	$33f[5/2]_2(7/2) \leftarrow 31d[3/2]_1(5/2)$	131	25.7	1
0.9432584	-0.09	$33f[5/2]_3(5/2) \leftarrow 31d[3/2]_1(3/2)$	129	25.2	1
0.9432927	-3.01	$33f[5/2]_2 \leftarrow 31d[3/2]_1$	$I = 0$	9.7	7*
0.9434423	8.82	$33f[5/2]_2(3/2) \leftarrow 31d[3/2]_1(3/2)$	129	27.1	1
0.9439311	12.44	$33f[7/2]_3(3/2) \leftarrow 31d[3/2]_1(1/2)$	131	26.3	1
0.9442232	3.99	$33f[7/2]_3(3/2) \leftarrow 31d[3/2]_1(3/2)$	131	18.4	2*
0.9445133	-5.13	$33f[5/2]_2(3/2) \leftarrow 31d[3/2]_1(1/2)$	129	11.1	5*
0.9453314	-6.37	$33f[7/2]_3(5/2) \leftarrow 31d[3/2]_1(5/2)$	131	26.4	1

*From several measurements of the transition frequency, however, without separate locking of the fixed-frequency laser.

continued on next page

continued from previous page

ν_{exp} THz	$\nu_{\mathrm{exp}} - \nu_{\mathrm{calc}}$ MHz	assignment	isotope	σ MHz	obs.
0.9457684	-6.93	$33f[7/2]_3(7/2) \leftarrow 31d[3/2]_1(5/2)$	131	25.9	1
0.9461421	-6.54	$33f[7/2]_3(5/2) \leftarrow 31d[3/2]_1(3/2)$	129	15.0	3*
1.2294925	-11.20	$33f[3/2]_2 \leftarrow 30d[3/2]_1$	$I = 0$	25.9	1
1.2340737	-6.10	$33f[5/2]_2 \leftarrow 30d[3/2]_1$	$I = 0$	19.9	2*
1.5528205	-7.90	$33f[3/2]_2(3/2) \leftarrow 29d[3/2]_1(1/2)$	129	27.5	1
1.5528950	-17.15	$33f[3/2]_1(3/2) \leftarrow 29d[3/2]_1(3/2)$	129	28.6	1
1.5529839	1.27	$33f[3/2]_2(7/2) \leftarrow 29d[3/2]_1(5/2)$	131	18.7	2*
1.5531011	-8.10	$33f[3/2]_2(5/2) \leftarrow 29d[3/2]_1(3/2)$	129	18.1	2*
1.5534389	4.16	$33f[3/2]_2 \leftarrow 29d[3/2]_1$	$I = 0$	10.6	6
1.5539935	-1.16	$33f[3/2]_1(3/2) \leftarrow 29d[3/2]_1(1/2)$	129	18.3	2*
1.5567437	-17.29	$33f[5/2]_2(5/2) \leftarrow 29d[3/2]_1(3/2)$	129	18.4	2*
1.5579813	1.53	$33f[5/2]_3(5/2) \leftarrow 29d[3/2]_1(3/2)$	129	23.3	1
1.5579952	-15.73	$33f[5/2]_2 \leftarrow 29d[3/2]_1$	$I = 0$	14.2	3*
1.5592224	-14.86	$33f[5/2]_2(3/2) \leftarrow 29d[3/2]_1(1/2)$	129	18.2	2*
6.2839675	45.53	$33f[3/2]_2(3/2) \leftarrow 21d[3/2]_1(1/2)$	129	2.8	6
6.2841242	52.37	$33f[3/2]_2(7/2) \leftarrow 21d[3/2]_1(5/2)$	131	2.8	6
6.2842415	43.78	$33f[3/2]_2(5/2) \leftarrow 21d[3/2]_1(3/2)$	129	2.8	6
6.2843042	48.39	$33f[3/2]_2(5/2) \leftarrow 21d[3/2]_1(3/2)$	131	2.8	5
6.2845619	49.79	$33f[3/2]_2 \leftarrow 21d[3/2]_1$	$I = 0$	2.8	6
6.2846333	44.75	$33f[3/2]_2(3/2) \leftarrow 21d[3/2]_1(1/2)$	131	3.1	4
6.2848371	44.39	$33f[3/2]_2(5/2) \leftarrow 21d[3/2]_1(5/2)$	131	6.1	1
6.2851251	36.84	$33f[3/2]_1(3/2) \leftarrow 21d[3/2]_1(1/2)$	129	6.6	1
10.1525175	92.48	$33f[3/2]_2(3/2) \leftarrow 18d[3/2]_1(3/2)$	129	7.1	1
10.1536217	97.51	$33f[3/2]_2(3/2) \leftarrow 18d[3/2]_1(1/2)$	129	7.4	1
10.1537673	98.07	$33f[3/2]_2(7/2) \leftarrow 18d[3/2]_1(5/2)$	131	7.0	1
10.1538822	93.96	$33f[3/2]_2(5/2) \leftarrow 18d[3/2]_1(3/2)$	129	6.9	1
10.1539446	97.69	$33f[3/2]_2(5/2) \leftarrow 18d[3/2]_1(3/2)$	131	6.7	1
10.1542039	99.89	$33f[3/2]_2 \leftarrow 18d[3/2]_1$	$I = 0$	7.2	1
10.1542650	91.93	$33f[3/2]_2(3/2) \leftarrow 18d[3/2]_1(1/2)$	131	7.2	1
10.1544868	96.63	$33f[3/2]_2(5/2) \leftarrow 18d[3/2]_1(5/2)$	131	7.7	1
10.1545891	96.37	$33f[3/2]_2(3/2) \leftarrow 18d[3/2]_1(3/2)$	131	7.1	1
10.1547805	90.03	$33f[3/2]_1(3/2) \leftarrow 18d[3/2]_1(1/2)$	129	7.0	1
10.1575137	73.62	$33f[5/2]_2(5/2) \leftarrow 18d[3/2]_1(3/2)$	129	6.9	1
10.1583901	86.63	$33f[5/2]_2(3/2) \leftarrow 18d[3/2]_1(3/2)$	131	7.1	1

*From several measurements of the transition frequency, however, without separate locking of the fixed-frequency laser.

continued on next page

continued from previous page

ν_{exp} THz	$\nu_{exp} - \nu_{calc}$ MHz	assignment	isotope	σ MHz	obs.
10.1586432	86.29	$33f[5/2]_2(7/2) \leftarrow 18d[3/2]_1(5/2)$	131	7.5	1
10.1587620	81.79	$33f[5/2]_2 \leftarrow 18d[3/2]_1$	$I = 0$	7.3	1
10.1588133	85.92	$33f[5/2]_2(5/2) \leftarrow 18d[3/2]_1(5/2)$	131	7.0	1
11.9928129	131.51	$33f[3/2]_2(3/2) \leftarrow 17d[3/2]_1(1/2)$	129	4.5	2
11.9929589	134.86	$33f[3/2]_2(7/2) \leftarrow 17d[3/2]_1(5/2)$	131	4.0	2
11.9930649	125.54	$33f[3/2]_2(5/2) \leftarrow 17d[3/2]_1(3/2)$	129	4.8	2
11.9931278	129.11	$33f[3/2]_2(5/2) \leftarrow 17d[3/2]_1(3/2)$	131	4.9	2
11.9933913	133.92	$33f[3/2]_2 \leftarrow 17d[3/2]_1$	$I = 0$	4.5	2
11.9934483	126.19	$33f[3/2]_2(3/2) \leftarrow 17d[3/2]_1(1/2)$	131	6.6	1
11.9936797	134.82	$33f[3/2]_2(5/2) \leftarrow 17d[3/2]_1(5/2)$	131	4.6	2
11.9939744	126.78	$33f[3/2]_1(3/2) \leftarrow 17d[3/2]_1(1/2)$	129	4.5	2
11.9966988	107.68	$33f[5/2]_2(5/2) \leftarrow 17d[3/2]_1(3/2)$	129	4.3	2
11.9972501	117.35	$33f[5/2]_2(3/2) \leftarrow 17d[3/2]_1(1/2)$	131	5.5	1
11.9978293	117.57	$33f[5/2]_2(7/2) \leftarrow 17d[3/2]_1(5/2)$	131	4.7	2
11.9979504	116.86	$33f[5/2]_2 \leftarrow 17d[3/2]_1$	$I = 0$	4.9	2
11.9980042	122.05	$33f[5/2]_2(5/2) \leftarrow 17d[3/2]_1(5/2)$	131	4.6	2
14.2445645	173.37	$33f[3/2]_2(3/2) \leftarrow 16d[3/2]_1(1/2)$	129	5.4	1
14.2447080	177.06	$33f[3/2]_2(7/2) \leftarrow 16d[3/2]_1(5/2)$	131	7.4	1
14.2448057	163.92	$33f[3/2]_2(5/2) \leftarrow 16d[3/2]_1(3/2)$	129	5.3	1
14.2451387	182.12	$33f[3/2]_2 \leftarrow 16d[3/2]_1$	$I = 0$	4.9	1

*From several measurements of the transition frequency, however, without separate locking of the fixed-frequency laser.

A.3 Observed transitions in high Rydberg states of H_2 by THz excitation

Table A.3: Experimentally observed transition frequencies ν_{exp} in H_2 with assignment of the upper levels as observed from the $40d0_2$ or the $20d2_1$ starting level.

$40d0_2$ starting level			$20d2_1$ starting level		
ν_{exp} THz	σ MHz	upper level	ν_{exp} THz	σ MHz	upper level
0.4330773	3.0	$45f0_3$	5.5750347	4.5	$35f2_2$
0.4831974	3.1	$22f2_3$	6.2047109	5.2	$40f2_2$

continued on next page

continued from previous page

$40d0_2$ starting level			$20d2_1$ starting level		
ν_{exp} THz	σ MHz	upper level	ν_{exp} THz	σ MHz	upper level
0.5032928	3.0	$46f0_3$	6.4817570	4.5	$43f2_2$
0.5686016	3.0	$47f0_3$	6.5617006	5.7	$44f2_2$
0.6299752	3.0	$48f0_3$	6.7062670	4.0	$46f2_2$
0.6876475	3.0	$49f0_3$	7.2120217	3.7	$56f2_2$
0.7929861	3.4	$51f0_3$	7.3769475	3.6	$61f2_2$
0.8411625	3.1	$52f0_3$	1.9051066	4.8	$54p0_1$
0.8866351	2.9	$53f0_3$	1.9425414	5.3	$55p0_1$
0.9296102	2.6	$54f0_3$	2.0015660	4.8	$23p2_1$
0.9702520	2.9	$55f0_3$	2.0317104	4.7	$57p0_1$
1.0087308	2.9	$56f0_3$	2.0636211	4.3	$58p0_1$
1.0451520	3.1	$57f0_3$			
1.0638604	3.5	$23f2_3$			
1.0799683	3.4	$58f0_3$			
1.1124779	3.0	$59f0_3$			
1.2546357	3.1	$64f0_3$			
1.3668089	3.5	$69f0_3$			
1.4570171	3.0	$74f0_3$			
1.5170310	4.2	$78f0_3$			
1.5306413	3.1	$79f0_3$			
1.5437322	5.3	$80f0_3$			
0.5723985	3.0	$47p0_1$			
0.6319820	3.0	$48p0_1$			
0.6885090	3.0	$49p0_1$			
0.7921660	3.8	$51p0_1$			
0.8394962	4.0	$52p0_1$			
0.8839160	3.2	$53p0_1$			
0.9252442	3.1	$54p0_1$			
0.9626818	3.8	$55p0_1$			
1.0518465	3.1	$57p0_1$			
1.0837579	3.6	$58p0_1$			
1.1149833	3.2	$59p0_1$			
1.2548830	3.3	$64p0_1$			

List of Figures

1.1 The electromagnetic spectrum. 2

2.1 Panel a): Chemical structure of *trans*-4′-(dimethylamino)-*N*-methyl-4-stilbazolium tosylate (DAST). Panel b): X-ray structure of DAST showing molecules from one unit cell projected along the crystallographic axes a and b. The SO_3^--group of the tosylate anion is shown in yellow and red. The ac crystallographic plane is the mirror plane. The lattice parameters are $a = 10.365\,\text{Å}$, $b = 11.322\,\text{Å}$ and $c = 17.893\,\text{Å}$ [45, 46]. Figure taken from Ref. [45]. 10

2.2 Panel a): Schematic representation of the THz generation process, where $\chi^{(2)}$ represents the nonlinear optical susceptibility tensor of DAST for THz generation. Panel b) Generation of tunable THz radiation by keeping one NIR laser at a fixed frequency (ν_{NIR2}), and tuning the frequency of the second NIR laser (ν_{NIR1}). 11

2.3 Panel a): Schematic representation of the optical axes of the DAST crystal (x_1, x_2, x_3) and the angles they make with respect to the crystallographic axes a, b, c. Angles shown are not drawn to scale. Panel b): Schematic representation of the cut of the DAST crystal. The dashed rectangle represents the as-grown crystal. The black, full parallelogram is a crystal cut so as to facilitate phase-matching in the difference-frequency generation process across the range $0.1 - 14\,\text{THz}$. $\vec{k}$ corresponds to the propagation direction of the NIR and THz beams. The blue colors show the polarization (dashed arrow) and propagation (full arrow) direction of the NIR beams for use with the cut crystal, red colors those for use with the as-grown crystal. 14

2.4 Panel a): THz peak power as measured by a bolometer. Sharp dips correspond to water absorption lines, broader features at 1.1 and 3.2 THz correspond to crystal absorptions. Panel b): THz peak power after normalization by window and filter absorptions (see text for details). Figures taken from [26]. For both panels, the red, solid line represents a normal-incident pump beam with polarization perpendicular to the b axis, the black, solid line represents a normal-incident NIR pump beam with a polarization parallel to the b axis and the blue squares a polarization parallel to the b axis and with an optimal angle of incidence. 15

2.5 Schematic representation of the Ti:Sa laser system used for generating short (10-500 ns), high-power NIR pulses of Fourier-transform-limited bandwidth, including bowtie-amplification system. BS: beamsplitter, FR: Fresnel rhomb, OI: optical isolator. 17

2.6 Schematic representation of the length-stabilized, confocal etalon used for frequency calibration of both NIR lasers and stabilization of the fixed-frequency NIR laser. PD: photo-diode, PBS: polarization beamsplitter, PZT: piezo-electric transducer, DC: dichroic mirror, FR: Fresnel rhomb, BS: beamsplitter, AOM: acousto-optic modulator. 21

2.7 Schematic representation of the setup used for Doppler-free spectroscopy of I_2 to perform calibration of absolute frequencies. PD: photo-diode, FR: Fresnel rhomb, AOM: acousto-optic modulator, PBS: polarization beamsplitter. 23

2.8 Schematic representation of the experimental setup used for performing vibrational spectroscopy in an ambient cell in the THz frequency range. PE: white polyethylene window; LE: lens; DAST: *trans*-4′-(dimethylamino)-*N*-methyl-4-stilbazolium tosylate crystal; FL: black polyethylene filter; OAPM: off-axis parabolic mirror. 24

2.9 Schematic representation of experimental setup constructed for recording sub-millimeter-wave spectra of high Rydberg states in Xe following VUV excitation. 26

2.10 Shift of the frequency of the $69p[3/2]_2(5/2) \leftarrow 84s[3/2]_1(3/2)$ transition (note that the assignment of the K quantum number for the 69p state is ambiguous) in ^{129}Xe in dependence on applied compensation fields. Spectra are shifted vertically by an offset corresponding to the value of the applied compensation field in mV / cm (between 0 mV / cm and 30 mV / cm). 29

2.11 Panel a): $59f[3/2]_1 \leftarrow 53d[3/2]_1$ transition of Xe that is split into a doublet because of a stray magnetic field present in the excitation region. Panel b): $70p[5/2]_2 \leftarrow 58d[3/2]_1$ transition of Xe with its transit-time limited linewidth of 150 kHz. 30

2.12 Schematic representation of experimental setup used for VUV-THz experiments. FR: Fresnel rhomb, PBS: polarization beamsplitter, AOM: acousto-optic modulator, OF: optical fiber, OI: optical isolator, OAPM: off-axis parabolic mirror, PE: white polyethylene window. 31

2.13 Schematic representation of experimental chamber of VUV-THz double resonance spectrometer. C, D, A: tilt angles of DAST crystal mount, B: horizontal displacement of crystal, E, F: tilt angles of off-axis parabolic mirror. TOF: time-of-flight, MCP: micro-channel plate, OAPM: off-axis parabolic mirror, PE: polyethylene. 32

2.14 Schematic representation of the mechanical system used to adjust the tilt angle of the DAST-crystal mount from outside the vacuum chamber (see text for details). 34

3.1 Spectra of the fundamental band of the CCl_3 asymmetric deformation mode of chloroform and selected isotopomers. The strong line on the far left-hand side of the spectra in a) and b) corresponds to a water line. The lines marked by asterisks correspond to impurities of $^{12}CDCl_3$ in panel a) and $^{12}CHCl_3$ in panels b) and c). In panel a), simulated profiles of the $^{12}CH^{35}Cl_3$ isotopomer, assuming values of -0.84 (dashed line), -0.86 (full line) and -0.88 (dotted line) for ζ_6 are displayed (see text for details). 39

4.1 Schematic representation of the energy level diagram of $^{132}Xe^+$, $^{131}Xe^+$ and $^{129}Xe^+$. The two spin orbit components of $^{132}Xe^+$ are shown and their ionization energies with respect to the $^1S_0$ ground state given in units of cm^{-1}. For $^{131}Xe^+$ and $^{129}Xe^+$, the isotope shifts of the spin-orbit components are given. The positions of the hyperfine levels are given relative to the center of gravity of the hyperfine structure and labeled by the F^+ quantum number (between 0 and 3 of $^{131}Xe^+$ $I = 3/2$ and between 0 and 2 for $^{129}Xe^+$ ($I = 1/2$)). Figure taken from Ref. [30]. 46

4.2 Schematic representation of ns, nd and np Rydberg series converging on different hyperfine levels of $^{129}Xe^+$. An interaction between an $ns, F = 3/2$ Rydberg series converging on the $F^+ = 2$, $J^+ = 3/2$ level and an $nd, F = 3/2$ series converging on the $F^+ = 1$, $J^+ = 3/2$ level is indicated by a grey arrow. 47

4.3 Spectrum of ^{129}Xe between $248 - 256$ GHz after excitation to initial states around $n = 82$ and final states around $n = 69$. Transition a: $69p[5/2]_2(5/2) \leftarrow 82d[3/2]_1(3/2)$, transition b: $69p[5/2]_2(5/2) \leftarrow 84s[3/2]_1(3/2)$. Transitions with the same final state can be used to quantify s,d splittings by calculating combination differences. 48

4.4 Sub-millimeter-wave spectra of Rydberg-Rydberg transitions of ^{132}Xe ($I = 0$), ^{131}Xe ($I = 3/2$) and ^{129}Xe ($I = 1/2$) that were recorded simultaneously in the range between 248 and 256 GHz. Spectra of ^{128}Xe, ^{130}Xe, ^{134}Xe and ^{136}Xe (all $I = 0$ isotopes) were also recorded but are not shown here because the transition frequencies were the same as for ^{132}Xe within our experimental resolution. The transitions labeled a and b in the top trace correspond to the $66f[3/2]_2 \leftarrow 83d[3/2]_1$ and $66f[3/2]_1 \leftarrow 83d[3/2]_1$ transitions of ^{132}Xe. The vertical scale of the spectra of ^{129}Xe and ^{131}Xe has been multiplied by a factor of 2. 50

4.5 Schematic representation of the excitation sequence (not to scale) used to study high Rydberg states of Xe below the $^2P_{3/2}$ ionization threshold. smm stands for "sub-millimeter-wave". 51

4.6 a) Time-of-flight mass spectrum of Xe^+ ions produced following field ionization of Xe Rydberg states using the sequence of pulsed electric fields depicted in panel b). c) Excitation scheme. The applied pulse sequence allowed for separating the isotopic distribution of the higher-lying, initial Rydberg state from that of the lower-lying, final state, as can be seen in the time-of-flight spectrum (see text for details). 52

4.7 Rydberg spectra of ^{129}Xe and ^{134}Xe recorded as a function of VUV wavenumber. a) Transition to $30d[3/2]_1$, b) transition to $32s[3/2]_1$ and c) transition to $31d[1/2]_1$ Rydberg states accessed from the $^1S_0$ ground state. Transitions marked by asterisks correspond to $nd[1/2]_1$ Rydberg series. Assignment bar gives principal quantum number n for the $nd[3/2]_1$ Rydberg series. The irregularly high intensities of the lowest-n transitions in ^{134}Xe as compared to ^{129}Xe are attributed to a leakage from the ^{132}Xe mass channel because a clear separation of these isotopes is difficult to achieve at low values of the principal quantum number and correspondingly high extraction voltages. . . 53

4.8 Rydberg levels observed in the sub-millimeter-wave spectra (see text for details). Note: drawing not to scale, p,f Rydberg states would be considerably lower in energy than s,d Rydberg states in the range of principal quantum number that is indicated. 54

4.9 Sub-millimeter-wave spectra recorded between $ns[3/2]_1$, $nd[3/2]_1$ Rydberg states and $np[1/2]_0$ states. Assignments for transitions (I)-(IX) are given by the energy level diagram. Transition labeled (1) is $70p[1/2]_0 \leftarrow 87d[3/2]_1$, transition (2) $68f[5/2_2] \leftarrow 90d[3/2]_1$, transition (3) $68f[3/2_2] \leftarrow 90d[3/2]_1$, and transition (4) $70f[5/2]_2 \leftarrow 97d[3/2]_1$ 56

4.10 Sub-millimeter-wave spectra showing transitions from $ns[3/2]_1$ Rydberg states to nf Rydberg states which are forbidden by the $\Delta l = \pm 1$ selection rule. (1) $69p[3/2]_2 \leftarrow 88s[3/2]_1$, (2) $66f[5/2]_2 \leftarrow 89s[3/2]_1$, (3) $69p[3/2]_1 \leftarrow 88s[3/2]_1$, (4) $66f[3/2]_2 \leftarrow 89s[3/2]_1$ and (5) $66f[3/2]_1 \leftarrow 89s[3/2]_1$ 58

4.11 Panel a): Calculated correlation diagram between $n = 60$ and $n = 100$ for ^{129}Xe taken from [30]. The grey rectangle marks a region where an interaction between $ns[3/2]_1(3/2)$ (black, thick, dashed line) and $(n-2)d[3/2]_1(3/2)$ (grey, thick, dashed line) series is predicted. Panel b): Comparison of experimentally determined (red and blue squares) and calculated values determined from a first analysis of transitions in ^{129}Xe, see text for details. . 60

4.12 Panel a): $70p[5/2]_2 \leftarrow 58d[3/2]_1$ transition in ^{132}Xe for different sub-millimeter-wave attenuations of 0 dB (top black trace), −5 dB (red trace), −10 dB (middle black trace), −15 dB (green trace) −20 dB (lower black trace) and −35 dB (blue trace). The scale of the blue trace was increased for clarity. . 63

4.13 Deviations of observed frequencies of the $70p[5/2]_2 \leftarrow 58d[3/2]_1$ transition of ^{132}Xe from the mean value of 311 923.229 (34) MHz as a function of sub-millimeter-wave attenuation. Error bars take into account solely the error in the determination of the transition frequency given in Table 4.4 that results from fitting a Lorentzian function to the observed transition. 65

4.14 Panels a)-d): Measurements of Rabi oscillations associated with the $70p[5/2]_2 \leftarrow 58d[3/2]_1$ transition of Xe for detunings $\Delta\nu = \delta/(2\pi)$ of 0 MHz, 0.54 MHz, 1.84 MHz and 3.14 MHz, respectively. Panels e) and f): Rabi oscillations recorded on resonance at VUV intensities reduced by a factor of 3 and 7, yielding values of $\gamma = 1.5$ and $\gamma = 1.1$, respectively. Panel g): Rabi oscillations for a mixture of 10% Xe in Ne, yielding a value of $\gamma = 1.5$. 67

5.1 Excitation scheme used to measure spectra of $33f \leftarrow nd$ Rydberg-Rydberg transitions of Xe. The transitions were detected by selective field ionization of the final 33f level. The figure illustrates the range of initial states corresponding to the frequency range from 0.9 THz ($n = 31$) to 14.3 THz ($n = 16$). 72

5.2 Spectrum of the $33f[5/2]_2 \leftarrow 17d[3/2]_1$ transition of Xe plotted as a function of the wave number $\tilde{\nu}_{\mathrm{NIR1}}$ of the tunable NIR laser (a) and as a function of the difference $\tilde{\nu}_{\mathrm{NIR1}} - \tilde{\nu}_{\mathrm{NIR2}}$ of the wave numbers of the tunable and fixed-frequency NIR lasers (b). The top and middle traces in panel (a) represent the Doppler-free absorption spectrum of I_2 and the transmission spectrum through an etalon, respectively. The asterisks designate transitions of ^{129}Xe and ^{131}Xe. 75

5.3 Spectra of the $33f \leftarrow 31d$ transition of Xe recorded using pulse lengths of a) 400 ns, b) 200 ns, c) 60 ns, d) 20 ns, e) 10 ns. The assignments of the lines labeled 1-8 are given in Table 5.1. The spectra have been shifted along the vertical axis for clarity. 76

5.4 Effect of the NIR pulse length on the spectral resolution with the example of the $33f[3/2]_1 \leftarrow 31d[3/2]_1$ transition of the $I = 0$ isotopes of Xe. a) and b) display two measured NIR pulse shapes and c) and d) the corresponding spectral lineshapes. 78

5.5 Fine and hyperfine structure of the $33f \leftarrow nd$ transitions of Xe for $n = 31$ (a), 21 (b), 18 (c), 17 (d) and 16 (e). The assignments of the lines labeled 1 to 8 are given in Table 5.1. Lines 9 and 10 correspond to the $33f[3/2]_2(5/2) \leftarrow 21d[3/2]_1(5/2)$ transitions of ^{131}Xe and $33f[3/2]_1(3/2) \leftarrow 21d[3/2]_1(1/2)$ of ^{129}Xe, respectively. 79

5.6 a) Time-of-flight (TOF) spectrum of Xe^+ ions formed following photoionization above the $^1S_0 \rightarrow {}^2P_{3/2}$ ionization threshold. b) Spectra of the $33f \leftarrow 31d$ transitions of ^{132}Xe (b), ^{131}Xe (c), and ^{129}Xe (d) recorded following selective field ionization of the 33f level and measuring the ion signal at the relevant TOF position. 82

6.1 Schematic representation of Rydberg series converging on different rotational levels of H_2^+. Panel a): Excitation of both series from an initial Rydberg level with rotationally mixed character ($N^+ = 0, 2$). Panel b): Excitation of both series from the different starting levels $40d0_2$ (excitation to a series converging on $N^+ = 0$) and $20d2_1$ (excitation to a series converging on $N^+ = 2$). Panel c): Excitation to states with mixed rotational character from the two starting levels of panel b) used to determine their relative energy spacing. 87

6.2 Panel a): Schematic representation of the experimental configuration used for excitation of the supersonic beam of H_2 molecules. Panel b): Excitation sequence used to access Rydberg series converging on either of the two lowest-lying rotational levels of para-H_2^+. 88

6.3 Panel a) p and f Rydberg series converging on the $N^+ = 0$ and $N^+ = 2$ ionization thresholds. Excitation to series colored opaque are forbidden by selection rules. Panel b) Relative energies $E = hc\,\mathrm{T}$ of selected states belonging to $n\mathrm{p}0_1$ and $n\mathrm{p}2_1$ Rydberg series. 91

6.4 Left column: transitions from the $40\mathrm{d}0_2$ state to $n\mathrm{p}0_1$ Rydberg states. Right column: transitions from the $20\mathrm{d}2_1$ state to $n\mathrm{p}0_1$ Rydberg states. 92

6.5 Schematic representation of the scheme used to determine the rotational spacing β. 93

6.6 Evolution of the effective quantum defect μ_{eff} of the $n\mathrm{p}0_1$ Rydberg series as a function of principal quantum number n and overall energy $E/hc = \mathrm{T}$. The dashed, vertical lines represent the positions of the $n\mathrm{p}2_1$ perturbers. Calculated values are marked as black circles, experimental values as blue crosses. 95

6.7 Frequency splitting between transitions from the $40\mathrm{d}0_2$ state to $n\mathrm{f}0_3$ and $n\mathrm{p}0_1$ Rydberg states. 96

6.8 Frequency splitting between transitions from the $40\mathrm{d}0_2$ state to $n\mathrm{f}0_3$ and $n\mathrm{p}0_1$ Rydberg states. 97

6.9 Transitions from the $20\mathrm{d}2_1$ state to $n\mathrm{f}2_2$ Rydberg states. 99

6.10 Frequency calibration for the $54\mathrm{f}0_3 \leftarrow 40\mathrm{d}0_2$ transition in H_2. Panel a) Doppler free I_2 absorption spectrum (top trace), etalon transmission spectrum (middle trace) and molecular transition (bottom trace) as a function of the absolute frequency of the tunable ring laser. Panel b) Absolute frequency of the transition obtained by subtraction of the absolute frequency of the fixed ring laser. 100

6.11 Different measurements of $54\mathrm{f}0_3 \leftarrow 40\mathrm{d}0_2$ transition in H_2 and their deviation from the mean value of $0.929\,609\,8(15)\,\mathrm{THz}$. Error bars represent a deviation of $\pm\sigma$, where σ was determined from the uncertainties in the determination of the line centers as obtained by fit of a Gaussian lineshape and the uncertainties associated with the determination of the line centers of the Doppler-free I_2 transitions. 101

List of Tables

1.1 Several properties of Rydberg states and their scaling with the principal quantum number n [38]. All values given for the hydrogen atom except for [a]. 5

4.1 Principal quantum numbers of the s and d Rydberg states of ^{132}Xe populated at the VUV wavenumbers marked by colored rectangles in Figure 4.8 and observed in the sub-millimeter-wave spectra. The underlined levels are those that were observed in several sub-millimeter-wave spectra and were used to build combination differences. 55

4.2 Experimentally determined values for level energies in ^{132}Xe given relative to the 66f$[5/2]_2$ state and compared to calculated values. Statistical uncertainties are given in parentheses. In addition, the level positions are subject to a systematic uncertainty of 200 kHz. 59

4.3 Experimentally determined energy splittings $\Delta E_{\mathrm{exp}}\,(n\mathrm{s}/(n-2)\mathrm{d})$ between $n\mathrm{s}[3/2]_1(3/2)$ and $(n-2)\mathrm{d}[3/2]_1(3/2)$ states as compared to calculated ones $\Delta E_{\mathrm{calc}}\,(n\mathrm{s}/(n-2)\mathrm{d})$ as a function of principal quantum number n. 61

4.4 Observed transition frequencies ω_{12} , FWHM and calculated Rabi frequencies Ω, as well as values Ω_{p} predicted from the attenuation factors for the 70p$[5/2]_2 \leftarrow$ 58d$[3/2]_1$ transition of ^{132}Xe (see text for details). Frequencies are given in units of angular frequency ($10^6\,\mathrm{s}^{-1}$). To convert to the observed transition frequencies and FWHM in units of MHz, division by the factor 2π is necessary. 64

4.5 Values of Ω and γ obtained from the analysis of Rabi oscillations for different detunings $\delta/(2\pi)$. The values of Ω and γ are given in units of angular frequency. 66

5.1 Assignments and relative positions (in cm^{-1}) of the fine and hyperfine-structure components of the 33f $\leftarrow$ 31d transitions of ^{129}Xe, ^{131}Xe and ^{132}Xe observed in Figure 5.3. 77

5.2 Comparison of the NIR laser pulses with the measured (exp) full widths at half-maximum (FWHM) of the Rydberg-Rydberg transitions. The calculated (calc) widths were determined by convolution and Fourier-transformation assuming a Gaussian temporal profile of the NIR pulses. 77

5.3 Observed and calculated frequencies of the $33f[3/2]_2 \leftarrow nd[3/2]_1$ and $33f[5/2]_2 \leftarrow nd[3/2]_1$ transitions for $n = 16, 17, 18, 21, 29, 30$ and 31. The calculated frequencies were obtained using the set of MQDT parameters reported in Ref. [30]. 81

6.1 Measured energies in para-H_2^+ relative to the $20d2_1$ state. Uncertainties resulting from fits of the line centers of observed transitions and from the determination of the line centers of the Doppler-free I_2 transitions of both lasers are given in parentheses (see Section 6.6). 94

A.1 Experimentally observed transition frequencies ν_{exp} as compared to calculated values [30] including observed full-widths at half-maximum Γ_{FWHM} obtained by fit of a Gaussian lineshape. Uncertainties for transition frequencies obtained from fit given in parentheses in units of the last two digits. Signal-to-noise ratios (SNR) and assignments also included. 105

A.2 Experimentally observed transition frequencies ν_{exp} as compared to calculated values [30] including assignments, the observed isotope, the experimental uncertainty σ and the number of times a peak was observed (obs.). Values for $I = 0$ isotopes were averaged because no isotope shift was observed. 108

A.3 Experimentally observed transition frequencies ν_{exp} in H_2 with assignment of the upper levels as observed from the $40d0_2$ or the $20d2_1$ starting level. . 110

Bibliography

[1] V. P. Wallace, A. J. Fitzgerald, S. Shankar, N. Flanagan, R. Pye, J. Cluff and D. D. Arnone, "Terahertz pulsed imaging of basal cell carcinoma ex vivo and in vivo", *British J. Dermatol.* **151**(2), 424–432 (2004).

[2] N. Karpowicz, H. Zhong, C. Zhang, K. Lin, J. Hwang, J. Xu and X. Zhang, "Compact continuous-wave subterahertz system for inspection applications", *Appl. Phys. Lett.* **86**(5), 054105 (2005).

[3] R. Kaindl, M. Carnahan, D. Hagele, R. Lovenich and D. Chemla, "Ultrafast terahertz probes of transient conducting and insulating phases in an electron-hole gas", *Nature* **423**(6941), 734–738 (2003).

[4] D. Basov and T. Timusk, "Electrodynamics of high-T_c superconductors", *Rev. of Mod. Phys.* **77**(2), 721–779 (2005).

[5] F. Maiwald, F. Lewen, B. Vowinkel, W. Jabs, D. G. Paveljev, M. Winnewisser and G. Winnewisser, "Planar Schottky Diode Frequency Multiplier for Molecular Spectroscopy up to 1.3 THz", *IEEE Microwave Guided Wave Letters* **9**(5), 198–200 (1999).

[6] D. T. Petkie, Th. M. Goyette, R. P. A. Bettens, S. P. Belov, S. Albert, P. Helminger and F. C. De Lucia, "A fast scan submillimeter spectroscopic technique", *Rev. Sci. Instr.* **68**(4), 1675–1683 (1997).

[7] R. Gendriesch, F. Lewen, G. Winnewisser and J. Hahn, "Precision Broadband Spectroscopy near 2 THz: Frequency-Stabilized Laser Sideband Spectrometer with Backward-Wave Oscillators", *J. Mol. Spectrosc.* **203**(1), 205–207 (2000).

[8] F. Lewen, E. Michael, R. Gendriesch, J. Stutzki and G. Winnewisser, "Terahertz Laser Sideband Spectroscopy with Backward Wave Oscillators", *J. Mol. Spectrosc.* **183**(1), 207–209 (1997).

[9] F. Lewen, R. Gendriesch, I. Pak, D. G. Paveliev, M. Hepp, R. Schieder and G. Winnewisser, "Phase locked backward wave oscillator pulsed beam spectrometer in the submillimeter wave range", *Rev. Sci. Instr.* **69**(1), 32–39 (1998).

[10] V. L. Vaks, A.N.Panin, S. A. Basov, A. V. Illyuk, S. I. Pripolzin, D. G. Peveliev and Y. I. Koshurinov, "Nonstationary spectroscopy of the 1–2.5 THz frequency band with the use of solid-state devices", *Radiophys. and Quantum Electronics* **52**(7), 511–517 (2009).

[11] G. Mouret, S. Matton, R. Bocquet, F. Hindle, E. Peytavit, J. F. Lampin and D. Lippens, "Far-infrared cw difference-frequency generation using vertically integrated and planar low temperature grown GaAs photomixers: application to H_2S rotational spectrum up to 3 THz", *Appl. Phys. B: Lasers and Optics* **79**(6), 725–729 (2004).

[12] E. Peytavit, S. Arscott, D. Lippens, G. Mouret, S. Matton, P. Masselin, R. Bocquet, J. F. Lampin, L. Desplanque and F. Mollot, "Terahertz frequency difference from vertically integrated low-temperature-grown GaAs photodetector", *Appl. Phys. Lett.* **81**(7), 1174–1176 (2002).

[13] Y.-S. Lee, *Principles of Terahertz Science and Technology*, Springer, New York (2009).

[14] J. Faist, F. Capasso, D. L. Sivco, C. Sirtori, A. L. Hutchinson and A. Y. Cho, "Quantum cascade laser", *Science* **264**(5158), 553–556 (1994).

[15] G. Scalari, C. Walther, M. Fischer, R. Terazzi, H. Beere, D. Ritchie and J. Faist, "THz and sub-THz quantum cascade lasers", *Laser Photon. Rev.* **3**(1-2), 45–66 (2009).

[16] L. Consolino, A. Taschin, P. Bartolini, S. Bartalini, P. Cancio, A. Tredicucci, H. E. Beere, D. A. Ritchie, R. Torre, M. S. Vitiello and P. De Natale, "Phase-locking to a free-space terahertz comb for metrological-grade terahertz lasers", *Nat. Commun.* **3**(1040), 1–5 (2012).

[17] H. W. Huebers, R. Eichholz, S. G. Pavlov and H. Richter, "High Resolution Terahertz Spectroscopy with Quantum Cascade Lasers", *J. Infrared Milli. Terahz. Waves* **34**(5-6), 325–341 (2013).

[18] M. S. Vitiello, L. Consolino, S. Bartalini, A. Taschin, A. Tredicucci, M. Inguscio and P. De Natale, "Quantum-limited frequency fluctuations in a terahertz laser", *Nat. Photon.* **6**(8), 525–528 (2012).

[19] D. Burghoff, T.-Y. Kao, N. Han, C. W. I. Chan, X. Cai, Y. Yang, D. J. Hayton, J.-R. Gao, J. L. Reno and Q. Hu, "Terahertz laser frequency combs", *Nat. Photonics* **8**(6), 462–467 (2014).

[20] H. Fueser and M. Bieler, "Terahertz Frequency Combs", *J. Infrared Milli. Terahz. Waves* **35**(8), 585–609 (2014).

[21] S. Bartalini, L. Consolino, P. Cancio, P. De Natale, P. Bartolini, A. Taschin, M. De Pas, H. Beere, D. Ritchie, M. S. Vitiello and R. Torre, "Frequency-Comb-Assisted Terahertz Quantum Cascade Laser Spectroscopy", *Phys. Rev. X* **4**(2) (2014).

[22] A. R. W. McKellar, "High-resolution infrared spectroscopy with synchrotron sources", *J. Mol. Spectrosc.* **262**(1), 1–10 (2010).

[23] S. Albert, K. K. Albert, P. Lerch and M. Quack, "Synchrotron-based highest resolution Fourier transform infrared spectroscopy of naphthalene ($C_{10}H_8$) and indole (C_8H_7N) and its application to astrophysical problems", *Faraday Discuss.* **150**, 71–99 (2011).

[24] S. Albert, P. Lerch, R. Prentner and M. Quack, "Tunneling and Tunneling Switching Dynamics in Phenol and Its Isotopomers from High-Resolution FTIR Spectroscopy with Synchrotron Radiation", *Angew. Chem. (int. ed. engl.)* **52**(1), 346–349 (2013).

[25] P. Fellgett, "A Propos de la Théorie du Spectromètre Interférentiel Multiplex", *J. Phys. Radium* **19**(3), 187–191 (1958).

[26] J. Liu, H. Schmutz and F. Merkt, "Generation of widely tunable Fourier-transform-limited terahertz pulses using narrowband near-infrared laser radiation", *J. Mol. Spectrosc.* **256**(1), 111–118 (2009).

[27] A. Schneider, M. Neis, M. Stillhart, B. Ruiz, R. U. A. Khan and P. Günter, "Generation of terahertz pulses through optical rectification in organic DAST crystals: theory and experiment", *J. Opt. Soc. Am. B* **23**(9), 1822–1835 (2006).

[28] J. Liu and F. Merkt, "Generation of tunable Fourier-transform-limited terahertz pulses in 4-*N*, *N*-dimethylamino-4'-*N*'-methyl stilbazolium tosylate crystals", *Appl. Phys. Lett.* **93**(13), 131105 (2008).

[29] M. Schäfer and F. Merkt, "Millimeter wave spectroscopy and multichannel quantum-defect-theory analysis of high Rydberg states of krypton: The hyperfine structure of $^{83}Kr^+$", *Phys. Rev. A* **74**(6), 062506 (2006).

[30] M. Schäfer, M. Raunhardt and F. Merkt, "Millimeter-wave spectroscopy and multichannel quantum-defect-theory analysis of high Rydberg states of xenon: The hyperfine structure of $^{129}Xe^+$ and $^{131}Xe^+$", *Phys. Rev. A* **81**(3), 032514 (2010).

[31] A. Osterwalder, A. Wüest, F. Merkt and Ch. Jungen, "High-resolution millimeter wave spectroscopy and multichannel quantum defect theory of the hyperfine structure in high Rydberg states of molecular hydrogen H_2", *J. Chem. Phys.* **121**(23), 11810–11838 (2004).

[32] H. J. Wörner, M. Grütter, E. Vliegen and F. Merkt, "Role of nuclear spin in photoionization: Hyperfine-resolved photoionization of Xe and multichannel quantum defect theory analysis", *Phys. Rev. A* **71**(5), 052504 (2005), see erratum in Phys. Rev. A 73, 059904(E) (2006).

[33] H. J. Wörner, S. Mollet, Ch. Jungen and F. Merkt, "Role of spins in molecular photoionization: Spectroscopy and dynamics of autoionizing Rydberg states of ortho-H_2", *Phys. Rev. A* **75**(6), 062511 (2007).

[34] D. Sprecher, J. Liu, T. Krähenmann, M. Schäfer and F. Merkt, "High-resolution spectroscopy and quantum-defect model for the gerade triplet np and nf Rydberg states of He_2", *J. Chem. Phys.* **140**, 064304 (2014).

[35] Th. A. Paul, J. Liu and F. Merkt, "Nuclear spin effects in the photoionization of krypton", *Phys. Rev. A* **79**(2), 022505 (2009).

[36] J. R. Rydberg, "Über den Bau der Linienspektren der chemischen Grundstoffe", *Z. Phys. Chem.* **5**(3), 227–232 (1890).

[37] H. J. Wörner, U. Hollenstein and F. Merkt, "Multichannel quantum defect theory of the hyperfine structure of high Rydberg states of ^{83}Kr", *Phys. Rev. A* **68**(3), 032510 (2003).

[38] T. F. Gallagher, *Rydberg Atoms*, Cambridge University Press, Cambridge (1994).

[39] F. Merkt and R. N. Zare, "On the lifetimes of Rydberg states probed by delayed pulsed field ionization", *J. Chem. Phys.* **101**(5), 3495–3505 (1994).

[40] U. Fano, "Quantum Defect Theory of l Uncoupling in H_2 as an Example of Channel-Interaction Treatment", *Phys. Rev. A* **2**(2), 353–365 (1970), see erratum in Phys. Rev. A 15, 817 (1977).

[41] M. J. Seaton, "Quantum defect theory", *Rep. Prog. Phys.* **46**(2), 167–257 (1983).

[42] Ch. Jungen, "Elements of Quantum Defect Theory", in M. Quack and F. Merkt (Editors), "Handbook of High-Resolution Spectroscopy", volume 1, pages 471–510, John Wiley & Sons, Chichester (2011).

[43] Ch. Haase, M. Beyer, Ch. Jungen and F. Merkt, *Unpublished result.* (2014).

[44] D. Sprecher, *Rovibronic and hyperfine interactions in Rydberg states of molecular hydrogen*, PhD thesis, ETH Zurich, CH-8093 Zurich, Switzerland (2013), Diss. ETH No. 21440.

[45] M. Jazbinsek, L. Mutter and P. Günter, "Photonic Applications With the Organic Nonlinear Optical Crystal DAST", *IEEE J. Sel. Topics Quantum Electron.* **14**(5), 1298–1311 (2008).

[46] F. Pan, M. S. Wong, C. Bosshard and P. Günter, "Crystal growth and characterization of the organic salt 4-N,N-dimethylamino-4′-N-methyl-stilbazolium tosylate", *Adv. Mater.* **8**(7), 592–595 (1996).

[47] S. R. Marder, J. W. Perry and W. P. Schaefer, "Synthesis of Organic Salts with Large Second-Order Optical Nonlinearities", *Science* **245**(4918), 626–628 (1989).

[48] X. Zhang, X. F. Ma, Y. Jin, T. Lu, E. P. Boden, P. D. Phelps, K. R. Stewart and C. P. Yakymyshyn, "Terahertz optical rectification from a nonlinear organic crystal", *Appl. Phys. Lett.* **61**(26), 3080–3082 (1992).

[49] T. Taniuchi, S. Okada and H. Nakanishi, "Widely tunable terahertz-wave generation in an organic crystal and its spectroscopic application", *J. Appl. Phys.* **95**(11), 5984 (2004).

[50] T. Taniuchi, S. Ikeda, S. Okada and H. Nakanishi, "Tunable Sub-Terahertz Wave Generation from an Organic DAST Crystal", *Jpn. J. Appl. Phys.* **44**(21), L652 (2005).

[51] K. Suizu, K. Miyamoto, T. Yamashita and H. Ito, "Random frequency accessible broad tunable THz-wave source using phase-matched DAST crystal DFG", *Proc. of SPIE* **6103**, 61030A–1 (2006).

[52] K. Suizu, K. Miyamoto, T. Yamashita and H. Ito, "High-power terahertz-wave generation using DAST crystal and detection using mid-infrared powermeter", *Opt. Lett.* **32**(19), 2885–2887 (2007).

[53] R. Boyd, *Nonlinear Optics*, Academic Press (2008).

[54] E. R. Cohen, T. Cvitaš, J. G. Frey, B. Holmström, K. Kuchitsu, R. Marquardt, I. Mills, F. Pavese, M. Quack, J. Stohner, H. L. Strauss, M. Takami and A. J. Thor, *Quantities, Units and Symbols in Physical Chemistry*, RSC Publishing, Cambridge, 3rd edition (2007).

[55] J. E. Midwinter and J. Warner, "The effects of phase matching method and of crystal symmetry on the polar dependence of third-order non-linear optical polarization", *Brit. J. of Appl. Phys.* **16**, 1135 (1965).

[56] F. Pan, G. Knöpfle, C. Bosshard, S. Follonier, R. Spreiter, M. S. Wong and P. Günter, "Electro-optic properties of the organic salt 4-N,N-dimethylamino-4'-N'-methylstilbazolium tosylate", *Appl. Phys. Lett.* **69**(1), 13 (1996).

[57] P. Y. Han, M. Tani, F. Pan and X.-C. Zhang, "Use of the organic crystal DAST for terahertz beam applications", *Opt. Lett.* **25**(9), 675–677 (2000).

[58] M. Walther, K. Jensby, S. R. Keiding, H. Takahashi and H. Ito, "Far-infrared properties of DAST", *Opt. Lett.* **25**(12), 911–913 (2000).

[59] R. Seiler, *Rydbergzustandsaufgelöste-Schwellenionisationsspektroskopie*, PhD thesis, Eidgenössische Technische Hochschule Zürich, ETH Zürich, CH-8093 Zürich, Switzerland (2004), Diss. ETH Nr. 15591.

[60] Th. A. Paul, *Development and spectroscopic applications of a solid-state vacuum ultraviolet laser system in atomic and molecular physics*, PhD thesis, ETH Zurich, CH-8093 Zurich, Switzerland (2008), Diss. ETH Nr. 17814.

[61] D. Sprecher, M. Beyer and F. Merkt, "Precision Measurements of the Ionization Energy of the $3d\sigma$ GK state of H_2", *Mol. Phys.* **111**(14–15), 2100–2107 (2013).

[62] *IodineSpec, simulation software*, Toptica GmbH (2008).

[63] A. L. Schawlow, "Spectroscopy in a new light", *Rev. Mod. Phys.* **54**(3), 697–707 (1982).

[64] S. Gerstenkorn, J. Vergès and J. Chevillard, *Atlas du Spectre d'Absorption de la Molécule d'Iode: 11 000–14 000 cm^{-1}*, Laboratoire Aimé-Cotton CNRS II, Orsay (1982), see correction in [155].

[65] H. Katô, M. Baba, S. Kasahara, K. Ishikawa, M. Misono, Y. Kimura, J. O'Reilly, H. Kuwano, T. Shimamoto, T. Shinano, C. Fujiwara, M. Ikeuchi, N. Fujita, M. H. Kabir, M. Ushino, R. Takahashi and Y. Matsunobu, *Doppler-Free High Resolution Spectral Atlas of Iodine Molecule 15000 to 19000 cm^{-1}*, Japan Society for the Promotion of Science, Tokyo (2000).

[66] I. Velchev, R. van Dierendonck, W. Hogervorst and W. Ubachs, "A Dense Grid of Reference Iodine Lines for Optical Frequency Calibration in the Range 571–596 nm", *J. Mol. Spectrosc.* **187**(1), 21–27 (1998).

[67] B. Bodermann, G. Bönsch, H. Knöckel, A. Nicolaus and E. Tiemann, "Wavelength measurements of three iodine lines between 780 nm and 795 nm", *Metrologia* **35**(2), 105–113 (1998).

[68] B. Bodermann, M. Klug, U. Winkelhoff, H. Knöckel and E. Tiemann, "Precise frequency measurements of I_2 lines in the near infrared by Rb reference lines", *Eur. Phys. J. D* **11**(2), 213–225 (2000).

[69] B. Bodermann, H. Knöckel and E. Tiemann, "Widely usable interpolation formulae for hyperfine splittings in the $^{127}I_2$ spectrum", *Eur. Phys. J. D* **19**(1), 31–44 (2002).

[70] H. Knöckel, B. Bodermann and E. Tiemann, "High precision description of the rovibronic structure of the I_2 B-X spectrum", *Eur. Phys. J. D* **28**(2), 199–209 (2004). The reference data for calibration were derived from a calculation of the iodine hyperfine structure by the IodineSpec program.

[71] E. Salumbides, K. Eikema, W. Ubachs, U. Hollenstein, H. Knöckel and E. Tiemann, "Improved potentials and Born-Oppenheimer corrections by new measurements of transitions of $^{129}I_2$ and $^{127}I^{129}I$ in the B $^3\Pi_{0_u^+}$ – X $^1\Sigma_g^+$ band system", *Eur. Phys. J. D* **47**(2), 171–179 (2008).

[72] M. Raunhardt, *Generation and spectroscopy of atoms and molecules in metastable states*, PhD thesis, ETH Zurich, CH-8093 Zurich, Switzerland (2009), Diss. ETH Nr. 18260.

[73] A. Osterwalder and F. Merkt, "Using High Rydberg States as Electric Field Sensors", *Phys. Rev. Lett.* **82**(9), 1831–1834 (1999).

[74] K. S. Eikema and W. Ubachs, "Precision Laser Spectroscopy in the Extreme Ultraviolet", in M. Quack and F. Merkt (Editors), "Handbook of High-Resolution Spectroscopy", volume 2, pages 1373–1408, John Wiley & Sons, Chichester (2011).

[75] G. Hilber, A. Lago and R. Wallenstein, "Broadly tunable vacuum-ultraviolet/extreme-ultraviolet radiation generated by resonant third-order frequency conversion in krypton", *J. Opt. Soc. Am. B* **4**(11), 1753–1764 (1987).

[76] R. Hilbig and R. Wallenstein, "Tunable VUV radiation generated by two-photon resonant frequency mixing in xenon", *IEEE J. Quantum Electron.* **19**(2), 194–201 (1983).

[77] A. H. Kung, "Third-harmonic generation in a pulsed supersonic jet of xenon", *Opt. Lett.* **8**(1), 24–26 (1983).

[78] F. Merkt and H. Schmutz, "Very high resolution spectroscopy of high Rydberg states of the argon atom", *J. Chem. Phys.* **108**(24), 10033–10045 (1998).

[79] M. Schäfer, M. Andrist, H. Schmutz, F. Lewen, G. Winnewisser and F. Merkt, "A 240–380 GHz millimetre wave source for very high resolution spectroscopy of high Rydberg states", *J. Phys. B: At. Mol. Opt. Phys.* **39**(4), 831–845 (2006).

[80] J. Pietilä, V.-M. Horneman, R. Anttila, B. Lemoine, F. Raynaud and J.-M. Colmont, "The perpendicular fundamental ν_5 of chloroform $^{12}CH^{35}Cl_3$: high resolution infrared study of the ν_5 band together with the millimetre-wave rotational spectrum", *Mol. Phys.* **98**(9), 549–557 (2000).

[81] J. H. Carpenter, P. J. Seo and D. H. Whiffen, "The Rotational Spectrum of Chloroform in Its Ground and Excited Vibrational States", *J. Mol. Spectrosc.* **170**(1), 215 – 227 (1995).

[82] R. Anttila, S. Alanko and V.-M. Horneman, "The C-H bending vibration ν_4 of chloroform $CH^{35}Cl_3$", *Mol. Phys.* **102**(14-15), 1537–1542 (2004).

[83] A. Ruoff and H. Bürger, "Schwingungsspektren und Kraftkonstanten symmetrischer Kreisel–I. $HCCl_3$ und $DCCl_3$", *Spectrochim. Acta A* **26**(4), 989 – 997 (1970).

[84] R. J. H. Clark, O. H. Ellestad and R. Escribano, "The vapour phase Raman spectra, Raman band contour analyses, Coriolis coupling constants, and force constants for

the molecules $F^{12}CH_3$, $F^{13}CH_3$, $H^{12}CCl_3$ and $H^{13}CCl_3$", *Mol. Phys.* **31**(1), 65–81 (1976).

[85] D. Bermejo, R. Escribano and J. M. Orza, "Absolute Raman intensities of $CHCl_3$ and $CDCl_3$ and force field for chloroform", **6**(3), 151–154 (1977).

[86] R. J. H. Clark and O. H. Ellestad, "The vapor phase Raman spectra, Raman band contour analyses, Coriolis coupling constants, and *e*-species force constants of the molecules SPF_3, $FCCl_3$, and $BrCCl_3$", *J. Mol. Spectrosc.* **56**(3), 386 – 398 (1975).

[87] Ch. Haase, J. Liu and F. Merkt, "Vibrational spectra of chloroform, freon-11 and selected isotopomers in the terahertz region", *J. Mol. Spectrosc.* **262**(1), 61–63 (2010).

[88] P. Pracna, A. Ceausu-Velcescu and V.-M. Horneman, "The ground and $\nu_6 = 1$ vibrational levels of $HC^{35}Cl_3$: The first high-resolution analysis of the ν_6 fundamental band", *J. Quant. Spectrosc. Radiat. Transfer* **113**(11), 1220 (2012).

[89] M. J. Frisch *et al.*, "GAUSSIAN 03, Revision D.01", (2004), Gaussian, Inc., Wallingford, CT.

[90] F. Merkt, "Molecules in High Rydberg States", *Ann. Rev. Phys. Chem.* **48**, 675–709 (1997).

[91] G. Herzberg and Ch. Jungen, "Rydberg Series and Ionization Potential of the H_2 Molecule", *J. Mol. Spectrosc.* **41**(3), 425–486 (1972).

[92] E. Miescher, "High resolution absorption spectrum of nitric oxide (NO) in the region of the first ionization limit", *Can. J. Phys.* **54**(20), 2074–2092 (1976).

[93] R. Seiler, U. Hollenstein, G. M. Greetham and F. Merkt, "Rydberg-state-resolved zero-kinetic-energy photoelectron spectroscopy", *Chem. Phys. Lett.* **346**(3–4), 201–208 (2001).

[94] J. Berkowitz, *Photoabsorption, photoionization and photoelectron spectroscopy*, Academic Press, New York (1979).

[95] B. Ruscic, D. Feller and K. A. Peterson, "Active Thermochemical Tables: dissociation energies of several homonuclear first-row diatomics and related thermochemical values", *Theor. Chem. Acc.* **133**(1), 1415–1 (2014).

[96] S. Willitsch, Ch. Jungen and F. Merkt, "Bending energy level structure and quasilinearity of the $\tilde{X}^+\ ^3B_1$ ground electronic state of NH_2^+", *J. Chem. Phys.* **124**(20), 204312 (2006).

[97] F. Merkt, S. Willitsch and U. Hollenstein, "High-resolution photoelectron spectroscopy", in M. Quack and F. Merkt (Editors), "Handbook of High-Resolution Spectroscopy", volume 3, chapter 7, pages 1617 – 1654, John Wiley & Sons, Chichester (2011).

[98] J. Liu, E. J. Salumbides, U. Hollenstein, J. C. J. Koelemeij, K. S. E. Eikema, W. Ubachs and F. Merkt, "Determination of the ionization and dissociation energies of the hydrogen molecule", *J. Chem. Phys.* **130**(17), 174306 (2009).

[99] J. Liu, D. Sprecher, Ch. Jungen, W. Ubachs and F. Merkt, "Determination of the ionization and dissociation energies of the deuterium molecule (D_2)", *J. Chem. Phys.* **132**(15), 154301 (2010).

[100] D. Sprecher, J. Liu, Ch. Jungen, W. Ubachs and F. Merkt, "Communication: The ionization and dissociation energies of HD", *J. Chem. Phys.* **133**(11), 111102 (2010).

[101] J. Komasa, K. Piszczatowski, G. Łach, M. Przybytek, B. Jeziorski and K. Pachucki, "Quantum Electrodynamics Effects in Rovibrational Spectra of Molecular Hydrogen", *J. Chem. Theory Comput.* **7**(10), 3105–3115 (2011).

[102] H. A. Cruse, Ch. Jungen and F. Merkt, "Hyperfine structure of the ground state of para-D_2^+ by high-resolution Rydberg-state spectroscopy and multichannel quantum defect theory", *Phys. Rev. A* **77**(4), 042502 (2008).

[103] R. F. Stebbings, C. J. Latimer, W. P. West, F. B. Dunning and T. B. Cook, "Studies of xenon atoms in high Rydberg states", *Phys. Rev. A* **12**(4), 1453–1458 (1975).

[104] C. E. Moore, *Atomic Energy Levels*, NBS Circular 467/3, National Bureau of Standards, Washington, D.C. (1958).

[105] V. L. Sukhorukov, I. D. Petrov, M. Schäfer, F. Merkt, M.-W. Ruf and H. Hotop, "Photoionization dynamics of excited Ne, Ar, Kr and Xe atoms near threshold", *J. Phys. B: At. Mol. Opt. Phys.* **45**(9), 092001 (2012).

[106] H. Beutler, "Über Absorptionsserien von Argon, Krypton und Xenon zu Termen zwischen den beiden Ionisierungsgrenzen $^2P^o_{3/2}$ und $^2P^o_{1/2}$", *Z. Phys.* **93**(3–4), 177–196 (1935).

[107] K. D. Bonin, T. J. McIlrath and K. Yoshino, "High-resolution laser and classical spectroscopy of xenon autoionization", *J. Opt. Soc. Am. B* **2**(8), 1275–1283 (1985).

[108] K. Maeda, K. Ueda and K. Ito, "High-resolution measurement for photoabsorption cross sections in the autoionization regions of Ar, Kr and Xe", *J. Phys. B: At. Mol. Opt. Phys.* **26**(9), 1541–1555 (1993).

[109] J. A. R. Samson and D. L. Ederer (Editors), *Vacuum Ultraviolet Spectroscopy*, Academic Press, San Diego (2000).

[110] G. Racah, "On a New Type of Vector Coupling in Complex Spectra", *Phys. Rev.* **61**(7–8), 537 (1942).

[111] U. Fano, "Sullo spettro di assorbimento dei gas nobili presso il limite dello spettro d'arco", *Nuovo Cimento* **12**(3), 154–161 (1935).

[112] U. Fano, "Effects of Configuration Interaction on Intensities and Phase Shifts", *Phys. Rev.* **124**(6), 1866–1878 (1961).

[113] U. Fano and J. W. Cooper, "Line Profiles in the Far-uv Absorption Spectra of the Rare Gases", *Phys. Rev.* **137**(5A), A1364–A1379 (1965).

[114] R. P. Madden and K. Codling, "New Autoionizing Atomic Energy Levels in He, Ne, and Ar", *Phys. Rev. Lett.* **10**(12), 516–518 (1963).

[115] R. P. Madden and K. Codling, "Recently Discovered Auto-Ionizing States of Krypton and Xenon in the λ380–600-Å Region", *J. Opt. Soc. Am.* **54**(2), 268–269 (1964).

[116] J. Z. Wu, S. B. Whitfield, C. D. Caldwell, M. O. Krause, P. van der Meulen and A. Fahlman, "High-resolution photoelectron spectrometry of selected ns$'$ and nd$'$ autoionization resonances in Ar, Kr, and Xe", *Phys. Rev. A* **42**(3), 1350–1357 (1990).

[117] K. D. Bonin and T. J. McIlrath, "Generation of tunable coherent radiation below 1000 Å by four-wave mixing in krypton", *J. Opt. Soc. Am. B* **2**(4), 527–534 (1985).

[118] W. E. Ernst, T. P. Softley and R. N. Zare, "Stark-effect studies in xenon autoionizing Rydberg states using a tunable extreme-ultraviolet laser source", *Phys. Rev. A* **37**(11), 4172–4183 (1988).

[119] M. Spieweck, M. Drescher, F. Gierschner, R. Irrgang and U. Heinzmann, "High-resolution experimental determination of the angular distribution and spin polarization of xenon $7d'$ and $9s'$ photoelectrons and comparison with theoretical results", *Phys. Rev. A* **58**(2), 1589–1591 (1998).

[120] A. Kortyna, M. R. Darrach, P.-T. Howe and A. Chutjian, "High-resolution study of xenon autoionization using direct vacuum-ultraviolet laser excitation", *J. Opt. Soc. Am. B* **17**(11), 1934–1942 (2000).

[121] U. Hollenstein, H. Palm and F. Merkt, "A broadly tunable extreme ultraviolet laser source with a 0.008 cm^{-1} bandwidth", *Rev. Sci. Instr.* **71**(11), 4023–4028 (2000).

[122] Ch. K. Rhodes (Editor), *Excimer Lasers*, volume 30 of *Topics in Applied Physics*, Springer, Berlin, 2nd edition (1984).

[123] I. D. Petrov, V. L. Sukhorukov, T. Peters, O. Zehnder, H. J. Wörner, F. Merkt and H. Hotop, "Autoionizing even $2\mathrm{p}^5_{1/2}\, n\ell'[K']_{0,1,2}$ ($\ell' = 1, 3$) Rydberg series of Ne: Comparison of many-electron theory and experiment", *J. Phys. B: At. Mol. Opt. Phys.* **39**(16), 3159–3176 (2006).

[124] K. Harth, M. Raab, J. Ganz, A. Siegel, M.-W. Ruf and H. Hotop, "Spectroscopy of neon Rydberg states detected by electron transfer to SF_6 molecules", *Opt. Commun.* **54**(6), 343–348 (1985).

[125] J. Ganz, M. Raab, H. Hotop and J. Geiger, "Changing the Beutler-Fano Profile of the Ne (ns') Autoionizing Resonances", *Phys. Rev. Lett.* **53**(16), 1547–1550 (1984).

[126] P. M. Dehmer, S. T. Pratt and J. L. Dehmer, "Photoelectron spectra of xenon dimer (Xe_2^*) obtained by resonantly enhanced multiphoton ionization", *J. Phys. Chem.* **91**(10), 2593–2598 (1987).

[127] P. R. Blazewicz, J. A. D. Stockdale, J. C. Miller, T. Efthimiopoulos and C. Fotakis, "Four-photon excitation of even-parity Rydberg states in krypton and xenon", *Phys. Rev. A* **35**(3), 1092–1098 (1987).

[128] T. Peters, T. Halfmann, U. Even, A. Wünnenberg, I. D. Petrov, V. L. Sukhorukov and H. Hotop, "Experimental and theoretical investigation of even $mp^5_{1/2}$ np' autoionizing resonances of rare gas atoms", *J. Phys. B: At. Mol. Opt. Phys.* **38**(2), S51–S64 (2005).

[129] S. T. Pratt, P. M. Dehmer and J. L. Dehmer, "Photoelectron studies of resonantly enhanced multiphoton ionization of H_2 via the $B'\ ^1\Sigma_u^+$ and D $^1\Pi_u$ states", *J. Chem. Phys.* **86**(4), 1727–1732 (1987).

[130] S. M. Koeckhoven, W. J. Buma and C. A. de Lange, "Four-photon excitation of autoionizing states of Ar, Kr, and Xe between the $^2P_{3/2}$ and $^2P_{1/2}$ ionic limits", *Phys. Rev. A* **51**(2), 1097–1109 (1995).

[131] M. J. J. Vrakking and Y. T. Lee, "Lifetimes of Rydberg states in zero-electron-kinetic-energy experiments. II. Electric field induced and collisional enhancement of Xe autoionization lifetimes", *J. Chem. Phys.* **102**(22), 8833–8841 (1995).

[132] M. J. J. Vrakking, "Role of Core Interactions and External Perturbations in the Autoionization of Xe", *J. Phys. Chem. A* **101**(36), 6761–6769 (1997).

[133] F. Merkt and A. Osterwalder, "Millimeter wave spectroscopy of high Rydberg states", *Int. Rev. Phys. Chem.* **21**(3), 385–403 (2002).

[134] M. Schäfer, *private communication* (2014).

[135] R. Loudon, *The Quantum Theory of Light*, Oxford University Press, New York, 3rd edition (2000).

[136] E. Fermi, "Sopra lo spostamento per pressione delle righe elevate delle serie spettrali", *Nuovo Cimento* **11**(3), 157–166 (1934).

[137] Ch. Haase, J. A. Agner and F. Merkt, "High-resolution Laser Spectroscopy Between 0.9 and 14.3 THz in a Supersonic Beam: Rydberg-Rydberg Transitions of Atomic Xe at intermediate n values", *J. Chem. Phys.* **138**, 244202 (2013).

[138] R. Seiler, Th. Paul, M. Andrist and F. Merkt, "Generation of programmable near-Fourier-transform-limited pulses of narrow-band laser radiation from the near infrared to the vacuum ultraviolet", *Rev. Sci. Instr.* **76**(10), 103103 (2005).

[139] R. L. Aggarwal and B. Lax, "Optical mixing of CO_2 lasers in the far-infrared", in Y. R. Shen (Editor), "Nonlinear Infrared Generation", chapter 2, pages 19–80, Springer, New York (1977).

[140] V. I. Korobov, "Leading-order relativistic and radiative corrections to the rovibrational spectrum of H_2^+ and HD^+ molecular ions", *Phys. Rev. A* **74**(5), 052506 (2006).

[141] V. I. Korobov, "Relativistic corrections of $m\alpha^6$ order to the rovibrational spectrum of H_2^+ and HD^+ molecular ions", *Phys. Rev. A* **77**(2), 022509 (2008).

[142] R. E. Moss, "Calculations for the vibration-rotation levels of H_2^+ in its ground and first excited electronic states", *Mol. Phys.* **80**(6), 1541–1554 (1993).

[143] V. I. Korobov, L. Hilico and J.-P. Karr, "Theoretical transition frequencies beyond 0.1 ppb accuracy in H_2^+, HD^+, and antiprotonic helium", *Phys. Rev. A* **89**(3), 032511 (2014).

[144] A. Carrington, I. R. McNab and C. A. Montgomerie, "Microwave electronic spectrum of the H_2^+ ion", *Chem. Phys. Lett.* **160**(3), 237–242 (1989).

[145] K. B. Jefferts, "Rotational Hfs spectra of H_2^+ molecular ions", *Phys. Rev. Lett.* **20**(2), 39–41 (1968).

[146] K. B. Jefferts, "Hyperfine Structure in the Molecular Ion H_2^+", *Phys. Rev. Lett.* **23**(26), 1476–1478 (1969).

[147] Z. W. Fu, E. A. Hessels and S. R. Lundeen, "Determination of the hyperfine structure of $H_2^+(\nu = 0, R = 1)$ by microwave spectroscopy of high-L $n = 27$ Rydberg states of H_2", *Phys. Rev. A* **46**(9), R5313–R5316 (1992).

[148] P. W. Arcuni, E. A. Hessels and S. R. Lundeen, "Series mixing in high-L Rydberg states of H_2: An experimental test of polarization-model predictions", *Phys. Rev. A* **41**(7), 3648–3662 (1990).

[149] L. Åsbrink, "The photoelectron spectrum of H_2", *Chem. Phys. Lett.* **7**(5), 549–552 (1970).

[150] F. Merkt and T. P. Softley, "Final-state interactions in the zero-kinetic-energy-photoelectron spectrum of H_2", *J. Chem. Phys.* **96**(6), 4149–4156 (1992).

[151] C. Chang, C.-Y. Ng, S. Stimson, M. Evans and C. W. Hsu, "Rotationally resolved vacuum ultraviolet pulsed field ionization-photoelectron vibrational bands for H_2^+ (X $^2\Sigma_g^+$, $v^+ = 0 - 18$)", *Chin. J. Chem. Phys.* **20**(4), 352–364 (2007).

[152] J. Shen, A. Borodin, M. Hansen and S. Schiller, "Observation of a rotational transition of trapped and sympathetically cooled molecular ions", *Phys. Rev. A* **85**, 032519 (2012).

[153] U. Bressel, A. Borodin, J. Shen, M. Hansen, I. Ernsting and S. Schiller, "Manipulation of Individual Hyperfine States in Cold Trapped Molecular Ions and Application to HD^+ Frequency Metrology", *Phys. Rev. Lett.* **108**, 183003 (2012).

[154] D. Sprecher, C. Jungen and F. Merkt, "Determination of the binding energies of the np Rydberg states of H_2, HD, and D_2 from high-resolution spectroscopic data by multichannel quantum-defect theory", *J. Chem. Phys.* **140**(10), 104303:1–18 (2014).

[155] S. Gerstenkorn and P. Luc, "Absolute iodine (I_2) standards measured by means of Fourier transform spectroscopy", *Revue de Physique Appliquée* **14**(8), 791–794 (1979).

Christa Haase

Date of Birth: March 18. 1987
Address: Allenmoosstrasse 4, 8057 Zürich, Switzerland
Nationality: German

Education

03/2009-10/2014	**Ph.D. studies in Physical Chemistry, ETH Zurich,** group of Prof. F. Merkt: "Development of a broadly tunable, narrowband terahertz radiation source and spectroscopic applications in atomic and molecular physics".
03/2009	**M.Sc. in Chemistry, ETH Zurich.**
03/2008 – 08/2008	**Master thesis, Stanford University**, group of Prof. R. Zare: "Cavity Ring-Down Spectroscopy as Applied to Organic Molecules: Implementation of the novel system GC-C-CRDS".
09/2007	**B.Sc. in Chemistry, ETH Zurich.**
03/2007-06/2007	**Bachelor thesis, ETH Zurich**, group of Prof. V. Sandoghdar: "A Single Molecule Study of Shpol'skii Matrices at Elevated Temperatures"
07/2004	**Abitur** (high-school degree)**, Karls-Gymnasium Stuttgart**, Germany.

Additional Activities

Research Projects

02/2006 – 07/2006	**ETH Zurich**, group of Prof. E. Carreira: Selective β-Glycosidation of Secondary Alcohols.
07/2005 – 08/2005	**University of Illinois at Urbana-Champaign** (research scholar, fully funded)**,** group of Prof. E. Oldfield: Synthesis of Nitrogen-Containing and Non-Nitrogen-Containing Bisphosphonates.

Teaching Activities

10/2009-02/2010	**Lecturer** for scientific English at the "Aprentas Berufsfachschule" in Basel, Switzerland.
04/2006 – present	**Teaching assistant** for various courses taught at the Laboratory of Physical Chemistry, ETH Zurich.

Activities in Various Associations

03/2009-11/2011	**Union of the Assistants at the Chemical Laboratories of ETH Zurich (VAC):** vice president until 11/2009, afterwards representative of the Laboratory of Physical Chemistry.

01/2006 – 01/2008	**Union of Chemistry Students at ETH Zurich (VCS):** President, vice-president, editor of the student newspaper, member of various university boards.

Activities before College

Before 10/2004	**Student internships in chemistry and electronics** at the University of Stuttgart, the Max-Planck Institute for Chemical Physics of Solids (Dresden), the State Environmental Agency (Stuttgart), and at Washington University in St. Louis, MO.

Awards and Distinctions

09/2012	**Best poster presentation award,** fall meeting of the Swiss Chemical Society (SCS).
02/2005 – 03/2009	**Scholarship holder** of the "Studienstiftung des deutschen Volkes" (German National Academic Merit Foundation).
03/2004	**Admission** to the College of Arts and Sciences at Cornell University, Ithaca, NJ.
02/2004	**Second place** and special award from the Minister for the Environment at the regional science competition of "Jugend Forscht".

Additional Skills

Languages
English (native), German (native), French (elementary)

Programming/Scientific Software
C++ , Matlab, Perl, Fortran, Mathematica, LATEX

Interests

Sports (ironman training, marathon training)

Publications

1. "Activity of nitrogen-containing and non-nitrogen-containing bishposphonates on tumor cell lines"
   Y. Zhang, A. Leon, Y. Song, D. Studer, C. Haase, L. A. Koscielski and E. Oldfield
   J. Med. Chem., **49**, 5804 (2006).

2. "High-precision optical measurements of $^{13}C/^{12}C$ isotope ratios in organic compounds at natural abundance"
   R. N. Zare, D. S. Kuramoto, C. Haase, S. M. Tan, E. R. Crosson and N. M. R. Saad
   Proc. Natl. Acad. Sci. U. S. A., **106**, 10928, 2009.

3. "Vibrational spectra of chloroform, freon-11 and selected isotopomers in the terahertz region"
   C. Haase, J. Liu and F. Merkt
   J. Mol. Spectrosc., **262**, 61, 2010.

4. "High-resolution laser spectroscopy between 0.9 and 14.3 THz in a supersonic beam: Rydberg-Rydberg transitions of atomic Xe at intermediate n values"
   C. Haase, J. A. Agner and F. Merkt
   J. Chem. Phys., **138**, 244202, 2013.

5. "The fundamental rotational interval of para-H_2^+ by MQDT-assisted Rydberg spectroscopy of H_2"
   C. Haase, M. Beyer, Ch. Jungen and F. Merkt
   J. Chem. Phys., **142**, 064310, 2015.

Talks

1. "Vibrational spectra of chloroform, freon-11 and selected isotopomers in the terahertz region"
   65th International Symposium on Molecular Spectroscopy, Ohio State University, Columbus, OH, USA, June 2010.

2. "Interactions of highly excited Rydberg atoms with their environment as studied by THz transitions in an atomic beam"
   66th International Symposium on Molecular Spectroscopy, Ohio State University, Columbus, OH, USA, June 2011.

3. "Development of a broadly tunable, narrowband terahertz radiation source"
   Physical-Chemistry Colloquium, ETH Zurich, Switzerland, December 2013.

Poster presentations

1. "Rovibrational spectroscopy of small organic molecules in the THz frequency region"
   SCS Fall Meeting, ETH Zurich, Switzerland, September 2010.

2. "Perturbations in the spectra of high Rydberg states"
   SCS Fall Meeting, EPF Lausanne, Switzerland, September 2011.

3. "High-resolution, mass-selective spectroscopy in a supersonic jet between 1-14 terahertz: Rydberg spectroscopy of Xe"
   Gordon Research Conference on Electronic Spectroscopy and Dynamics, Bates College, Lewiston, ME, USA, July 2012.

4. "High-resolution, mass-selective spectroscopy in a supersonic jet between 1-14 terahertz: Rydberg spectroscopy of Xe"
   SCS Fall Meeting, ETH Zurich, Switzerland, September 2012.

5. "High-resolution, mass-selective spectroscopy between 1-14 terahertz: Rydberg spectroscopy of Xe Atom"
   11th European Conference on Atomic and Molecular Physics, Aarhus University, Aarhus, Denmark, June 2013.

6. "High-resolution, mass-selective spectroscopy in a supersonic jet between 1-14 terahertz"
   Leopoldina Symposium, ETH Zurich, Switzerland 2013.